# Enhanced Performance and Stability of Planar Heterojunction Solar Cells via Hole Transport Layer Engineering and Low-Cost Fabrication

by

Elaheh Habibzadeh

A thesis

presented to the University of Waterloo

in fulfillment of the

thesis requirement for the degree of

Doctor of Philosophy

in

Chemistry

Waterloo, Ontario, Canada, 2026

© Elaheh Habibzadeh 2026

## Examining Committee Membership

The following served on the Examining Committee for this thesis. The decision of the Examining Committee is by majority vote.

| | |
|---|---|
| External Examiner: | Jun Gao<br>Professor, Department of Physics, Engineering Physics & Astronomy<br>Queen's University |
| Supervisor | Kam Tong Leung<br>Professor, Department of Chemistry<br>University of Waterloo |
| Internal Member | Vivek Maheshwari<br>Associate Professor, Chemistry<br>University of Waterloo |
| Internal Member | Daniel Thomas<br>Associate Professor, Chemistry<br>University of Guelph |
| Internal Member | Siva Sivoththaman<br>Professor, Electrical and Computer Engineering<br>University of Waterloo |

## Author's Declaration

I hereby declare that I am the sole author of this thesis. This is a true copy of the thesis, including any required final revisions, as accepted by my examiners.

I understand that my thesis may be made electronically available to the public.

# Abstract

Global energy demand has grown extensively in recent decades, and it has continued to rely on fossil fuels that are accompanied with environmental concerns. This has intensified the research for renewable energy alternatives with solar power standing out as a leading candidate due to its abundance, scalability and rapidly declining costs. As photovoltaic (PV) technologies have evolved significantly, their widespread adoption continues to face barriers in efficiency, stability and manufacturing costs.

While inorganic semiconductors such as crystalline silicon remain dominant due to their favorable band gap and long-term stability, hybrid solar cells such as organic–inorganic heterojunction solar cells have gained increasing attention for their ability to combine the tunability and ease of processing of organics with the superior charge transport and stability of inorganics. In this work, we have investigated the stabilization of planar heterojunction solar cells through the incorporation of dimethyl sulfoxide (DMSO) into PEDOT:PSS-based hole transport layers (HTLs). The acidic and hygroscopic nature of PEDOT:PSS is a well-known source of device instability, leading to accelerated degradation under ambient conditions. By employing DMSO as a cosolvent alongside ethylene glycol and methanol, this work demonstrates that optimized modification enhances electrical conductivity, reduces recombination, and markedly improves stability. Devices incorporating DMSO-treated PEDOT:PSS films retain nearly 89.4% of their initial efficiency after 72 hours of ambient storage, in contrast to the sharp decline seen in control devices without DMSO. Atomic force microscopy (AFM) and X-ray photoelectron spectroscopy (XPS) confirm improved surface morphology and a favorable redistribution of conductive domains. The findings establish DMSO modification as a practical, cost-effective strategy for producing more inherently resilient heterojunction solar cells.

Following these insights, we introduce dimethyl sulfone ($DMSO_2$) as a solid-state additive for PEDOT:PSS films. Unlike liquid cosolvents, $DMSO_2$ crystallizes upon drying, inducing a unique reorganization of polymer microstructures that enhances phase separation and alignment of conductive PEDOT chains. The resulting films exhibit superior conductivity, improved charge transport, and greater stability against moisture induced degradation. Devices fabricated with $DMSO_2$-doped PEDOT:PSS achieve efficiencies up to 15.5% (EMD2) and an average $T_{80}$ of ~913 h of ambient storage (ED2), a substantial improvement over conventional treatment. Through a combination of external quantum efficiency (EQE), AFM, and conductivity analyses, this work

highlights the ability of $DMSO_2$ to simultaneously enhance efficiency and extend ambient storage longevity, offering an environmentally benign and scalable pathway for advancing PEDOT:PSS-based solar technologies.[1,2]

We also address the challenge of electrode optimization by introducing a rapid and low-cost method of shadow mask fabrication by desktop 3D printing. While electrode geometry is critical to current collection efficiency, series resistance reduction, and overall photovoltaic performance, traditional fabrication techniques are expensive, time-consuming, and inflexible. By employing polyethylene terephthalate glycol-modified (PETG) filaments for 3D printing, this study demonstrates a streamlined approach to fabricating custom shadow masks for top electrode manufacturing in hours rather than weeks. Comparative testing of three geometries (comb-like busbar, central busbar, and crossed busbar) shows that the central busbar design achieves superior efficiency enhancement by 21.62% and improves the fill factor by reducing resistive losses and balancing optical transparency. This work illustrates how low-cost additive manufacturing can democratize device prototyping, accelerate design iterations, and lower research and production costs without compromising performance.

In summary, this dissertation presents a cohesive exploration of strategies to improve efficiency, stability, and fabrication simplicity of planar heterojunction solar cells. Through targeted material modifications and innovative fabrication methods, the studies collectively highlight pathways to bridge laboratory innovation with commercial feasibility. Together, these contributions underscore the critical role of polymer modification and accessible fabrication in the evolution of next-generation solar cells, with the ultimate goal of advancing the prospects of clean, scalable, and sustainable energy technologies.

# Acknowledgements

I would like to express my deepest gratitude to my supervisor, Dr. Kam Tong Leung, for his invaluable guidance and support throughout my doctoral studies. His understanding and patience made this journey far beyond my expectations. His encouragement and insightful feedback have been instrumental in shaping both my research and my professional growth.

I am also sincerely thankful to my advisory committee members Dr. Yuning Li, Dr. Vivek Maheshwari and Dr. Daniel Thomas for their time, valuable suggestions, and constructive feedback, which greatly contributed to the quality and direction of my work.

My heartfelt appreciation goes to my colleagues and collaborators in the lab. I wish to thank Dr. Joseph Thomas, my main trainer, for his guidance, generosity in sharing knowledge, and countless discussions that helped me develop my skills as a researcher. I am also grateful to Dr. Nina Heinig, Dr. Lei Zhang, Dr. Wenyu Gao, Dr. Frank Guan, Dr. Hanieh Farkhondeh, and Dr. Mahdi Beedel for sharing their expertise, providing technical assistance, and fostering a collaborative and supportive environment. I must thank Kim Rawson, who went above and beyond to assist me through all the challenges along the way. I could not have made it here without her help and support.

I would also like to acknowledge the Waterloo Advanced Technology Laboratory (WATLab) for providing excellent research facilities and a stimulating environment for innovation. Special thanks to NSERC (Natural Sciences and Engineering Research Council of Canada) for the financial support that made this research possible.

Finally, I wish to thank my family for their unconditional love and support whenever I needed it most. To the love of my life, Pooya, thank you for making this journey enjoyable, for your endless encouragement, for listening to hours of discussion about my projects, and for always telling me I was right, no matter what!

# Dedication

To my mom, Fariba, for her love and encouragement.

To my father, who supported me every step of the way.

To my beautiful sister, Shahrzad, and her lovely family; Mehdi and little Nick.

And to my partner, Pooya, the rock of my life.

# Table of Contents

Examining Committee Membership ..... ii

Author's Declaration ..... iii

Abstract ..... iv

Acknowledgements ..... vi

Dedication ..... vii

List of Figures ..... xi

List of Tables ..... xv

List of Equations ..... xvi

List of Abbreviations ..... xvii

Chapter 1 Introduction ..... 1

1.1 Global energy demand and environmental challenges ..... 1

1.2 Working principles: Basic photovoltaic effect ..... 1

1.3 Fundamentals of solar cells ..... 4

1.4 Evolution of solar cells ..... 7

1.4.1 First generation of solar cells: Monocrystalline and polycrystalline silicon solar cells ..... 8

1.4.2 Second generation of solar cells: Thin film solar cells ..... 9

1.4.3 Third generation of solar cells: The promising technology ..... 10

1.5 Structure of organic–inorganic heterojunction solar cell ..... 13

1.5.1 n-type silicon wafer ..... 14

1.5.2 $SiO_X$ interfacial layer ..... 14

1.5.3 PEDOT:PSS polymer ..... 15

1.5.4 Electrodes ..... 16

1.6 Characterization methods ..... 18

1.6.1 X-ray photoelectron spectroscopy....18
1.6.2 Time-of-flight secondary ion mass spectrometry....20
1.6.3 Atomic force microscopy....22
1.6.4 Conductivity....24
1.6.5 Solar cell performance measurement....26
1.7 Scope of thesis....30
Chapter 2 Stabilization of Planar Heterojunction Solar Cells using a Dimethyl Sulfoxide Treated Hole Transport Layer....33
2.1 Introduction....33
2.2 Experimental Details....35
2.3 Results and Discussion....37
2.4 Conclusion....47
Chapter 3 Enhancing Performance and Stability of PEDOT:PSS-based Organic–Inorganic Planar Heterojunction Solar Cells through Dimethyl Sulfone Doping....48
3.1 Introduction....48
3.2 Experimental Details....51
3.3 Results and Discussion....52
3.4 Conclusion....66
Chapter 4 Rapid Low-Cost Fabrication of Shadow Masks using FDM 3D Printing for Precise Top-Electrode Patterning in Planar Silicon Heterojunction Solar Cells....67
4.1 Introduction....67
4.2 Experimental Details....71
4.3 Results and Discussion....73
4.4 Conclusion....83
Chapter 5 Conclusion and Future Work....85

5.1 Stabilization of planar heterojunction solar cells using a dimethyl sulfoxide treated hole transport layer ..... 85

5.2 Enhancing performance and stability of PEDOT:PSS-based planar organic–inorganic heterojunction solar cells through dimethyl sulfone doping ..... 86

5.3 Rapid low-cost fabrication of shadow masks using FDM 3D printing for precise top electrode patterning in planar silicon heterojunction solar cells ..... 86

5.4 Future work ..... 87

References ..... 92

Appendix ..... 124

# List of Figures

Figure 1.1: (a) A semiconductor absorbs a photon. (b) This promotes an electron from the valence band to the conduction band, creating a hole in the valence band. (c) The resulting electron and hole are transported to the electrodes for collection driven by an appropriate electric field. .....2

Figure 1.2: (a) A photon excites an electron in a semiconductor material with a low dielectric constant, generating an exciton (dashed green oval). (b) The exciton diffuses to the interface with a second material that has an offset in energy levels. (c) At the interface, the exciton dissociates into free charge carriers, which transfer into the second material. (d) The separated charges are then collected by the electrodes. .....3

Figure 1.3: J-V curve of a solar cell. $PD_{Max}$ is the maximum output power density (also known as maximum power point), given by the product of current density at maximum power ($J_{MP}$) and voltage at maximum power ($V_{MP}$). $J_{SC}$ is the short-circuit current density and $V_{OC}$ is the open-circuit voltage. 5

Figure 1.4: National Renewable Energy Laboratory chart tracking the highest confirmed conversion efficiencies for various photovoltaic technologies. This plot is courtesy of the National Renewable Energy Laboratory, Golden, CO.[34] .....8

Figure 1.5: Illustration of a typical device structure of a heterojunction solar cell. .....14

Figure 1.6: Photograph of a Thermo-VG Scientific ESCALab 250 microprobe XPS system. .....19

Figure 1.7: Photograph of a Thermo Scientific Nexsa G2 XPS system. .....20

Figure 1.8: Photograph of an ION-TOF 5 (IONTOF GmbH) time of flight secondary ion spectrometer with a 2 m reflectron TOF analyzer in negative ion mode, using a 30 kV $Bi_3^+$ analysis beam and a 5 kV $Ar_{2000}^+$ cluster ion sputter source. .....22

Figure 1.9: Photograph of an Asylum Research Cypher ES AFM with enclosed scanner. .....24

Figure 1.10: Photograph of an Ecopia HMS-5300 Hall effect measurement system for semiconductor carrier mobility and concentration. A four-point probe sample mount is shown in the right panel. ....26

Figure 1.11: Photograph of a PV Measurements IV5 I–V analyzer with probe station for solar cell testing. .....28

Figure 1.12: Photograph of a PV Measurements QEX10 EQE analyzer with light-tight enclosure and adjustable sample stage for photovoltaic device testing. .....30

Figure 2.1: Illustration of the device structure of a heterojunction solar cell. .....36

Figure 2.2: (a) Current density-voltage (J-V) curves for as-fabricated EM, EMD1, EMD3, and EMD5 solar cell samples, (b) J-V curves of EMD3 after 0 h, 48 h,72 h, 144 h, 168 h and 216 h of ambient storage and of EM after 0 h, 24 h, and 72 h of ambient storage. (c) Solar cell performance parameters

($J_{SC}$, $V_{OC}$, FF, and PCE) as functions of ambient storage time for EMD3 and EM cells. (d) Corresponding EQE spectra of as-fabricated EM and EMD3 solar cells. .....39
Figure 2.3: Solar cell performance parameters (a) $J_{SC}$, (b) $V_{OC}$, (c) FF, and (d) PCE of EM and three EMD3 cells as fabricated (black bars) and after 72 h of ambient storage (red bars). .....41
Figure 2.4: (a) Sheet resistance and (b) conductivity of EM, EMD1, EMD3 and EMD5 films as-deposited on glass substrates (black) and after 72 h of ambient storage (red). .....42
Figure 2.5: (a1, a2) XPS spectra of the S 2p region (left) and AFM images of (b1, b2) topography (center) and (c1, c2) phase (right) of EMD3 (a1, b1, c1) and EM films deposited on silicon substrates (a2, b2, c2). .....44
Figure 2.6: Schemes of proton sharing between (a) $PSS^-$ and EG and (b) PSSH and DMSO. .....45
Figure 3.1: (a) Sheet resistance and (b) conductivity of EM, ED2 and EMD2 films spin-coated on glass substrates. .....53
Figure 3.2: AFM images of surface topography (left column) and phase retrace (center column) and 3D perspective views of surface topography (right column) of (a1, a2, a3) EM, (b1, b2, b3) ED2 and (c1, c2, c3) EMD2 films spin-coated on silicon substrates. .....54
Figure 3.3: (a) XPS spectra of the S 2p regions for (top) EM, (middle) ED2 and (bottom) EMD2 films deposited on silicon. (b) the PEDOT/PSS ratio measured by the corresponding XPS depth profiling spectra of the EM, ED2 and EMD2 films (top 20 nm). (c) TOF-SIMS depth profiles of $C_8H_7SO_3^-$ (characteristic of PEDOT), $F^-$, $SiO_2^-$ and $Si^-$ fragments obtained with a 5 keV $Ar_{2000}^+$ sputtering beam and a 30 keV $Bi_3^+$ analysis beam. .....55
Figure 3.4: Illustrations of interactions of (a1) ethylene glycol (EG) with two PSSH (with interaction energy of –1.41 eV) and proton sharing of (a2) dimethyl sulfoxide (DMSO) with two PSSH (–1.69 eV) and (a3) dimethyl sulfone (DMSO2) with two PSSH (–1.89 eV), along with illustrations of interactions of (b1) EG with one $PSS^-$ (–1.20 eV) and proton sharing of (b2) DMSO with one PSSH (–1.22 eV) and (b3) $DMSO_2$ with one PSSH (–0.96 eV).[220] .....57
Figure 3.5: Illustration of the architecture of a heterojunction solar cell based on a cosolvent-treated PEDOT:PSS film on a silicon substrate. .....59
Figure 3.6: (a) Current density-voltage (J-V) profiles and (b) external quantum efficiency (EQE) spectra for as-fabricated EM, ED2 and EMD2 solar cell samples with the best performance. .....60
Figure 3.7: Degradation trends of solar cell performance metrics: $V_{OC}$, $J_{SC}$, FF and PCE as functions of ambient storage times for (a) EM (b) ED2 and (c) EMD2 solar cells. .....63

Figure 4.1: Electricity generated (kilowatt-hour per capita) from (a) coal and gas, and (b) solar, wind, and nuclear in Canada, Europe, USA and China from 2000-2024.Data are generated from Ember-energy.org website.[288] ..... 67
Figure 4.2: Fabrication workflow for PEDOT:PSS/Si heterojunction solar cells. (a) n-type Si(100) chips were sonicated for 10 min in acetone and IPA, then rinsed with ultrapure water. (b) Si chips were etched in 5% HF for 2 min, rinsed, and $N_2$ dried. (c) A 200-nm thick Al layer was deposited on the back sides of the chips to be used as the bottom electrode. (d) A PEDOT:PSS formulation (ED2 or EMD2) was dispensed and spin-coated at 4000 rpm for 60 s to form a uniform film. (e) The coating was annealed in air on a hotplate at 110 °C for 10 min. (f) A 50 nm Ag layer was sputter-deposited through a shadow mask (comb-like busbar, central busbar, or crossed busbar) to define the top electrode. All sputtering steps (for the bottom Al and top Ag electrodes) were performed in the same dual-target magnetron system (EMD 575X). ..... 72
Figure 4.3: Schematic representations of solar cells with selected top electrode designs: (a) comb-like busbar, (b) crossed busbar, and (c) central busbar. ..... 72
Figure 4.4: Photographs of shadow masks, with a central busbar design, made with (a, c) PLA and (b, d) PETG before (a, b) and after (c, d) undergoing the magnetron sputtering deposition process. The mask openings (gaps) that define the widths of deposited fingers and busbars are 350 microns wide, and the mask thickness is set to 400 microns. ..... 75
Figure 4.5: Shadow mask holders manufactured by CNC micro machining technique used for sputter-depositing silver. Right panel: Top cover with the central busbar pattern of the shadow mask. Left panel: Bottom holder with inset to tightly fix the Si substrate with a Ag central busbar top electrode sputter-deposited. The Si substrate is sandwiched snugly between the top cover and the bottom holder by means of four screws. ..... 77
Figure 4.6: Photographs of assembly of four shadow masks (top panel) and of their corresponding silver electrodes (lower panel), with (a1, b1) comb-like busbar, (a2, b2) crossed busbar and (a3, b3) central busbar electrode design made by 3D printing, and with (a4, b4) CNC micro machining. Sample grids (b1-b4) are $10\times10$ $mm^2$ and enlarged for better visualization. ..... 79
Figure 4.7: (a, b) Current density-voltage (J-V) curves and (c, d) external quantum efficiency (EQE) spectra of (a, c) EMD2 and (b, d) ED2 based solar cells with selected top electrode designs. ..... 81
Figure 5.1: SEM images demonstrating the tunability of microstructured silicon surfaces textured by RIE: (a) Periodic square array, (b) periodic hexagonal array, (c) alternating triangle matrix, and (d) randomly textured surface morphology produced under modified etching conditions. ..... 90

Figure 5.2: Device characterization of a PEDOT:PSS/textured-Si heterojunction solar cell fabricated on a textured silicon substrate using the EM solution. (a) SEM image of the textured surface coated with EM (b) J–V characteristics under AM 1.5G illumination.....91

# List of Tables

Table 3.1: Solar cell performance metrics including $V_{OC}$, $J_{SC}$, FF and PCE for as-fabricated EM, ED2 and EMD2 solar cell samples. The solar cell sample number is indicated after the hyphen. Samples marked with asterisks represent the respective EM, ED2, and EMD2 solar cell samples with the best performance and their J-V and EQE data are shown in Figure 3.6.....61
Table 4.1: Average photovoltaic performance metrics of ED2 and EMD2 solar cells fabricated with selected 3D-printed top electrode designs (comb-like busbar, crossed busbar, and central busbar). ...80

# List of Equations

Equation 1.1 ..... 4
Equation 1.2 ..... 4
Equation 1.3 ..... 6
Equation 1.4 ..... 18

# List of Abbreviations

| Abbreviation | Full Form |
|---|---|
| **$ABX_3$** | Generic perovskite chemical formula (A = cation, B = metal, X = halide) |
| **ABS** | Acrylonitrile butadiene styrene |
| **AFM** | Atomic Force Microscopy |
| **Ag** | Silver |
| **Al** | Aluminum |
| **AM1.5** | Air Mass 1.5 |
| **AM1.5G** | Air Mass 1.5 Global |
| **AM2** | Air Mass 2 |
| **a-Si** | Amorphous silicon |
| **BK7** | Borosilicate crown glass |
| **C101** | cis-Bis(isothiocyanato)(2,2′-bipyridyl-4,4′-dicarboxylato)(4,4′-bis(5-hexylthiophen-2-yl)-2,2′-bipyridyl)ruthenium(II) |
| **CAD** | Computer-Aided Design |
| **CdTe** | Cadmium telluride |
| **CIGS** | Copper indium gallium selenide |
| **CIS** | Copper indium selenide ($CuInSe_2$) |
| **$cm^2$** | Square centimeter |
| **CNC** | Computer Numerical Control |
| **c-Si** | Crystalline silicon |
| **CVD** | Chemical Vapor Deposition |
| **DC** | Direct Current |
| **DMSO** | Dimethyl sulfoxide |
| **$DMSO_2$** | Dimethyl sulfone |
| **BE** | Binding Energy |
| **EDOT** | 3,4-Ethylene-dioxy-thiophene |
| **EQE** | External Quantum Efficiency |
| **ESCA** | Electron Spectroscopy for Chemical Analysis |
| **ETL** | Electron Transport Layer |
| **eV** | Electron Volt |
| **$\varepsilon_r$** | Relative permittivity (dielectric constant) |

| | |
|---|---|
| **FF** | Fill Factor |
| **$FF_0$** | Ideal Fill Factor |
| **FTO** | Fluorine-Doped Tin Oxide |
| **fs** | Femtosecond |
| **GaAs** | Gallium arsenide |
| **$H_2O$** | Water |
| **HOMO** | Highest Occupied Molecular Orbital |
| **HSC(s)** | Heterojunction Solar Cell(s) |
| **HTL** | Hole Transport Layer |
| **IEC** | International Electrotechnical Commission |
| **IPCE** | Incident Photon-to-Current (Electron) Efficiency |
| **ITO** | Indium-Doped Tin Oxide |
| **IV / I–V** | Current–Voltage |
| **J–V** | Current Density–Voltage |
| **$J_{MP}$** | Current Density at Maximum Power |
| **$J_{SC}$** | Short-Circuit Current Density |
| **ISOS** | International summit on organic photovoltaic stability |
| **LUMO** | Lowest Unoccupied Molecular Orbital |
| **MEMS** | Microelectromechanical Systems |
| **meV** | Milli Electron Volt |
| **$N_2$** | Nitrogen |
| **$N_3$** | cis-Bis(isothiocyanato)bis(2,2′-bipyridyl-4,4′-dicarboxylato)ruthenium(II) |
| **N719** | Di-tetrabutylammonium cis-bis(isothiocyanato)bis(2,2′-bipyridyl-4,4′-dicarboxylato)ruthenium(II) |
| **NREL** | National Renewable Energy Laboratory |
| **$NiO_X$** | Nickel oxide |
| **nm** | Nanometer |
| **OLED** | Organic Light-Emitting Diode |
| **PCE** | Power-Conversion Efficiency |
| **$PD_{MAX}$** | Maximum Output Power Density |
| **PEDOT:PSS** | Poly(3,4-Ethylene-dioxy-thiophene):Poly(styrene sulfonate) |
| **PERC** | Passivated Emitter and Rear Cell |

| | |
|---|---|
| **PETG** | Polyethylene Terephthalate Glycol-Modified |
| **PLA** | Polylactic Acid |
| **p–n** | Junction between p-type and n-type regions |
| **p-type** | Hole-doped semiconductor |
| **$P_{in}$** | Input (Incident) Power |
| **ps** | Picosecond |
| **PSS** | Poly(styrene sulfonate) |
| **PTAA** | Poly(triarylamine) |
| **PV** | Photovoltaic |
| **PVD** | Physical Vapor Deposition |
| **QD** | Quantum Dot |
| **RF** | Radio Frequency |
| **RH** | Relative Humidity |
| **$R_{sh}$** | Shunt Resistance |
| **$R_s$** | Series Resistance |
| **Si** | Silicon |
| **$SiO_2$** | Silicon Dioxide |
| **SIMS** | Secondary Ion Mass Spectrometry |
| **$SnO_2$** | Tin Dioxide |
| **spiro-OMeTAD** | 2,2′,7,7′-Tetrakis[N,N-di(4-methoxyphenyl)amino]-9,9′-spirobifluorene |
| **TCO** | Transparent conductive oxide |
| **TFT** | Thin film transistor |
| **$TiO_2$** | Titanium Dioxide |
| **TOF-SIMS** | Time-of-flight secondary ion mass spectrometry |
| **UV** | Ultraviolet |
| **$V_{OC}$** | Open-Circuit Voltage |
| **VOCs** | Volatile Organic Compounds |
| **$V_{MP}$** | Voltage at Maximum Power |
| **XPS** | X-Ray Photoelectron Spectroscopy |
| **Z907** | cis-Bis(isothiocyanato)(2,2′-bipyridyl-4,4′-dicarboxylato)(4,4′-di-nonyl-2′-bipyridyl)ruthenium(II) |
| **ZnO** | Zinc Oxide |
| **µm** | Micrometer |

# Chapter 1
# Introduction

## 1.1 Global energy demand and environmental challenges

Driven by population growth and development, global energy demand continues to rise each year, and it is still met largely by fossil fuels. In 2024, fossil fuels accounted for roughly 86% of the world's primary energy mix.[3] This heavy reliance has led to significant greenhouse gas emissions and climate change concerns, underscoring an urgent need for cleaner, sustainable energy sources. Renewable energy technologies including solar, wind, and hydro power have experienced rapid growth and they now contribute a substantial share of new power capacity.[4] However, despite renewables providing about one-third of global electricity in 2024, they still supplied only ~8% of total global energy demand.[3] Scaling up renewable energy is thus essential to meet future demand and climate goals. Predictions indicate that the renewable energy contribution to the electricity sector will increase from 30% in 2023 to 46% by 2030, with the vast majority of this expansion coming from solar and wind power.[5] Among the green options, solar energy stands out for its abundance and scalability as the sunlight striking the Earth each hour could theoretically power humanity's annual energy needs. As solar costs have plummeted over the past decade, photovoltaic (PV) installations have surged, making solar power one of the fastest growing electricity sources worldwide. Solar energy delivers emission-free electricity and enhances energy security by reducing dependence on fossil fuels. As renewables do not require ongoing fuel purchases, their long-term costs tend to be lower and they are predicted to fall further as technology advances.[6,7] In this context, research into advanced and affordable solar cell technologies is of paramount importance to improve efficiency, reduce costs and enable vast involvement of solar panels to meet global energy demand with clean power.

## 1.2 Working principles: Basic photovoltaic effect

The PV effect is the process by which light, or photons, striking a semiconductor material creates a number of electron-hole pairs. Internal electric fields at the semiconductor junctions or selective contacts cause separation of the electron–hole pairs and drive the charge carriers to their respective electrodes, where they are collected to generate voltage and current.[8] Electron–hole pair dissociation differs between inorganic and organic semiconductors. When photons with energy equal to or greater than the bandgap of the inorganic semiconductor are absorbed, electrons are excited from the valence band into the conduction band, generating the charge carriers. In these semiconductors, dissociation can thermally occur at ambient temperature as the exciton has relatively low binding energy and

higher screening effect (Figure 1.1). On the other hand, organic semiconductors have lower screening effect and higher exciton binding energy, which does not allow for thermal dissociation under ambient conditions after photon illumination. Following a different path, the created exciton gets in contact with another material and diffuses to the interface of the second material, which leads to offset energy levels (Figure 1.2).

Inorganic crystalline semiconductors typically have high dielectric constants and delocalized electronic states and the binding energy of the created exciton is very small (often just a few meV).[9] However, organic solar cells suffer from lower efficiencies caused by the inherently low dielectric constant of most organic semiconductors ($\varepsilon_r < 6$). Low relative permittivity keeps excitons tightly bound (on the order of several hundred meV) and promotes unwanted charge carrier recombination.[9–13] By comparison, typical inorganic semiconductors and lead-halide perovskites possess larger dielectric constants ($\varepsilon_r > 10$), which lead to low exciton binding energy of roughly 10 meV and practically reduce recombination losses.[14]

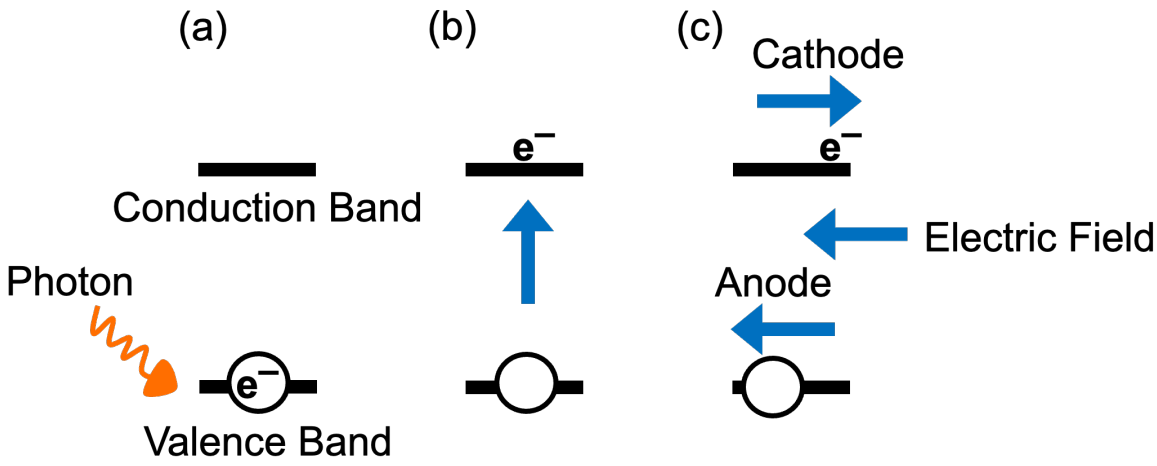



**Figure 1.1:** (a) A semiconductor absorbs a photon. (b) This promotes an electron from the valence band to the conduction band, creating a hole in the valence band. (c) The resulting electron and hole are transported to the electrodes for collection driven by an appropriate electric field.

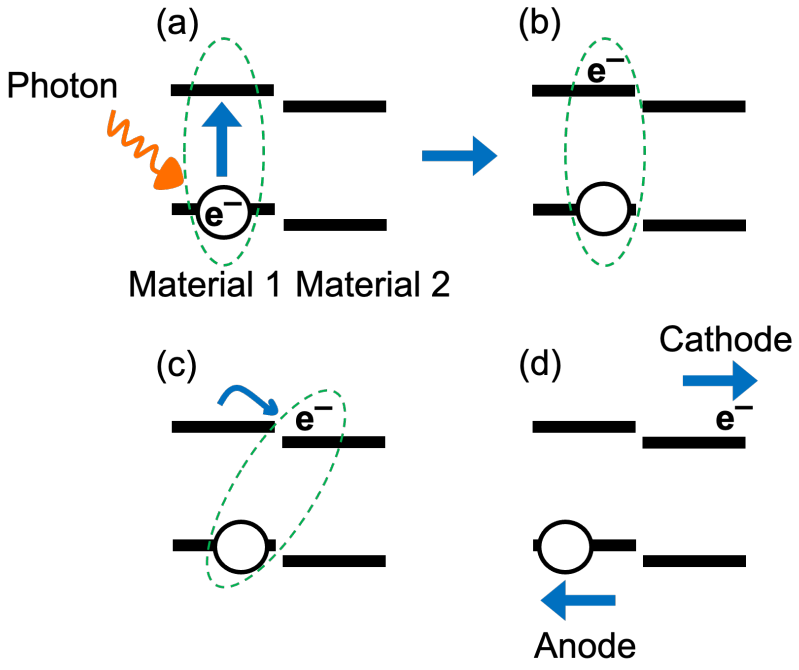



**Figure 1.2:** (a) A photon excites an electron in a semiconductor material with a low dielectric constant, generating an exciton (dashed green oval). (b) The exciton diffuses to the interface with a second material that has an offset in energy levels. (c) At the interface, the exciton dissociates into free charge carriers, which transfer into the second material. (d) The separated charges are then collected by the electrodes.

A p–n junction is formed between a p-type and an n-type semiconductor regions that are obtained by introduction of appropriate dopants. When the junction is formed, electrons diffuse from n to p region and holes from p to n region, leaving behind fixed ionized donors and acceptors. This creates a depletion region with an internal electric field and a built-in potential that opposes further diffusion. At thermal equilibrium the drift and diffusion currents cancel each other, so no net external current flows. Voltage and external current appear only when the junction is biased or illuminated. The connection of p-type and n-type semiconductor regions produces the built-in potential of this p-n junction. The original study by Shockley and Queisser in 1961 under 6000 K black body spectrum predicted a maximum theoretical efficiency of about 30% for a crystalline silicon solar cell with 1.1 eV bandgap. This semi-empirical analysis showed that the peak efficiency occurs at a band gap of roughly 1.1 eV, which is essentially the optical band gap of crystalline silicon.[15] Researchers then refined the Shockley and Queisser model by considering wafer thickness, absorption by free charge carriers, Auger recombination losses, and the light-trapping benefits of surface texturing. These

additions yield the modern Shockley and Queisser limit: roughly 33% for crystalline silicon and 28% for amorphous silicon under AM1.5G illumination. Therefore, the modern Shockley and Queisser limit defines the maximum theoretical conversion efficiency of a single-junction solar cell at approximately 33% under standard illumination conditions, bounded by fundamental losses in photon utilization and recombination.[16] In summary, the PV effect involves three fundamental processes: (1) the generation of charge carriers through photon absorption within the junction materials; (2) the separation of these photogenerated charge carriers at the junction interface; and (3) the collection of these carriers at the appropriate terminals of the junction.[17]

## 1.3 Fundamentals of solar cells

Critical performance metrics of a solar cell can be obtained from a current density vs voltage (J-V) plot shown in Figure 1.3, and they include the short-circuit current density ($J_{SC}$), the open-circuit voltage ($V_{OC}$), and the fill factor (FF), which together define the power-conversion efficiency (PCE). Specifically, PCE is determined by the relationship:

$$PCE = \frac{Output\ power\ (electric)}{Input\ power\ (light)} = \frac{V_{OC}\ \times J_{SC} \times\ FF}{P_{in}} \qquad \text{Equation } \mathbf{1.1}$$

where FF is:

$$FF = \frac{J_{MP} \times V_{MP}}{J_{SC} \times V_{OC}} \qquad \text{Equation } \mathbf{1.2}$$

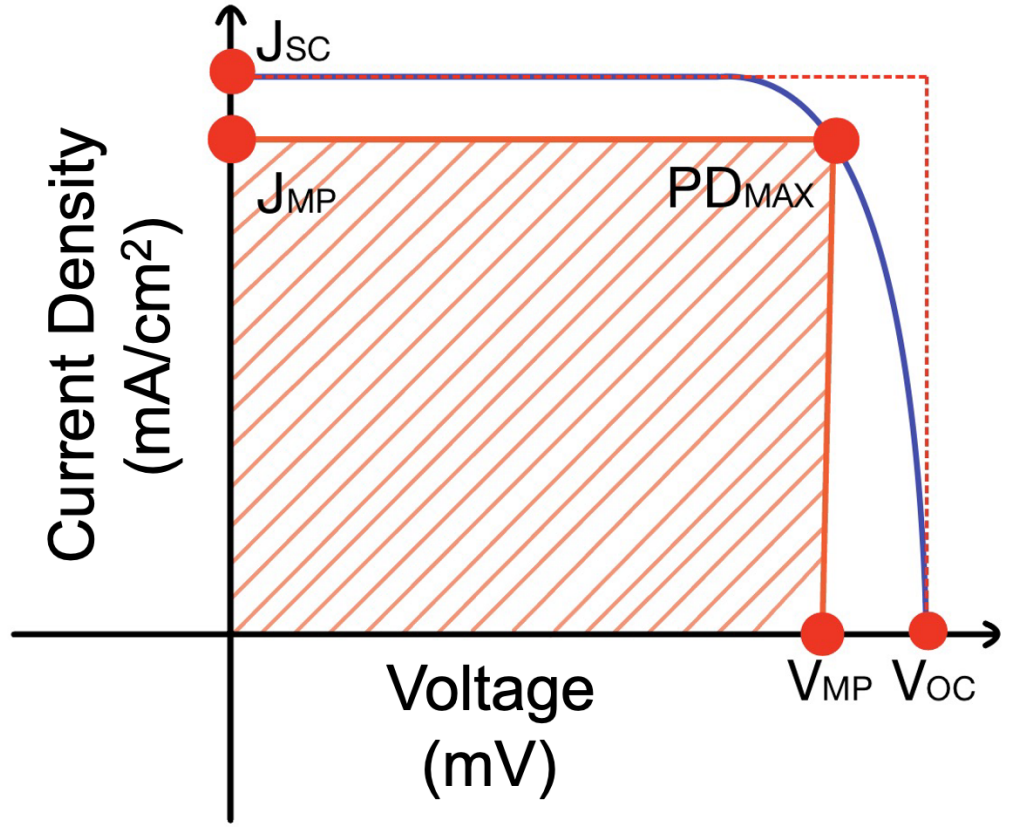



**Figure 1.3:** J-V curve of a solar cell. $PD_{Max}$ is the maximum output power density (also known as maximum power point), given by the product of current density at maximum power ($J_{MP}$) and voltage at maximum power ($V_{MP}$). $J_{SC}$ is the short-circuit current density and $V_{OC}$ is the open-circuit voltage.

$J_{SC}$ represents the maximum current density achievable when the solar cell is operated with no external voltage applied (i.e., under short-circuit condition). It directly correlates to the number of photogenerated charge carriers collected. $V_{OC}$ is the maximum voltage that the cell can deliver when no external current is drawn (i.e. under open-circuit condition), and it is governed by the energy difference between the electron and hole quasi-Fermi levels. FF is the ratio of the maximum power density from the solar cell ($V_{MP} \times J_{MP}$) to the upper-bound reference power density given by $V_{OC} \times J_{SC}$. FF indicates how effectively the cell converts photogenerated carriers into electrical power, thus reflecting the overall quality and efficiency of charge extraction within the device.

FF is affected by two types of resistance existing in the device: series resistance ($R_S$) and shunt resistance ($R_{Sh}$):[18]

$$\mathrm{FF} = \mathrm{FF}_0\left(1 - R_S\frac{J_{SC}}{V_{OC}}\right)\left(1 - \frac{1}{R_{Sh}}\frac{V_{OC}}{J_{SC}}\right) \qquad \text{Equation } \mathbf{1.3}$$

where $FF_0$ is the ideal fill factor with no losses arising from parasitic resistance rooting from $R_S$ and charge recombination at the interfaces. FF becomes smaller when the conductivity of electrode material is low and a defective electrode interface is created due to the poor deposition method.[19] In a solar cell, contact resistance refers to the resistance at the interface where a metal contact is connected to the semiconductor. If this contact is poor, it restricts current flow right at the entry/exit point. Series resistance is the total resistance that the current experiences along its intended path through the cell, including contact resistance, the metal fingers/busbars, and the transport/semiconductor layers. A high series resistance wastes power and lowers the fill factor. On the other hand, shunt resistance represents unwanted low-resistance paths that allow the current to leak sideways across the cell and bypass the external circuit. Shunt resistance is typically caused by defects or contamination, and a low shunt resistance reduces voltage and efficiency. For optimal performance, solar cells need low contact and series resistances, and high shunt resistance.

A p-n junction can be classified based on its structural and energetic characteristics. A traditional p-n junction solar cell employs a single semiconductor material with controlled doping variations, resulting in continuous and smooth energy band bending. In contrast, a heterojunction solar cell consists of two distinct semiconductor materials interfaced together, each with different electronic properties. This arrangement creates abrupt energy-level steps at the interface, effectively aiding in selective charge carrier extraction. For a Schottky junction that forms at a metal-semiconductor interface, energy bands inside the semiconductor bend significantly close to the interface due to the alignment of the Fermi level of the semiconductor with that of the metal. The extent and shape of this band bending depend on the specific metal-semiconductor combination. The PV performance of a Schottky junction solar cell is limited primarily by the Schottky barrier height determined by the difference between the metal work function and the relevant band edge of the semiconductor (conduction band for n-type, valence band for p-type). This barrier determines how effectively electrons or holes can be transported across the metal-semiconductor interface and be extracted.

Organic–inorganic heterojunction solar cells (HSCs) have emerged as a particularly intriguing class of photovoltaic devices, by taking the advantages of both organic and inorganic semiconductors. While versatile and processable via cost-effective solution methods, organic semiconductors possess

inherently low dielectric constants ($\varepsilon_r < 6$, where $\varepsilon_r$ is also known as the relative permittivity). This low dielectric constant results in tightly bound excitons (with exciton binding energies often exceeding 300 meV), limiting free charge carrier generation and enhancing recombination. On the other hand, inorganic semiconductors, including silicon, metal oxides, and hybrid perovskites, typically exhibit significantly higher dielectric constants ($\varepsilon_r > 10$), which lead to reduced exciton binding energies (of typically a few to tens of meV) and efficient generation of free charge carriers. At the interface of an organic–inorganic HSC, the stark difference in dielectric properties creates beneficial energetic offsets and interfacial electric fields. This interfacial energetics facilitates rapid exciton dissociation at the interface into free electrons and holes. The inorganic layer commonly serves as an efficient electron-hole generation and dissociation medium, while the organic semiconductor contributes to the charge transport, absorption tunability, ease of processing, and morphological control. Thus, by carefully selecting and engineering materials and the interface chemistry, an organic–inorganic HSC synergistically integrates the corresponding strengths of organic and inorganic components. For example, employing an n-type silicon substrate coated with a p-type organic polymer can significantly enhance the device performance. In this heterojunction structure, the conduction band of n-type silicon must be aligned energetically with the lowest unoccupied molecular orbital (LUMO) of the p-type polymer, creating a favorable offset that effectively blocks electron transfer into the organic layer, thus reducing recombination losses. Meanwhile, the valence band of silicon should be aligned closely with the highest occupied molecular orbital (HOMO) of the organic layer, facilitating efficient hole extraction. The addition of cosolvents or additives can improve the conductivity and morphology of the organic polymers, further optimizing interfacial energetics and charge transport properties that ultimately enhance the overall device performance.[20–31] The chemistry underlying the synthesis, interface functionalization, and morphological optimization of these hybrid structures remains central to ongoing efforts aimed at increasing their photovoltaic performance and operational stability.

## 1.4 Evolution of solar cells

Solar cells can be primarily classified into three generations.[32] The first generation consists of bulk silicon solar cells, including single-crystalline and polycrystalline cells. The second generation encompasses thin-film solar cells such as cadmium telluride (CdTe), copper indium gallium selenide (CIGS), gallium arsenide (GaAs), copper indium selenide ($CuInSe_2$) and amorphous silicon cells. The third generation, which is the category to be discussed in more detail, includes organic solar cells, organic–inorganic heterojunction solar cells, perovskite solar cells, dye-sensitized solar cells and

quantum dot-sensitized solar cells.[32,33] Figure 1.4 shows the evolution of different categories of solar cells, as reported by the National Renewable Energy Laboratory (NREL).

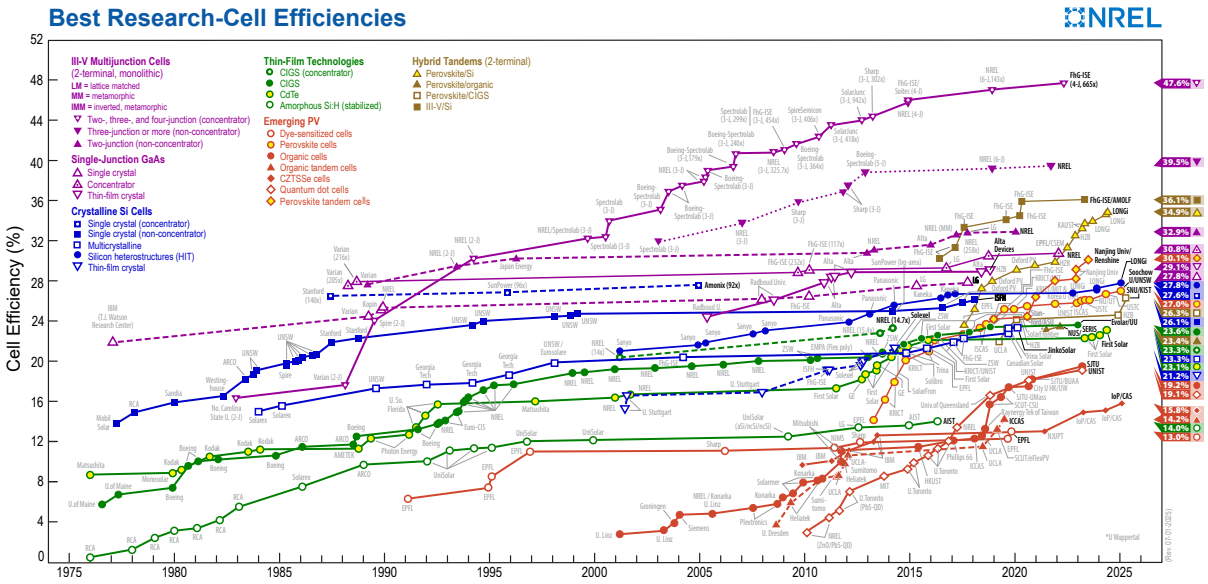



**Figure 1.4:** National Renewable Energy Laboratory chart tracking the highest confirmed conversion efficiencies for various photovoltaic technologies. This plot is courtesy of the National Renewable Energy Laboratory, Golden, CO.[34]

### 1.4.1 First generation of solar cells: Monocrystalline and polycrystalline silicon solar cells

Monocrystalline silicon solar cell is the very first cell that was introduced in 1954.[35] The defectless and continuous single-crystal lattice is typically grown using the Czochralski crystal pulling process.[36] Czochralski growth melts silicon near its melting point (1414 °C) in a quartz crucible, which makes crystal pulling and wafering capital-intensive with high energy consumption.[37] As the absence of grain boundaries enhances charge carrier mobility and lowers the recombination,[36,38] monocrystalline Si cells achieve very high efficiencies even in low-light conditions when compared to polycrystalline ones. However, the complex and energy-intensive manufacturing process of monocrystals is very energy demanding.[39] In recent years, mass production of raw silicon has made these cells price-competitive with thin-film alternatives.[39–43] The current highest efficiency for a single junction monocrystalline solar cell is 26.81%.[44]

Polycrystalline (multicrystalline) silicon solar cells are made by melting silicon feedstock and casting it into square crucibles, where the melt undergoes directional solidification to form an ingot with multiple crystal grains.[45,46] This directional solidification process is much less complex and less expensive compared to that of monocrystalline solar cells, which initially led to the widespread adoption of polycrystalline solar cells in large-scale commercial applications.[47–51] However, the grainy texture of polycrystalline cells causes lower efficiency due to increased recombination losses at the grain boundaries.[38,52] Since the cost gap between polycrystalline and monocrystalline Si solar cells has narrowed over the past decade, monocrystalline solar cells now make up 84% of the market, while polycrystalline cells account for 11%.[53] The first polycrystalline silicon solar cell was introduced in 1981, and its efficiency has reached 24.4% since then.[54,55]

To date, conventional first generation of solar cells, particularly silicon PV, dominate 98% of current market.[56] Crystalline silicon cells have achieved power conversion efficiencies exceeding 26% in the laboratory and ~23% in mass production of passivated emitter rear cell (or PERC) technology, with long-term stability over 25 years.[44,57–59] They form the backbone of today's solar industry due to their high efficiency and reliability. Recent industry announcements, such as Longi Green Energy's achievement of 27.81% efficiency for a hybrid interdigitated back contact cell, reported by PV-magazine,[60] demonstrate this progress.[61] This efficiency was certified by the Institute for Solar Energy Research in Hamelin, Germany indicating its credibility.

### 1.4.2 Second generation of solar cells: Thin film solar cells

Inorganic thin-film PV technologies or second generation of solar cells (including amorphous silicon, CdTe, CIGS, GaAs solar cells) have also reached notable efficiencies since their first fabrication. These ultrathin films can be deposited on glass, metal foils and flexible polymers for making lightweight and bendable devices. The reduction of active material contributes to lowering the cost significantly. However, the large scale fabrication of these cells are complex and their production was limited by the necessity of having control over the entire process until 2006.[62,63] At that time, the increase of the silicon price shifted the attention toward these devices and the number of published papers showed an exponential growth.[63] One of the widely manufactured solar cells in this category is the amorphous silicon cells, which were much cheaper to make than the first generation solar cells that were first developed in 1965.[63] Lower efficiencies (9.5-12.24% as reported by producers and 8% advertised for commercial uses) and stability were, however, expected because much thinner layers were involved. Other thin film cells such as CIGS/CIS and CdTe showed more competitive results to crystalline solar cells with less energy demanding productions.[63] For example, a record efficiency of

27.6% has been reported for a single junction GaAs thin film solar cell under 1 sun illumination at 25 ºC.[64] Material scarcity,[65] high cost of CdTe[66] and environmental concerns[67] are the major drawbacks of their manufacturing process.

### 1.4.3 Third generation of solar cells: The promising technology

The third generation of solar cells are more diverse. The utilization of different materials reduces the cost of solar energy significantly while providing high efficiencies.[68–71] These solar cells were first introduced in 2001 by Martin Green.[72] Today, the highest certified power-conversion efficiency for a single-junction perovskite solar cell is 26.7%.[73] Four main types of third-generation devices are organic solar cells, perovskites solar cells, dye sensitized solar cells and quantum dot solar cells.

Organic solar cells use carbon-based molecular or polymer semiconductors and they offer advantages in terms of light weight, flexibility, potential for low-cost roll-to-roll manufacturing, solution processibility at low temperatures by implementing green solvents.[74–77] Over the past decade, improvements in organic donor and acceptor materials as well as device architectures have boosted the efficiency of single junction organic solar cells from 1% (under AM2 illumination) to nearly 20.8% (under AM1.5G at 1000 W/m$^2$).[78,79] In another example, a single junction organic solar cell with an asymmetric non-fullerene acceptor (Z8) has achieved 20.2% efficiency.[78] Despite this progress, organic solar cells still trail inorganic cells in efficiency and they tend to suffer from stability issues (such as photo-degradation, and oxygen/moisture sensitivity) that have so far limited their commercial adoption.[80–83]

Organic–inorganic heterojunction solar cells are typically formed by combining a crystalline silicon substrate (most often n-type c-Si) with a solution processable organic semiconductor layer (of polymer or small molecules) that serves as a charge-selective contact.[84–88] The purpose is to take advantage of the strengths of both types of materials, with silicon providing a high-quality photovoltaic absorber and transport medium, while the organics offering chemically tunable charge selective layers that are solution processible and can be deposited and baked under low-temperature condition (typically room temperature to below 200 °C).[49,84,89] The electronic properties of polymers such as their energy levels (LUMO/HOMO) and band gap can be tuned simply by addition of cosolvents or additives. Thanks to their versatile mechanical properties, organic layers can be used in flexible devices as well.[84,90] Conductive polymers (e.g., PEDOT:PSS) or small molecules can function as dopant-free hole/electron-selective partners to silicon, forming a heterojunction structure without any need for conventionally expensive, complex and energy demanding emitter diffusion or

ion implantation preparation.[91] Simply coating a p-type polymer such as PEDOT:PSS onto an n-type silicon wafer yields a functional solar cell, thereby avoiding the thermal budgets of diffused p–n junctions. Electrons and holes are then separated, transported, and collected by electrodes. In recent studies on PEDOT:PSS/Si heterojunction solar cells, the shared strategy is to engineer interfaces and tune the work function of PEDOT:PSS to strengthen the built-in electric field, improve charge separation, and suppress recombination.[92–94] The present work will focus on this particular type of solar cells, with details of the cell structure given in the next section.

Perovskite solar cells have attracted a lot of recent attention. Metal-halide perovskites ($ABX_3$) are used as the light absorber and their performances have risen rapidly from their first photovoltaic demonstration in 2009.[95] These materials exhibit high absorption coefficients ($2.5 \times 10^4$ $cm^{-1}$ to $8.7 \times 10^4$ $cm^{-1}$)[96] and long carrier-diffusion lengths (>1 μm in some polycrystalline films [97] and >175 μm in single crystals[98]), which allows the photons to become mobile charges. They have the least defective electronic structures with tunable band gaps (~1.2 to ≥ 2.3 eV), which make them particularly attractive for single-junction and tandem cells. Perovskite solar cells can be fabricated by low temperature and solution-based processes, while flexible substrates and multiple slot-die/printing routes have been demonstrated for a scalable coating.[99–101] Typically, these cells have a five layer structure. The $ABX_3$ layer with a tunable band gap absorbing most photons in the visible region even with thickness < 1 μm.[102,103] Below the $ABX_3$ layer lies the electron transport layer (ETL), for which $SnO_2$ or $TiO_2$ is usually used. The conduction band of the ETL must align with that of $ABX_3$ to extract the electrons, block the holes, and reduce the recombination losses.[104,105] The layer in charge of receiving the holes is called the hole transport layer (HTL). Unlike the ETL, the HTL such as doped 2,2′,7,7′-Tetrakis[N,N-di(4-methoxyphenyl)amino]-9,9′-spirobifluorene (or spiro-OMeTAD), poly[bis(4-phenyl)(2,4,6-trimethylphenyl)amine (or PTAA) or $NiO_x$ could block electrons and facilitate the creation of internal electric field that drives the charge transport.[106] Finally, the electrons and hole carriers are transferred to the appropriate electrodes, which could be Fluorine-doped Tin Oxide (FTO) or Indium-doped Tin Oxide (ITO) in the front and a carbon or metal based electrode in the rear side. Even though the commercialization of perovskite solar cells has already been achieved in 2021 by Saule Technologies,[107] it faces significant obstacles such as the stability issue. Solar cells are supposed to be capable of withstanding harsh environmental conditions in terms of temperature, humidity and exposure to the full solar spectrum, but high relative humidity has been found to significantly reduce the device life. The highest PCE record of 26.7% for a single junction perovskite

solar cell was made by University of New South Wales and Soochow University and confirmed by NREL.[73]

A dye sensitized solar cell has four main components: (1) photoanode, (2) dye sensitizer (or light harvester), (3) electrolyte, and (4) counter electrode.[108,109] The photoanode is a nanostructured semiconductor (particles, rods, tubes, cones, wires and leaves) that is coated on a transparent conductive oxide (TCO) glass substrate such as ITO and FTO. The most common photoanode is $TiO_2$ due to its low cost, abundance and lack of toxicity.[110] However, ZnO is believed to outperform $TiO_2$.[111] After photoanode deposition and sintering, the coated glass is soaked in a dye solution, such as Di-tetrabutylammonium cis-bis(isothiocyanato)bis(2,2′-bipyridyl-4,4′-dicarboxylato)ruthenium(II) (or N719), cis-Bis(isothiocyanato)bis(2,2′-bipyridyl-4,4′-dicarboxylato)ruthenium(II) (or N3), cis-Bis(isothiocyanato)(2,2′-bipyridyl-4,4′-dicarboxylato)(4,4′-bis(5-hexylthiophen-2-yl)-2,2′-bipyridyl)ruthenium(II) (or C101) and cis-Bis(isothiocyanato)(2,2′-bipyridyl-4,4′-dicarboxylato)(4,4′-di-nonyl-2′-bipyridyl)ruthenium(II) (or Z907), so the dye can chemically bind to the $TiO_2$. The important component that absorbs the photon and converts it to energy is the dye, so it should be able to absorb the most amount of photons in the visible range.[112] The process begins when a photon strikes a dye molecule that is adsorbed onto the surface of a porous $TiO_2$ layer. The energy of the photon excites an electron in the dye, promoting it from the ground state (HOMO) into the excited state (LUMO). The excited electron in LUMO has enough energy to transfer into the conduction band of the $TiO_2$. This transfer is extremely fast (typically occurring within 100 fs – 100 ps)[113] and the electron hops from the dye into the photoanode. From there, the electron migrates through the interconnected $TiO_2$ network, moves into FTO/ITO, and then flows into the external circuit.[110] From the stable and low resistant counter electrode, the electrons are then transported to the electrolyte to facilitate the redox reaction.[114] In order to avoid charge recombination and the reductions in $V_{OC}$ and $J_{SC}$, different additives such as pyridine and its derivatives, 4-tert-butyl pyridine, and N-methyl benzimidazole are added to the electrolyte.[115] Electrolytes can be solid, liquid or quasi-solid. Typically, solvents with higher dielectric constants and moderate viscosity are used as the organic solvents in the liquid electrolytes.[71] Redox couple is also added as a reduction/oxidation agent to the electrolytes to enhance the performance.[116] The highest PCE reported so far is 15.2% under AM1.5G, which has used pre-adsorbed hydroxamic-acid monolayers to optimize co-sensitized $TiO_2$ photoanodes.[117] Plastic substrates restrict the thermal processing of a dye sensitized solar cell to below 150 °C. Under those mild conditions, binder-free $TiO_2$ films tend to crack, adhere weakly, admit moisture and oxygen, and develop high electrical resistance, all of which shorten the device

life. Achieving competitive performance will require low-temperature encapsulation and redesigned pastes or interlayers that bond the semiconductor firmly to plastic without high-heat sintering, thereby boosting both efficiency and stability.[71]

In quantum dot (QD) solar cells, the absorbing material is a continuous, nanoscale solid film (or layer) of colloidal QDs (such as PbS, CdS and CdSe) sandwiched between an ETL and a metal back contact. Like a thin-film semiconductor junction, the generated electrons and holes percolate through the QD network toward the opposite electrodes. Therefore the implementation of electrolyte is not necessary for the charge transfer, especially in the solid-state designs.[118] The QD sensitized solar cell is slightly different from QD solar cells, as it makes use of a monolayer or a few layers of QD sensitizers as coating on a mesoporous film of photoanode (such as $TiO_2$) and the remaining pores are filled with a liquid or solid redox electrolyte. In this QD sensitized solar cell, the excited electrons are injected into the $TiO_2$ film while the holes are transported through the electrolyte to the counter electrode. As isolated QDs do not transfer the charges laterally, $TiO_2$ and the electrolyte provide the main charge transfer media. The numerous outstanding features of QDs, such as size-tunable band gap, broad absorption spectrum, discrete energy levels, excellent transport and optical properties, have generated a lot of interest about these cells.[119–121] The necessity of having electrolyte (specifically liquid ones) in the QD sensitized solar cell structure represents their major stability and corrosion issues.[121–123] The highest PCEs reported for a solid state QD solar cell (based on perovskites) and a QD sensitized solar cell are 18.1% and 19.1%, respectively.[34,124]

## 1.5 Structure of organic–inorganic heterojunction solar cell

A typical organic–inorganic heterojunction solar cell is composed of five key components: the n-type silicon wafer, a $SiO_2$ interfacial layer, the p-type organic layer (PEDOT:PSS), the bottom and top electrodes (aluminum and silver, respectively). Each component plays a distinct role in light absorption, charge separation, and carrier transport, collectively determining the device's efficiency, stability, and manufacturability. When n-type silicon comes in contact with PEDOT:PSS with a high work function, band bending forms in Si, creating a built-in electric field that separates photogenerated carriers. Electrons are driven through the n-Si and collected at the aluminum bottom electrode, while holes are selectively transferred from the Si valence band into the HOMO of PEDOT:PSS and extracted at the silver top electrode. The LUMO of PEDOT:PSS lies high in energy, helping to block electrons and reduce interfacial recombination (Figure S1-1). Figure 1.5 shows a typical device structure of a heterojunction solar cell. The following sections describe the structure, function, and material properties of these components in more detail.

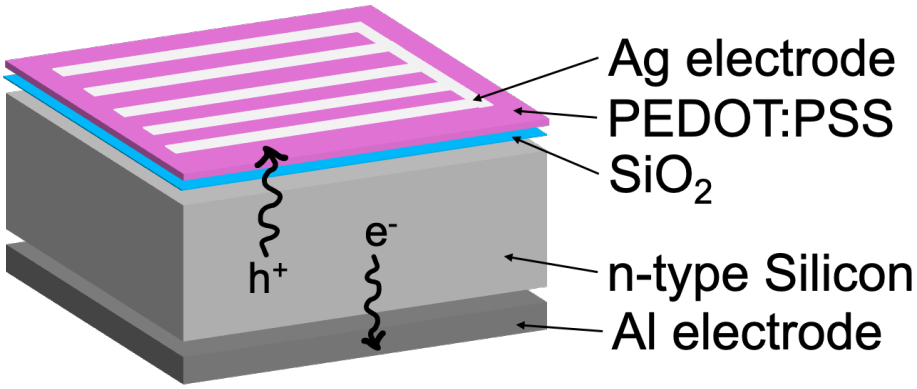



**Figure 1.5:** Illustration of a typical device structure of a heterojunction solar cell.

### 1.5.1 n-type silicon wafer

A phosphorus-doped n-type silicon wafer provides electrons as the majority carriers and holes the minority carriers in the material.[125] As light-induced degradation would cause loss of stability in a boron-doped p-type wafer but not in an n-type wafer, the latter exhibits superior stability under solar exposure. The lack of boron in these phosphorus-doped Si wafers also eliminates the possibility of oxygen-boron defect formation. In addition, n-type Si wafers demonstrate longer minority-carrier (holes) diffusion lengths and higher tolerance to impurities such as iron and copper that are responsible for recombination losses. All of these factors contribute to the enhancement of PCE of corresponding solar cells.[126] The integration of an n-type Si wafer with a p-type component make n-type Si a suitable substrate for heterojunction solar cells.

### 1.5.2 $SiO_X$ interfacial layer

In planar PEDOT:PSS/Si heterojunction solar cells, an ultrathin uniform interfacial $SiO_x$ layer between PEDOT:PSS and Si primarily serves to passivate interface defects and to improve carrier selectivity.[127] The native or thermally grown $SiO_x$ saturates dangling bonds at the Si surface and thereby suppresses Shockley–Read–Hall recombination at the organic–inorganic junction, which directly supports higher $V_{OC}$ and FF compared with an unpassivated contact.[128,129] At the same time, when the $SiO_x$ is kept in the tunneling regime (typically $\leq$ 1–2 nm), holes can tunnel from the Si valence band into the high work function PEDOT:PSS, while electrons encounter a larger barrier. This asymmetry makes the contact more hole selective and reduces interfacial recombination losses under forward bias.[130] The $SiO_x$ also helps the Si surface to experience more favorable band bending consistent with the PEDOT:PSS work function, making a stronger built-in field, which is essential in devices where the bottom electrode is at the rear of the Si wafer and the top electrode sits on

PEDOT:PSS.[127] Collectively, these effects allow the cell to achieve the good optical and solution processability properties of PEDOT:PSS while controlling the Si/organic interface.

### 1.5.3 PEDOT:PSS polymer

Poly(3,4-ethylenedioxythiophene):poly(styrene sulfonate) (or PEDOT:PSS) is composed of the positively charged PEDOT backbone and the negatively charged PSS polyanion (Figure S1-2).[131,132] The PEDOT component is a π-conjugated polymer that is a derivative of polythiophene and is synthesized from the 3,4-Ethylene-dioxy-thiophene (or EDOT) monomer. PEDOT is characterized by high electrical conductivity up to 300 S/cm, excellent stability in its oxidized state, and high transparency when prepared as a thin film.[133,134] Doping the PEDOT with a counter ion is a crucial step to make it soluble and stable in water. One of the most common counter ions is the water-soluble PSS. It acts as a p-type doping agent, balancing charges during polymerization, enhancing hole mobility along the PEDOT backbone, and improving dispersion in polar solvents such as water.[135] There are three major interactions in PEDOT:PSS systems: (1) electrostatic attraction between $PEDOT^+$ and PSS chains, (2) π-π noncovalent interactions among adjacent chains of PEDOT, and (3) interchain entanglements between the long PSS chains.[136] Depending on the ratio of PEDOT to PSS, PEDOT:PSS can be used as a p-type component or electrode because the ratio affects the conductivity properties of the polymer.[137] The mechanism by which the conductivity of PEDOT:PSS can be increased by over 100 times has been studied and confirmed with various characterization techniques. Ouyang et al.[138] first reported that the increase in interchain interaction between PEDOT chains promotes the change of polymer morphology from coil or benzoid form to an extended fibril or quinoid structure. The change in morphology promotes a better phase separation and a smoother charge hopping by reduction of energy barrier.[138] The addition of high boiling point organic solvents or inorganic compounds, such as ethylene glycol (EG), dimethyl sulfoxide (DMSO), methanol, ionic liquids, surfactants, salts, sulfuric acid, methanesulfonic acid, maleic acid and nitric acid, before or after treatment can contribute to conductivity and performance enhancement.[88,139–144]

PEDOT:PSS has been widely used as a p-type organic semiconductor in heterojunction solar cells with an n-type silicon substrate. The popularity of this polymer in different applications can be attributed to its environmental friendliness, processibility in solution, solubility in water or at low temperature, cost-effectiveness, tunable conductivity, and transparency to visible light.[145–147] Spin coating is one of the simplest methods for forming reproducible and uniform films of PEDOT:PSS on a substrate with controlled thickness obtained by adjusting the speed of rotation.[148,149]

Although PEDOT:PSS is widely used for its high conductivity, transparency, and solution-processability, its electrical and structural integrity can deteriorate significantly when the film is exposed to sustained high relative humidity (RH) or ultraviolet (UV) radiation.[150,151] As the sulfonic acid groups in PSS are acidic, they narrow the choice of compatible materials that could come in contact with it. For example, the PEDOT:PSS/ITO interface is very sensitive to the environmental factors such as humidity, oxygen and pH, and the ITO electrode could corrode and lose its stability if it gets in contact with a PEDOT:PSS layer.[147] The hygroscopic nature of PSS makes it quite vulnerable to moisture uptake from the environment, which increases its sheet resistance and accelerates device degradation.[151] Approaches to improve the stability mainly seek to neutralize the acidity through reduction/removal of PSS component and promote phase separation of the conductive PEDOT and insulating PSS. These strategies include addition of base/buffer to raise the pH, introduction of cross-linkers to increase hydrophobicity, and addition of polar solvents and ionic liquids.[152,153]

### 1.5.4 Electrodes

Silver (Ag) makes an excellent top electrode in an organic–inorganic heterojunction solar cell because of its high conductivity, reflectivity, smooth surface and low cost (relative to gold or platinum), leading to minimal resistive losses (compared to a gold film) and minimal reduction of FF and PCE.[154] The work function of pristine Ag is ~4.3 eV, which makes it well aligned with a commonly used HTL such as a PEDOT:PSS film with a work function of 4.7 – 5.4 eV.[155,156] This alignment minimizes charge accumulation at the interface and reduces recombination, which improves charge collection and ultimately the performance of the hybrid solar cell device. Furthermore, silver is compatible with scalable deposition techniques (such as sputtering and thermal evaporation), which enable precise control over film morphology and thickness that are critical for achieving a high quality, uniform electrode without damaging the underlying organic layer during fabrication. Together, these properties make silver a cost-effective benchmark electrode material for high efficiency heterojunction solar cells. Aluminum (Al), on the other hand, could be used as a very conductive, low cost and opaque back electrode in a heterojunction solar cell. The well matched work function of 4.1 – 4.3 eV makes this metal in good alignment with the conduction band of the n-type silicon substrate to facilitate efficient electron collection.[157] Similar to Ag, Al is compatible with scalable deposition techniques such as thermal evaporation and sputtering, enabling its easy industrial adoption.[158] Furthermore, its abundance and recyclability support sustainable large-scale solar cell manufacturing.[159]

In silicon-organic heterojunction solar cells, such as those utilizing an n-type crystalline silicon substrate and a PEDOT:PSS film as the HTL, the choice of metal electrode and its deposition technique play a pivotal role in determining device performance and manufacturability. In vacuum thermal evaporation, an important type of physical vapor deposition, the metal is annealed resistively or with an electron beam in high vacuum until the metal vaporises, producing atomically clean Ag or Al films that condense gently on the polymer without mechanical stress or solvent exposure.[160–162] Thermal evaporation allows for the gentle deposition of high-purity metal films with precise thickness control, low sheet resistance and excellent interface quality, making it ideal for top contacts over sensitive organic layers such as PEDOT:PSS without causing thermal or physical damage. However, the method is not easily scalable due to the energy demand and need for high-vacuum systems, which drive up cost.[163] A more scalable alternative is DC or RF magnetron sputtering, where a plasma of an inert gas (usually Argon) is used to dislodge atoms from a target material onto the substrate.[164] Sputtering offers strong adhesion, conformal coverage, and compatibility with industrial-scale fabrication, especially for the top electrode (such as Ag, and Au) and bottom electrode (such as Al).[165] Care must be taken to limit ion damage to PEDOT:PSS, which could be achieved typically by lowering the power or adding an ultrathin buffer layer.[164]

In both sputtering and evaporation, shadow masks are widely used for electrode patterning. A shadow mask is a reusable stencil commonly made from laser cut stainless steel or nickel, which defines where metal is to be deposited. It allows for physical patterning without photolithography, making it highly compatible with organic layers and laboratory-scale solar cell fabrication. While shadow masks avoid wet processing that can degrade PEDOT:PSS, they suffer from resolution limits and edge blurring, particularly in high-aspect-ratio features. In spite of this challenge, for research and small-area device fabrication, shadow masks remain a cost-effective and non-destructive method of electrode patterning, particularly in conjunction with magnetron sputtering.[166–168] Once the electrode pattern is defined, reliable electrical contact must be established with the patterned regions.

In this context, other techniques such as screen printing are also used in crystalline silicon photovoltaics due to their low cost, simplicity and scalability. Among these contact-forming approaches, Ag pastes are widely used due to their high conductivity and well-established processing methods. Conventional Ag pastes require curing usually by a fast 750–850 °C belt fire that would destroy organic polymers, but newer low-temperature Ag paste formulations allowing curing at 150–200 °C in 10–20 min or flash-sintering in seconds could preserve the integrity of the polymer.[163,169] Emerging methods like inkjet and spray coating do not need high vacuum chamber to proceed and

they offer low temperature, ambient condition deposition of metal nanoparticle inks, but their lack of long-range uniformity and industrial throughput compared to physical vapour deposition methods remain notable barriers to adoption in high-efficiency hybrid solar cells.[170–172]

## 1.6 Characterization methods

### 1.6.1 X-ray photoelectron spectroscopy

X-ray Photoelectron Spectroscopy (XPS), also commonly known as Electron Spectroscopy for Chemical Analysis (ESCA), is a highly surface sensitive analytical technique widely used in materials science to investigate the chemical composition, electronic states, and empirical formula of materials at their surface region.[173] Fundamentally, XPS operates by irradiating the surface of the material of interest with X-rays, from typically Al Kα or Mg Kα sources, resulting in the emission of photoelectrons. The kinetic energy of these emitted electrons ($E_K$) is measured by a spectrometer, and it allows determination of the binding energy ($E_B$) characteristic of the elements present in specific chemical states by using the Einstein equation:

$$E_K = h\nu - E_B - \phi \qquad \text{Equation } \mathbf{1.4}$$

where $E_K$ is the kinetic energy of the emitted electron, $h\nu$ is the energy of the incoming photon, $E_B$ is the binding energy of the electron in the atom or solid, and $\phi$ is the work function of the spectrometer.

The binding energies serve as unique fingerprints of the chemical states, enabling the identification and quantification of surface chemical species.[174] One of the primary strengths of XPS is its surface sensitivity, which arises due to the short inelastic mean free path of photoelectrons in solids, typically limiting analytical depth to 1–10 nm. This makes XPS uniquely suited for probing surfaces and, when coupled with careful sputtering with argon monomer or cluster ions, interfaces in thin films, composites, and coated materials can be analyzed as functions of sputtering depth to reveal the interfacial chemistry that critically influences properties such as adhesion, catalytic activity, corrosion resistance, and electrical conductivity. XPS is particularly valuable for studying conductive polymer blends, such as PEDOT:PSS, which are extensively employed in organic electronics due to their tunable conductivity and ease of processing. The conductivity of PEDOT:PSS can be greatly influenced by modifications involving solvents and additives, and other post-processing treatments. XPS provides a robust method to quantify these changes by accurately measuring the ratio between the conductive PEDOT and insulating PSS components at the surface and in the near-surface region. Alterations in the PEDOT-to-PSS ratio significantly correlate with variations in conductivity, as

increased PEDOT presence generally corresponds to enhanced electrical transport due to improved charge mobility and reduced insulating barriers.[87,175,176] Furthermore, XPS can reveal subtle shifts in binding energies, reflecting changes in the chemical environment around specific atoms. This sensitivity to chemical shifts allows researchers to infer mechanisms responsible for improved conductivity, such as reduced coulombic interactions or better chain alignment within the PEDOT:PSS matrix. Additionally, by examining the sulfur peaks in XPS spectra, the differentiation between the sulfonate groups of PSS and the thiophene sulfur in PEDOT is straightforward, making it easy to track compositional changes upon solvent treatment. XPS therefore provides critical insights into both the chemical composition and electronic structure at the material surfaces, and it is particularly suited for investigating conductive polymer systems like PEDOT:PSS. Its ability to quantify the PEDOT-to-PSS ratio and to detect subtle chemical shifts makes XPS indispensable for evaluating how solvent modifications impact the conductivity and overall performance of polymeric materials in electronic applications. In the present work, the instruments used for the XPS studies are Thermo VG Scientific ESCALab 250 microprobe (Figure 1.6) and Thermo Scientific Nexsa G2 XPS system (Figure 1.7).

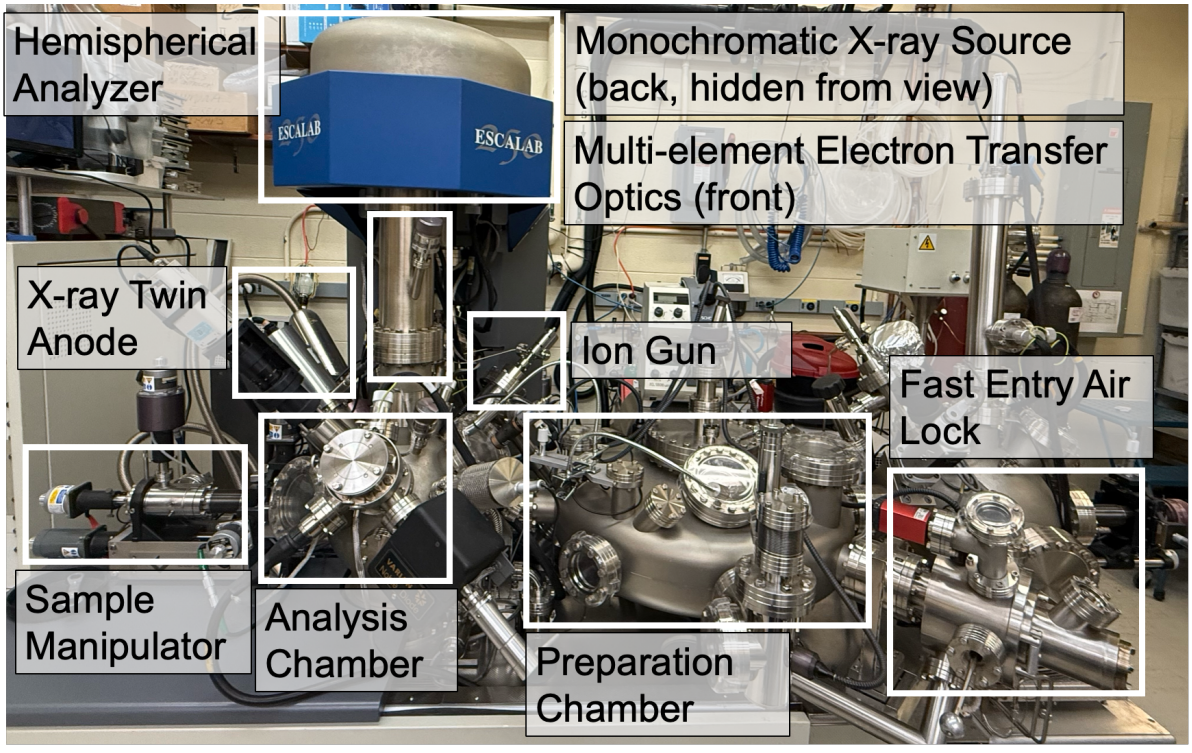



**Figure 1.6:** Photograph of a Thermo-VG Scientific ESCALab 250 microprobe XPS system.

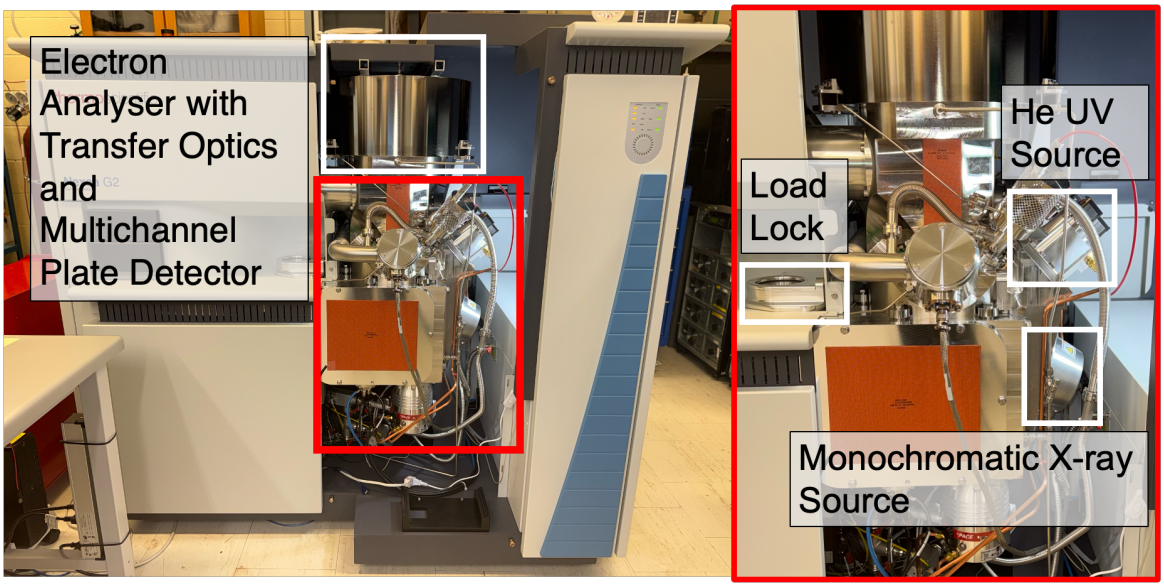



**Figure 1.7:** Photograph of a Thermo Scientific Nexsa G2 XPS system.

### 1.6.2 Time-of-flight secondary ion mass spectrometry

Time-of-Flight Secondary Ion Mass Spectrometry (TOF-SIMS) is a highly sensitive surface analysis technique that provides detailed chemical information from the outermost atomic layers of a material (Figure 1.8). The method relies on bombarding the surface with a focused beam of primary ions, which causes the ejection of atoms, molecular fragments, and intact molecular ions from the top one to two nanometers. Known as secondary ions, these ejected species are accelerated into a time-of-flight mass spectrometer, where their mass-to-charge ratios are measured. Because lighter ions reach the detector more quickly than the heavier ones, this allows the generation of high-resolution mass spectra across a wide mass range with excellent sensitivity. A key strength of TOF-SIMS lies in its extreme surface sensitivity, making it particularly well suited for analysing thin films and coatings, where subtle variations in composition at the surface often control functional properties. Another important feature is its ability to generate chemical images by rastering the ion beam, allowing spatially resolved maps of the distribution of elements and chemical species across the surface, with lateral resolution down to the sub-micron scale. By rastering, the beam is deflected in a controlled grid-like pattern over a chosen surface area, so that spectra are collected at many different positions. These individual measurements can then be combined to reconstruct a two-dimensional chemical map of the sample surface.[177]

The applications of TOF-SIMS are broad, spanning materials science, semiconductors, catalysis, and polymer research. With the advent of cluster ion sputtering sources to remove soft materials

cleanly with considerably less interlayer mixing, it has become a particularly important tool for polymers because it not only detects trace levels of additives, dopants, or contaminants, but also provides molecular information that helps to explain how these chemical modifications influence macroscopic properties. In the case of polymer films such as PEDOT:PSS, TOF-SIMS can reveal how cosolvents or additives alter the chemical composition at the film surface, which in turn influences conductivity and charge transport. This ability to correlate nanoscale chemistry with bulk properties makes TOF-SIMS especially relevant for understanding the performance of conducting polymer films.

When compared with XPS, TOF-SIMS offers complementary information and insights. XPS probes deeper into the surface, typically the top 5–10 nanometers and provides reliable quantitative information on chemical state composition. It is especially powerful for identifying oxidation states and stoichiometry. However, its spatial resolution is limited, and it lacks the ability to distinguish complex molecular fragments. TOF-SIMS, on the other hand, is less quantitative but it provides depth profiles with much higher surface sensitivity, superior trace chemical detection, and the capability to detect and map organic fragments with sub-micron spatial resolution. In practice, the two methods are often used together, with XPS to quantify chemical states and TOF-SIMS to reveal molecular distributions and surface heterogeneity.

TOF-SIMS, as implemented in instruments such as ION-TOF SIMS 5, is primarily a static SIMS technique that operates at low primary ion doses to analyse the outermost 1–2 nm of a surface with exceptional molecular specificity and high mass resolution. While the SIMS method is inherently surface sensitive, its capability can be extended to probe buried interfaces through the depth profiling approach. By combining repeated static analyses with gradual and gentle sputtering cycles (e.g., ion beams with low near-surface damage from the argon gas cluster ion source), it is possible to obtain three-dimensional chemical profiles of polymer films. This makes TOF-SIMS a valuable technique for studying polymer–substrate interfaces or multilayer structures, since it can be used to reveal whether additives or cosolvents remain uniformly distributed, segregate to the surface, or migrate to the polymer–substrate interface. Such interfacial information is critical in systems such as organic–inorganic heterojunction solar cells with such organic films as PEDOT:PSS, where the efficiency of the device depends not only on the bulk composition of HTL but also on the arrangement of phases and additives near the interfaces. In summary, TOF-SIMS combines extreme surface sensitivity, molecular specificity, and high-resolution imaging with the ability to probe buried interfaces through

depth profiling. These features make it a uniquely powerful tool for investigating the chemistry of conducting polymer films.

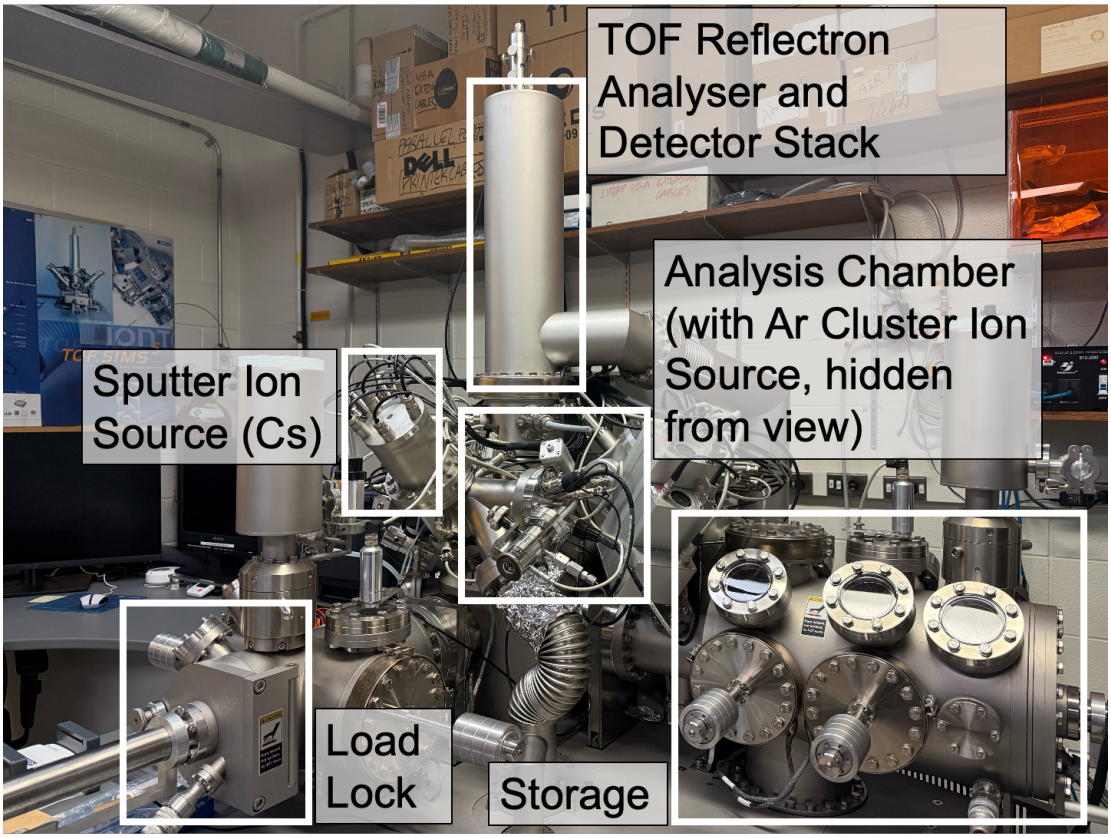



**Figure 1.8:** Photograph of an ION-TOF 5 (IONTOF GmbH) time of flight secondary ion spectrometer with a 2 m reflectron TOF analyzer in negative ion mode, using a 30 kV $Bi_3^+$ analysis beam and a 5 kV $Ar_{2000}^+$ cluster ion sputter source.

### 1.6.3 Atomic force microscopy

Atomic Force Microscopy (AFM) is one of the most fundamental scanning probe microscopy techniques used extensively for investigating the surface topography, morphology, and roughness of especially nonconducting materials at nanoscale resolution (Figure 1.9). In tapping mode, a sharp probe (typically silicon or silicon nitride) mounted on a cantilever is driven to oscillate near its mechanical resonance while approaching the sample. The tip intermittently touches the surface at the bottom of each oscillation cycle. Changes in the oscillation amplitude and phase arising from tip–sample interactions are detected by a laser reflected from the cantilever onto a photodiode. Feedback electronics maintain a constant setpoint (a fraction of the free oscillation amplitude) by adjusting the

z-position as the probe scans across the x-y surface of the material, thereby recording the sample topography.[178,179]

One critical advantage of AFM in tapping mode is the substantial reduction of lateral (shear) forces compared to continuous contact (as in contact mode), which helps to preserve delicate or soft surfaces while still producing detailed three-dimensional images. The vertical (z) resolution of AFM routinely reaches sub-nanometer levels, while lateral (x–y) resolution is limited by the tip radius (typically ~10 nm) and by the chosen oscillation amplitude. Owing to this balance of gentleness and resolution, tapping-mode AFM is widely used across materials science, polymer chemistry, biological sciences, and microelectronics.[179,180]

In the context of polymer research, tapping mode is particularly valuable for studying the morphology and surface characteristics of conductive polymer blends such as PEDOT:PSS. Beyond height (topography), the simultaneously acquired phase (or energy-dissipation) channel provides qualitative contrast related to variations in viscoelasticity, adhesion, and composition. This enables visualization of how PEDOT-rich and PSS-rich domains distribute on the film surface, offering insight into phase separation and aggregation phenomena that strongly influence electrical performance and functional properties.[181,182] Moreover, AFM in tapping mode enables precise quantification of surface roughness parameters. Surface roughness critically influences properties such as electrical conductivity, adhesion, optical transparency, and mechanical stability of polymer films. By accurately measuring the roughness parameters, including root-mean-square (RMS) roughness and peak-to-valley distances, AFM helps to correlate morphological characteristics with the observed device performance, facilitating optimization of fabrication processes and material treatments.[183]

While tapping mode greatly mitigates sample damage, improper settings can still introduce artifacts. Excessively driven amplitude or too-low amplitude setpoints can cause hard tapping, local indentation, or tip/surface wear, while environmental factors (e.g., humidity and capillary layers) can affect the phase contrast. Careful selection of cantilever stiffness, resonance frequency, free amplitude, setpoint ratio, and feedback gains is therefore essential, especially for softer polymer surfaces, to obtain reliable morphology and phase data without altering the sample. In summary, tapping-mode AFM is a powerful and gentle method for characterizing the nanoscale surface structure of polymer films such as PEDOT:PSS. By combining high-resolution topography with phase/dissipation contrast and robust roughness quantification, taping-mode AFM links microscopic structural features to macroscopic functional performance in advanced polymeric materials.

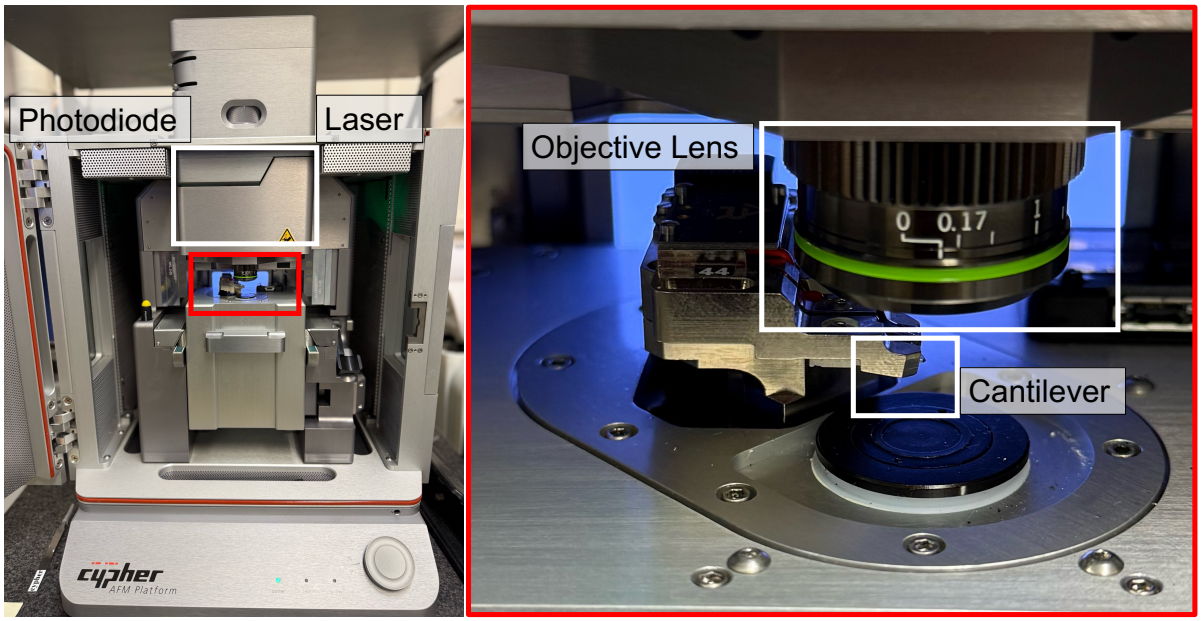



**Figure 1.9:** Photograph of an Asylum Research Cypher ES AFM with enclosed scanner.

### 1.6.4 Conductivity

The four-probe van der Pauw method is a widely recognized and reliable electrical characterization technique extensively employed to determine the sheet resistance and conductivity of thin films and coatings. Originally developed by Leo J. van der Pauw in 1958, this technique remains fundamental in materials research due to its accuracy, simplicity, and versatility.[184] At its core, the van der Pauw method involves applying current through two contacts on a thin sample and measuring the resultant voltage between two other contacts. By strategically placing four small and symmetrical electrical contacts on the periphery of a thin-film sample, it is possible to accurately determine the sheet resistance and thus the electrical conductivity, independent of the shape of the support on which the sample is mounted, provided that the sample is uniform in thickness, isotropic, and free of holes (Figure 1.10).

The central advantage of the four-probe van der Pauw method is its capability to minimize errors stemming from contact resistance. Unlike the two-probe technique, which incorporates significant contact resistance in its measurement, the four-probe method effectively excludes these effects by separating current-carrying electrodes from voltage-sensing electrodes. Consequently, it provides a more precise and accurate measurement of the intrinsic electrical properties of the material under investigation.

The process of determining the sheet resistance involves passing a known current between two adjacent contacts while simultaneously measuring the resulting voltage drop between the other two contacts. Repeating this measurement by rotating the arrangement of contacts ensures improved accuracy and reproducibility of the results. The sheet resistance ($R_S$) derived from these measurements can subsequently be converted into conductivity by taking into account the film thickness. Accurate thickness measurements are therefore essential when calculating conductivity values.[185]

The van der Pauw technique has extensive applications in materials science, semiconductor research, photovoltaics, and polymer electronics. In polymer thin-film research, this method is especially valuable for assessing changes in electrical conductivity resulting from processing modifications, such as the introduction of cosolvents or additives. For example, conductive polymer films such as PEDOT:PSS frequently exhibit significant enhancements in conductivity upon solvent modification due to improved phase separation, crystallinity, and network formation within the polymer matrix.[186] Employing the van der Pauw four-probe method enables clear, quantitative analysis of these improvements, facilitating the direct correlation between fabrication conditions, structural modifications, and the resulting electronic performance.

In summary, the van der Pauw four-probe conductivity and sheet resistance test stands out as an essential measurement for quantitatively evaluating the electrical properties of thin-film polymeric materials. Its simplicity, accuracy, and capability to exclude contact resistance make it particularly suitable for studying subtle yet impactful changes in conductivity associated with processing techniques, additives, and cosolvents. Understanding these correlations is fundamental for optimizing polymer electronic materials for advanced technological applications.




**Figure 1.10:** Photograph of an Ecopia HMS-5300 Hall effect measurement system for semiconductor carrier mobility and concentration. A four-point probe sample mount is shown in the right panel.

### 1.6.5 Solar cell performance measurement

Accurate measurement of solar cell performance is critical in photovoltaic research, particularly in guiding improvements in material selection and device architecture, and in overall efficiency optimization. One of the fundamental tools employed to determine the efficiency of photovoltaic devices is current-voltage (I–V) or current density vs voltage (J-V) characterization. This measurement provides detailed insights into essential parameters such as $J_{SC}$, $V_{OC}$, FF, and PCE (Figure 1.3). Typically, these measurements are performed by using specialized commercial solar cell characterization systems, such as the PV Measurements IV5 system, known for their reliability and accuracy.

The PV Measurements IV5 system integrates precision electronics to measure the current response of a photovoltaic cell or module under an applied voltage sweep (Figure 1.11). During an I–V measurement, the solar cell is illuminated by an artificial solar simulator replicating the spectral distribution and intensity of sunlight, typically standardized to the AM1.5G (Air Mass 1.5 Global) spectrum that corresponds to the terrestrial solar conditions at the surface of the Earth. The illumination intensity unit commonly used is 100 mW $cm^{-2}$ (equivalent to 1 Sun), enabling comparability across various studies and technologies.

To ensure accurate and reproducible measurements, a standardized calibration procedure is used. Before performing an I–V measurement, the solar simulator intensity is calibrated using a well-defined reference cell. In this context, a silicon reference cell such as the PVM782 with a BK7 window is widely employed. With a known and stable response, the reference cell ensures that the output of the simulator precisely matches the standard illumination intensity. Calibration reduces

uncertainties and facilitates meaningful comparisons between results obtained from different photovoltaic devices and those reported by other research groups.[187]

The solar simulator employed for the IV5 measurement setup typically falls into different performance categories, including class ABA, indicating high standards of spectral match (class A), spatial uniformity (class B), and temporal stability (class A). Such classification ensures minimal variability in measurements and enhances data reliability, critical for scientific reporting and device optimization. In this system, spatial uniformity is graded as Class B, which according to the international electrotechnical commission or IEC 60904-9 allows up to 5% variation in irradiance across the illuminated area. This means that the simulator delivers ≥95% uniform irradiance. Spectral matching to AM1.5G assures that the light incident upon the cell accurately simulates real-world sunlight conditions, thereby making the measured performance indicative of practical outdoor performance.[188]

The measured I–V curves reveal fundamental device characteristics, directly correlating to internal processes such as charge generation, transport, recombination, and extraction. Analysis of these curves provides not only the baseline efficiency metrics but also diagnostic information enabling identification of loss mechanisms. Parameters derived from the I–V measurements such as the fill factor and open-circuit voltage provide insights into interface quality, active layer properties, and carrier recombination dynamics. Consequently, these metrics become essential tools for researchers aiming to understand, optimize, and develop improved photovoltaic materials and structures. In summary, I–V measurements by using precision systems such as the PV Measurements IV5 under calibrated conditions provide an essential foundation for photovoltaic research. Accurate calibration using a Si reference cell and employing a standardized solar simulator under AM1.5G conditions ensures reliable performance metrics, which guide both fundamental understanding and practical improvement of solar cell technologies.[18]

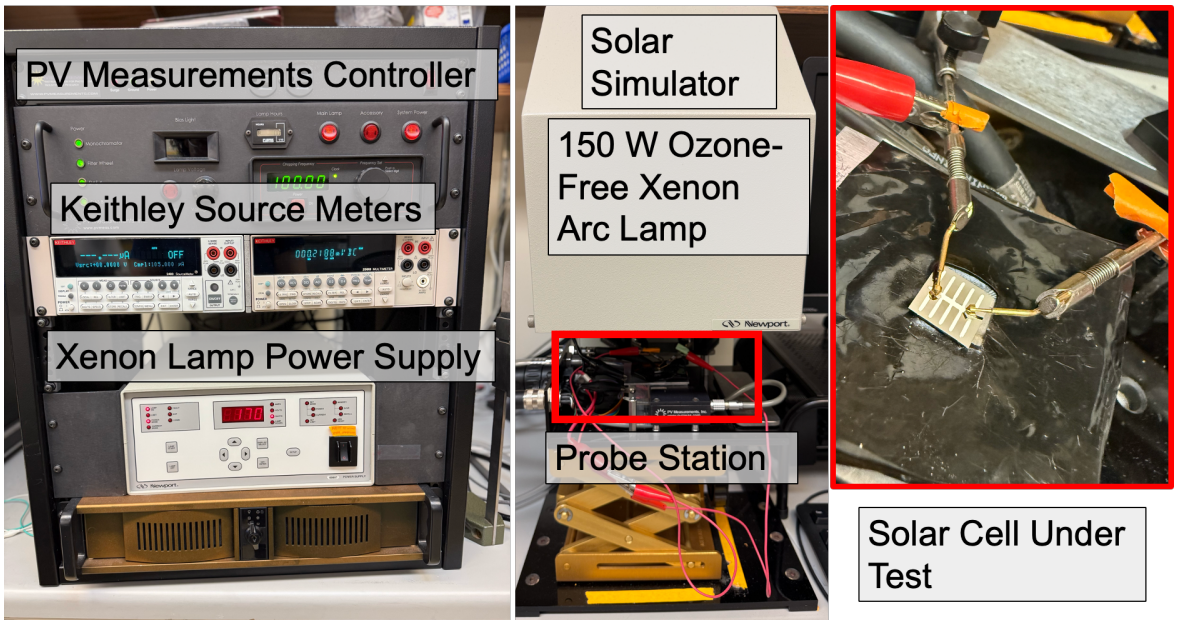



**Figure 1.11:** Photograph of a PV Measurements IV5 I–V analyzer with probe station for solar cell testing.

External Quantum Efficiency (EQE) measurement is another fundamental characterization technique widely used in photovoltaic research to quantify the efficiency with which a solar cell converts incident photons into charge carriers (electrons or holes) collected at the electrodes. Also known as incident photon-to-electron conversion efficiency (IPCE), EQE is defined as the ratio of the number of electrons collected by the external circuit to the number of photons incident upon the solar cell at a specific wavelength. Consequently, the EQE spectrum provides valuable wavelength-dependent information regarding the effectiveness of photon absorption, charge generation, and collection efficiency within the photovoltaic device.[189] In practice, an EQE measurement involves illuminating the solar cell with monochromatic light of varying wavelengths while simultaneously measuring the photocurrent produced.

Figure 1.12 shows the optical measurement chamber of the PV Measurements QEX10 quantum efficiency system, which measures how efficiently a solar cell converts light into electrical current as a function of wavelength. Typically, a calibrated photodiode is employed to determine the precise photon flux incident on the device at each wavelength. The monochromatic probe beam, generated by a xenon arc lamp and filtered through a dual-grating monochromator, enters the chamber through the reflective optical path and is focused onto the test cell mounted on the sample stage. The mirrors and focusing optics ensure that the beam size remains uniform across all wavelengths, minimizing

chromatic aberration. Electrical contacts connect the device to the measurement electronics, which detect the photocurrent response synchronized to the modulated monochromatic beam. The system compares this response to a National Institute of Standards and Technology (NIST) traceable reference photodiode reading to calculate the EQE, generating a spectral map of how effectively the cell converts photons of each wavelength into current.[190] The EQE spectrum so obtained therefore enables detailed analysis of spectral response characteristics, which are crucial for understanding device limitations, identifying loss mechanisms, and informing strategies for optimization.[18]

EQE is particularly valuable when examining the impact of modifications in device architecture, such as variations in the top electrode geometry. For instance, changing the design of the shadow mask used for deposition of the top electrode influences the active area geometry, current density distribution, and ultimately charge collection efficiency. By comparing the EQE spectra obtained from different electrode designs, it becomes possible to precisely evaluate how geometry changes affect charge extraction pathways, charge carrier recombination losses, and overall device performance. Improved electrode designs can enhance charge collection efficiency, manifested as increased current density and enhanced EQE values at particular wavelengths that are indicative of more effective charge extraction and reduced recombination losses.[191–194]

EQE measurement therefore serves as a powerful diagnostic tool in photovoltaic research, linking device architecture directly to electrical performance. Unlike standard IV measurement, which only provides integrated device parameters under broad illumination, EQE reveals how efficiently photons of different wavelengths are converted into current. This spectral resolution allows researchers to pinpoint which layers or interfaces limit performance. Because different layers in a solar cell absorb light in different spectral regions, the shape of the EQE spectrum reveals where losses occur. EQE essentially acts like a spectral fingerprint of the device that is systematically driven by the relationship between cell architecture including the top electrode geometry, current density improvement, and spectral response enhancement. Ultimately, EQE provides critical insights necessary to optimize photovoltaic device configurations for enhanced performance and reliability.

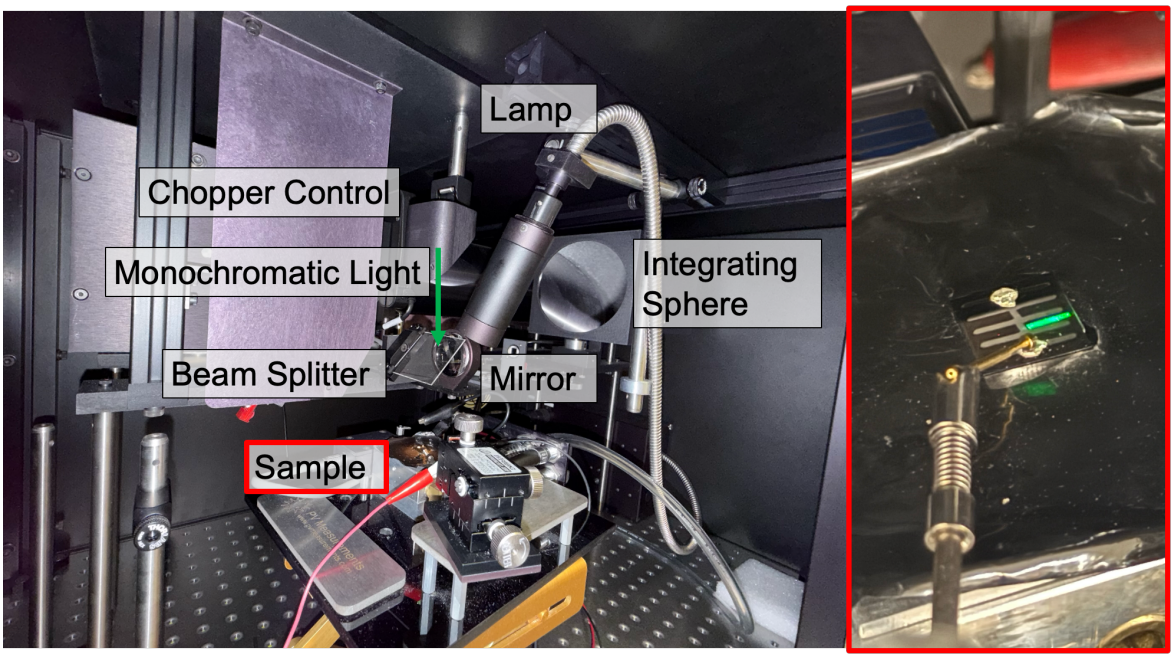



**Figure 1.12:** Photograph of a PV Measurements QEX10 EQE analyzer with light-tight enclosure and adjustable sample stage for photovoltaic device testing.

## 1.7 Scope of thesis

In the remaining of this thesis, three separate studies on PEDOT:PSS/Si heterojunction solar cells (HSCs) are presented. In Chapter 2, we seek to address the critical issue of long-term stability and performance degradation in PEDOT:PSS based HSCs. Despite their attractive combination of low cost, flexibility, and high efficiency, HSCs commonly suffer from instability due to environmental degradation of their HTLs. As a widely used HTL, PEDOT:PSS deteriorates rapidly due to its intrinsic acidic and hygroscopic nature, which negatively impacts the overall solar cell performance. To tackle this challenge, DMSO is strategically introduced as a cosolvent into PEDOT:PSS, in combination with other cosolvents (ethylene glycol and methanol) reported in the literature. As DMSO facilitates phase separation between the conductive PEDOT and insulating PSS components, the resulting treated PEDOT:PSS film is expected to have significantly improved electrical conductivity, charge carrier mobility, and ambient stability. This study demonstrates that DMSO addition at an optimized concentration (3 wt%) is found to enhance remarkably both the conductivity and stability. Solar cells incorporating DMSO-modified PEDOT:PSS maintain approximately 89.4% of their initial PCE after 72 hours of ambient storage, compared to the control cell that experiences severe degradation within the same period. This improvement is attributed primarily to better PEDOT

domain connectivity and minimized charge recombination, as a result of favorable interaction between DMSO and the PEDOT:PSS polymer blend. Detailed surface analyses including AFM and XPS confirm morphological improvements, with more PEDOT-rich domains and fewer insulating PSS-rich surface regions. More importantly, the addition of DMSO has reduced the need for additional protective encapsulation, thus simplifying the fabrication process while significantly enhancing intrinsic device stability. Overall, this work establishes the efficacy of DMSO as a cost-effective and practical solution for developing highly stable and efficient HSCs, opening a new avenue toward the commercial viability of solution-processed photovoltaic technologies.

Building upon the insights obtained from the first study, we seek, in Chapter 3, to further enhance the performance and ambient stability of HSCs by using an alternative cosolvent additive, dimethyl sulfone ($DMSO_2$), for PEDOT:PSS, along with ethylene glycol and methanol. Unlike the liquid cosolvent DMSO, solid-state $DMSO_2$ crystallizes upon drying, which causes unique reorganization of PEDOT:PSS microstructures and alignment of the conductive PEDOT chains. These changes are expected to significantly improve the film morphology, conductivity, and device efficiency. The core objective is to evaluate the comparative advantages of $DMSO_2$ doping, with the focus on the effects on film morphology and long-term stability. Due to the strong hydrogen-bonding capability of $DMSO_2$ with sulfonic acid groups of PSS, the addition of $DMSO_2$ could lead to a superior phase separation and better-defined conductive pathways within the polymer films. Through EQE, AFM, and conductivity measurements, $DMSO_2$ is found to effectively reorganize PEDOT chains into a more ordered network, enhancing both lateral and vertical conductivity. Solar cells employing PEDOT:PSS films doped with ethylene glycol, methanol, and $DMSO_2$ are also found to achieve remarkable efficiencies up to 15.5%. Furthermore, devices employing ethylene glycol and $DMSO_2$ exhibit substantial stability improvements, with an average $T_{80}$ of ~913 hours of ambient storage. This impressive stability performance is attributed to the unique ability of $DMSO_2$ in mitigating the degradation mechanisms by reducing free hygroscopic PSS on the film surface, thus lowering susceptibility to environmental moisture-related degradation processes. This work therefore validates $DMSO_2$ as a powerful additive, demonstrating its dual role in significantly boosting photovoltaic performance and intrinsic device longevity. These findings not only represent an important advancement over conventional cosolvent strategies but also offer a viable and eco-friendly method to increase both efficiency and durability of PEDOT:PSS-based solar cells.

In Chapter 4, we focus on optimization of electrode design through an innovative, low-cost, and rapid prototyping technique involving desktop 3D printing of shadow masks. The deposition of the

top electrode in a solar cell is a crucial step in photovoltaic device fabrication, which could directly impact the device efficiency, current collection, and series resistance. Traditional shadow mask fabrication methods involving laser machining and photolithography are generally costly, time-consuming, and restrictive, limiting rapid iterations and innovation in electrode designs. This study seeks to demonstrate the practicality and effectiveness of polyethylene terephthalate glycol-modified (PETG) filament-based 3D printed shadow masks for electrode patterning in silicon heterojunction solar cells. PETG masks with three distinct electrode geometries (comb-like busbar, central busbar, and crossed busbar) have been designed and are used to evaluate their impact on solar cell performance metrics ($V_{OC}$, $J_{SC}$, FF, and PCE). The results indicate that 3D-printed masks provide significant advantages in terms of prototyping speed, cost reduction, and geometrical flexibility. Specifically, the central busbar design substantially improves the PCE (up to 21.6%) and fill factor (up to 16.4%) compared to those obtained with conventional comb-like busbar electrodes. These improvements are attributed to optimized current transport pathways, reduced resistive losses, and balanced optical transparency. More importantly, the rapid fabrication process reduces the prototyping cycles from weeks (using the traditional methods) to mere hours, therefore significantly accelerating the optimization process. This approach addresses the need for accessible, affordable, and quick-turnaround methods to build solar cells with optimized photovoltaic performance. Despite the slightly lower resolution compared to conventional masks, the PETG 3D-printed masks have proven to be more than adequate for typical laboratory-scale applications, providing an ideal balance between performance, ease-of-use, and cost efficiency.

Together, these three studies provide a cohesive and comprehensive exploration into improving the efficiency, stability, and fabrication simplicity of planar heterojunction solar cells, contributing meaningfully toward their future commercial viability and advancement in sustainable energy technologies. Finally, we present, in Chapter 5, concluding remarks and some thoughts on potential directions for future work.

# Chapter 2
# Stabilization of Planar Heterojunction Solar Cells using a Dimethyl Sulfoxide Treated Hole Transport Layer

## 2.1 Introduction

Heterojunction solar cells (HSCs) have the benefit of combining the advantages of both organic and inorganic groups of materials.[42] The low cost and flexibility of the fabrication process, easy processibility using simple solutions with high degree of tunability, and great potential for achieving high efficiencies have made HSCs promising devices for green energy generation.[195] The incorporation of highly conductive and transparent organic polymers by spin-coating makes the treatment of hole transport layer (HTL) of a HSC much simpler.[196] One of the most popular p-type organic polymers that has been used extensively as the HTL in solution-processed solar cells is poly(3,4ethylenedioxythiophene)-poly(styrenesulfonate) or PEDOT:PSS. Not only is a thin film of PEDOT:PSS highly transparent in the visible light (400-800 nm) region, its high electrical conductivity of $10^{-2}$ to $10^{3}$ S/cm achievable by simply adding cosolvents also makes a PEDOT:PSS film highly desirable in advanced electronic devices including solar cells.[147] The existing ionic interaction between the positively charged conjugated PEDOT and the water-soluble PSS with a negative charge results in a homogenous and conductive polymer blend.[197] The conductivity of the film formed by spin-coating a PEDOT:PSS aqueous solution has been found to strongly depend on the amount of PEDOT in the core relative to that of PSS in the shell.[198] Therefore, the majority of the treatment methods, including doping, solution post-processing, and bilayer treatment, have focused on increasing the ratio of the conductive PEDOT core to the insulating hydrophilic PSS shell.[199]

The addition of cosolvents to PEDOT:PSS before the coating step or through post-treatment methods has been found to enhance the conductivity of the polymer. These treatments generally cause a reduction of the coulombic interaction between PEDOT and PSS that transforms the spherical morphology of the grains to a more ellipsoidal shape to facilitate a better charge transfer while removing the insulating hygroscopic PSS from the surface.[141–143,200–203] The solution processability of PEDOT:PSS with different cosolvents such as dimethylsulfoxide (DMSO), ethylene glycol (EG), and methanol has been found to enhance the electrical conductivity through reconstruction of the PEDOT domains in the PSS matrix.[87,135,139,204–207] These methods mainly affect the quality of the as-formed films in terms of morphology and crystallinity, aggregation and film adhesion, surface passivation, charge carrier mobility, and light absorption.[198] Despite its many advantages, PEDOT:PSS is prone to

degradation upon prolonged exposure to ambient conditions because of its acidic and hygroscopic nature, which has led to a decrease in the overall performance and stability of the solar cells.[208,209] DMSO has been reported to facilitate better dispersion of PSS, resulting in a more homogeneous film and thereby leading to an increased charge carrier mobility and reduced charge recombination.[210] The addition of mixed cosolvents of methanol and EG has also been found to improve the performance of solar cells that were made with modified PEDOT:PSS.[139] Here, we investigate the impact of adding DMSO to the PEDOT:PSS solution containing methanol and EG on the longevity of the HSCs. The stability of HSCs after fabrication is an under-explored area that could offer new perspectives on developing more durable solar cells. Most stability studies have focused on introducing techniques involving encapsulation of already fabricated solar cells rather than making more stable solar cells without further modification. There is therefore an acute need to develop intrinsically stable solar cells to lower the cost of production and to further reduce the complexity of the process. We show that HSCs fabricated with our DMSO added, cosolvents-modified PEDOT:PSS solutions require no additional post-fabrication step in markedly reducing degradation while being kept under ambient conditions over an extended duration.

## 2.2 Experimental Details

Highly conducting grade PEDOT:PSS (PH1000) was purchased from Clevios and filtered by using a 0.45 μm polyvinylidene fluoride syringe filter to remove any fine particles prior to use. All the other chemicals were obtained from commercial sources and were used as purchased. The control cosolvent solution of PEDOT:PSS (denoted here as EM) contained 8 wt% ethylene glycol (EG) and 8 wt% methanol, with PEDOT:PSS making up the remaining solution. Three cosolvent solutions containing DMSO as an additional cosolvent were prepared with selected DMSO concentrations of 1 wt% (designated here as EMD1), 3 wt% (EMD3) and 5 wt% (EMD5) added to the control cosolvent solution of PEDOT:PSS (EM). A 0.25 wt% FS-300 surfactant has been premixed in the EM and EMD cosolvent solutions prior to the spin-coating process.

Single-side polished, phosphorus-doped n-type silicon (100) wafers (Virginia Semiconductor Inc.) with thickness of 280 ± 25 μm and resistivity of 0.04-0.07 Ω-cm were cut into 10×10 $mm^2$ chips. These Si chips were ultrasonicated in acetone and then in isopropyl alcohol (IPA) for 10 min each, and they were also rinsed by ultrapure water (with resistivity of 18.2 MΩ cm at 21.6 °C) after each round of sonication. The Si chips were then immersed in 5% HF for 2 min to remove the native oxides from the surface followed by rinsing with ultrapure water and drying with a nitrogen stream. A dual target magnetron sputtering system (EMS 575X) was used to deposit a 200 nm thick film of aluminum on the unpolished side of a Si chip to serve as the bottom electrode. The Si chip was then allowed to grow a layer of silicon oxide on the surface of its polished side for 20 min in ambient conditions. Optimization of the thickness of the as-grown oxide layer has been discussed in our previous work.[88] PEDOT:PSS solutions prepared with different cosolvents (EM, EMD1, EMD3 and EMD5) were spin-coated on the Si substrates at a rate of 4000 rpm for 1 min. The resulting PEDOT:PSS coated Si substrates were then baked for 10 min on a hotplate at 110 °C in air, before depositing by magnetron sputtering a 50 nm thick Ag film through a comb-like busbar shadow mask to serve as the top electrode of the solar cell. A schematic structure of a typical HSC is shown in Figure 2.1.

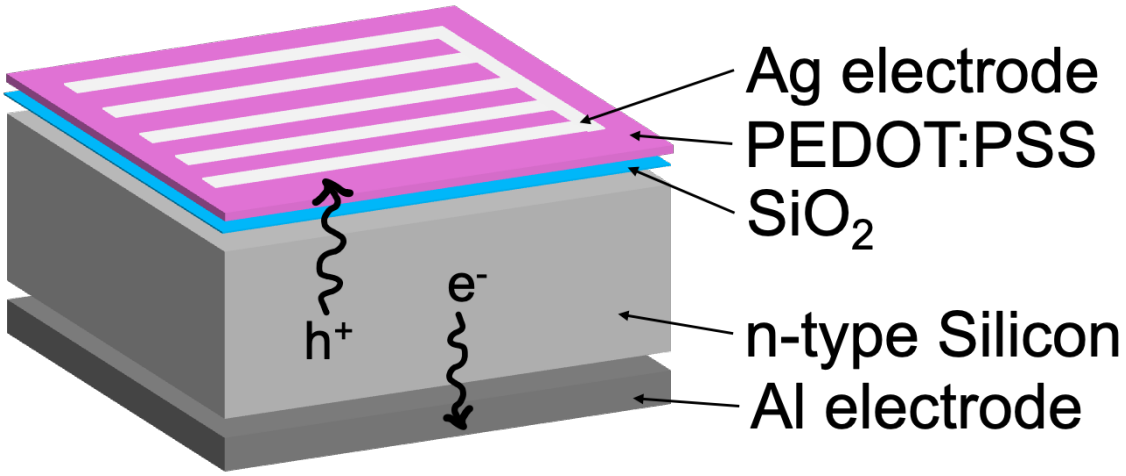



**Figure 2.1:** Illustration of the device structure of a heterojunction solar cell.

To prepare the films for sheet resistance and conductivity measurement, 1×1 $cm^2$ glass substrates were sonicated in ultrapure water containing Alconox detergent for 10 min, followed by 10 min sonication each in ultrapure water, acetone and IPA. EM and EMD films were then spin-coated onto these substrates and baked under the same conditions used for the polymer coating in the solar cell process. The sheet resistance and conductivity of the EM and EMD films were measured in a van der Pauw configuration by using a Hall effect measurement system (Ecopia HMS-5300). A UV-vis-NIR spectrophotometer (PerkinElmer Lambda 1050) was used to collect the reflectance spectra of the film samples. X-ray photoelectron spectroscopy (XPS) studies were conducted in a Thermo Scientific Nexsa G2 system, employing a monochromatic Al $K_\alpha$ source (1486.8 eV photon energy). CasaXPS software was used for peak fitting of characteristic photopeak features with appropriate subtraction of the Shirley background. The topography and surface roughness were examined by using tapping-mode atomic force microscopy (AFM) in an Asylum Cypher system. Samples for both XPS and AFM were prepared on silicon substrates, using the same fabrication procedure employed in solar cell fabrication.

The solar cell performance was characterized by using current density vs voltage (J-V) and external quantum efficiency (EQE) measurements in a PV Measurements IV5 and a QEX10 systems, respectively. The J-V characteristics were obtained under an illumination intensity of 100 mW/$cm^2$ (1 Sun), using a class ABA solar simulator equipped with an AM1.5G filter. In order to calibrate the intensity of the light source, a Si reference cell (PVM782 with a BK7 window) was used before performing any measurements and during the J-V measurements, an illuminated device area of 8.4×8.4 $mm^2$ was defined. The EQE measurements were carried out under monochromatic light,

obtained by using a dual-grating monochromator with a xenon arc lamp, along with a germanium photodiode detector. Typical area illuminated for EQE measurements was approximately 1×3.5 $mm^2$.

## 2.3 Results and Discussion

To investigate the effect of DMSO on the performance of HSCs, EM solutions containing additional selected amounts of DMSO were used to fabricate solar cells. After fabrication, the devices were stored in small boxes (to keep them dust-free) under laboratory ambient conditions; specifically, at 1 atm, 20 – 23 °C, and 30 – 50% relative humidity. No glove-box processing, vacuum storage or encapsulation was used. The solar cell performance data of HSCs fabricated using EM solution (i.e., without DMSO) is also collected for reference. Figure 2.2a shows the current density vs voltage (J-V) curves of the as-fabricated EM, EMD1, EMD3 and EMD5 cells. Evidently, there is significant improvement in the J-V curve for the EMD3 cell relative to the EM cell, while the J-V curve for EMD1 is similar to EM and that for EMD5 appears considerably worse than both EM and EMD1. The solar cell performance parameters of EMD1, EMD3, EMD5, and EM cells are compared in Table S2-1 (Appendix). The EMD3 cell is found to exhibit the best result, with short-circuit current density ($J_{SC}$) of 30.1 mA/$cm^2$, open-circuit voltage ($V_{OC}$) of 642.4 mV, fill factor (FF) of 69.4% and power conversion efficiency (PCE) of 13.4%. Figure 2.2b compares the J-V curves of the EMD3 cell as-fabricated (i.e., with 0 h of ambient storage) and over an extended period of ambient storage time, up to 216 h, and of EM cells as-fabricated and after 48 h and 72 h of ambient storage. Figure 2.2c presents the storage stability trends of solar cell performance metrics of the EMD3 and EM devices obtained from their respective J-V curves (Figure 2.2b). These solar cell performance data are also summarized in Table S2-2 (Appendix). While EMD3 maintains relatively stable $J_{SC}$, $V_{OC}$, FF, and PCE over time, EM shows considerable decline in all except $J_{SC}$ parameters, indicating poor stability. For example, the PCE for EMD3 (13.4%) is found to be remarkably stable, with a reduction of 10.6% (to 12.0%) after 72 h and 27.9% (to 9.7%) after 216 h of ambient storage. In contrast, the EM cell has a significant 34.4% decrease in PCE from 11.4% to 7.4% in just 24 h (Figure 2.2c). Figure 2.2d compares the EQE spectra of the EMD3 and EM as-fabricated cells. While the two EQE spectra are found to be nearly the same, the discernibly small difference indicates that the EMD3 cell is slightly higher in light absorption and carrier collection efficiency than the EM cell over the 400 - 900 nm region. Furthermore, no discernible differences are found in the EQE profiles of EMD3 and EM after 72 h of ambient storage time (not shown), suggesting that EQE data are not very sensitive to degradation changes.

In Table S2-3 (Appendix), we show the excellent reproducibility in the similar and consistently high solar cell performance metrics obtained for additional EMD3 cells (that we prepared separately). All the EMD3 cells are also found to remain stable for at least 72 h post-fabrication, and they follow the same degradation trends as shown in Figure 2.2c. It should be noted that there is also excellent reproducibility in our fabrication of the reported solar cells. Table S2-4 (Appendix) shows the solar cell performance data for six EMD3 cells separately fabricated on different dates. Three of these cells are used to obtain their degradation trends discussed above and are depicted in Table S2-3. The spans between the minimum and maximum values are 3.4%, 3.3%, 6.6% and 8.1% of the average values for $J_{SC}$, $V_{OC}$, FF and PCE, respectively (Table S2-4). Furthermore, the reproducibility of making the same measurement at different times for the same cells is illustrated for EMD3 and EM cells in Table S2-5 (Appendix). These data are within 0.3%, 0.1%, 0.1% and 0.9% of the average values for $J_{SC}$, $V_{OC}$, FF and PCE, respectively.

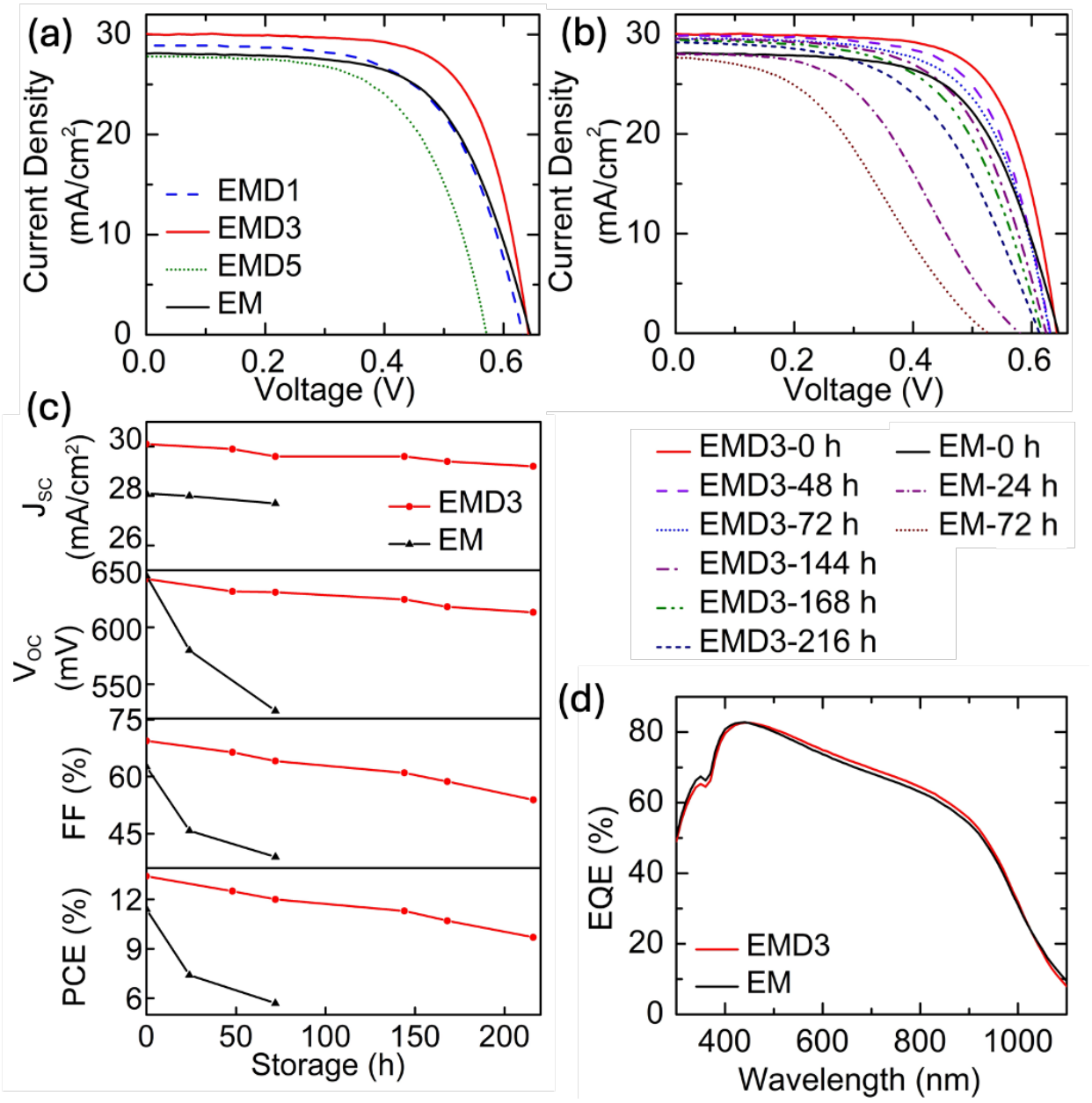



**Figure 2.2:** (a) Current density-voltage (J-V) curves for as-fabricated EM, EMD1, EMD3, and EMD5 solar cell samples, (b) J-V curves of EMD3 after 0 h, 48 h,72 h, 144 h, 168 h and 216 h of ambient storage and of EM after 0 h, 24 h, and 72 h of ambient storage. (c) Solar cell performance parameters ($J_{SC}$, $V_{OC}$, FF, and PCE) as functions of ambient storage time for EMD3 and EM cells. (d) Corresponding EQE spectra of as-fabricated EM and EMD3 solar cells.

Figure 2.3 and Table S2-3 compare the degradation of solar cell performance parameters, including $J_{SC}$, $V_{OC}$, FF and PCE, after 72 h of ambient storage for the EM and three EMD3 cells.

Evidently, the EM cell undergoes significant degradation as its $J_{SC}$, $V_{OC}$, FF, and PCE drop by 1.4%, 18.3%, 37.9% and 50.1% from their respective as-fabricated values after 72 h of ambient storage. On the other hand, the EMD3 cells exhibit, on average, a reduction of 0.8% in $J_{SC}$, 1.4% in $V_{OC}$, 12.0% in FF and 13.9% in PCE after 72 h of ambient storage. The three best-performing EMD3 devices (#1, #2, and #3 in Table S2-4) are found to remain highly consistent with one another after 72 hours of ambient storage, with all key performance values staying within the experimental variation. These small variations among the devices highlight the strong reproducibility of the DMSO-modified design. In contrast, the reference solar cell (EM) shows clear degradation over the same period, which confirms the improved stability of the EMD3 cells. These results demonstrate that high efficiency and good reproducibility can potentially be achieved without any post-fabrication treatment (such as encapsulation).

DMSO facilitates the separation of PEDOT from PSS, increasing the connectivity of PEDOT domains and formation of a more robust conductive network.[211] In our study, the addition of DMSO at an optimized wt% to PEDOT:PSS plays a crucial role in the creation of a high-quality film with improved ionic conductivity, charge transport, and mechanical/thermal stability, while preventing rapid degradation due to environmental factors. The partial removal of the insulating and hygroscopic PSS from the surface is another contributing factor that allows DMSO to simultaneously enhance conductivity and make the cell more resilient to degradation over time.[212]

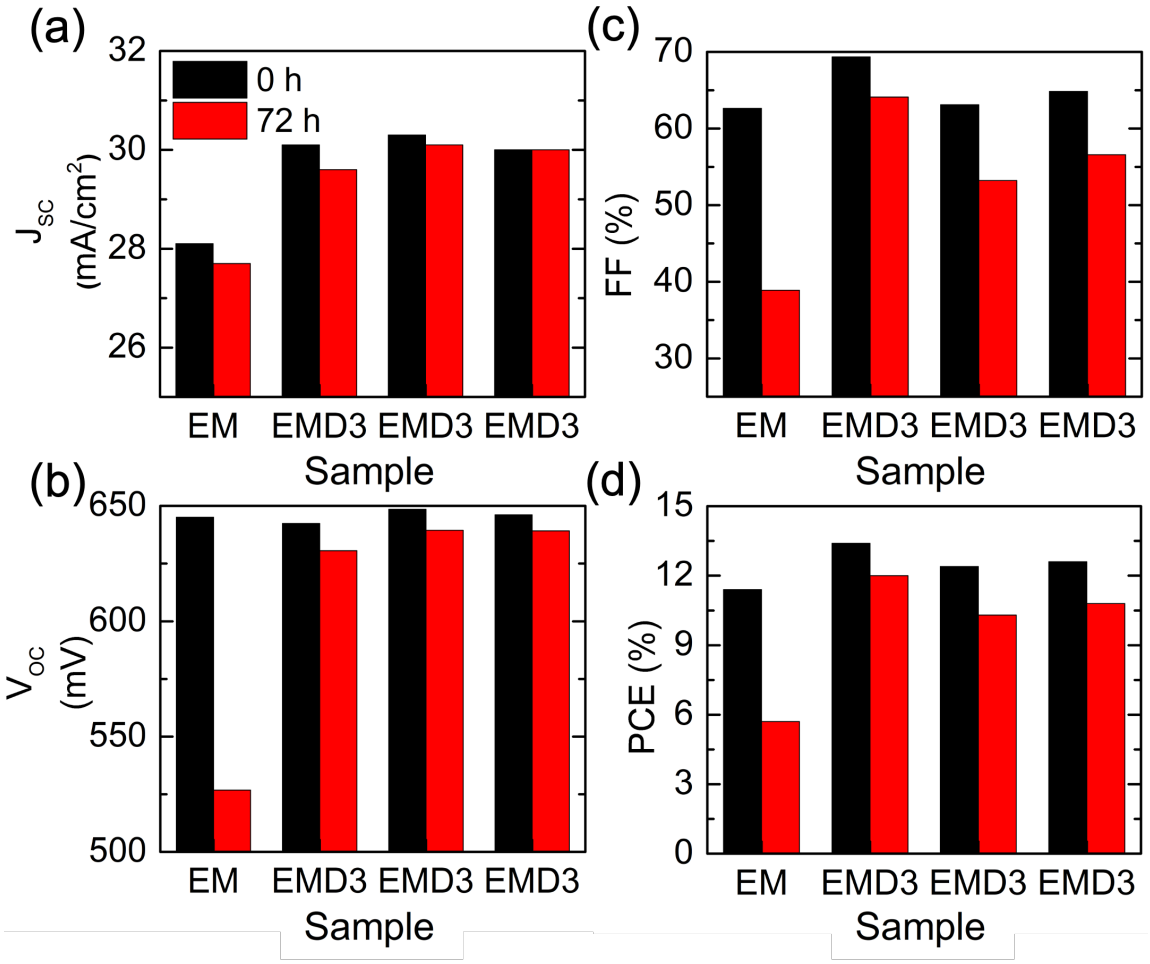



**Figure 2.3:** Solar cell performance parameters (a) $J_{SC}$, (b) $V_{OC}$, (c) FF, and (d) PCE of EM and three EMD3 cells as fabricated (black bars) and after 72 h of ambient storage (red bars).

The sheet resistance ($R_S$) and conductivity of EM, EMD1, EMD3 and EMD5 films used for fabricating the aforementioned solar cells are measured and they are shown in Figure 2.4 to compare the changes in conducting properties and stability before and after 72 h of ambient storage. Among the as-deposited film samples (black bars), EMD1 has a lower $R_S$ (Figure 2.4a) and, correspondingly, a slightly higher conductivity than EM (Figure 2.4b). The as-deposited EMD3 film has the lowest $R_S$ and the highest conductivity while the as-deposited EMD5 film has the highest $R_S$ and the lowest conductivity, which shows that addition of too much or not enough DMSO can be counterproductive.[204,213,214] After 72 h of ambient storage (red bars), the $R_S$ value of the EM film appears more than double and there is a correspondingly large decrease in the conductivity, which confirms that the EM film is more vulnerable to environmental factors and the degradation process. For the EMD1 film, the changes in $R_S$ and conductivity after 72 h of ambient storage are,

respectively, somewhat lower and higher than EM but both $R_S$ and conductivity remain considerable, suggesting that the addition of 1 wt% DMSO only has a small impact. For the EMD3 and EMD5 films both with large enough DMSO wt%, there are considerably smaller increases in $R_S$ and corresponding decreases in conductivity (red bars) relative to their respective as-deposited values (black bars), confirming the positive effect of DMSO on reducing the degradation effect on performance upon ambient storage.

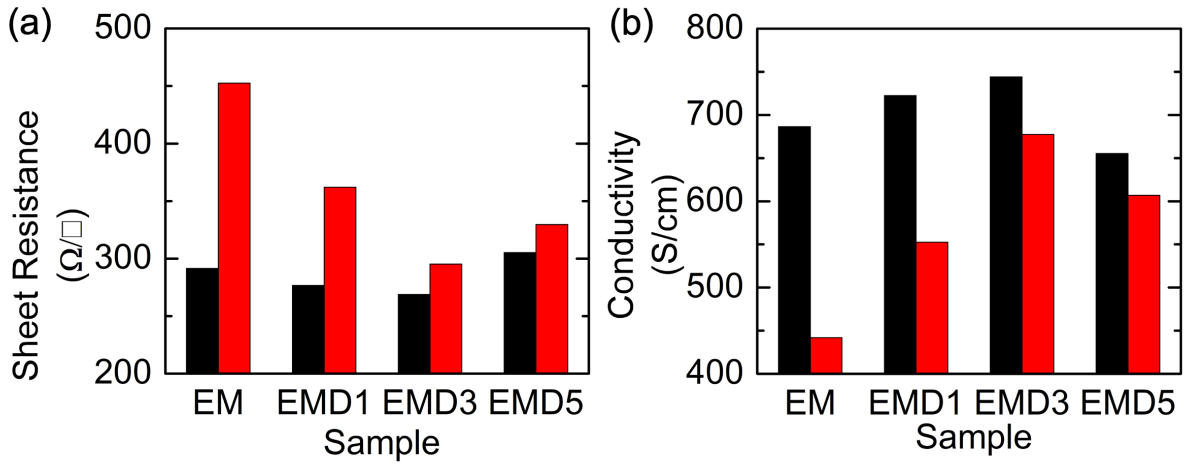



**Figure 2.4:** (a) Sheet resistance and (b) conductivity of EM, EMD1, EMD3 and EMD5 films as-deposited on glass substrates (black) and after 72 h of ambient storage (red).

Figure 2.5a compares the XPS spectra of the S 2p region for the as-deposited EMD3 and EM films (on silicon substrates). The relative composition ratio of PEDOT to PSS components in the samples can be obtained by comparing the intensities (or peak areas) of their respective characteristic S 2p peaks. Evidently, in EMD3 (Figure 2.5a1) the S $2p_{3/2}$ ($2p_{1/2}$) peak of PEDOT at 163.7 eV (164.9 eV) binding energy is found to be weaker than that of PSS at 168.1 eV (169.2 eV).[139,215] There is a notable increase in the ratio of PEDOT to PSS in EMD3 (0.452, Figure 2.5a1) compared to EM (0.419, Figure 2.5a2), which is consistent with the decrease in $R_S$ and the corresponding increase in conductivity of the EMD3 film (arising from the presence of DMSO in PEDOT:PSS), relative to the EM film.

Figures 2.5b-2.5c show the corresponding AFM topography and phase images of the EMD3 and EM films, both of which exhibit very similar morphology with ellipsoidal grains. Cosolvents in both samples appear to facilitate elongation of the PEDOT chains and thus close packing of grains, which contributes to a smoother charge carrier transfer.[140,216] The root mean square (RMS) roughness of EMD3 is found to be 2.5 nm (Figure 2.5b1) while that for EM is 2.3 nm (Figure 2.5b2). The slightly

rougher surface of the sample with added DMSO (EMD3) shows that enlarged fibrillary structures with aggregated PSS and closely packed PEDOT have a more oriented morphology.[216] While a smoother surface might be preferred for providing better interfacial contacts, a moderate level of roughness could increase light absorption, which may account for the observed EQE enhancement across the 400–900 nm range. [88,217] The reflectance spectra of the silicon substrate and the EM, EMD1, EMD3, and EMD5 films (deposited on silicon substrates) are shown in Figure S2-1 (Appendix). With the exception of the Si substrate, the reflectance spectra of all the polymer films appear very similar to one another, which is in accord with that the reflectance properties of these polymer films appear not to account for the differences in the performance data of the solar cells obtained from these films. However, the marginal 0.2 nm difference in RMS roughness is consistent with the slightly more reflective EMD3 film than EM with the difference within the margin of experimental errors.

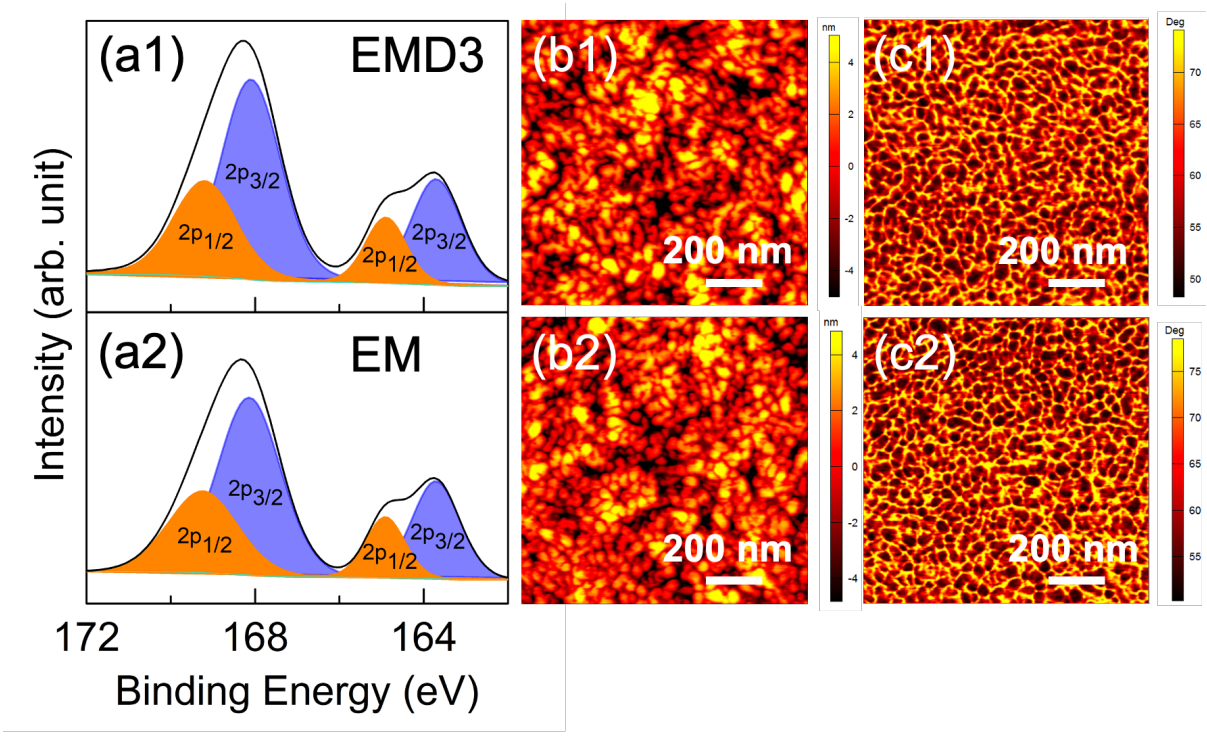



**Figure 2.5:** (a1, a2) XPS spectra of the S 2p region (left) and AFM images of (b1, b2) topography (center) and (c1, c2) phase (right) of EMD3 (a1, b1, c1) and EM films deposited on silicon substrates (a2, b2, c2).

The use of this simple one-step modification is found to greatly improve the longevity of the HSCs. One of the key features of DMSO in PEDOT:PSS solution that is distinctive from EG is the stronger interaction of DMSO with protonated $PSS^-$.[218] Specifically, the vacuum interaction energy of the DMSO-PSSH complex (–1.22 eV) is more negative than that for the EG-PSSH complex (–1.01 eV). This indicates that the interactions are energetically more favorable for DMSO-PSSH, with a more negative value corresponding to a stronger interaction that leads to a more stable complex. As the primary type of interaction is hydrogen bonding, the oxygen atom in DMSO facilitates unusually strong hydrogen bonding with the –S–O–H moiety in the sulfonic acid group of PSSH (with the hydrogen bond length between PSSH and DMSO of 1.05 Å).[219] Furthermore, as the methyl hydrogens in DMSO interact with the two sulfonate oxygen atoms in PSSH (Figure 2.6), this has led to complete coverage of PSSH and reduction in the interactions of the $–SO_3H$ groups in PSSH with other PSS and PEDOT chains. As a result, the excess insulating PSSH shells can be separated from the $PSS^-$ modified $PEDOT^+$.[216,218,219]

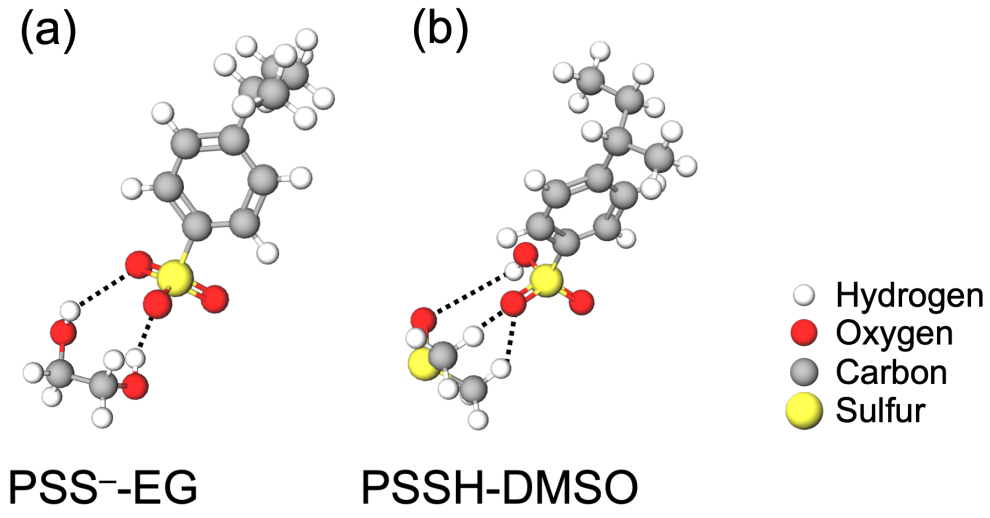



**Figure 2.6:** Schemes of proton sharing between (a) $PSS^-$ and EG and (b) PSSH and DMSO.

DMSO can also cause PSS to aggregate and create pathways for charge movement.[139,212,220,221] This makes the implementation of DMSO as a cosolvent a promising approach to conductivity enhancement. On the other hand, because EG can only provide two strong hydrogen bonds with $PSS^-$, incorporation of these two cosolvents with different mechanisms together can improve the electrical conductivity of PEDOT:PSS solution. The bonding formation of PSSH to DMSO causes rearrangement of the PEDOT chain and improves the phase separation of the PSSH matrix while stabilizing the PSSH matrix. The removal of the insulating PSSH shells that cover the conductive PEDOT moiety enhances the electrical conductivity. Furthermore, it has been reported that methanol has the same phase separation effect and it can also be used to improve the wettability of PEDOT:PSS.[88,222] In the standard form of PEDOT:PSS in electronic applications, PEDOT is the cationic part of the polymer while PSS is negatively charged. Different pH conditions and local chemical environments during or post fabrication could therefore shift the equilibrium toward more PSSH.[223] Due to the phase separation, PSSH and PEDOT complexes coexist in the solution.[186,212,224] DMSO is an excellent candidate for enhancing the conductivity and stability of PEDOT:PSS due to its strong interaction with the insulating PSSH component. This interaction between DMSO and the sulfonic acid group of PSSH (polystyrene sulfonic acid) is stronger than the interaction between PSS and PSS and that between PEDOT and PSS. This therefore allows DMSO to more effectively remove the insulating PSS shell surrounding the conductive PEDOT chains, enabling the PEDOT chains to aggregate and form a more conductive pathway. The removal or reduction of the PSS shell is a primary route for increasing the electrical conductivity of PEDOT:PSS. The effectiveness of DMSO

in removing the PSSH shell can pave the way for a second solvent such as EG, with a different interaction mechanism, to target the remaining PSS chains. This combined approach results in a significant improvement in conductivity compared to employing just DMSO. As the acidity of PEDOT:PSS that leads to its fast degradation is caused by PSS, removal of PSS also protects the electrodes from corrosion and leads to longer stability.[225,226] It should be noted that too high concentration of cosolvents could counteract the desired effects by acting as insulating materials themselves or introducing cracks to the film.[204,213,214]

In addition, DMSO can enhance the mechanical stability of PEDOT:PSS films, largely due to the structural and morphological changes that DMSO induces within the polymer network. As a secondary dopant that reorganizes the PEDOT structure, DMSO facilitates more effective ordering of PEDOT chains. This organized structure improves crystallinity and results in a denser, more uniform film, which contributes to better mechanical stability along with enhanced electrical conductivity. The most important way that DMSO strengthens mechanical stability is by reducing the amount of PSS, an insulating and relatively brittle component, that covers the PEDOT chains. This reduction decreases the hydrophilic nature of the PEDOT layer, making it less prone to swelling and degradation in humid conditions, which would otherwise reduce the structural integrity of the film. By facilitating PEDOT alignment and its phase separation from PSS, DMSO-treated films can improve flexibility and resistance to crack propagation and to environmental factors, such as humidity and moisture, which are common challenges for PEDOT in electronic applications.[212,227,228]

To date, the highest reported efficiencies for simple planar heterojunction solar cell structures have typically been less than 16%,[87,88,92,93,229–232] achieved without the implementation of elaborate techniques such as micro/nano-texturing of the substrate, addition of anti-reflection coatings or passivation layers, and fabrication of the more complex perovskite solar cells. Most if not all of these processes are generally not cost effective, because they involve the use of more complex procedures and advanced equipment.[233–238] Furthermore, the stability of this type of solar cells in the following days after fabrication is unclear as it is often not reported in the literature.

The most common approach to enhancing the stability of solar cells is encapsulation. This process involves adding a protective layer to shield the cells from environmental factors such as moisture, oxygen, UV exposure and mechanical damage. Techniques used for encapsulation include spin coating, atomic layer deposition (ALD), plasma-enhanced chemical vapor deposition (PECVD), roll-to-roll printing, screen printing, and lamination.[225,239–243] However, any additional step could introduce complication into the process and increase the cost of fabrication. Techniques such as ALD

and PECVD that produce high quality and conformal coatings are expensive and time consuming, especially for large scale production. Additionally, some encapsulation materials may have limited compatibility with specific types of solar cells, particularly organic or organic–inorganic solar cells, where chemical reactions between the encapsulant and active materials could negatively impact performance. Here, we have demonstrated the fabrication of solar cells that are intrinsically more stable by avoiding extra costly steps. In the present work, the sample cells are stored under ambient conditions with no further protection or modification. DMSO incorporated to EM-added PEDOT:PSS is found to have a remarkably positive effect on the stability of these planar heterojunction solar cells.

## 2.4 Conclusion

In this study, the effects of adding DMSO to EM-added PEDOT:PSS solutions used in HSCs have been investigated. Our experiments demonstrate that DMSO can enhance both the electrical conductivity and the longevity of these solar cells. The addition of DMSO to methanol and EG cosolvents facilitates the deposition of a more homogeneous PEDOT:PSS film, improving charge carrier mobility and phase separation of PEDOT and PSS, as DMSO effectively removes the PSS shells and thus improves conductivity and stability. Indeed, the interaction of DMSO with PSSH, which complements that of EG with $PSS^-$, is particularly beneficial in increasing the PEDOT-to-PSS ratio while maintaining the integrity of the film interfaces. The most notable results are obtained with our EMD3 sample, which exhibits minimal efficiency loss (10.6% of its as-fabrication value) 72 h after fabrication, highlighting the potential for achieving more stable solar cells. In contrast, the control sample (EM), with no DMSO added, shows rapid degradation. It is noteworthy that no special care or protection has been applied to these cells while they are being stored under ambient conditions. This suggests that the simple addition of DMSO to the existing EG and methanol cosolvents could be the key to improving the stability and performance of PEDOT:PSS-based solar cells potentially without any need for encapsulation. These findings suggest that the DMSO-EM-PEDOT:PSS approach can be broadly extended to other PEDOT:PSS-based applications, offering a simple strategy for enhancing conductivity and long-term stability across various organic and optoelectronic devices.

# Chapter 3
# Enhancing Performance and Stability of PEDOT:PSS-based Organic–Inorganic Planar Heterojunction Solar Cells through Dimethyl Sulfone Doping

## 3.1 Introduction

Heterojunction solar cells (HSCs), including organic–inorganic photovoltaics, often employ a thin film of poly(3,4-ethylenedioxythiophene):poly(styrenesulfonate) (PEDOT:PSS) as the hole-transport layer (HTL) or anode buffer due to its transparency, solution processability, and considerable conductivity. However, pristine PEDOT:PSS films have an intrinsically low electrical conductivity (typically 0.1-1 S/cm) and they suffer from poor environmental stability because of the insulating, hygroscopic, and acidic nature of the PSS component.[244,245] These drawbacks lead to increased series resistance and gradual device performance degradation under ambient conditions. Improving the conductivity and stability of PEDOT:PSS films is therefore crucial for advancing reliable HSC performance.

A well-established strategy to enhance the conductivity of PEDOT:PSS films is to use polar cosolvents or dopants, including dimethyl sulfoxide (DMSO), ethylene glycol (EG), and methanol. These cosolvents can be added as a premixed solution or applied sequentially to PEDOT:PSS. Such solvent treatments can increase the conductivity of the film by several orders of magnitude through morphological and structural rearrangements in the PEDOT:PSS matrix.[138,226,246–248] Without proper modification, solar cells made with pristine PEDOT:PSS on planar silicon yield only ~2.4% power conversion efficiency (PCE) because the unmodified film has low conductivity and poor interfacial wetting that raises the series resistance and recombination losses.[139] Introducing a methanol-ethylene glycol cosolvent blend has been shown to enhance the electrical conductivity of PEDOT:PSS and boost the PCE performance of the resulting polymer/Si solar cells significantly to 14.6%.[88] In addition, adding 5% v/v DMSO to PEDOT:PSS has also been reported to lower the film resistivity by 1–2 orders of magnitude and raise the conductivity up to almost 1230 S/cm and the PCE to 11%.[204] This dramatic improvement is attributed to the formation of well-organized PEDOT-rich domains, thereby improving the interface contact. As a polar molecule, DMSO interacts with the hydrophilic PSS chains, weakening the coulombic PEDOT to PSS coupling and driving a phase separation between the conductive PEDOT and the insulating PSS.[182,246] X-ray photoelectron spectroscopy (XPS) analyses have confirmed that cosolvent-treated PEDOT:PSS films have an increased PEDOT

to PSS ratio (near the film surface) as a result of the partial removal and/or redistribution of the insulating PSS moiety.[87,135,139,143,199,205,249] Concurrently, strong van der Waals interactions between DMSO and the polymer chains induce a conformational change of PEDOT from a coil-like, benzoid structure to a more extended, planar quinoid form.[138,204,207,219,250–253] This combination of PSS phase segregation and polymer backbone planarization results in a more continuous and effective charge-transport network. Recent reports indicate that DMSO treatment enhances organization in PEDOT:PSS, leading to higher mobility and a transport regime that is less "hopping" limited and more "band-like".[254,255]

There is a continued strong interest in new additives for further improving the PEDOT:PSS film morphology, conductivity, and especially long-term stability.[151,208] One promising candidate is dimethyl sulfone ($DMSO_2$ or D2 for short). Also known as methylsulfonylmethane (or MSM), D2 is a small sulfonyl-containing molecule that has been explored as a "green" cosolvent for PEDOT:PSS.[218] In contrast to liquid DMSO, $DMSO_2$ is a solid at room temperature (with a melting point of 109 °C) and it crystallizes out upon drying the PEDOT:PSS film. This unique behavior effectively reorganizes the polymer microstructure. The in-situ crystallization of $DMSO_2$ molecules induces organization and self-alignment of neighboring PEDOT chains.[218,256] Specifically, as fibrous $DMSO_2$ microcrystals form, they trigger the long PSS chains to reorient along their length, which leads to the alignment of the attached PEDOT chains into an extended linear conformation. The ordered PEDOT chains enhance the in-plane conductivity [257,258] (for lateral transport to contacts) and through-plane conductivity [259](for vertical transport to the Si substrate).

It has been observed by using field-emission scanning electron microscopy that $DMSO_2$-doped PEDOT:PSS films develop embedded needle-like crystallites and a fibrillar polymer texture, indicative of an aligned morphology not achievable with conventional liquid additives such as DMSO.[218] Such structural reorganization leads to a more homogeneous and interconnected conductive network with enhanced charge transport. It has also been reported that a very high conductivity of 1080 S/cm can be obtained for PEDOT:PSS films by using a premixed PEDOT:PSS+$DMSO_2$ solution followed by post treatment with solvents such as water, methanol and ethanol.[218] As $DMSO_2$ is chemically inert (with fully oxidized sulfur atom) and non-hygroscopic, it can therefore make PEDOT:PSS more stable under ambient conditions. Indeed, $DMSO_2$-doped PEDOT:PSS films have been found to retain almost 90% of their initial conductivity even after 60 days of exposure to humid air, whereas films processed with liquid dopants often degrade faster due to moisture uptake and/or oxidation.[151] While solvent additives generally boost performance, addressing the degradation issues

requires specific strategies such as implementing non-acidic additives, crystallizers, or encapsulants. This improved stability is attributed not only to establishment of an aligned morphology by $DMSO_2$ crystallites discussed above, but also to the reduction of free PSS, which is hygroscopic and acidic and is primarily responsible for degradation. Given these advantages, $DMSO_2$ has emerged as an attractive green cosolvent to replace or to supplement DMSO in enhancing the PEDOT:PSS film used for heterojunction solar cells.

HSCs involving PEDOT:PSS and silicon are prone to performance degradation when exposed to ambient moisture and oxygen.[260] Encapsulation methods, such as solution-processed spin-coated polymer barriers, ultrathin oxide layers grown by atomic layer deposition (ALD), moisture blocking $SiO_x$ shells deposited by plasma enhanced chemical vapour deposition (PECVD), multilayer barrier foils patterned by roll-to-roll slot-die or flexographic printing, UV curable edge seals or encapsulant pastes applied by screen printing, and conventional glass/glass lamination with ethylene-vinyl acetate or related interlayers, have proven to be among the most effective to tackle these stability issues.[225,239_243,261_266] By adding a protective barrier layer (e.g. a thin $Al_2O_3$ coating by ALD), researchers have observed markedly improved device lifetimes, as the encapsulant blocks the ingress of oxygen and water that would otherwise deteriorate the active layers.[240,267] Despite being the most successful type of encapsulation method for organic and flexible electronics, the ALD technique is chemistry-specific and expensive.[268,269] It is noteworthy that even with encapsulation, acidic or hygroscopic layers could still initiate slow burn-in losses. There is, therefore, an acute need for improving the intrinsic stability of these solar cells.[270]

In our recent work (Chapter 2), we have explored the use of DMSO as an additional cosolvent to EG and methanol cosolvent-treated PEDOT:PSS in order to improve the long-term performance and stability of the resulting HSCs. In the present work, we examine the use of $DMSO_2$ to improve the performance and longevity of HSCs through a comparative study of PEDOT:PSS-based HTLs formulated with selected cosolvents: ethylene glycol + methanol (EM), ethylene glycol + $DMSO_2$ (ED2), and ethylene glycol + methanol + $DMSO_2$ (EMD2), along with a small percentage of surfactant. Incorporating EG, $DMSO_2$, and surfactant into the HTL improves electrical conductivity, film morphology, uniformity, and ambient stability, establishes a high-quality interface, and increases open circuit voltage ($V_{OC}$), short circuit current density ($J_{SC}$), fill factor (FF), and PCE in planar silicon HSCs. Among the tested formulations, $DMSO_2$ provides superior improvements in conductivity, morphology, and ambient stability, and the resulting higher charge-carrier mobility and

more uniform microstructure (relative to untreated films) enhance both device performance and longevity.

## 3.2 Experimental Details

PEDOT:PSS (PH1000, Clevios) was filtered through a 0.45 μm polyvinylidene fluoride syringe filter and used without further treatment. All other reagents were obtained commercially and used as received. Three PEDOT:PSS solutions were prepared with the following compositions: EM: 8 wt% EG and 8 wt% methanol; ED2: 8 wt% EG and 3 wt% $DMSO_2$; and EMD2: 8 wt% EG, 8 wt% methanol, and 3 wt% $DMSO_2$, all with 0.25 wt% FS-300 and PEDOT:PSS making up the balance. The surfactant FS-300 (purchased from Fluka Analytical) was mixed into each cosolvent-added solution just before spin-coating the solution onto the Si substrate.

Phosphorus-doped n-type Si(100) wafers (single-side polished, 280 ± 25 μm thick, 100 ± 0.3 mm in diameter and 0.04–0.07 Ω cm resistivity; Virginia Semiconductor Inc.) were cut into 10×10 $mm^2$ chips. The chips were sonicated for 10 min each in acetone and isopropanol, rinsed with ultrapure water, dipped in 5% HF for 2 min to remove the native oxide, then rinsed again and dried under nitrogen. A 200-nm thick Al layer was sputter-coated onto the back (unpolished) side of the Si substrate to form the bottom electrode. The front (polished) side was left in air for 20 min to grow a thin $SiO_2$ layer (less than 2 nm thick), following the optimized procedure used in chapter 2.[88] Each PEDOT:PSS solution was spin-coated at 4000 rpm for 60 s onto the Si substrate, giving a uniform film. The film was baked at 110 °C on a hotplate for 10 min in air. To complete the HSC device, a 50-nm thick Ag layer was sputter-coated through a shadow mask to form the top electrode.

Sheet resistance and conductivity of the polymer film were measured in the van der Pauw geometry by using an Ecopia HMS-5300 Hall effect measurement system. For these measurements, 10×10 $mm^2$ glass substrates were sonicated for 10 min each in ultrapure water with Alconox, ultrapure water, acetone and isopropanol. EM, ED2 and EMD2 films were then spin-coated onto these glass substrates and baked under the same conditions as those used in the solar cell fabrication process. Surface topography was recorded by tapping-mode atomic force microscopy (AFM) in an Asylum Cypher microscope.

X-ray photoelectron spectroscopy (XPS) was performed in a Thermo Nexsa G2 Microprobe using a monochromatic X-ray beam (Al Kα). XPS depth profiling measurements were conducted by using a 4 kV $Ar_{1000}^+$ cluster ion beam for sample sputtering. The films were deposited on silicon substrates using the same spin coating and baking conditions as those used for the solar cell fabrication. The

XPS spectra were fitted by using the CasaXPS software to extract composition information about individual chemical states after appropriate removal of the Shirley background.

Time-of-flight secondary ion mass spectrometry (TOF-SIMS) experiments were carried out in an ION-TOF SIMS 5 instrument equipped with an extended dynamic range analyser running in a negative polarity mode. Films were deposited on silicon using the same spin coating and baking conditions as the solar cell fabrication process. Secondary ions were probed with a 30 kV $Bi_3^+$ ion beam, while material removal for depth profiling was achieved by using a 5 kV $Ar_{2000}^+$ cluster ion source. Profiles were recorded in non-interlaced spectrometry mode with a 200 µs cycle time, employing a 150×150 µm² analysis area inside a 400×400 µm² sputter crater. Spectra were mass-calibrated against the characteristic $C_x^-$ fragments.

Solar-cell performance was evaluated with current density vs voltage (J-V) and external quantum-efficiency (EQE) measurements in an IV5 and a QEX10 systems from PV Measurements, respectively. J-V curves were taken under AM 1.5 G illumination at 100 mW $cm^{-2}$ (1 Sun) calibrated with a PVM782 Si reference cell. The typical illuminated device area was 7.7×7.7 $mm^2$. EQE spectra were recorded with monochromatic light from a xenon lamp and with a germanium photodiode over an illuminated area of 1×3.5 mm².

## 3.3 Results and Discussion

The conductivity and sheet resistance measurements were obtained by using the van der Pauw four-probe method for the EM, ED2 and EMD2 films (Figure 3.1). Evidently, both EM and EMD2 films exhibit higher sheet resistance ($R_S$) than the ED2 film. The EMD2 film is found to deliver the highest electrical conductivity (1076.6 S/cm), outperforming ED2 (1021.1 S/cm) and EM (987.6 S/cm).

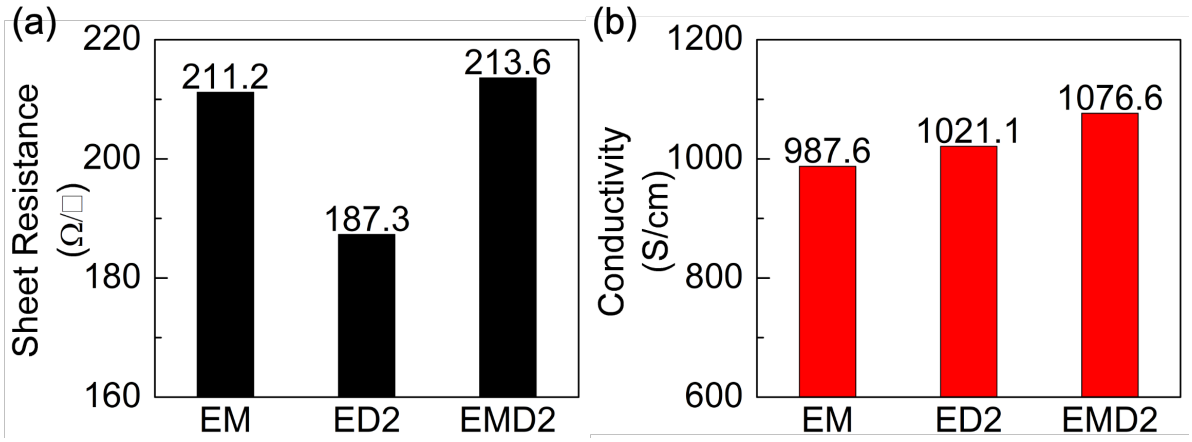



**Figure 3.1:** (a) Sheet resistance and (b) conductivity of EM, ED2 and EMD2 films spin-coated on glass substrates.

AFM analysis of the EM, ED2 and EMD2 films shown in Figure 3.2 indicates that EMD2 has the highest surface concentration of conductive PEDOT domains. Its topography image (Figure 3.2c1) reveals the dense surface region of bright protrusions and the largest RMS roughness (2.24 nm, Figure 3.2c3), both of which are signatures of abundant, long PEDOT-rich grains. The high RMS value arises from a transition from random granular domains to oriented, enlarged fibrillary structures, in which PEDOT:PSS appear to be strongly segregated into PSS aggregates and PEDOT aggregates. [231,271–273] These large, tightly packed PEDOT domains give EMD2 the largest bulk conductivity. In contrast, the ED2 film (Figure 3.2b3) shows the smallest RMS roughness (1.74 nm). Its topography image (Figure 3.2b1) contains fewer but more closely packed PEDOT aggregates than EM (Figure 3.2a1), forming a more linear network with shorten percolation paths. High packing density enlarges the inter-grain contact area and compresses the PSS shells between adjacent PEDOT chains, thus lowering the junction resistance that contributes to lower $R_S$. These results highlight the morphological alignment advantages afforded by the combined EG and $DMSO_2$ cosolvent treatment. The lowest RMS of ED2 suggests that the smoother surface of ED2 with the lowest $R_S$ minimizes the amounts of pinholes and gaps, suppressing shunt paths and reducing series resistance at the metal contact to film interface despite having fewer large domains overall. Finally, the AFM image of the EM film (Figure 3.2a1) shows more isolated and sharper PEDOT protrusions, which result in an intermediate RMS roughness (1.86 nm). These protrusions also show less connection with one another than those of ED2 and EMD2.

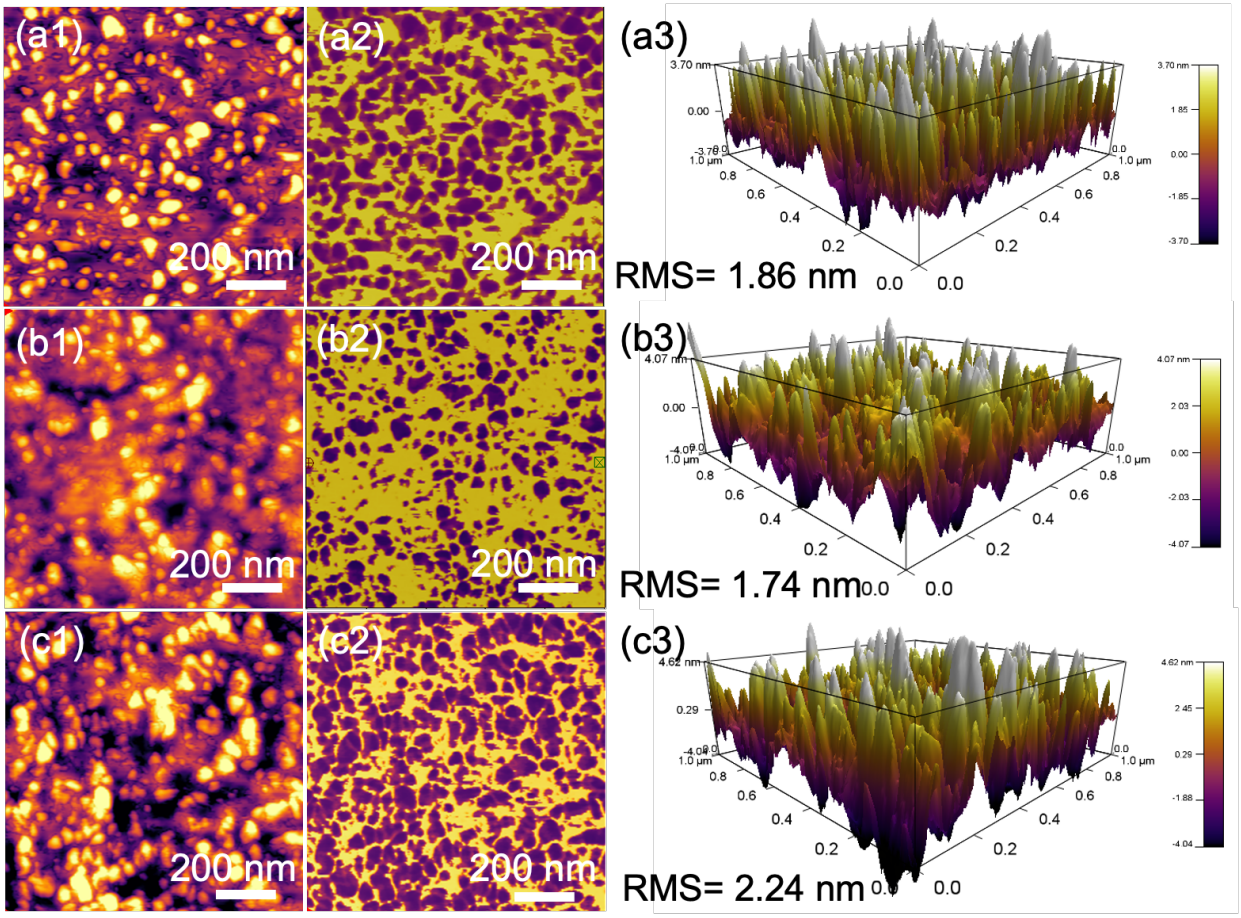



**Figure 3.2:** AFM images of surface topography (left column) and phase retrace (center column) and 3D perspective views of surface topography (right column) of (a1, a2, a3) EM, (b1, b2, b3) ED2 and (c1, c2, c3) EMD2 films spin-coated on silicon substrates.

XPS is used to determine the chemical-state compositions for PEDOT and PSS moieties before and after modification at the top surface (Figure 3.3a). The ratio of PEDOT to PSS components in the samples can be obtained by using the fitted peak areas of their respective S 2p photopeaks. For the EM film, the S $2p_{3/2}$ (S $2p_{1/2}$) peak of PEDOT at 163.6 eV (164.8 eV) is found to be lower in binding energy than the S $2p_{3/2}$ (S $2p_{1/2}$) peak of $PEDOT^+$ at 164.6 eV (165.8 eV).[139,215] The S $2p_{3/2}$ (S $2p_{1/2}$) peaks at 168.0 eV (169.1 eV) and at 168.1 eV (169.3 eV) correspond to $PSS^-$ and PSSH, respectively. The ratios of $PSS^-$/PSSH in EM, ED2, and EMD2 are determined from the appropriate peak areas in the XPS spectra. EMD2 exhibits the lowest PSSH content, with a $PSS^-$/PSSH ratio of 10, whereas the ratios in EM and ED2 are 6 and 5, respectively. On the other hand, the ratios of $PEDOT^+$/PEDOT in EM (0.8), ED2 (0.6), and EMD2 (0.7) are found to be quite similar to one another.

Using an argon cluster ion (4 kV $Ar_{1000}^+$) source, we collect depth-profiling XPS spectra of the polymer films as a function of the sputtering time (Figure S3-1). Figure 3.3b shows the fitted intensity ratio of the PEDOT to PSS component as a function of the sputtering time. Evidently, EMD2 maintains the highest overall PEDOT/PSS ratio throughout the sputtering depth region, which is indicative of a uniform and consistent conductive network throughout the near surface region of the film (estimated to be top 20 nm). The ratios for ED2 and EM are found to follow nearly the same trend, and both are lower than EMD2 throughout the sputtering depth, which demonstrates the constructive effect of proper solvent engineering with all three cosolvents in the EMD2 film.

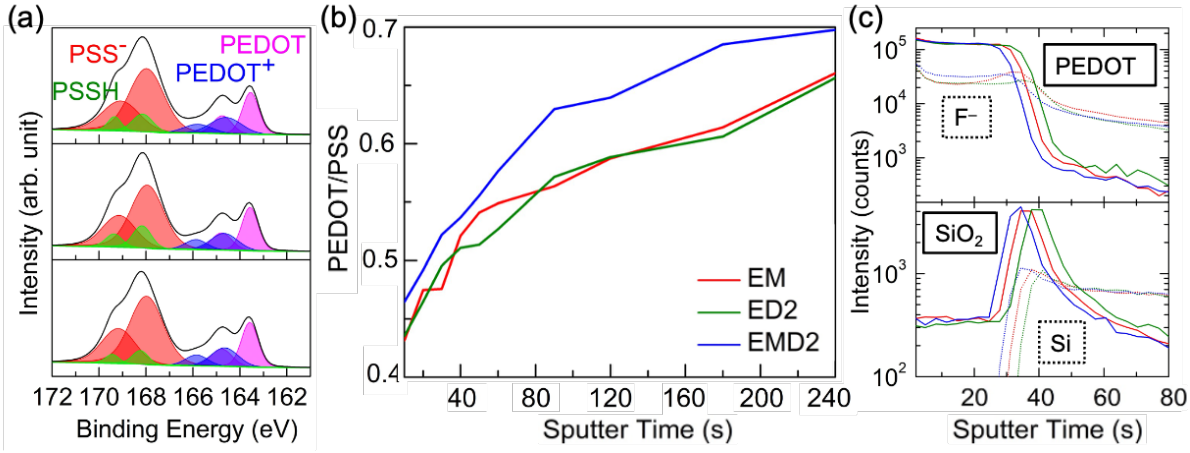



**Figure 3.3:** (a) XPS spectra of the S 2p regions for (top) EM, (middle) ED2 and (bottom) EMD2 films deposited on silicon. (b) the PEDOT/PSS ratio measured by the corresponding XPS depth profiling spectra of the EM, ED2 and EMD2 films (top 20 nm). (c) TOF-SIMS depth profiles of $C_8H_7SO_3^-$ (characteristic of PEDOT), $F^-$, $SiO_2^-$ and $Si^-$ fragments obtained with a 5 keV $Ar_{2000}^+$ sputtering beam and a 30 keV $Bi_3^+$ analysis beam.

The role of the interface in solar cell performance is examined by using TOF-SIMS depth profiling. The sample is sputtered with a 5 keV Ar cluster ion ($Ar_{2000}^+$) beam, gentle enough to limit damage to the near surface region of the polymer film, while secondary ions are analyzed using a 30 kV $Bi_3^+$ ion beam. Figure 3.3c shows the depth profiles of $C_8H_7SO_3^-$ fragment that is characteristic of PEDOT, $SiO_x$ from the interface, Si from the substrate, and $F^-$ from the surfactant. Evidently, the characteristic PEDOT fragment in EMD2 is found to be removed after a discernibly shorter sputtering time than EM and ED2, with ED2 taking the longest sputtering time. These profiles are therefore consistent with the trend of the film thickness: EMD2 < EM < ED2. The $F^-$ profile is largely uniform across the film thickness.

There are substantial differences in the interactions between $DMSO_2$ and the other previously studied cosolvent molecules such as EG and DMSO, which contribute to the observed differences in the properties. Each PSS chain contains sulfonic acid groups ($–SO_3H$) and is often denoted as PSSH when protonated. Polar cosolvents and additives have a strong screening effect, which contributes to the conductivity improvement.[249] $DMSO_2$ is a small polar molecule with a sulfonyl (O=S=O) group, allowing it to form multiple hydrogen bonds with PSS. First-principle calculations have shown that the oxygen atoms in $DMSO_2$ create hydrogen bonds with the –S–OH groups of PSSH, while the hydrogen atoms of its methyl groups interact with the other sulfonate oxygens (Figure 3.4).[218] Uniquely, a bifunctional [218,274] $DMSO_2$ molecule can simultaneously bind with two separate PSSH units (one on each of the two sulfonyl oxygen atoms) and create a "bridging effect". On the other hand, DMSO has a single sulfoxide group (S=O) and can form only one strong hydrogen bond with –S–OH at a time while the hydrogen atoms of the two methyl groups of DMSO are interacting with other sulfonate oxygens. For consistency, the following interactions are compared based on the coordination with two PSSH monomers. This bridging effect of $DMSO_2$ leads to a notably strong total interaction energy. The reported calculated interaction energies of $DMSO_2$ with two PSSH chains is on the order of –1.89 eV in vacuum and –1.12 eV with water solvation, which are more negative than those of common additives such as EG (with interaction energies with two PSSH of –1.41 eV in vacuum and –1.02 eV with water solvation) or DMSO (–1.69 eV in vacuum and –1.22 eV with water solvation) forming hydrogen bonding with one $PSS^-$.[218] The dual hydrogen-bond capability of $DMSO_2$ with two PSSH units therefore gives it a potent ability to bind and screen the sulfonic acid sites on PSS more effectively.[218,256]

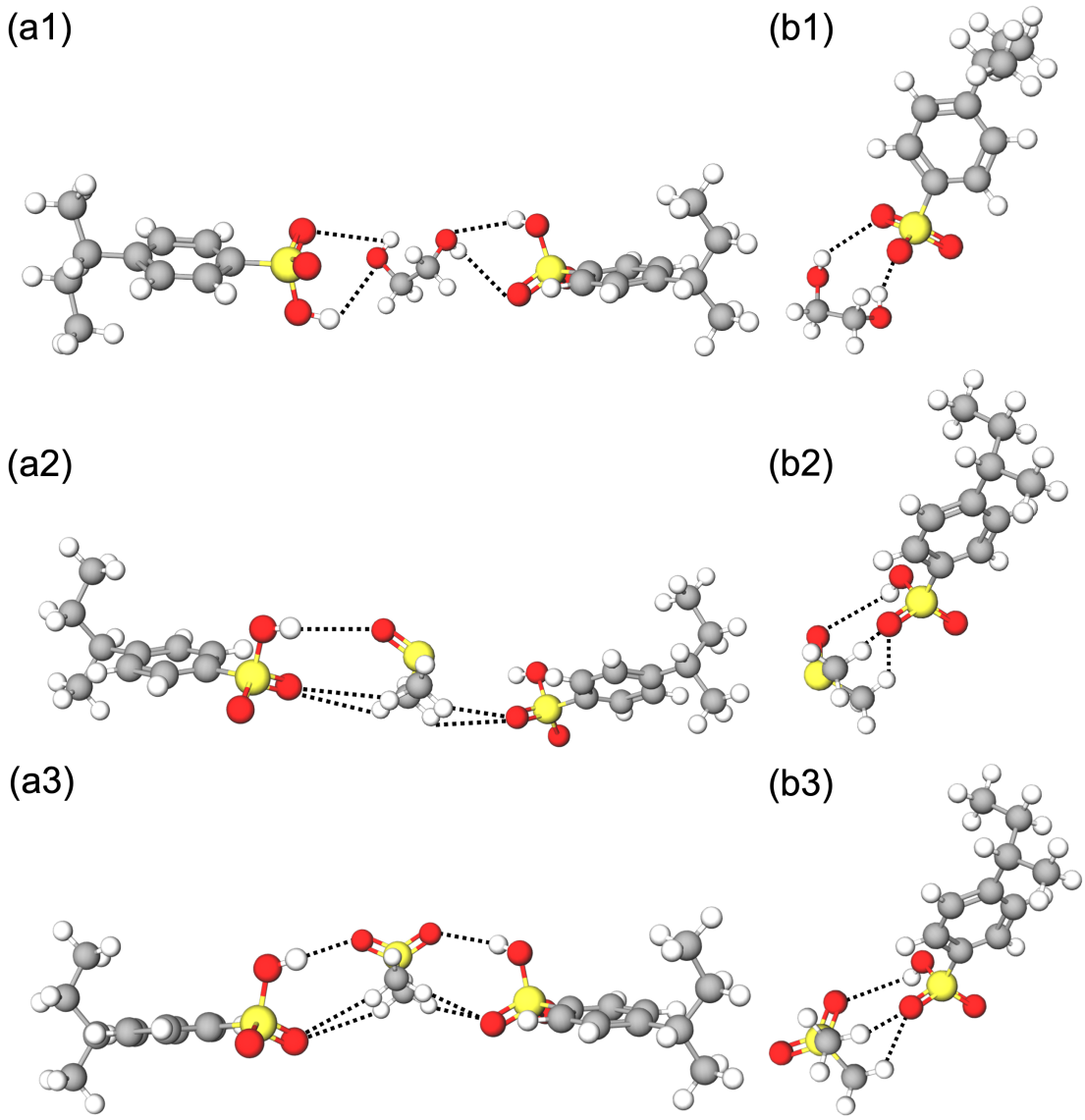



**Figure 3.4:** Illustrations of interactions of (a1) ethylene glycol (EG) with two PSSH (with interaction energy of –1.41 eV) and proton sharing of (a2) dimethyl sulfoxide (DMSO) with two PSSH (–1.69 eV) and (a3) dimethyl sulfone (DMSO2) with two PSSH (–1.89 eV), along with illustrations of interactions of (b1) EG with one $PSS^-$ (–1.20 eV) and proton sharing of (b2) DMSO with one PSSH (–1.22 eV) and (b3) $DMSO_2$ with one PSSH (–0.96 eV).[220]

The consequences of this strong $DMSO_2$–PSS interaction are significant for the PEDOT:PSS microstructure reorganization. After the $DMSO_2$ molecules are attached to PSS, the prospect of PSS monomers interacting with other PSS or PEDOT chains is diminished. In effect, $DMSO_2$ saturates the

sulfonate sites, breaking up the "insulating" PSS-rich shell that normally surrounds the PEDOT matrix. Simulation studies have reported that polar solvents such as $DMSO_2$ or DMSO preferentially bind to PSS over PEDOT (because PEDOT lacks the polar groups required for H-bonding), thereby pulling the PSS chains apart and reducing the PSS–PSS cohesion while weakening the coulombic PEDOT–PSS association simultaneously.[218] This leads to a phase separation where excess PSS is disentangled from the PEDOT-rich domains. Therefore, a PEDOT:PSS film doped with $DMSO_2$ could achieve higher conductivity than an undoped film, caused by the in-situ crystallization of $DMSO_2$.

Ethylene glycol (EG) is a high boiling point, polar additive well-known for enhancing the conductivity of PEDOT:PSS. As a high boiling point cosolvent, EG undergoes slow evaporation, which allows for better molecular rearrangement of PEDOT:PSS (during drying) that leads to improved film morphology, uniformity, and electrical conductivity.[205] The thermal stability of the high boiling point cosolvent enables processing at elevated temperatures without instant evaporation, which provides a better control over the baking condition. The presence of EG alongside $DMSO_2$ also produces a synergistic effect. In a PEDOT:PSS dispersion, some sulfonic groups exist as sulfonate anions ($PSS^-$) that are balanced by the positively charged $PEDOT^+$. $DMSO_2$ primarily target the protonated $PSS^-$ (PSSH) via strong H-bonds, while EG could bind strongly to the deprotonated $PSS^-$ (by forming strong H-bonds through the two –OH groups). Any remaining PSS moiety is largely isolated to distinct regions or is in a swollen state that does not impede charge transport.[218] This can promote a transition of PEDOT segments from a coiled "benzoid" conformation toward a more planar "quinoid" conformation that is associated with enhanced conjugation length and conductivity. Hence, PEDOT and PSS segregate efficiently in the EMD2 formulation, thanks to the synergistic action of EG and $DMSO_2$.

The effect of increased ratio of $PSS^-$/PSSH observed above suggests that more $PSS^-$ on the surface could potentially contribute to increases in surface dipole and work function, with PSSH remaining neutral and insulating.[175,223,275–277] PEDOT and PSS phase separation occurs similarly in ED2 and EMD2, but the methanol present in EMD2 could help to remove the neutral, segregated PSSH during spin coating.[88] In contrast, although EM contains methanol (which could help to remove PSSH), its initial phase segregation is less efficient than when $DMSO_2$ is present. As a result, EM cannot achieve the same improvement as EMD2, likely because insufficient PSSH is segregated in the first place for methanol to effectively remove it. In this system, EG is the only cosolvent that effectively promotes phase segregation. The PSSH removal could account for the trend in the thickness of the EM, ED2

and EMD2 films. In particular, EMD2 is the thinnest film (44 nm) as most of the insulating components have left the film, while ED2 is the thickest one (52 nm) and EM is the intermediate (48 nm).

To investigate the effect of $DMSO_2$ on the performance and stability of solar cells, three cosolvent-treated PEDOT:PSS solutions (EM, ED2, and EMD2) were pre-mixed and spin-coated onto silicon substrates. Figure 3.5 shows the schematic architecture of a typical heterojunction solar cell fabricated using one such film as the hole transport layer and the silicon substrate as the electron transport layer. To assure the reproducibility of our preparation, multiple solar cells employing these cosolvent-treated PEDOT:PSS have also been prepared. The J-V curves of all solar cell samples are shown in Figure S3-2. Table 3.1 summarizes their corresponding solar cell performance data, which show good consistency among solar cells fabricated separately with, e.g., the reproducibility error in PCE generally less than 6.5%. J-V profiles and EQE spectra of the EM, ED2 and EMD2 solar cell samples with the best performance are shown in Figure 3.6. Evidently, EMD2 exhibits the highest PCE of 15.5% and outperforms ED2 with a PCE of 14.5% and EM with a PCE of 13.4%.

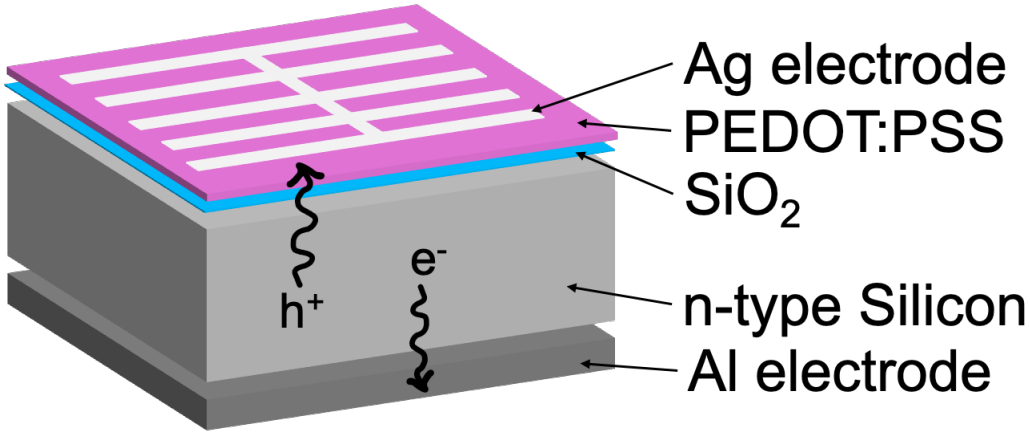



**Figure 3.5:** Illustration of the architecture of a heterojunction solar cell based on a cosolvent-treated PEDOT:PSS film on a silicon substrate.

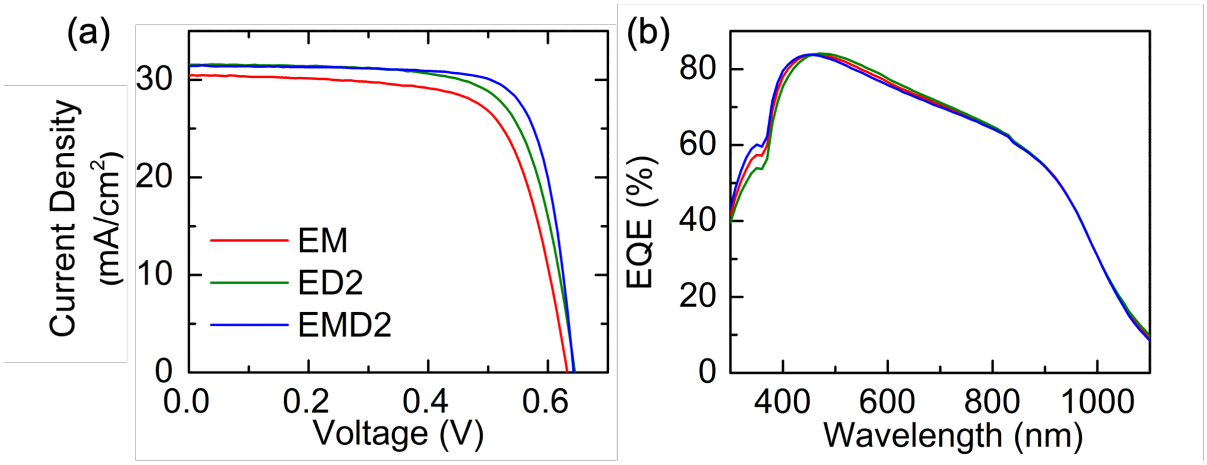



**Figure 3.6:** (a) Current density-voltage (J-V) profiles and (b) external quantum efficiency (EQE) spectra for as-fabricated EM, ED2 and EMD2 solar cell samples with the best performance.

**Table 3.1:** Solar cell performance metrics including $V_{OC}$, $J_{SC}$, FF and PCE for as-fabricated EM, ED2 and EMD2 solar cell samples. The solar cell sample number is indicated after the hyphen. Samples marked with asterisks represent the respective EM, ED2, and EMD2 solar cell samples with the best performance and their J-V and EQE data are shown in Figure 3.6.

| **Samples** | **$V_{OC}$ (mV)** | **$J_{SC}$ ($mA/cm^2$)** | **FF (%)** | **PCE (%)** |
|---|---|---|---|---|
| EM-1* | 632.3 | 30.5 | 69.7 | 13.4 |
| EM-2 | 633.3 | 28.0 | 71.4 | 12.7 |
| EM-3 | 625.1 | 30.0 | 66.7 | 12.5 |
| Average | 630.2 ± 4.5 | 29.5 ± 1.3 | 69.3 ± 2.4 | 12.9 ± 0.5 |
| ED2-1* | 645.1 | 31.6 | 71.1 | 14.5 |
| ED2-2 | 636.6 | 29.4 | 70.7 | 13.2 |
| ED2-3 | 632.3 | 28.7 | 70.6 | 12.8 |
| ED2-4 | 629.4 | 30.6 | 73 | 14.1 |
| ED2-5 | 634.5 | 29.0 | 70.7 | 13.0 |
| Average | 635.6 ± 6 | 29.8 ± 1.2 | 71.2 ± 1 | 13.5 ± 0.7 |
| EMD2-1 | 643.2 | 29.5 | 74.7 | 14.2 |
| EMD2-2* | 642.8 | 31.6 | 76.5 | 15.5 |
| EMD2-3 | 636.4 | 28.6 | 73.4 | 13.4 |
| EMD2-4 | 646.3 | 31.3 | 73.5 | 14.9 |
| EMD2-5 | 639.0 | 29.6 | 71.2 | 13.4 |
| Average | 641.5 ± 3.9 | 30.1 ± 1.3 | 73.8 ± 2 | 14.3 ± 0.9 |

Solar cells have been stored in air under ambient conditions with relative humidity (RH) < 30% at room temperature and their performance data are remeasured in the following days post-fabrication to assess their stability. Figure 3.7 shows the degradation trends in $V_{OC}$, $J_{SC}$, FF, and PCE as functions of ambient storage time after fabrication for three typical samples of EM, ED2, and EMD2 solar cells. Figure S3-3 shows the corresponding trends with the solar cell performance parameters normalized to their respective as-fabricated values to better reflect percentage changes. We have used the consensus stability assessment to estimate the amount of time post-fabrication when PCE drops to 80% of its initial (as-fabricated) value (commonly denoted as $T_{80}$). The temporal stabilities of all three solar cells EM, ED2, and EMD2 have been quantitatively assessed according to ISOS protocol described by Khenkin et al.[278] This approach ensures methodological reproducibility and facilitates comparison

with other reported stability studies. In accord with the ISOS guidelines, the $T_{80}$ value is determined by linear interpolation between the two measurement points that bracket the 80% value of the PCE of the as-fabricated cell. The stability data for each solar cell sample ($T_{80}$) are averaged and summarized in Table S3-1. Evidently, there are discernible differences in the degradation rates of the performance metrics among the solar cell samples over ambient storage time. While ED2 exhibits generally the least degradation (reflecting higher stability) with $T_{80}$ of 913.1 ± 132.9 h, greater performance degradation proceeds faster for EMD2 ($T_{80}$ of 261.0 ± 39.9 h) and EM ($T_{80}$ of 166.4 ± 69.9 h) over significantly shorter average ambient storage times.

The EM devices displayed the most rapid efficiency decay. The $T_{80}$ among the three EM cells are found to be between 86 and 208 h, indicating pronounced instability under ambient storage. The degradation trajectory is dominated by an early decline in FF and a modest loss in $V_{OC}$, characteristic of interfacial degradation and increased series resistance at the organic–inorganic junctions. By contrast, the ED2 series exhibits markedly superior stability. Their $T_{80}$ values are in the range of 823 – 1066 h, over four times longer than that of the EM series. The slower efficiency decay and the more gradual decrease in FF (from ~71% to ~ 60%) indicate a more resilient contact interface and improved charge extraction, arising from compositional or morphological stabilization of the interfaces. The intermediate performing EMD2 devices are found to have $T_{80}$ values between 233 h to 307 h, corresponding to ambient stability longer than EM but significantly shorter than ED2. The main performance loss again originates from FF deterioration, although the concurrent drops in PCE and $V_{OC}$ are milder than those in the EM devices. The moderate improvement over EM implies that partial modification or doping in the device architecture enhances stability but does not fully suppress degradation pathways active in ambient exposure.

Collectively, these results clearly establish the following stability order: ED2 ≫ EMD2 > EM. The $T_{80}$ parameter provides a consistent and quantitative basis for comparing degradation kinetics across different solar cells. These findings highlight that while the ED2 configuration retains over 80% of its as-fabricated efficiency for more than 1000 h, the unmodified EM devices suffer from rapid decay within the first 200 h. The observed trend underscores the decisive role of interface engineering and compositional optimization in mitigating ambient degradation in PEDOT:PSS/Si heterostructures. The EM devices thus represent an unstable baseline, likely limited by unoptimized and unstable interfaces.

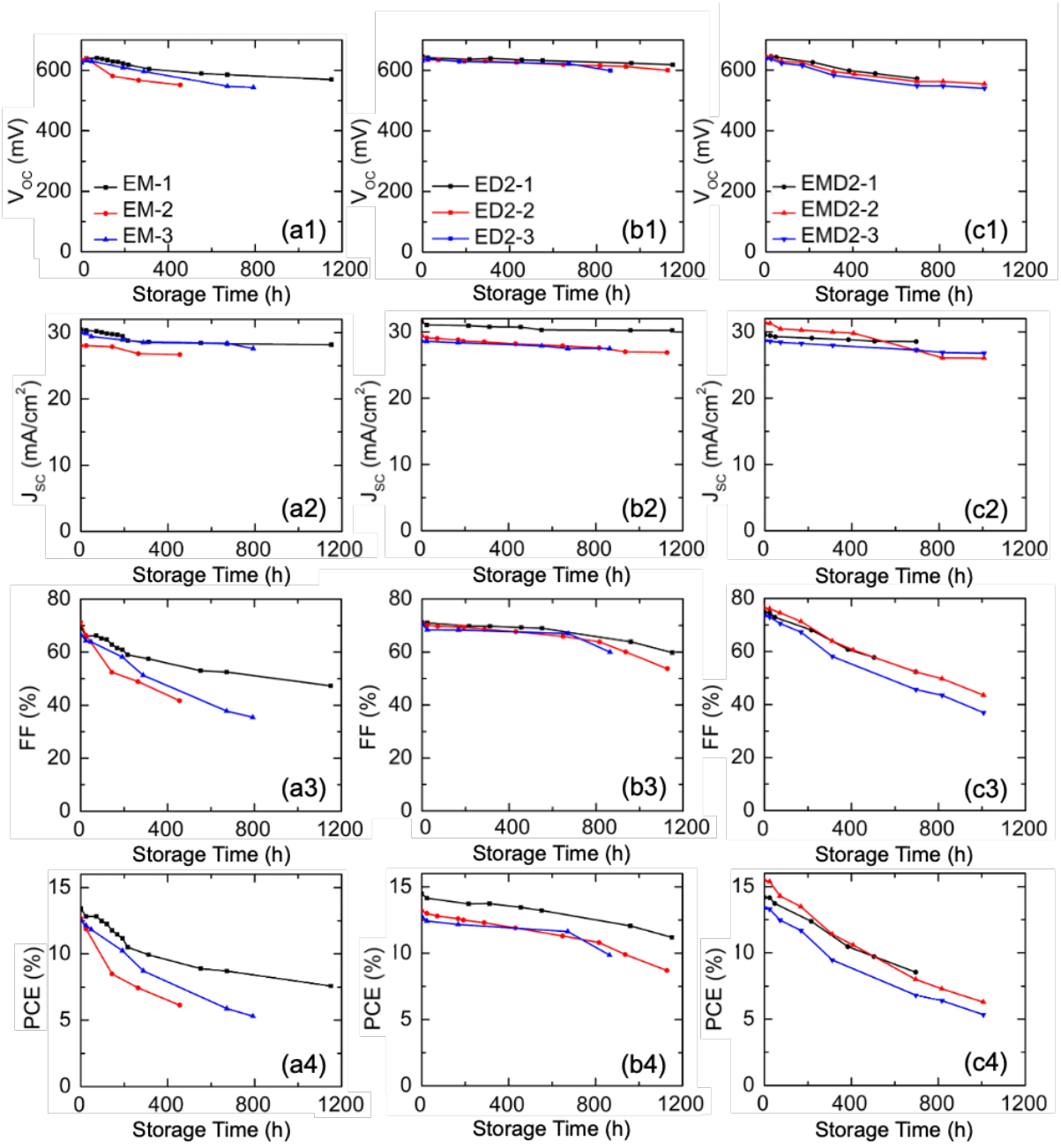



**Figure 3.7:** Degradation trends of solar cell performance metrics: $V_{OC}$, $J_{SC}$, FF and PCE as functions of ambient storage times for (a) EM (b) ED2 and (c) EMD2 solar cells.

The observed higher $R_S$ (Figure 3.1) for EM and EMD2 causes their corresponding solar cell performance to degrade more quickly than ED2, despite their generally high intrinsic electrical conductivities. In contrast, the tightly packed $DMSO_2$-based microstructure of ED2 exhibits the lowest $R_S$, allowing the ED2 film to maintain high performance in both FF and PCE. These

conductivity values, together with the photovoltaic results, reinforce our hypothesis that the presence of EG and $DMSO_2$ in the cosolvents drives more efficient phase separation than EG and methanol. The resulting charge-transport enhancement boosts $V_{OC}$ from 630.2 mV for EM to 635.6 mV for ED2 and to 641.5 mV for EMD2 on average (Table 3.1). The same mechanism also leads to higher FFs, as the reduced $R_S$ associated with superior phase separation enables more efficient current extraction. The AFM morphology is also consistent with earlier reports that increased surface roughness could enhance device performance (Figure 3.2).[139,231] Although the rougher surface raises the sheet resistance of the EMD2 film measured by the van der Pauw method, vertical charge transport remains efficient, yielding the highest FF and PCE of 76.5% and 15.5% in EMD2-2, respectively. Based on the $PSS^-$/PSSH ratio, EMD2 retains the smallest amount of PSSH suggesting the presence of a larger dipole at the film surface and at the film/top-electrode interface. Consequently, EMD2 delivers better solar-cell performance than EM and ED2.

There are, however, conflicting reports about why and how exactly the conductivity of PEDOT:PSS increases after cosolvent treatment. The dominant mechanism depends on the specific additives, their physicochemical properties, and the processing method used. There are several proposed, often overlapping, mechanisms: (i) phase separation that enlarges PEDOT-rich grains and shortens intergrain hopping distances; (ii) screening of Coulomb interactions by highly polar solvents; (iii) removal of excess insulating PSS from the surface; (iv) conformational rearrangements that foster tighter connectivity among PEDOT chains; and (v) true doping effects introduced by certain reagents.[249] In our $DMSO_2$-treated systems, the combination of XPS, TOF-SIMS AFM, and conductivity data strongly supports mechanisms (i-iv) while there is no clear evidence for chemical re-doping. These processes are consistent with the observed increases in conductivity and stability. While these findings identify the most plausible mechanisms, their relative contributions cannot yet be distinguished. Without complementary computational modeling or further in situ characterization, the detailed mechanism remains unclear.

As demonstrated by the stability trends of the samples, the presence of methanol in cosolvent-treated PEDOT:PSS appears to accelerate the degradation of the EM and EMD2 solar cells. Solar cells made with ED2 films are more stable than those based on EMD2, and both ED2 and EMD2 solar cells out-perform the EM cell. Both EM and EMD2 films contain small volatile methanol molecules, which evaporate quickly during the baking step. It has been reported that even though the methanol-containing PEDOT:PSS solution spreads fully during the coating process, consistent with good wettability, the high vapour pressure and rapid evaporation cause the formation of

nanoaggregates or agglomerates, instead of a smooth film.[279] Wettability helps the solution spread evenly across the entire surface before the solvent evaporates, leading to the formation of a uniform film. It has been well established that solvent evaporation strongly affects film formation, even in polymer systems.[279] When a solvent evaporates too quickly, Marangoni instabilities could be triggered in polymer films deposited by spin coating. This effect occurs because evaporation creates surface tension gradients that drive the liquid to flow. Material moves from areas of lower surface tension toward areas of higher surface tension, generating convection cells.[280–282] These convection cells cause variations in the thickness and roughness of the film. In contrast, when solvents evaporate slowly, Marangoni flow does not develop, allowing smoother surfaces to form. The convection cells created by the Marangoni effect appear as small "hills" and "valleys" on the polymer film. As the valleys represent the thinner regions of the film, they are stabilized by the entanglement of the polymer chains.[281,282] The absence of methanol, as a solvent with a high evaporation rate, in the ED2 film is in good accord with the formation of a smooth film with the lowest RMS roughness.[281] ED2 does not suffer from the nanoaggregate formation caused by the rapid evaporation of methanol, which ensures a more uniform film and helps maintain its structural integrity over time.

As discussed before, high-boiling-point solvents such as ethylene glycol do not create the same extent of mechanical defects. As more time is needed to dry during a thermal treatment, the polymer is given more opportunity to undergo slow organization of its conductive network.[205,249,254,283] Furthermore, these solvents remain in the film after the baking (with just water removal) and continue to affect the polymer structure and contribute to PEDOT and PSS phase separation. For additives or cosolvents with a boiling point lower than water (such as methanol or isopropyl alcohol), they evaporate very quickly, after which crystallization starts with water as the remaining solvent.[228,254] Inclusion of EG in the PEDOT:PSS film also reduces the water uptake and enhances the ductility and mechanical properties of the film.[228,284] Therefore, by having the most uniform and smooth film with the lowest $R_S$ of all, the ED2 solar cell is the most stable one with the least rate of degradation over 91**3** hours. While previous PEDOT:PSS/Si solar cell studies have improved efficiency through interfacial or structural engineering, their performance remains not inherently stable, relying on external encapsulation or barrier layers to maintain durability. In contrast, our $DMSO_2$ modified system achieves intrinsic stability by restructuring PEDOT:PSS at the molecular level, suppressing hygroscopic and acidic degradation pathways. This inherent robustness underscores the significance and novelty of our work achieving both high efficiency and long-term stability without additional protective layers.[231,285,286]

## 3.4 Conclusion

The present study demonstrates that incorporating dimethyl sulfone ($DMSO_2$) into PEDOT:PSS significantly enhances both the initial as-fabricated efficiency and the long-term stability of planar heterojunction solar cells. Specifically, $DMSO_2$ improves conductivity through morphological realignment and screening effect between PEDOT and PSS. When combined with EG, $DMSO_2$ creates an even more conductive and stable film through phase separation that leads to a noticeable PSSH removal in the presence of methanol. Despite methanol improving wettability and being effective at PSSH removal, it compromises the long-term stability due to the formation of nanoagglomerates upon rapid evaporation. Thus, ED2 formulations are preferable for extended device stability with $T_{80}$ of 913 h on average, while EMD2 provides the best PCE performance of 15.5%. The ED2 or EMD2 solutions can also be used for other durable PEDOT:PSS-based device applications.

# Chapter 4

# Rapid Low-Cost Fabrication of Shadow Masks using FDM 3D Printing for Precise Top-Electrode Patterning in Planar Silicon Heterojunction Solar Cells

## 4.1 Introduction

Solar cells are critical for the global shift toward renewable energy sources. These devices harness sunlight to generate electricity through the photovoltaic (PV) effect, providing an important foundation for sustainable energy solutions. Figure 4.1 illustrates the growing importance of solar energy as a sustainable power source, offering scalability with minimal environmental impact relative to other low-carbon sources such as nuclear energy.[287] In Canada, the considerable low solar energy production highlights a critical need for increased investment and policy support to accelerate its development and to keep up with global clean energy goals.[288]

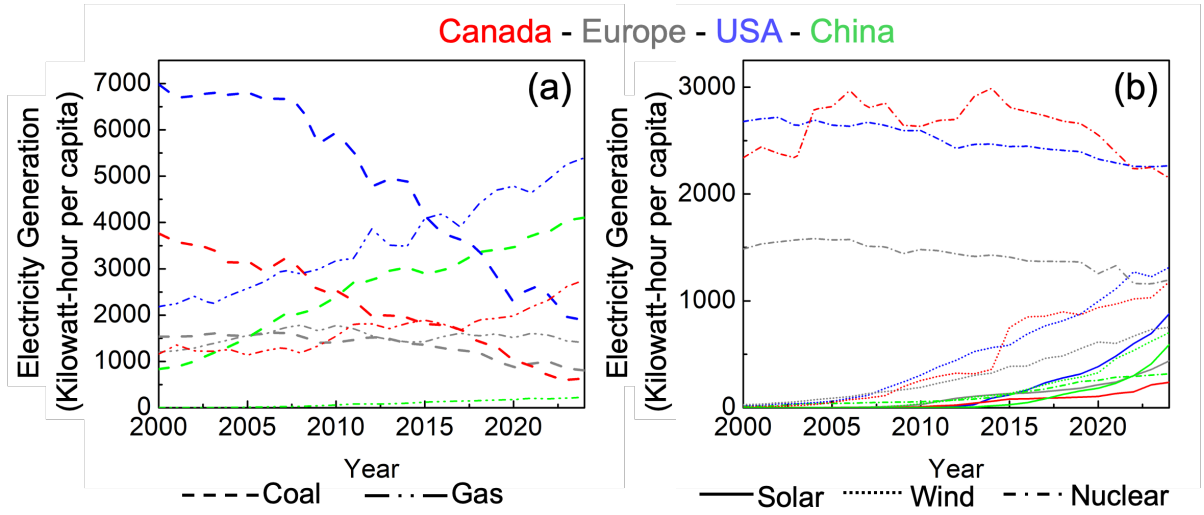



**Figure 4.1:** Electricity generated (kilowatt-hour per capita) from (a) coal and gas, and (b) solar, wind, and nuclear in Canada, Europe, USA and China from 2000-2024.Data are generated from Ember-energy.org website.[288]

The efficiency and performance of PV devices are greatly influenced by the design and quality of their top and bottom electrodes, which are responsible for collecting and transporting charge carriers generated by light absorption.[289] The top electrode, in particular, plays a critical role, as it must be not only highly electrical conducting to allow charge collection and transport but also sufficiently

optically transparent to permit light penetration and pass-through. The top electrode must also provide robust adhesion and good contact to the underlying layers in the device architecture.[290] Several methods have been developed to balance optimizing properties such as transparency, conductivity, and adhesion, and lowering cost across a diverse range of PV technologies, including silicon, thin-film, hybrid organic–inorganic cells, and perovskite solar cells.[170] Consequently, the deposition of the top electrode is a critical step in PV device fabrication, and this key step requires precise techniques to produce the optimal device performance.

When depositing the rear (or bottom) electrode in a silicon heterojunction solar cell, no specific patterning is required. The objective is simply to coat the rear surface of the substrate uniformly while preventing any sputtered metal from leaking onto the front side. By contrast, the front (or top) electrode of the solar cell must be patterned carefully, because the geometry of the metallic grid determines the lateral path length for charge carriers and therefore influences both the series resistance and the overall electrical performance of the device.[291,292]

A variety of deposition techniques have been developed to address the diverse requirements of the top-electrode fabrication in PV devices. Among the most prevalent methods are physical vapor deposition (PVD, including sputter deposition and thermal evaporation),[164,165,293,294] screen printing,[170,171] chemical vapor deposition (CVD),[295] and electrodeposition.[296] Magnetron sputtering, for example, is widely adopted due to its ability to produce uniform, adherent thin films over a large area, making it suitable for both research and industrial applications while outperforming other PVD methods.[165,297] Low-temperature processing, excellent scalability, and high uniformity, combined with its overall versatility and flexibility of using Al, Zn, Ag or alloy targets, have made this technique a popular choice for sputter-depositing a variety of advanced device components, such as TCO films, buffer/reflective layers, and electrodes on such important substrates as silicon wafers.[172] While thermal evaporation is scalable with a good control over the condition, it has difficulties in providing uniform deposition and therefore high quality interfaces.[298] Screen printing is an attractive method because of its cost-effectiveness and compatibility with thick-film applications, such as in silicon-based solar cells.[171,172] Electrodeposition has gained popularity due to its simplicity and low cost, particularly for depositing chalcogenide materials used in thin-film PV devices.[296] Indeed, each of these techniques presents its own unique advantages and trade-offs, in terms of cost, material utilization, scalability, and the quality of the deposited films, all of which require careful consideration based on the specific PV device architecture and application.

The need for precise electrode patterning to enhance device efficiency has motivated the development of innovative approaches in fabrication. One such approach involves the use of shadow masks, which are templates that selectively expose areas of the substrate to the deposition material (target), enabling the creation of finely patterned electrodes.[166] Shadow masks are placed and fixed between the material source, such as a sputtering target, and the substrate. This method allows simultaneous deposition and precise structuring of thin material layers. Shadow masks are commonly used in CVD and PVD, and they are essential to the fabrication of optoelectronic devices, microelectromechanical systems (MEMS), PV devices and sensors.

Unlike traditional photolithographic techniques, shadow masks eliminate the need for photoresists and their associated processing steps such as resist spin-coating, pattern exposure, and lift-off, thus significantly reducing processing time and cost.[167] Additionally, shadow masks facilitate the deposition and structuring of materials on nonplanar substrates or substrates chemically incompatible with photoresists. There are a variety of techniques for manufacturing shadow masks, including laser-micro machining,[168] computer numerical control (CNC) micro machining,[299] photolithography,[300] photochemical machining,[301] stencil (screen) printing,[302] and electroforming (for, e.g., Ni or Ni-Co shadow masks).[303,304] Traditionally, shadow masks are fabricated from hard materials such as stainless steel or silicon, which offer high precision but are often expensive and time-consuming to produce, particularly those with miniature features used in small-scale or research applications.[305] These conventional methods can pose barriers for researchers seeking rapid prototyping or customization of electrode designs.

When compared to home-scale 3D printing based on fused-deposition modeling, the primary disadvantages of industrial shadow-mask fabrication methods, such as laser micro-machining, photochemical etching, electroforming, and silicon micromachining, lie in their higher cost, longer production times, and the necessity for specialized facilities, such as cleanrooms or advanced chemical handling infrastructure.[303] On the other hand, home-scale 3D printing with poly lactic acid (PLA) or polyethylene terephthalate glycol-modified (PETG) filaments offer notable advantages, including rapid prototyping (< 1 h), reproducibility, significantly lower production cost, and considerable geometric flexibility without significant investment.[306] PLA and PETG filaments emit significantly fewer volatile organic compounds (VOCs) than ABS and are commonly used on open desktop printers, but basic ventilation or localized extraction is still advisable to limit exposure to ultrafine particles and residual VOCs, especially during prolonged printing. In particular, PETG has an order of magnitude less emission of VOCs than acrylonitrile butadiene styrene (ABS) during 3D

printing.[307] The primary VOC emitted from ABS filaments is styrene, with a reported emission rate ranging from 10 to 113 μg/min depending on the 3D printer model. In contrast, PLA filaments mainly release lactide (3,6-dimethyl-1,4-dioxane-2,5-dione) at a much lower rate of 4–5 μg/min across tested 3D printers. ABS therefore poses a greater safety concern due to a higher emission rate and styrene.[308–310]

3D printing also comes with some trade-offs. In particular, 3D-printed shadow masks are found to exhibit lower resolution, typically limited to 50 μm for vertical resolution and 180 μm for lateral resolution (as in, e.g., a Bambu Lab A1 mini 3D Printer with a 0.2 mm nozzle),[311] and rough edges caused by the extrusion-based printing process, which result in inferior accuracy and potentially blurred features during deposition.[312] Additionally, these masks have limited mechanical durability, a low thermal threshold (with a glass transition temperature or $T_g$ of 75-80 °C for PETG [313,314] and 55-60 °C for PLA[315]), and potential outgassing issues under vacuum or elevated-temperature deposition conditions. However, for depositing the top electrode using a 3D-printed shadow mask, the thermal and mechanical stability of a PETG mask is adequate, which would significantly reduce time, cost, and resource demand. Among the materials examined here, PETG therefore offers the most practical balance for laboratory-scale shadow mask fabrication, combining lower VOC emissions compared to other filaments with good dimensional stability under sputtering conditions and a tunable feature resolution of approximately 60–80 μm in our work. There are other alternative fused filament fabrication thermoplastics, such as high-temperature or annealable grade PLA,[316] acrylonitrile styrene acrylate (a UV durable alternative to ABS)[317] and newer low warp/high heat filaments. However, these materials can show emission profiles different from PETG, so enclosed printing and ventilation remain advisable.[307] Nylon filament also represents a potential candidate, but its strong hygroscopic nature can lead to variable behavior under vacuum or elevated-temperature processing, limiting its reliability for repeated deposition use.[318] Resin-based additive manufacturing methods (e.g., stereolithography or digital light projection) could further enhance resolution (< 50 μm) and mechanical durability, albeit with the need for controlled ventilation and post-curing steps which increase both complexity and cost.[319–321] Finally, a notable advantage of employing 3D-printed shadow masks is the ability to rapidly fabricate structures with various geometries with a low turn-around time (within an hour), enabling detailed studies of their impacts on PV device performance. In this study, we examine how three shadow masks with selected geometries affect critical photovoltaic parameters, such as open-circuit voltage ($V_{OC}$), short-circuit current density ($J_{SC}$), fill factor (FF), and power conversion efficiency (PCE), through their different impacts on light absorption and charge

carrier collection efficiency. One of the masks was fabricated by CNC micro machining and the other two were produced using a home-scale 3D printer that requires no specialized ventilation.

## 4.2 Experimental Details

A stock solution of PEDOT:PSS (Clevios, PH1000) was passed through a 0.45 μm polyvinylidene fluoride syringe filter and used directly without any modification. All other chemicals were obtained commercially and used as supplied. Two PEDOT:PSS dispersions were prepared with cosolvents. ED2 solution contained 3 wt% dimethyl sulfoxide ($DMSO_2$), 8 wt% ethylene glycol (EG), 0.25 wt% FS-300 surfactant (Fluka Analytical), with the remainder made up by PEDOT:PSS. EMD2 solution had the same $DMSO_2$ and EG loadings but also with 8 wt% methanol, along with 0.25 wt% FS-300 and PEDOT:PSS balance. The surfactant FS-300 was thoroughly mixed in ED2 and EMD2 before the respective solutions were used for deposition.

Figure 4.2 shows a schematic diagram of the key steps used for the fabrication of a heterojunction solar cell. Briefly, a single-side polished, phosphorus-doped n-type Si(100) wafer (100 mm diameter, with thickness 280 ± 25 μm, and resistivity 0.04–0.07 Ω cm; Virginia Semiconductor Inc.) was diced into 10×10 $mm^2$ chips. Each chip was sonicated for 10 min in acetone followed by 10 min in isopropanol (IPA), rinsed with ultrapure water (with resistivity of 18.2 MΩ cm at 21.6 °C), etched in 5% HF for 2 min to remove the native oxide, then rinsed again and dried under a nitrogen stream. A 200 nm aluminium layer was sputter-coated onto the rear unpolished side of a Si chip to serve as the bottom electrode. The front polished surface of the Si chip was exposed to ambient air for 20 min, allowing a thin $SiO_2$ interlayer (~2 nm thick) to regrow, in line with our optimization reported earlier.[88] The PEDOT:PSS mixture (ED2 or EMD2) was spin-coated at 4000 rpm for 60 s, producing a uniform coating that was subsequently annealed in air at 110 °C for 10 min on a hotplate. Using shadow masks of three different designs: comb-like busbar, central busbar, and crossed busbar, a 50 nm silver layer was sputter-coated to define the top electrode with different geometrical patterns. Sputtering of the rear and front surfaces of the Si chip was performed by using a dual-target magnetron sputtering system (Electron Microscopy Sciences 575X). Schematic diagrams of the resulting solar cells with the three top electrode designs are shown in Figure 4.3.

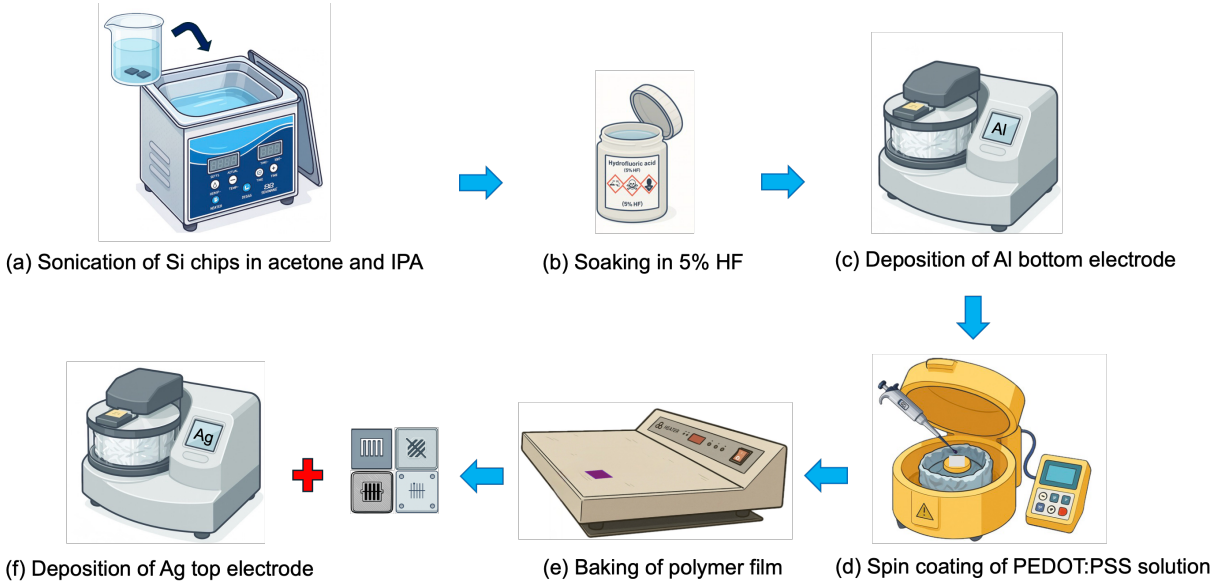



**Figure 4.2:** Fabrication workflow for PEDOT:PSS/Si heterojunction solar cells. (a) n-type Si(100) chips were sonicated for 10 min in acetone and IPA, then rinsed with ultrapure water. (b) Si chips were etched in 5% HF for 2 min, rinsed, and $N_2$ dried. (c) A 200-nm thick Al layer was deposited on the back sides of the chips to be used as the bottom electrode. (d) A PEDOT:PSS formulation (ED2 or EMD2) was dispensed and spin-coated at 4000 rpm for 60 s to form a uniform film. (e) The coating was annealed in air on a hotplate at 110 °C for 10 min. (f) A 50 nm Ag layer was sputter-deposited through a shadow mask (comb-like busbar, central busbar, or crossed busbar) to define the top electrode. All sputtering steps (for the bottom Al and top Ag electrodes) were performed in the same dual-target magnetron system (EMD 575X).

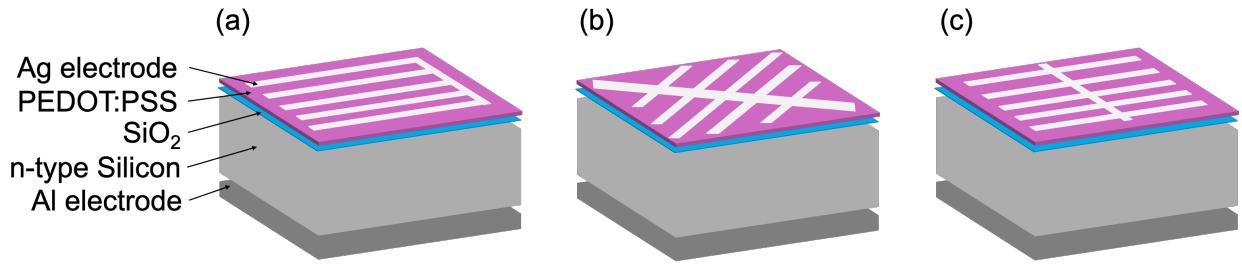



**Figure 4.3:** Schematic representations of solar cells with selected top electrode designs: (a) comb-like busbar, (b) crossed busbar, and (c) central busbar.

Atomic force microscopy (AFM) images of surface morphology were captured in tapping mode in an Asylum Cypher microscope. Photovoltaic performance was assessed via current–voltage (IV) and external quantum efficiency (EQE) measurements using a IV5 and a QEX10 systems from PV Measurements, respectively. IV curves were recorded under simulated AM 1.5 G illumination (100 $mW/cm^2$) calibrated against a PVM782 silicon reference cell and an active area of $8\times8$ $mm^2$. EQE spectra were obtained with monochromatic light from a xenon lamp and with a germanium photodiode, over an illuminated spot of $1\times3.5$ $mm^2$.

## 4.3 Results and Discussion

Additive manufacturing now offers a novel way to create custom shadow masks with unprecedented flexibility. Using a desktop 3D printer, it is possible to fabricate masks with almost any geometry, enabling quick design iterations for electrode patterns. 3D-printed shadow masks provide a cost-effective alternative to traditional mechanically milled or etched metal masks. Instead of ordering expensive custom metal stencils, researchers can now design a mask in computer-aided design (CAD) software and 3D-print out the mask in-house within hours, which can then be used for depositing metal electrodes and contacts. The layer-by-layer fused deposition modeling (FDM) process provides surprisingly good accuracy for patterns in the millimeter to sub-millimeter scale. For example, a recent study has demonstrated that micro-patterned electrodes via a PLA 3D-printed mask could achieve fine line features and complex shapes that would be challenging to cut from steel.[306] The additive manufacturing approach also minimizes warping and distortion of the pattern because the mask is built up layer by layer, which enables even complicated designs to retain good dimensional fidelity in X–Y and thickness. More importantly, 3D printing allows greater design freedom. Furthermore, 3D printing allows us to produce multiple masks for pennies, making it economically feasible to use a fresh (disposable) mask for each deposition if so preferred. Busbars, cross-grids and fractal layouts, as well as other unconventional electrode architectures can be manufactured simply by editing the digital design, without the long lead time or high cost of making a new physical stencil each time. This makes it ideal for experimenting with electrode geometry in research. Here, we demonstrate this concept for fabricating the top electrodes with 3D-printed shadow masks of three different grid patterns. The masks are reusable for many deposition cycles, especially if printed in a durable thermoplastic such as PETG. Common FDM filaments such as PLA, PETG, and ABS have all been tested as shadow mask materials before.[322,323] ABS (with $T_g$ of 101 °C) has been found to perform better due to its higher heat resistance, resulting in less propensity for warping under the temperature of deposition,[324] and to its capacity to produce sharper edges. However, as the amount of

VOC emission for ABS is an order of magnitude higher than that for PETG, the use of ABS would require an enclosed printing enclosure and air filtration/ventilation.[307] In our study, PETG and PLA are used instead. Photographs of typical PLA and PETG 3D-printed masks are shown in Figures 4.4a and 4.4b, respectively. While both are found to produce sufficiently precise electrode masks, PLA appears to have a deformation issue due to its lower $T_g$ (Figure 4.4c). In order to avoid this problem, transparent PETG filament with a higher $T_g$ is therefore used and the resulting masks are found to have no sign of bending or distortion even after multiple uses (Figure 4.4d).

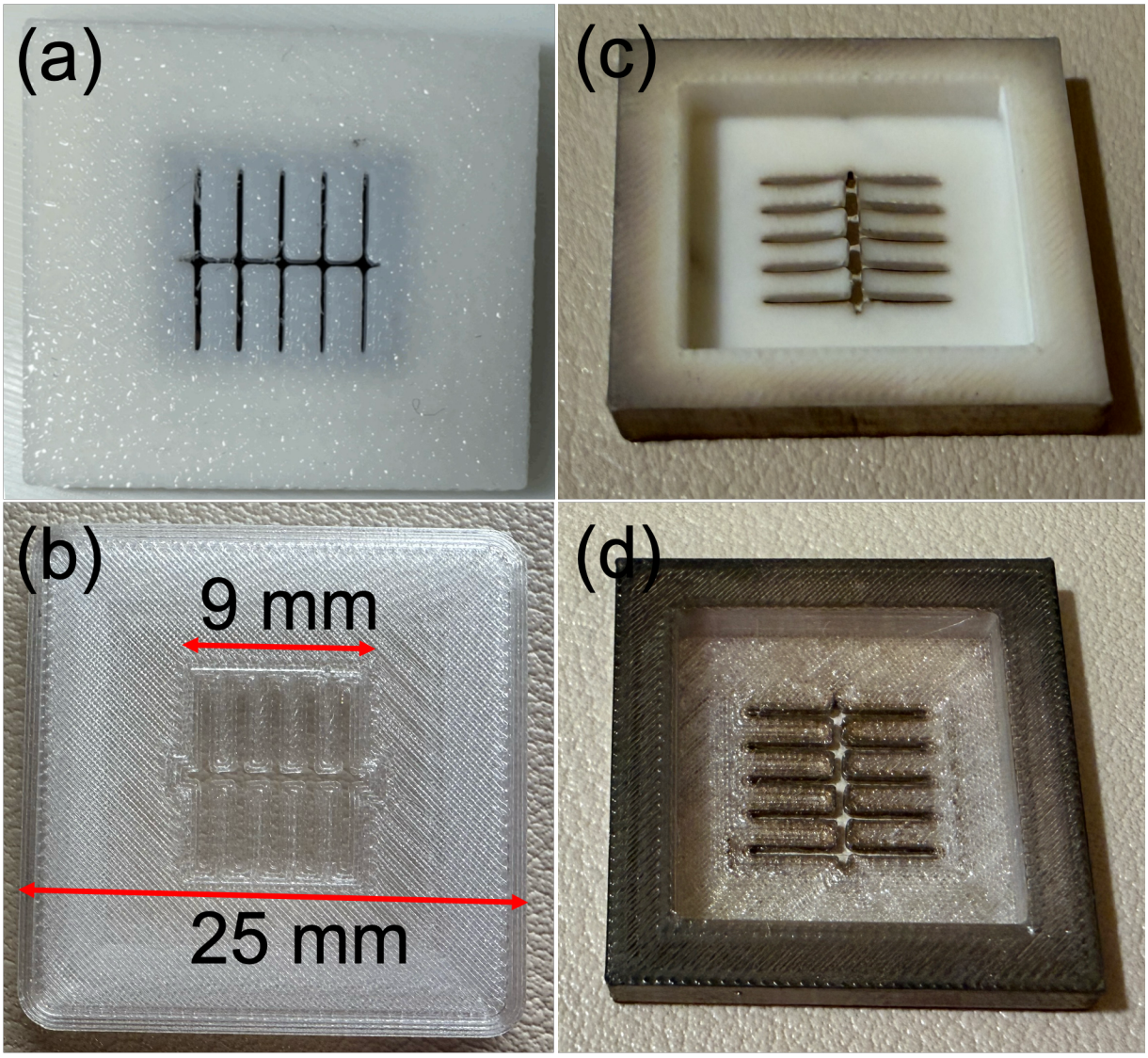



**Figure 4.4:** Photographs of shadow masks, with a central busbar design, made with (a, c) PLA and (b, d) PETG before (a, b) and after (c, d) undergoing the magnetron sputtering deposition process. The mask openings (gaps) that define the widths of deposited fingers and busbars are 350 microns wide, and the mask thickness is set to 400 microns.

The 3D printer used in these experiments was an A1 mini system manufactured by Bambu Lab with a 0.2 mm nozzle installed. The filament for the masks was PETG Translucent by Bambu Lab ($T_g$ = 70 °C, [325] $T_{mp}$ = 228 °C), the base polymer of which contains no additive

pigments and thus the polymer appears translucent. For the printing settings, the calibrated values for the filament from the manufacturer's website were used.

Although the feature resolution of 3D-printed masks is generally lower than those obtained by photolithography and etched metal stencils, 3D-printed masks are more than adequate for typical solar cell electrode application. Feature sizes on the order of 60-80 microns are easily achievable with a 0.2 mm nozzle.[325] This is adequate for printing shadow masks with electrode widths (fingers and busbars) and finger spacings (i.e., the gaps between two adjacent deposited fingers) commonly used in laboratory-scale silicon cells. The mask thickness can be tuned and is often set to 400 microns to ensure that the mask lies flat and blocks metal effectively without excessive edge shadowing. The finger and busbar width are set to 350 microns. Although we could print features with a smaller width, the 300 – 350 microns range is in practice the smallest size to ensure good accuracy for both 3D printing and sputter coating.

Using 3D-printed masks for metallization is straightforward. The printed mask (often consisting of a frame with inset to hold a substrate) is appropriately aligned onto the solar cell, and then metal is deposited by evaporation or sputtering to only coat the exposed regions. After deposition, the mask is simply lifted off, leaving a patterned metal electrode of the desired design. This process eliminates multiple steps compared to photolithography as there is no photoresist coating, developing, or etching involved. As a result, the turnaround from the design of the pattern to a finished electrode can be completed in less than 8 hours, which is excellent for rapid prototyping and design optimization.

Figure 4.5 shows a comparable shadow mask manufactured in our machine shop by using conventional CNC micro machining. It should be noted that the small round cut-out at each end is mechanically required in the machining process, and these cut-outs are not desirable because they allow the metallization to spill onto the edges and even the back of the wafer, potentially compromising electrical isolation. Not only the overall cost of the milled mask is substantially higher than the 3D-printed PETG mask, the turnaround time could also be significantly longer (~40 days), depending on the job queue and availability of our machine shop.

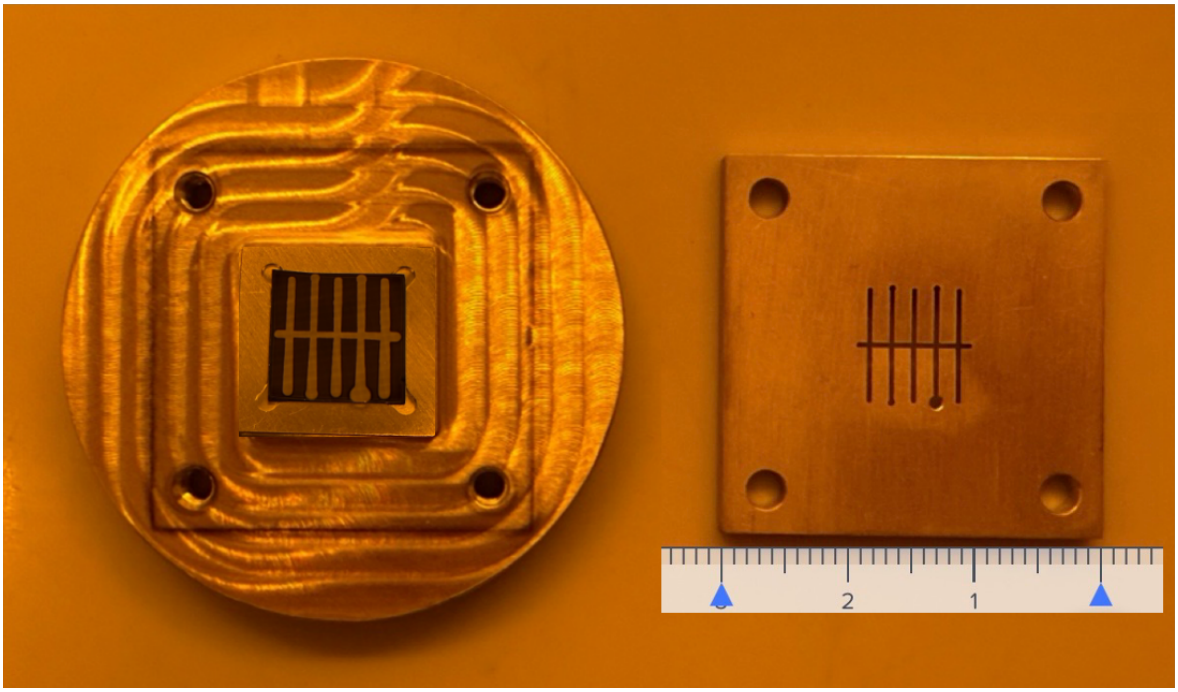



**Figure 4.5:** Shadow mask holders manufactured by CNC micro machining technique used for sputter-depositing silver. Right panel: Top cover with the central busbar pattern of the shadow mask. Left panel: Bottom holder with inset to tightly fix the Si substrate with a Ag central busbar top electrode sputter-deposited. The Si substrate is sandwiched snugly between the top cover and the bottom holder by means of four screws.

The primary role of busbars and fingers of the top electrode is to facilitate collection and conduction of photogenerated current with minimal resistive voltage drop. In a solar cell, carriers are generated uniformly across the illuminated device area and must travel laterally (in the emitter or conducting top layer known as the hole transport layer (HTL)) to reach a metal contact grid (busbars or fingers), and then travel through the metal grid to the terminal of the cell. If the path is too long or the sheet resistance too high, significant ohmic losses could occur, which manifest as a reduced FF with lower voltage at high current (i.e. a sloping I–V curve near the knee at $V_{OC}$). In our cells, the PEDOT:PSS layers of EMD2 and ED2 compositions are found to have moderate sheet resistances of 211.2 and 187.3 (Ω/□), respectively. While the silver fingers greatly lower the resistivity at their locations, the photogenerated current still needs to flow through PEDOT:PSS to reach those fingers. In a conventional comb-like busbar design with a busbar located along one edge, the longest distance (worst-case) for current travel is the entire length of the finger, from one (open) end of the finger to the opposite end terminated at the busbar. By contrast, a central busbar design reduces this maximum

travel distance by half, in which case carriers only travel from an open end of the finger to at most the center busbar (which is approximately half the span of the cell) instead of the full length as in the comb-like busbar design. A crossed busbar potentially halves the distance in two directions (vertical and horizontal), providing even shorter paths within each quadrant.

Optimizing the electrode finger spacing (the distance between adjacent deposited metal fingers, corresponding to the opaque regions of the shadow mask) is also crucial for maximizing solar cell performance because the electrical power loss due to emitter resistance is dependent upon the finger spacing.[326] To minimize this loss, the electrode finger spacing should be kept small. The surface current is collected by the fingers and is passed onto the busbar, which then deliver it to the external circuit. This reduction in travel distance directly lowers the resistive power loss in the emitter layer, as the fractional resistive power loss in this layer is proportional to the square of the finger spacing.[326] Consequently, these diminished electrical losses lead to an enhancement in the FF of the solar cell. Although reducing the spacing between electrode fingers allows for an increase in the number of grid lines and thereby can improve the fill factor (FF), it could also raise the level of optical shadowing, which can diminish the overall power output.[327,328]

Our experimental results show a clear influence of the top contact pattern on the FF and overall performance of the solar cell. Previous studies have used 3D printed shadow masks mainly for microelectrode and thin-film transistor fabrication, focusing on print fidelity and process feasibility rather than device optimization.[322,329] Here, we apply PETG-based 3D-printed masks to fabricate the top electrodes in planar silicon heterojunction solar cells, and we demonstrate how different electrode geometries could directly influence photovoltaic performance metrics such as FF and PCE. In the present work, three grid designs are evaluated: (1) a conventional comb-like busbar, (2) a central busbar, and (3) a crossed busbar (with one busbar and one line crossing at the center, dividing the grid into four quadrants). Figure 4.6 shows the images of four top electrodes with silver sputter-coated using different shadow masks onto the PEDOT:PSS layers of the heterojunction solar cells. Samples (b1), (b2), and (b3) were sputtered through their respective 3D-printed masks (a1, a2, a3), whereas sample (b4) was sputtered using a mask fabricated by CNC micro machining (a4). In sample (b4), the limitations of the CNC micromachining process are evident from the distorted line ends, where the tool's limited radius produced excessive rounding and loss of linearity in the pattern. Unlike the minor curvature observed in other electrodes, this deviation resulted in noticeable widening and silver leakage at the edges.

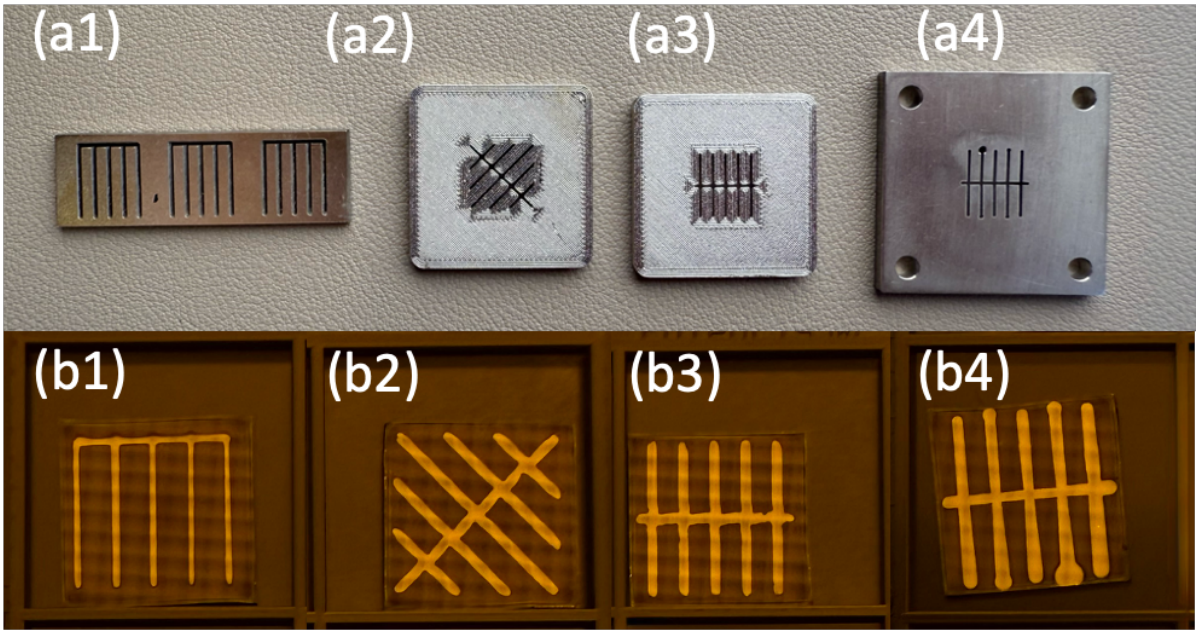



**Figure 4.6:** Photographs of assembly of four shadow masks (top panel) and of their corresponding silver electrodes (lower panel), with (a1, b1) comb-like busbar, (a2, b2) crossed busbar and (a3, b3) central busbar electrode design made by 3D printing, and with (a4, b4) CNC micro machining. Sample grids (b1-b4) are 10×10 $mm^2$ and enlarged for better visualization.

Table 4.1 compares the solar cell performance data obtained for cosolvent-added PEDOT:PSS EMD2 and ED2 cells fabricated with the top electrodes based on the 3D-printed shadow masks of the three busbar designs (Figure 4.6). These data in Table 4.1 are obtained by averaging the respective values from several EMD2 (Table S4-1) and ED2 cells (Table S4-2) separately prepared with the respective conditions. Figures 4.7a and 4.7b show, respectively, current density-voltage curves of the best performing EMD2 and ED2 cells fabricated with three different top electrodes. Evidently, the crossed busbar design provides a significant increase in FF by 11% (from 63.4% to 70.4%) for EMD2 cells and by 13% (from 61.6% to 69.6%) for ED2 cells, when compared to cells fabricated with the conventional comb-like busbar design. However, for EMD2 cells drops in $V_{OC}$ (1.8%) and $J_{SC}$ (6.5%) are also observed for the crossed busbar design. The increase in FF and decrease in $J_{SC}$ offset each other, and the average PCE increases by only 2.5%. A similar trend is observed with the ED2 cells where the observed decreases in $V_{OC}$ (0.3%) and $J_{SC}$ (10.1%) for the crossed busbar design relative to the comb-like busbar design appear to enhance the PCE by 1.8%. In an attempt to achieve a better balance between reducing the series resistance while not increasing the shading effect considerably, a third mask with the central busbar design is fabricated. This central busbar design provides the ED2

and EMD2 solar cells with enhanced PCE and FF relative to the comb-like busbar design. In EMD2 cells, while FF shows a remarkable improvement of 16.4% compared to comb-like busbar design, $V_{OC}$ and $J_{SC}$ are also found to increase slightly (by 0.1% and 2.7%, respectively). The corresponding PCE is found to increase considerably by 20.2% to 14.3%. This result has also been observed with the ED2 cells, with 1.2% increase in $V_{OC}$, 15.6% improvement in FF, slight increase in $J_{SC}$ by 3.5% and 21.6% increase in PCE (all relative to cells with the conventional comb-like busbar electrodes).

**Table 4.1:** Average photovoltaic performance metrics of ED2 and EMD2 solar cells fabricated with selected 3D-printed top electrode designs (comb-like busbar, crossed busbar, and central busbar).

| Samples | $V_{OC}$ (mV) | $J_{SC}$ (mA/cm$^2$) | FF (%) | PCE (%) |
|---|---|---|---|---|
| EMD2 Comb-like busbar | 641.1 ± 6.5 | 29.3 ± 0.4 | 63.4 ± 0.2 | 11.9 ± 0.3 |
| EMD2 Crossed busbar | 629.6 ± 10.2 (-1.8%) | 27.4 ± 0.6 (-6.5%) | 70.4 ± 2.3 (+11.0%) | 12.2 ± 0.6 (+2.5%) |
| EMD2 Central busbar | 641.5 ± 3.9 (+0.1%) | 30.1 ± 1.3 (+2.7%) | 73.8 ± 2 (+16.4%) | 14.3 ± 0.9 (+20.2%) |
| ED2 Comb-like busbar | 628.1 ± 12.9 | 28.8 ± 0.8 | 61.6 ± 3.0 | 11.1 ± 0.6 |
| ED2 Crossed busbar | 626.1 ± 5.2 (-0.3%) | 25.9 ± 1.0 (-10.1%) | 69.6 ± 2.3 (+13.0%) | 11.3 ± 0.7 (+1.8%) |
| ED2 Central busbar | 635.6 ± 6 (+1.2%) | 29.8 ± 1.2 (+3.5%) | 71.2 ± 1.0 (+15.6%) | 13.5 ± 0.7 (+21.62%) |

*The percentage changes in the performance metrics for the crossed busbar and central busbar cells relative to the respective comb-like busbar cells are given in parentheses.

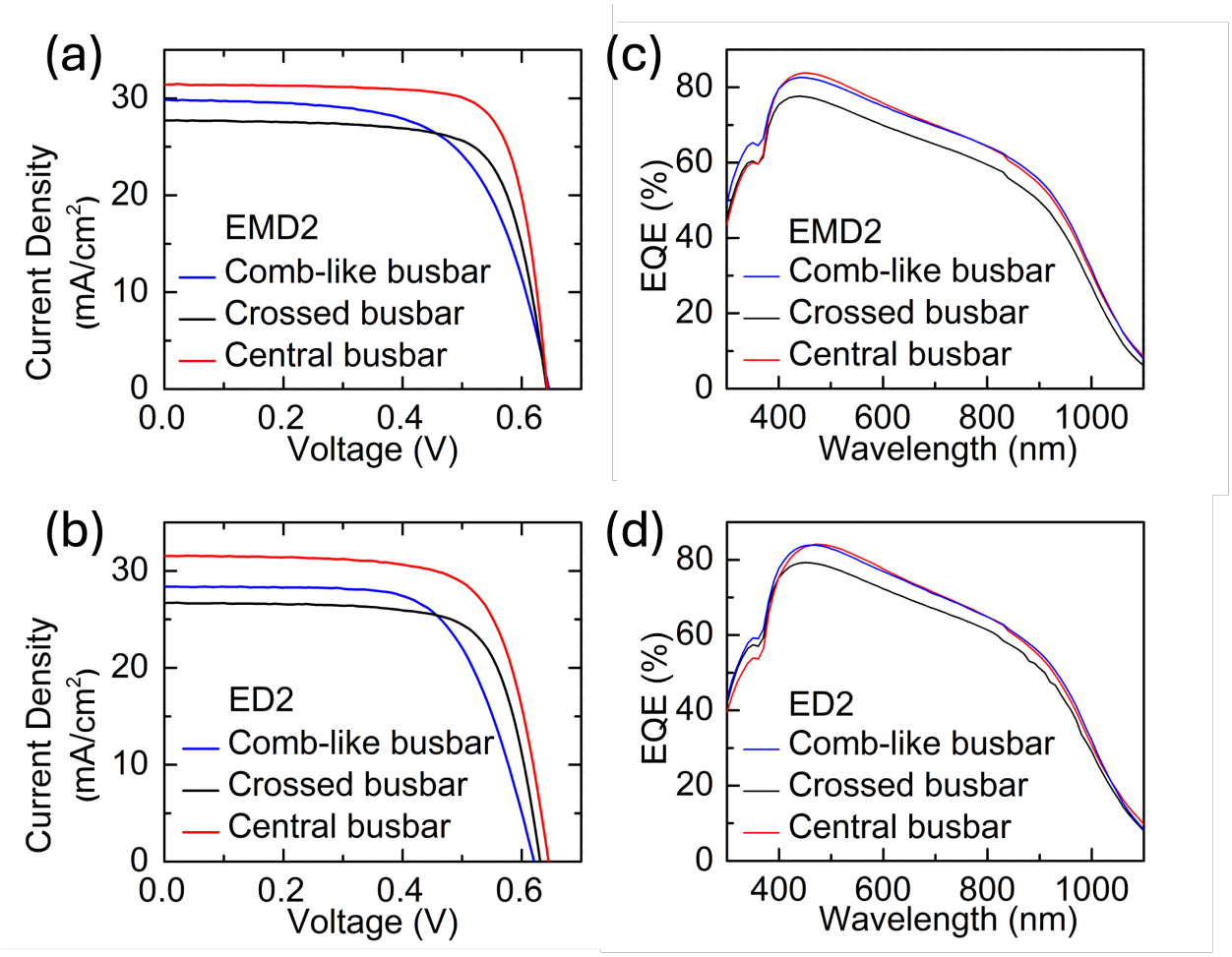



**Figure 4.7:** (a, b) Current density-voltage (J-V) curves and (c, d) external quantum efficiency (EQE) spectra of (a, c) EMD2 and (b, d) ED2 based solar cells with selected top electrode designs.

To evaluate the effects of these top electrode designs on the optical and electrical performance in heterojunction solar cells, we show in Figures 4.7c and 4.7d the corresponding EQE spectra of EMD2 and ED2 based solar cells obtained with the three top electrode designs (comb-like busbar, crossed busbar, and central busbar). Evidently, the EMD2 and ED2 solar cells with the comb-like busbar top electrodes exhibit the highest EQE over the visible to near-infrared spectral range (400–1000 nm), indicating superior optical transparency due to minimal shading by the electrode structure. However, despite this optical advantage, the comb-like busbar design suffers from increased lateral resistive losses in the PEDOT:PSS layer and longer current collection paths, which reduce the FF. In contrast, solar cells with the central busbar electrodes show only a slight reduction in EQE in the 300–400 nm range, attributable to shading from the centrally placed busbar. This minor optical penalty is compensated by a significant improvement in FF, likely due to shorter lateral conduction paths in both the PEDOT:PSS and silver grid, thereby reducing the series resistance and enhancing the power output. The crossed busbar design, while theoretically offering the shortest collection distances by dividing the cell into quadrants, introduces the most severe optical losses. The corresponding EQE spectrum displays a broad suppression throughout the 400-1100 nm range, indicating that increased shading from orthogonal busbars reduces photogeneration uniformly across the cell. Furthermore, a more complex metal geometry could potentially create local current congestion or dead zones, e.g., at the intersection of the busbars, weakening effective carrier collection. Overall, the EQE data validate that the central busbar structure offers the best trade-off between resistive loss mitigation and optical transparency, making it the optimal design among those tested for this heterojunction solar cell architecture.

Interpreting these findings requires understanding the trade-offs between resistive losses and optical losses in different electrode geometries. The central busbar design clearly improves the FF by reducing the lateral resistive losses in the PEDOT:PSS/Si heterojunction solar cell. The general consensus in photovoltaic literature shows that the top (or front) electrode accounts for the largest relative power loss and re-designing the front grid pattern can effectively improve the performance of the solar cells.[330] In our study, shortening the finger lengths and increasing the busbar connectivity improves the solar cell performance.[326,331] Although a crossed busbar top electrode could theoretically provide shorter paths at the ends, the long central crossings introduce extra series resistance that offsets some of the benefits. In addition, the electrode fingers are uniformly distributed along the ~13 mm long diagonal of the cell, with a wider spacing between each finger compared to the central busbar region, where the fingers are more closely packed. Indeed, reducing the spacing between

electrode fingers without introducing significant shading could lower the emitter resistive loss and improve both the FF and PCE. For this cell system, a single centrally located busbar with radial fingers therefore appears to be the most effective design among those tested.

Other more complex designs, including radial or spoke-like grids, fractal/leaf-vein inspired networks and multi-busbar/hybrid layouts can be used to further improve the top electrode. As these designs are very difficult to make mechanically, 3D printing offers a viable approach for manufacturing these electrodes. Further investigations with measurement of the solar cell performance metrics could guide the design of future heterojunction solar cells with optimized metallization patterns for the top electrodes. In addition, beyond photovoltaic applications, 3D printing could enable rapid prototyping of shadow masks for other thin-film technologies, including TCO coatings, sensors, MEMS electrodes, and optoelectronic devices such as OLEDs and TFTs.[329,332–334]A particularly promising extension is in the area of microfluidic and electrochemical systems, where 3D-printed PETG or ABS channel networks are integrated with patterned metal or oxide electrodes (Ag, Au, Pt, ITO) deposited via shadow masking on glass substrates.[335–337] The assembled structures could then function as compact microfluidic electrochemical cells that are widely applicable in biosensing, photoelectrochemical studies, and miniature fuel-cell testing.[338–341]. Together, these insights highlight 3D printing as a versatile tool for accelerating electrode optimization and device fabrication across next generation of thin film and electrochemical technologies.

## 4.4 Conclusion

This work highlights the potential of using a desktop 3D-printer for manufacturing shadow masks with optimal designs for developing the top electrode used in silicon heterojunction solar cells. While conventional fabrication methods offer higher resolution, the PETG-based 3D printing approach provides substantial advantages in terms of production speed, cost-effectiveness, design flexibility, and accessibility. Among the electrode configurations tested (comb-like busbar, central busbar, and crossed busbar), the central busbar layout provides the best overall solar cell performance and a good balance between series resistance reduction and shading effect minimization. The central busbar top electrode design reduces the series resistance significantly, leading to enhanced FF and $V_{OC}$, and ultimately improving PCE by 20.2% in EMD2 and 21.6% in ED2 cells, when compared to the traditional comb-like busbar configuration. EQE analyses reinforce these findings, validating that the central busbar design offers effective compromise between optical transparency and reduced resistive

losses. This novel and practical approach can thus facilitate rapid electrode prototyping, driving further optimization and wider adoption of solar cell technology.

# Chapter 5
# Conclusion and Future Work

The global transition toward sustainable energy demands continuous innovation in PV technology. Among emerging approaches, organic–inorganic heterojunction solar cells have attracted significant attention because they combine the excellent electronic properties of crystalline silicon with the tunability and solution processability of organic materials. Despite the impressive PCE that has been achieved so far, the progress of organic–inorganic HSCs remains constrained by fundamental challenges such as limited conductivity and environmental stability of HTL. In addition, a successful commercialization requires a feasible production with less complexity and lower costs associated with the fabrication process.

This thesis focusses on three research projects targeting the current obstacles. First, the role of DMSO as a cosolvent in modifying the PEDOT:PSS HTL to enhance conductivity and stability is investigated. Second, $DMSO_2$ is explored as a novel additive capable of inducing morphological reorganization and unprecedented long-term performance. Finally, a rapid and cost-effective approach for top electrode fabrication based on 3D-printed shadow masks is developed to accelerate device prototyping and to optimize current collection. Together, these studies demonstrate a comprehensive strategy that advances both the materials and device engineering aspects of organic–inorganic HSC technology.

## 5.1 Stabilization of planar heterojunction solar cells using a dimethyl sulfoxide treated hole transport layer

The intrinsic properties of PEDOT:PSS, notably its transparency, processability, and compatibility with solution-based fabrication, make it a leading candidate for use as the HTL in planar organic–inorganic HSCs. However, its acidic and hygroscopic nature as well as the insulating characteristics of the PSS component often limit device performance and lead to rapid degradation under ambient conditions. Addressing these limitations requires modification of the PEDOT:PSS microstructure to enhance charge transport and environmental stability. In Chapter 2, DMSO was introduced as a cosolvent alongside EG and methanol to modify PEDOT:PSS. DMSO reduces coulombic interactions between PEDOT and PSS, promoting phase separation and transforming the grain morphology into more conductive, elongated domains. These structural changes increase charge carrier mobility, suppress recombination, and enhance conductivity by several orders of magnitude. Optimization of

the DMSO concentration has revealed that a 3 wt% DMSO formulation (EMD3) yields the best performance. Solar cells fabricated with this modified HTL achieve a PCE of 13.4% with $J_{SC}$ of 30.1 mA/cm$^2$, $V_{OC}$ of 642.4 mV, and FF of 69.4%. More significantly, the devices maintain 89.4% of their initial efficiency after 72 h of ambient exposure without encapsulation, whereas the control devices (without DMSO) degrade by nearly 50% in the same period. XPS and AFM analyses confirm increased PEDOT/PSS ratios, more oriented fibrillary structures, and reduced hygroscopicity in DMSO treated films. These results demonstrate that DMSO cosolvent engineering is a simple yet powerful route to achieving more conductive and intrinsically stable HTLs.

## 5.2 Enhancing performance and stability of PEDOT:PSS-based planar organic–inorganic heterojunction solar cells through dimethyl sulfone doping

Building upon the improvements achieved with DMSO, we introduce, in Chapter 3, $DMSO_2$ as a solid additive with unique physicochemical properties for PEDOT:PSS modification. Unlike liquid cosolvents (such as DMSO), $DMSO_2$ crystallizes upon drying, inducing alignment of PEDOT chains and promoting a highly ordered, interconnected conductive network. Its strong bifunctional hydrogen bonding with PSS disrupts the insulating shell more effectively than DMSO, while its nonhygroscopic nature improves resistance to moisture induced degradation. Devices fabricated with $DMSO_2$ modified PEDOT:PSS exhibit remarkable improvements in both performance and longevity. The highest performing configuration, combining EG, methanol, and $DMSO_2$ (EMD2), achieves a PCE of 15.5%, surpassing both EM and ED2 based devices in efficiency with a $T_{80}$ of 261 hours. On the other hand, ED2 demonstrated significant stability reaching a $T_{80}$ of 913 hours, an exceptional improvement over conventional PEDOT:PSS solar cells. Advanced characterizations including XPS, TOF-SIMS and AFM have revealed substantial microstructural reorganization and increased PEDOT domain connectivity. The synergistic interactions of EG (targeting deprotonated $PSS^-$), $DMSO_2$ (targeting protonated PSSH), and methanol (facilitating removal of residual PSSH) yield films with reduced thickness, enhanced conductivity (>1000 S cm$^{-1}$), and improved interface quality. These findings establish $DMSO_2$ as a highly effective, environmentally benign additive for next generation of HTL engineering.

## 5.3 Rapid low-cost fabrication of shadow masks using FDM 3D printing for precise top electrode patterning in planar silicon heterojunction solar cells

While HTL optimization addresses the intrinsic material limitations of organic–inorganic HSCs, device performance is also strongly influenced by the geometry and resistive losses of the top

electrode. Traditional electrode fabrication techniques, such as photolithography and precision machining, are costly and time-consuming, and they require specialized infrastructure, posing challenges for iterative research and prototyping. In Chapter 4, we present a novel solution using FDM 3D printing with PETG filaments to fabricate reusable shadow masks for electrode deposition. This approach enables rapid (< 1 h) production of complex electrode patterns with significant cost reduction and geometric flexibility, without the need for cleanroom facilities. Three top electrode configurations: comb-like busbar, central busbar, and crossed busbar have been designed and evaluated. Among them, the central busbar design delivers the best balance of optical transparency and electrical conductivity, improving PCE and FF by up to 21.6% and 16.4%, respectively, compared to conventional designs (such as the comb-like busbar design). These enhancements are attributed to reduced lateral charge transport distances, minimized series resistance, and optimized current collection pathways. EQE measurements have confirmed superior carrier collection and lower resistive losses. This work demonstrates that 3D-printed shadow masks are not only a powerful research tool for rapid design iteration but also a scalable and cost-effective solution for commercial device manufacturing.

Together, these three projects presented in this dissertation represent a comprehensive advancement in planar heterojunction solar cell technology. First, we have demonstrated that at the material level DMSO and $DMSO_2$ can be used to significantly enhance the conductivity, morphology, and intrinsic stability of PEDOT:PSS films. Second, at the device level we show that engineering using 3D-printed electrode patterning optimizes current collection and enables rapid prototyping for design optimization. These improvements have led to organic–inorganic HSCs with PCEs reaching 15.5%, improved ambient stability over hundreds of hours, and fabrication strategies compatible with large scale, low-cost production. The approaches presented here are broadly applicable to other thin-film photovoltaic technologies, including perovskites, organic solar cells, multi-junction and tandem solar cells. Indeed, the targeted molecular engineering of the HTL, combined with innovative device fabrication techniques, could overcome critical limitations of planar silicon heterojunction solar cells in one important aspect of ambient stability without sacrificing PCE performance.

## 5.4 Future work

The work presented in this dissertation has demonstrated the potential of PEDOT:PSS as a low-temperature, solution-processable HTL for planar crystalline silicon heterojunction solar cells. While the basic viability of PEDOT:PSS/Si devices has been established in the previous chapters, with reported efficiencies approaching 15-16% in optimized planar structures, several fundamental

limitations continue to restrict performance and long-term stability. The main obstacles are interface recombination velocities caused by unpassivated surface states, suboptimal energy-level alignment between PEDOT:PSS and silicon, lack of light trapping, and chemical degradation induced by the acidic nature of PSS. Future work must therefore pay attention to a more fundamental strategy of interface engineering. The enhancement of intrinsic conductivity and stability of PEDOT:PSS film as the HTL layer has been extensively studied in this dissertation. At this point, combining chemical passivation, polymer neutralization, controlled surface microstructures, and advanced characterization have been used to unlock the full potential of hybrid heterojunction photovoltaics.

Surface passivation and work-function alignment represent a potential approach to improve PCE and/or stability. Self-assembled monolayers (SAMs) such as carbazole-based (2-(3,6-Dimethoxy-9H-carbazol-9-yl)ethyl)phosphonic acid (or MeO-2PACz)[342] or trichloro(3,3,3-trifluropropyl)silane [343] have been shown to dramatically reduce surface recombination and raise the built-in potential in perovskite and organic photovoltaics. Similar approaches have recently been applied to silicon, with MeO-2PACz improving the open-circuit voltage by up to 53 mV (from 1071 mV to 1124 mV).[344] The effectiveness of the SAM can then be correlated with device-level metrics such as $V_{OC}$, $J_{SC}$, FF, and PCE.

Equally important is addressing the inherent acidity of PEDOT:PSS, which has been implicated in long-term degradation of silicon surfaces.[223,345] Promising strategies to neutralize the sulfonic acid groups of PSS include post-deposition rinsing with dilute bases (e.g., ammonium hydroxide) to remove residual acidity, and the incorporation of additives with zwitterionic characteristics to buffer the PSS phase.[226,346] In parallel, molecular dopants such as 2,3,5,6-Tetrafluoro-7,7,8,8-tetracyanoquinodimethane (or F4-TCNQ) can be introduced to raise the work function of PEDOT:PSS toward 5.18 eV, improving band alignment with the silicon valence band.[347] These approaches are practical and compatible with standard spin-coating or spray-coating processes and can significantly enhance device stability without sacrificing conductivity.

Another good opportunity arises from the use of reactive ion etching (RIE) to define micro- and nanoscale topographies on the silicon surface prior to PEDOT:PSS deposition. Most reported devices rely on conventional alkaline-etched random pyramids or deep “black silicon” textures with improved optical absorption but offer little control over geometry and interface interactions.[242,348,349] In contrast, RIE enables precise tuning of feature size (width), depth, and slope (of sidewall). By engineering shallow, periodic textures with controlled sidewall angles, it becomes possible to balance light trapping with increased junction area while preserving passivation quality.[350] Recent optical design

studies by Li et al., have shown that shallow, microscale periodic texture patterns (<200 nm deep) on silicon wafers can significantly improve absorption and photocurrent while minimizing surface area and consequently recombination losses. Periodic checkerboard-like geometries with optimized period (400–800 nm) and duty cycle (~50%) have been shown to deliver photocurrents above 28 mA/cm$^2$ with strong angular response. These findings directly support the use of engineered shallow textures in PEDOT:PSS/Si heterojunctions, where these geometrical parameters influence optical performance, interfacial passivation, and device efficiency without the drawbacks of deep, high aspect ratio texturing.[350] Moreover, RIE introduces distinct surface chemistries (e.g., oxidized or fluorinated residues) that may interact differently with organic layers, presenting new opportunities for further studying the interface.

Possible integration of these modifications could enable a level of performance optimization that has not been systematically explored yet. By implementing different passivation and PEDOT:PSS formulations and combining them with a series of textured substrates of varying feature size, pitch, and aspect ratio, it may be possible to map the complex interplay between geometry, optical scattering, carrier collection, and recombination. For example, applying SAMs to planar and RIE-textured silicon could offer two synergistic benefits: chemical passivation of surface traps in different substrates and energy-level tuning of the corresponding PEDOT:PSS/Si junction.

While previous studies have shown that surface structuring can enhance photocurrent considerably by more than 30% [351] and improve angular response,[352] most of these reports still do not include optimization of the optical texture (feature size, period, or shape) and the interface/passivation chemistry. Although some studies do examine how passivation quality or conformality changes with increasing texture roughness or aspect ratio, a broad, systematic optimization of texture parameters together with interface engineering (e.g., passivation layers or polymer HTLs) for simultaneous optical and electronic gains remains rare. This leaves a great opportunity to investigate how geometry and chemistry correlatively affect the device efficiency.[353–358] Experimental work should focus on solution or vapor–phase SAM deposition following standard RCA cleaning, with careful characterization by XPS and Kelvin probe force microscopy. Advanced characterization methods such as cross-sectional SEM, TEM, and TOF-SIMS can be used to quantify conformality, while EQE and UV–Vis measurements can assess light-trapping performance

Some preliminary work has already been carried out to demonstrate the tunability of microstructure design and surface morphology achievable through RIE, as illustrated in Figure 5.1. Different pattern geometries, including square and hexagonal lattices as well as randomly textured

morphologies, highlight the high degree of control possible in tailoring the surface structure to influence both optical and interfacial properties.

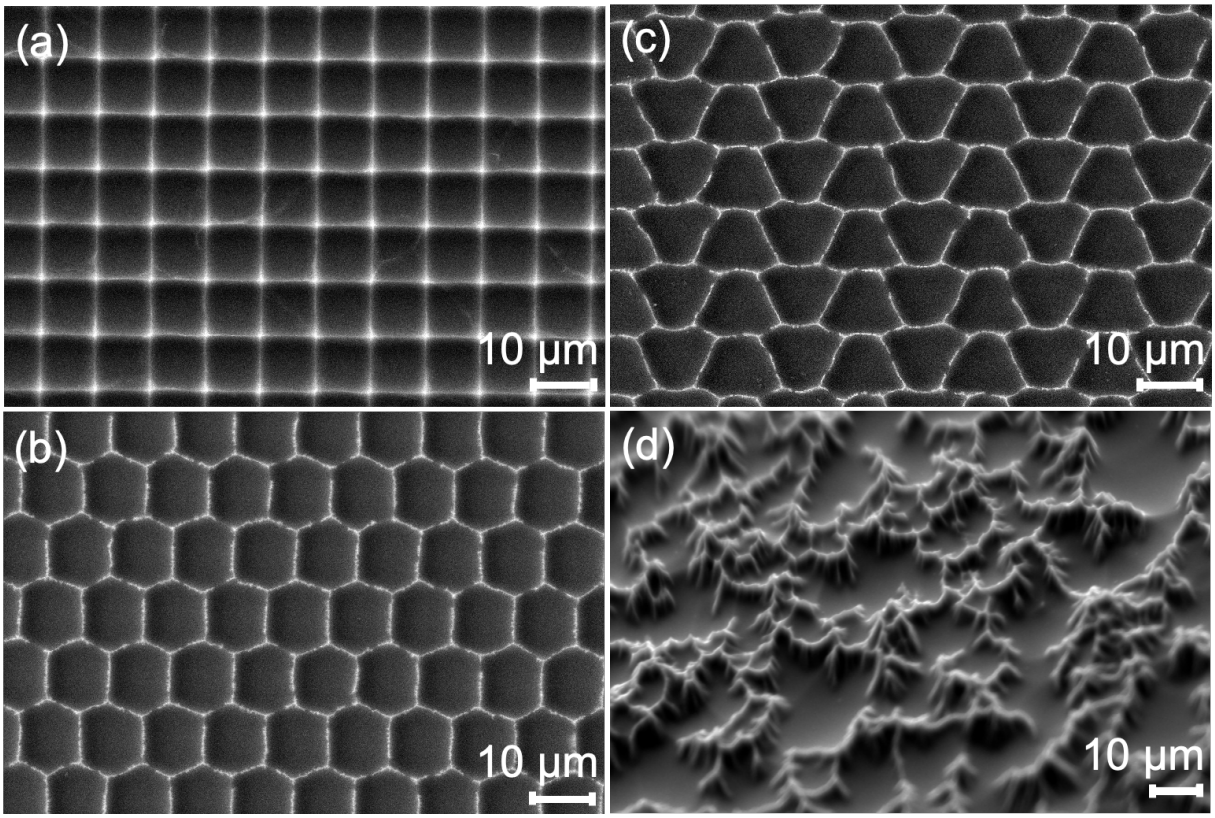



**Figure 5.1:** SEM images demonstrating the tunability of microstructured silicon surfaces textured by RIE: (a) Periodic square array, (b) periodic hexagonal array, (c) alternating triangle matrix, and (d) randomly textured surface morphology produced under modified etching conditions.

The preliminary device performance of a PEDOT:PSS/Si heterojunction solar cell fabricated on one such textured substrate using the EM solution is shown in Figure 5.2. Despite a reasonable $J_{SC}$ (31 mA/cm$^2$), the device exhibits a low $V_{OC}$ (383.9 mV), a poor fill factor (43.4%), and a PCE of only 5.2%. These results suggest that, although surface texturing can improve optical absorption and $J_{SC}$, effective surface passivation and interface engineering are essential for achieving competitive device performance. The significant recombination losses observed here underscore the importance of combining microstructural optimization with chemical strategies such as SAMs, dielectric interlayers, or acid-neutralized PEDOT:PSS formulations to suppress interface defects, improve energy-level alignment, and fully exploit the potential of the textured architecture.

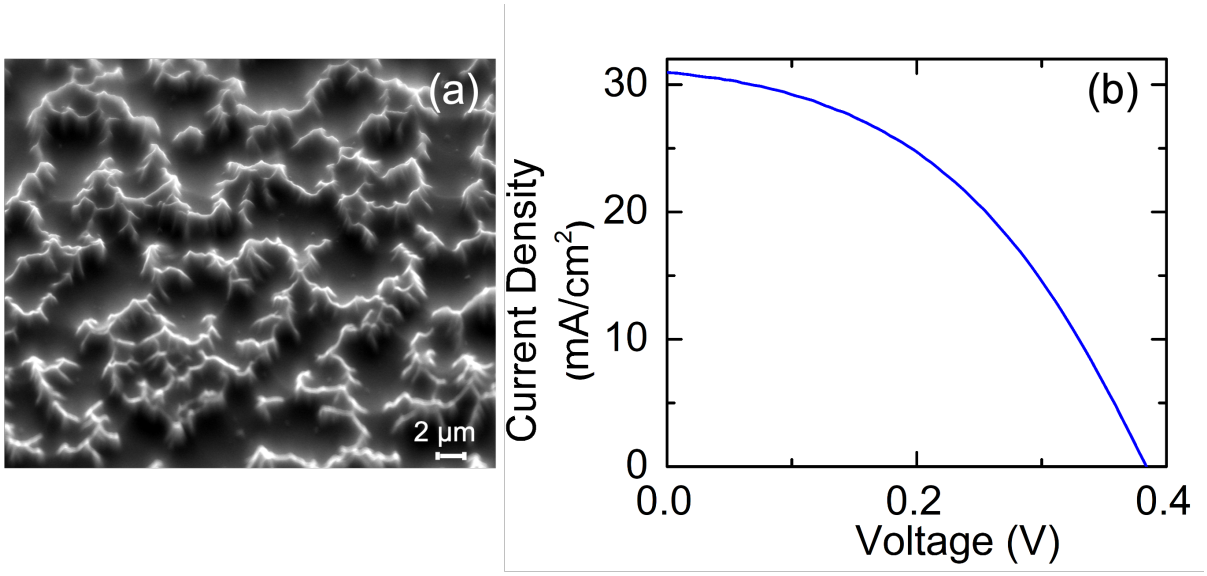



**Figure 5.2:** Device characterization of a PEDOT:PSS/textured-Si heterojunction solar cell fabricated on a textured silicon substrate using the EM solution. (a) SEM image of the textured surface coated with EM (b) J–V characteristics under AM 1.5G illumination.

In conclusion, promising future research lies not only in changes to PEDOT:PSS processing but in the synergistic design of interface chemistry, polymer functionality and surface geometry. By incorporating SAM-based passivation, acid-neutralized PEDOT:PSS, controlled work-function tuning and RIE-defined textures, it should be possible to significantly enhance the performance, stability, and manufacturability of hybrid PEDOT:PSS/Si heterojunction solar cells. Such an approach would represent a practical development over existing literature, in which these elements have typically been explored in isolation, and could form the foundation for next-generation organic–inorganic photovoltaic architectures.

# References


(1) Staples, C. A.; Williams, J. B.; Craig, G. R.; Roberts, K. M. Fate, Effects and Potential Environmental Risks of Ethylene Glycol: A Review. *Chemosphere* **2001**, *43* (3), 377–383. https://doi.org/10.1016/s0045-6535(00)00148-x.

(2) Butawan, M.; Benjamin, R. L.; Bloomer, R. J. Methylsulfonylmethane: Applications and Safety of a Novel Dietary Supplement. *Nutrients* **2017**, *9* (3), 290. https://doi.org/10.3390/nu9030290.

(3) Energy Institute. *Energy Institute*; https://www.energyinst.org/home (accessed 2025-07-24).

(4) *2024 — IPCC*. https://www.ipcc.ch/2024/ (accessed 2025-07-25).

(5) *Global overview – Renewables 2024 – Analysis*. IEA. https://www.iea.org/reports/renewables-2024/global-overview (accessed 2025-07-25).

(6) Izam, N. S. M. N.; Itam, Z.; Sing, W. L.; Syamsir, A. Sustainable Development Perspectives of Solar Energy Technologies with Focus on Solar Photovoltaic—A Review. *Energies* **2022**, *15* (8), 2790. https://doi.org/10.3390/en15082790.

(7) Halkos, G. E.; Gkampoura, E.-C. Reviewing Usage, Potentials, and Limitations of Renewable Energy Sources. *Energies* **2020**, *13* (11), 2906. https://doi.org/10.3390/en13112906.

(8) Zhang, C.; Zhang, J.; Ma, X.; Feng, Q. *Semiconductor Photovoltaic Cells*; Springer Singapore: Singapore, 2021. https://doi.org/10.1007/978-981-15-9480-9.

(9) Knupfer, M. Exciton Binding Energies in Organic Semiconductors. *Appl. Phys. A* **2003**, *77* (5), 623–626. https://doi.org/10.1007/s00339-003-2182-9.

(10) Koster, L. J. A.; Shaheen, S. E.; Hummelen, J. C. Pathways to a New Efficiency Regime for Organic Solar Cells. *Adv. Energy Mater.* **2012**, *2* (10), 1246–1253. https://doi.org/10.1002/aenm.201200103.

(11) Brebels, J.; Manca, J. V.; Lutsen, L.; Vanderzande, D.; Maes, W. High Dielectric Constant Conjugated Materials for Organic Photovoltaics. *J. Mater. Chem. A* **2017**, *5* (46), 24037–24050. https://doi.org/10.1039/C7TA06808E.

(12) Chen, S.; Tsang, S.-W.; Lai, T.-H.; Reynolds, J. R.; So, F. Dielectric Effect on the Photovoltage Loss in Organic Photovoltaic Cells. *Adv. Mater.* **2014**, *26* (35), 6125–6131. https://doi.org/10.1002/adma.201401987.

(13) Hughes, M. P.; Rosenthal, K. D.; Ran, N. A.; Seifrid, M.; Bazan, G. C.; Nguyen, T.-Q. Determining the Dielectric Constants of Organic Photovoltaic Materials Using Impedance Spectroscopy. *Adv. Funct. Mater.* **2018**, *28* (32), 1801542. https://doi.org/10.1002/adfm.201801542.

(14) Lin, Q.; Armin, A.; Nagiri, R. C. R.; Burn, P. L.; Meredith, P. Electro-Optics of Perovskite Solar Cells. *Nat. Photonics* **2015**, *9* (2), 106–112. https://doi.org/10.1038/nphoton.2014.284.

(15) Shockley, W.; Queisser, H. J. Detailed Balance Limit of Efficiency of *p-n* Junction Solar Cells. *J. Appl. Phys.* **1961**, *32* (3), 510–519. https://doi.org/10.1063/1.1736034.

(16) Zanatta, A. R. The *Shockley–Queisser* Limit and the Conversion Efficiency of Silicon-Based Solar Cells. *Results Opt.* **2022**, *9*, 100320. https://doi.org/10.1016/j.rio.2022.100320.

(17) Dixit, A.; Saxena, A.; Sharma, R.; Behera, D.; Mukherjee, S. Solar Photovoltaic Principles. In *Solar PV Panels - Recent Advances and Future Prospects*; IntechOpen, 2023. https://doi.org/10.5772/intechopen.109730.

(18) Green, M. A. Solar Cells: Operating Principles, Technology, and System Applications. **1981**.

(19) Zou, S.; Ye, X.; Wu, C.; Cheng, K.; Fang, L.; Tang, R.; Shen, M.; Wang, X.; Su, X. Complementary Etching Behavior of Alkali, Metal-Catalyzed Chemical, and Post-Etching of Multicrystalline Silicon Wafers. *Prog. Photovolt. Res. Appl.* **2019**, *27* (6), 511–519. https://doi.org/10.1002/pip.3125.

(20) Peet, J.; Kim, J. Y.; Coates, N. E.; Ma, W. L.; Moses, D.; Heeger, A. J.; Bazan, G. C. Efficiency Enhancement in Low-Bandgap Polymer Solar Cells by Processing with Alkane Dithiols. *Nat. Mater.* **2007**, *6* (7), 497–500. https://doi.org/10.1038/nmat1928.

(21) Zhao, L.; Zhao, S.; Xu, Z.; Qiao, B.; Huang, D.; Xu, X. Two Effects of 1,8-Diiodooctane on PTB7-Th:PC71BM Polymer Solar Cells. *Org. Electron.* **2016**, *34*, 188–192. https://doi.org/10.1016/j.orgel.2016.04.014.

(22) Bernardo, G.; Gaspar, H.; Pérez, G. E.; Shackleford, A. S. D.; Parnell, A. J.; Bleuel, M.; Mendes, A.; King, S. M.; Parnell, S. R. Impact of 1,8-Diiodooctane on the Morphology of Organic Photovoltaic (OPV) Devices – A Small Angle Neutron Scattering (SANS) Study. *Polym. Test.* **2020**, *82*, 106305. https://doi.org/10.1016/j.polymertesting.2019.106305.

(23) Reisdorffer, F.; Haas, O.; Le Rendu, P.; Nguyen, T. P. Co-Solvent Effects on the Morphology of P3HT:PCBM Thin Films. *Synth. Met.* **2012**, *161* (23), 2544–2548. https://doi.org/10.1016/j.synthmet.2011.08.005.

(24) Guo, L.; Li, Q.; Ren, J.; Xu, Y.; Zhang, J.; Zhang, K.; Cai, Y.; Liu, S.; Huang, F. Halogenated Thiophenes Serve as Solvent Additives in Mediating Morphology and Achieving Efficient Organic Solar Cells. *Energy Environ. Sci.* **2022**, *15* (12), 5137–5148. https://doi.org/10.1039/D2EE02553A.

(25) Sehar Abbasi, M.; Li, C.; Gao, J.; Wang, S.; Wang, S.; Lin, Q.; Xie, G.; Nawaz Khan, S.; Zhang, J.; Zhang, X.; Cai, Y.; Huang, H. High Performance All-Polymer Solar Cells Enabled with Solvent and Solid Dual Additives. *J. Mater. Chem. A* **2024**, *12* (45), 31284–31290. https://doi.org/10.1039/D4TA06013J.

(26) Araújo, F. L.; Amorim, D. R. B.; Torres, B. B. M.; Coutinho, D. J.; Faria, R. M. Effects of Additive-Solvents on the Mobility and Recombination of a Solar Cell Based on PTB7-Th:PC71BM. *Sol. Energy* **2019**, *177*, 284–292. https://doi.org/10.1016/j.solener.2018.11.027.

(27) Yan, S.; Lv, L.; Ning, Y.; Qin, L.; Li, C.; Liu, X.; Hu, Y.; Lou, Z.; Teng, F.; Hou, Y. Effects of Solvent Additives on Trap-Assisted Recombination in P3HT:ICBA Based Polymer Solar Cells. *Phys. Status Solidi A* **2015**, *212* (10), 2169–2173. https://doi.org/10.1002/pssa.201532250.

(28) Kim, Y. J.; Ahn, S.; Wang, D. H.; Park, C. E. A Mechanistic Understanding of a Binary Additive System to Synergistically Boost Efficiency in All-Polymer Solar Cells. *Sci. Rep.* **2015**, *5* (1), 18024. https://doi.org/10.1038/srep18024.

(29) Liu, Y.; Fan, Q.; Liu, H.; Jalan, I.; Jin, Y.; Stam, J. van; Moons, E.; Wang, E.; Lu, X.; Inganäs, O.; Zhang, F. In Situ Optical Spectroscopy Demonstrates the Effect of Solvent Additive in the Formation of All-Polymer Solar Cells. *J. Phys. Chem. Lett.* **2022**, *13* (50), 11696–11702. https://doi.org/10.1021/acs.jpclett.2c03397.

(30) Cao, X.; Xie, L.; Zhu, X.; Lv, J.; Fan, H. The Principles of Selecting Green Solvent Additives for Optimizing the Phase Separation Structure of Polymer Solar Cells Based on PTB7:PC71BM. *Eur. Polym. J.* **2022**, *180*, 111603. https://doi.org/10.1016/j.eurpolymj.2022.111603.

(31) Liu, D.; Zhang, H.; Shen, H.; Jiang, Z.; Liu, X.; Chen, H.; Peng, Q.; Yang, J.; Chen, Y.; Ding, J.; Qi, X.; Gong, X. Balancing Carrier Mobility with Solvent-Solid Hybrid Additives for High-Performance Non-Fullerene Organic Solar Cells. *Chem. Eng. J.* **2025**, *508*, 161037. https://doi.org/10.1016/j.cej.2025.161037.

(32) Solak, E. K.; Irmak, E. Advances in Organic Photovoltaic Cells: A Comprehensive Review of Materials, Technologies, and Performance. *RSC Adv.* **2023**, *13* (18), 12244–12269. https://doi.org/10.1039/d3ra01454a.

(33) Soonmin, H.; Hardani; Nandi, P.; Mwankemwa, B. S.; Malevu, T. D.; Malik, M. I. Overview on Different Types of Solar Cells: An Update. *Appl. Sci.* **2023**, *13* (4), 2051. https://doi.org/10.3390/app13042051.

(34) *Best Research-Cell Efficiency Chart | Photovoltaic Research | NREL*. https://www.nrel.gov/pv/cell-efficiency (accessed 2025-08-05).

(35) Chapin, D. M.; Fuller, C. S.; Pearson, G. L. A New Silicon P-n Junction Photocell for Converting Solar Radiation into Electrical Power. *J. Appl. Phys.* **1954**, *25* (5), 676–677. https://doi.org/10.1063/1.1721711.

(36) Czochralski Method. *Wikipedia*; 2025 (accessed 2025-08-05).

(37) Ranjan, S.; Balaji, S.; Panella, R. A.; Ydstie, B. E. Silicon Solar Cell Production. *Comput. Chem. Eng.* **2011**, *35* (8), 1439–1453. https://doi.org/10.1016/j.compchemeng.2011.04.017.

(38) Takihara, M.; Takahashi, T.; Ujihara, T. Minority Carrier Lifetime in Polycrystalline Silicon Solar Cells Studied by Photoassisted Kelvin Probe Force Microscopy. *Appl. Phys. Lett.* **2008**, *93* (2), 021902. https://doi.org/10.1063/1.2957468.

(39) Jester, T. L. Crystalline Silicon Manufacturing Progress. *Prog. Photovolt. Res. Appl.* **2002**, *10* (2), 99–106. https://doi.org/10.1002/pip.414.

(40) Kalogirou, S. A. Chapter Nine - Photovoltaic Systems. In *Solar Energy Engineering*; Kalogirou, S. A., Ed.; Academic Press: Boston, 2009; pp 469–519. https://doi.org/10.1016/B978-0-12-374501-9.00009-1.

(41) Victoria, M.; Haegel, N.; Peters, I. M.; Sinton, R.; Jäger-Waldau, A.; del Cañizo, C.; Breyer, C.; Stocks, M.; Blakers, A.; Kaizuka, I.; Komoto, K.; Smets, A. Solar Photovoltaics Is Ready to Power a Sustainable Future. *Joule* **2021**, *5* (5), 1041–1056. https://doi.org/10.1016/j.joule.2021.03.005.

(42) Wright, M.; Uddin, A. Organic—Inorganic Hybrid Solar Cells: A Comparative Review. *Sol. Energy Mater. Sol. Cells* **2012**, *107*, 87–111. https://doi.org/10.1016/j.solmat.2012.07.006.

(43) Doshi, P.; Rohatgi, A.; Ropp, M.; Chen, Z.; Ruby, D.; Meier, D. L. Rapid Thermal Processing of High-Efficiency Silicon Solar Cells with Controlled in-Situ Annealing. *Sol. Energy Mater. Sol. Cells* **1996**, *41–42*, 31–39. https://doi.org/10.1016/0927-0248(95)00119-0.

(44) Lin, H.; Yang, M.; Ru, X.; Wang, G.; Yin, S.; Peng, F.; Hong, C.; Qu, M.; Lu, J.; Fang, L.; Han, C.; Procel, P.; Isabella, O.; Gao, P.; Li, Z.; Xu, X. Silicon Heterojunction Solar Cells with up to 26.81% Efficiency Achieved by Electrically Optimized Nanocrystalline-Silicon Hole Contact Layers. *Nat. Energy* **2023**, *8* (8), 789–799. https://doi.org/10.1038/s41560-023-01255-2.

(45) Lan, C. W.; Lan, W. C.; Lee, T. F.; Yu, A.; Yang, Y. M.; Hsu, W. C.; Hsu, B.; Yang, A. Grain Control in Directional Solidification of Photovoltaic Silicon. *J. Cryst. Growth* **2012**, *360*, 68–75. https://doi.org/10.1016/j.jcrysgro.2012.01.007.

(46) Camel, D.; Cierniak, E.; Drevet, B.; Cabal, R.; Ponthenier, D.; Eustathopoulos, N. Directional Solidification of Photovoltaic Silicon in Re-Useable Graphite Crucibles. *Sol. Energy Mater. Sol. Cells* **2020**, *215*, 110637. https://doi.org/10.1016/j.solmat.2020.110637.

(47) Vorob'ev, A. N.; Sid'ko, A. P.; Kalaev, V. V. Advanced Chemical Model for Analysis of Cz and DS Si-Crystal Growth. *J. Cryst. Growth* **2014**, *386*, 226–234. https://doi.org/10.1016/j.jcrysgro.2013.10.022.

(48) Hallam, B.; Herguth, A.; Hamer, P.; Nampalli, N.; Wilking, S.; Abbott, M.; Wenham, S.; Hahn, G. Eliminating Light-Induced Degradation in Commercial p-Type Czochralski Silicon Solar Cells. *Appl. Sci.* **2018**, *8* (1), 10. https://doi.org/10.3390/app8010010.

(49) Ballif, C.; Haug, F.-J.; Boccard, M.; Verlinden, P. J.; Hahn, G. Status and Perspectives of Crystalline Silicon Photovoltaics in Research and Industry. *Nat. Rev. Mater.* **2022**, *7* (8), 597–616. https://doi.org/10.1038/s41578-022-00423-2.

(50) Lan, C. W. Twenty Years Crystal Growth of Solar Silicon: My Serendipity Journey. *J. Cryst. Growth* **2024**, *626*, 127480. https://doi.org/10.1016/j.jcrysgro.2023.127480.

(51) Vicari Stefani, B.; Kim, M.; Zhang, Y.; Hallam, B.; Green, M. A.; Bonilla, R. S.; Fell, C.; Wilson, G. J.; Wright, M. Historical Market Projections and the Future of Silicon Solar Cells. *Joule* **2023**, *7* (12), 2684–2699. https://doi.org/10.1016/j.joule.2023.11.006.

(52) Adamczyk, K.; Søndenå, R.; Stokkan, G.; Looney, E.; Jensen, M.; Lai, B.; Rinio, M.; Di Sabatino, M. Recombination Activity of Grain Boundaries in High-Performance Multicrystalline Si during Solar Cell Processing. *J. Appl. Phys.* **2018**, *123* (5), 055705. https://doi.org/10.1063/1.5018797.

(53) Di Sabatino, M.; Hendawi, R. Crystallization Processes for Photovoltaic Silicon Ingots: Status and Perspectives. *J. Cryst. Growth* **2024**, *641*, 127772. https://doi.org/10.1016/j.jcrysgro.2024.127772.

(54) Green, M. A.; Dunlop, E. D.; Yoshita, M.; Kopidakis, N.; Bothe, K.; Siefer, G.; Hao, X. Solar Cell Efficiency Tables (Version 63). *Prog. Photovolt. Res. Appl.* **2024**, *32* (1), 3–13. https://doi.org/10.1002/pip.3750.

(55) Sharma, I.; Bisht, N.; Patil, P. R.; Pawar, P. S.; Yadav, R. K.; Kim, Y. T.; Heo, J. Smart Materials in Energy Storage Devices. In *Smart Materials for Science and Engineering*; John Wiley & Sons, Ltd, 2024; pp 191–219. https://doi.org/10.1002/9781394186488.ch11.

(56) Philipps, D. S.; Ise, F.; Warmuth, W.; GmbH, P. P. Photovoltaics Report (accessed 2025-11-20).

(57) Oh, W.; Bae, S.; Kim, S.; Park, N.; Chan, S.-I.; Choi, H.; Hwang, H.; Kim, D. Analysis of Degradation in 25-Year-Old Field-Aged Crystalline Silicon Solar Cells. *Microelectron. Reliab.* **2019**, *100–101*, 113392. https://doi.org/10.1016/j.microrel.2019.06.084.

(58) Jordan, D. C.; Kurtz, S. R.; VanSant, K.; Newmiller, J. Compendium of Photovoltaic Degradation Rates. *Prog. Photovolt. Res. Appl.* **2016**, *24* (7), 978–989. https://doi.org/10.1002/pip.2744.

(59) Chen, R.; Tong, H.; Zhu, H.; Ding, C.; Li, H.; Chen, D.; Hallam, B.; Chong, C. M.; Wenham, S.; Ciesla, A. 23.83% Efficient Mono-PERC Incorporating Advanced Hydrogenation. *Prog. Photovolt. Res. Appl.* **2020**, *28* (12), 1239–1247. https://doi.org/10.1002/pip.3243.

(60) pv magazine. *pv magazine International: News from the photovoltaic and storage industry: market trends, technological advancements, expert commentary, and more;* https://www.pv-magazine.com/ (accessed 2025-10-15).

(61) *Longi claims world's highest efficiency for silicon solar cells – pv magazine International*. https://www.pv-magazine.com/2025/04/14/longi-claims-worlds-highest-efficiency-for-silicon-solar-cells/ (accessed 2025-07-25).

(62) Chopra, K. L.; Paulson, P. D.; Dutta, V. Thin-film Solar Cells: An Overview. *Prog. Photovolt. Res. Appl.* **2004**, *12* (2–3), 69–92. https://doi.org/10.1002/pip.541.

(63) Maalouf, A.; Okoroafor, T.; Jehl, Z.; Babu, V.; Resalati, S. A Comprehensive Review on Life Cycle Assessment of Commercial and Emerging Thin-Film Solar Cell Systems. *Renew. Sustain. Energy Rev.* **2023**, *186*, 113652. https://doi.org/10.1016/j.rser.2023.113652.

(64) Kayes, B. M.; Nie, H.; Twist, R.; Spruytte, S. G.; Reinhardt, F.; Kizilyalli, I. C.; Higashi, G. S. 27.6% Conversion Efficiency, a New Record for Single-Junction Solar Cells under 1 Sun Illumination. In *2011 37th IEEE Photovoltaic Specialists Conference*; 2011; pp 000004–000008. https://doi.org/10.1109/PVSC.2011.6185831.

(65) Tai, Y.; Zhang, X.; Li, J.; Zheng, Y.; Liu, G.; Zhang, J.; Zeng, G.; Yakubov, K.; Alla, C. Research on Ultra-Thin Cadmium Telluride Heterojunction Thin Film Solar Cells. *Renew. Sustain. Energy Rev.* **2025**, *207*, 114996. https://doi.org/10.1016/j.rser.2024.114996.

(66) Zweibel, K. Thin Film PV Manufacturing: Materials Costs and Their Optimization. *Sol. Energy Mater. Sol. Cells* **2000**, *63* (4), 375–386. https://doi.org/10.1016/S0927-0248(00)00057-X.

(67) Curtin, A. M.; Vail, C. A.; Buckley, H. L. CdTe in Thin Film Photovoltaic Cells: Interventions to Protect Drinking Water in Production and End-of-Life. *Water-Energy Nexus* **2020**, *3*, 15–28. https://doi.org/10.1016/j.wen.2020.03.007.

(68) Arici, E.; Hoppe, H.; Schäffler, F.; Meissner, D.; Malik, M. A.; Sariciftci, N. S. Hybrid Solar Cells Based on Inorganic Nanoclusters and Conjugated Polymers. *Thin Solid Films* **2004**, *451–452*, 612–618. https://doi.org/10.1016/j.tsf.2003.11.026.

(69) Hashmi, S. G., Halme, J., Ma, Y., Saukkonen, T., Lund, P. (2014). A Single-Walled Carbon Nanotube Coated Flexible PVC Counter Electrode for Dye-Sensitized Solar Cells. Adv. Mater. Interfaces, 1: 1300055. doi: 10.1002/admi.201300055.

(70) Zhong, M.; Yang, D.; Zhang, J.; Shi, J.; Wang, X.; Li, C. Improving the Performance of CdS/P3HT Hybrid Inverted Solar Cells by Interfacial Modification. *Sol. Energy Mater. Sol. Cells* **2012**, *96*, 160–165. https://doi.org/10.1016/j.solmat.2011.09.041.

(71) Shah, N.; Shah, A. A.; Leung, P. K.; Khan, S.; Sun, K.; Zhu, X.; Liao, Q. A Review of Third Generation Solar Cells. *Processes* **2023**, *11* (6), 1852. https://doi.org/10.3390/pr11061852.

(72) Green, M. A. Third Generation Photovoltaics: Ultra-High Conversion Efficiency at Low Cost. *Prog. Photovolt. Res. Appl.* **2001**, *9* (2), 123–135. https://doi.org/10.1002/pip.360.

(73) *Highest Perovskite Solar Cell Efficiencies (2025 Update)*. Fluxim. https://www.fluxim.com/research-blogs/perovskite-silicon-tandem-pv-record-updates (accessed 2025-07-25).

(74) Chen, L. X. Organic Solar Cells: Recent Progress and Challenges. *ACS Energy Lett.* **2019**, *4* (10), 2537–2539. https://doi.org/10.1021/acsenergylett.9b02071.

(75) Kaltenbrunner, M.; White, M. S.; Głowacki, E. D.; Sekitani, T.; Someya, T.; Sariciftci, N. S.; Bauer, S. Ultrathin and Lightweight Organic Solar Cells with High Flexibility. *Nat. Commun.* **2012**, *3*, 770. https://doi.org/10.1038/ncomms1772.

(76) Sun, L.; Fukuda, K.; Someya, T. Recent Progress in Solution-Processed Flexible Organic Photovoltaics. *Npj Flex. Electron.* **2022**, *6* (1), 89. https://doi.org/10.1038/s41528-022-00222-3.

(77) Zhang, S.; Ye, L.; Zhang, H.; Hou, J. Green-Solvent-Processable Organic Solar Cells. *Mater. Today* **2016**, *19* (9), 533–543. https://doi.org/10.1016/j.mattod.2016.02.019.

(78) Zhu, L.; Zhang, M.; Zhou, G.; Wang, Z.; Zhong, W.; Zhuang, J.; Zhou, Z.; Gao, X.; Kan, L.; Hao, B.; Han, F.; Zeng, R.; Xue, X.; Xu, S.; Jing, H.; Xiao, B.; Zhu, H.; Zhang, Y.; Liu, F. Achieving 20.8% Organic Solar Cells via Additive-Assisted Layer-by-Layer Fabrication with Bulk *p-i-n* Structure and Improved Optical Management. *Joule* **2024**, *8* (11), 3153–3168. https://doi.org/10.1016/j.joule.2024.08.001.

(79) Tang, C. W. Two-layer Organic Photovoltaic Cell. *Appl. Phys. Lett.* **1986**, *48* (2), 183–185. https://doi.org/10.1063/1.96937.

(80) He, Y.; Li, N.; Heumüller, T.; Wortmann, J.; Hanisch, B.; Aubele, A.; Lucas, S.; Feng, G.; Jiang, X.; Li, W.; Bäuerle, P.; Brabec, C. J. Industrial Viability of Single-Component Organic Solar Cells. *Joule* **2022**, *6* (6), 1160–1171. https://doi.org/10.1016/j.joule.2022.05.008.

(81) Mateker, W. R.; McGehee, M. D. Progress in Understanding Degradation Mechanisms and Improving Stability in Organic Photovoltaics. *Adv. Mater.* **2017**, *29* (10), 1603940. https://doi.org/10.1002/adma.201603940.

(82) Duan, L.; Uddin, A. Progress in Stability of Organic Solar Cells. *Adv. Sci.* **2020**, *7* (11), 1903259. https://doi.org/10.1002/advs.201903259.

(83) Ding, P.; Yang, D.; Yang, S.; Ge, Z. Stability of Organic Solar Cells: Toward Commercial Applications. *Chem. Soc. Rev.* **2024**, *53* (5), 2350–2387. https://doi.org/10.1039/D3CS00492A.

(84) Jäckle, S.; Liebhaber, M.; Gersmann, C.; Mews, M.; Jäger, K.; Christiansen, S.; Lips, K. Potential of PEDOT:PSS as a Hole Selective Front Contact for Silicon Heterojunction Solar Cells. *Sci. Rep.* **2017**, *7* (1), 2170. https://doi.org/10.1038/s41598-017-01946-3.

(85) He, J.; Gao, P.; Ling, Z.; Ding, L.; Yang, Z.; Ye, J.; Cui, Y. High-Efficiency Silicon/Organic Heterojunction Solar Cells with Improved Junction Quality and Interface Passivation. *ACS Nano* **2016**, *10* (12), 11525–11531. https://doi.org/10.1021/acsnano.6b07511.

(86) Khang, D.-Y. Recent Progress in Si-PEDOT:PSS Inorganic–Organic Hybrid Solar Cells. *J. Phys. Appl. Phys.* **2019**, *52* (50), 503002. https://doi.org/10.1088/1361-6463/ab3f64.

(87) Thomas, J. P.; Leung, K. T. Defect-Minimized PEDOT:PSS/Planar-Si Solar Cell with Very High Efficiency. *Adv. Funct. Mater.* **2014**, *24* (31), 4978–4985. https://doi.org/10.1002/adfm.201400380.

(88) Thomas, J. P.; Leung, K. T. Mixed Co-Solvent Engineering of PEDOT:PSS to Enhance Its Conductivity and Hybrid Solar Cell Properties. *J. Mater. Chem. A* **2016**, *4* (44), 17537–17542. https://doi.org/10.1039/C6TA07410C.

(89) Ravele, T.; Fuku, X. G.; Kebede, M. A. Review of Organic–Inorganic Heterojunction Hybrid Solar Cells with Embedded Plasmonic Nanocrystals: Recent Advances and Future Perspectives. *Energy Fuels* **2025**, *39* (13), 6026–6044. https://doi.org/10.1021/acs.energyfuels.4c05517.

(90) Luo, R.; Li, H.; Du, B.; Zhou, S.; Zhu, Y. A Simple Strategy for High Stretchable, Flexible and Conductive Polymer Films Based on PEDOT:PSS-PDMS Blends. *Org. Electron.* **2020**, *76*, 105451. https://doi.org/10.1016/j.orgel.2019.105451.

(91) Carrillo-Sendejas, J. C.; Reyes-Molina, R.; Mansurova, S.; Kudriavtsev, Y.; Baldovino-Pantaleón, O.; Olivares, A. J.; Cosme, I. Analytical Study of Hybrid PEDOT:PSS/Si/PFN Heterojunction Interfaces for Doping-Free Applications. *Mater. Sci. Semicond. Process.* **2023**, *155*, 107240. https://doi.org/10.1016/j.mssp.2022.107240.

(92) Chen, J.; Lu, Z.; Wang, X.; Luo, Y.; Ma, Y.; Lou, G.; Chi, D.; Huang, S. Highly Efficient Organic/Silicon Hybrid Solar Cells with a MoO3 Capping Layer. *Nanomater. Basel Switz.* **2024**, *14* (20), 1630. https://doi.org/10.3390/nano14201630.

(93) Cui, Y.; Xiong, Y.; Wang, J.; Zhang, Y.; Yu, W. Significantly Enhancing the Performance of PEDOT: PSS/Si Hybrid Solar Cells by Simply Introducing a MoOX Interface Layer. *J. Alloys Compd.* **2025**, *1029*, 180782. https://doi.org/10.1016/j.jallcom.2025.180782.

(94) Wang, J.; Zhou, W.; Wei, Q.; Liu, G.; Yuan, X.; Pen, H.; Zhang, G.; Wang, R.; Wang, C.; Yang, Y. Effect of Au@MoS2 Contacted PEDOT:PSS on Work Function of Planar Silicon Hybrid Solar Cells. *Adv. Mater. Interfaces* **2023**, *10* (23), 2300187. https://doi.org/10.1002/admi.202300187.

(95) Kojima, A.; Teshima, K.; Shirai, Y.; Miyasaka, T. Organometal Halide Perovskites as Visible-Light Sensitizers for Photovoltaic Cells. *J. Am. Chem. Soc.* **2009**, *131* (17), 6050–6051. https://doi.org/10.1021/ja809598r.

(96) Shirayama, M.; Kadowaki, H.; Miyadera, T.; Sugita, T.; Tamakoshi, M.; Kato, M.; Fujiseki, T.; Murata, D.; Hara, S.; Murakami, T. N.; Fujimoto, S.; Chikamatsu, M.; Fujiwara, H. Optical Transitions in Hybrid Perovskite Solar Cells: Ellipsometry, Density Functional Theory, and Quantum Efficiency Analyses for $CH_3NH_3PbI_3$. *Phys. Rev. Appl.* **2016**, *5* (1), 014012. https://doi.org/10.1103/PhysRevApplied.5.014012.

(97) Stranks, S. D.; Eperon, G. E.; Grancini, G.; Menelaou, C.; Alcocer, M. J. P.; Leijtens, T.; Herz, L. M.; Petrozza, A.; Snaith, H. J. Electron-Hole Diffusion Lengths Exceeding 1 Micrometer in an Organometal Trihalide Perovskite Absorber. *Science* **2013**, *342* (6156), 341–344. https://doi.org/10.1126/science.1243982.

(98) Dong, Q.; Fang, Y.; Shao, Y.; Mulligan, P.; Qiu, J.; Cao, L.; Huang, J. Electron-Hole Diffusion Lengths > 175 μm in Solution-Grown $CH_3NH_3PbI_3$ Single Crystals. *Science* **2015**, *347* (6225), 967–970. https://doi.org/10.1126/science.aaa5760.

(99) You, J.; Hong, Z.; Yang, Y. (Michael); Chen, Q.; Cai, M.; Song, T.-B.; Chen, C.-C.; Lu, S.; Liu, Y.; Zhou, H.; Yang, Y. Low-Temperature Solution-Processed Perovskite Solar Cells with High Efficiency and Flexibility. *ACS Nano* **2014**, *8* (2), 1674–1680. https://doi.org/10.1021/nn406020d.

(100) Fu, F.; Feurer, T.; Jäger, T.; Avancini, E.; Bissig, B.; Yoon, S.; Buecheler, S.; Tiwari, A. N. Low-Temperature-Processed Efficient Semi-Transparent Planar Perovskite Solar Cells for Bifacial and Tandem Applications. *Nat. Commun.* **2015**, *6* (1), 8932. https://doi.org/10.1038/ncomms9932.

(101) Shin Thant, K. K.; Seriwattanachai, C.; Jittham, T.; Thamangraksat, N.; Sakata, P.; Kanjanaboos, P. Comprehensive Review on Slot-Die-Based Perovskite Photovoltaics: Mechanisms, Materials, Methods, and Marketability. *Adv. Energy Mater.* **2025**, *15* (5), 2403088. https://doi.org/10.1002/aenm.202403088.

(102) Nie, T.; Fang, Z.; Ren, X.; Duan, Y.; Liu, S. (Frank). Recent Advances in Wide-Bandgap Organic–Inorganic Halide Perovskite Solar Cells and Tandem Application. *Nano-Micro Lett.* **2023**, *15*, 70. https://doi.org/10.1007/s40820-023-01040-6.

(103) Zhang, X.; Wang, X.; Liu, H.; Chen, R. Defect Engineering of Metal Halide Perovskite Optoelectronic Devices. *Prog. Quantum Electron.* **2022**, *86*, 100438. https://doi.org/10.1016/j.pquantelec.2022.100438.

(104) Du, B.; He, K.; Tian, G.; Che, X.; Song, L. Robust Electron Transport Layers of SnO2 for Efficient Perovskite Solar Cells: Recent Advances and Perspectives. *J. Mater. Chem. C* **2023**, *11* (40), 13625–13646. https://doi.org/10.1039/D3TC02445H.

(105) Vanaraj, R.; Murugesan, V.; Rathinam, B. The Role of Optimal Electron Transfer Layers for Highly Efficient Perovskite Solar Cells—A Systematic Review. *Micromachines* **2024**, *15* (7), 859. https://doi.org/10.3390/mi15070859.

(106) Afre, R. A.; Pugliese, D. Perovskite Solar Cells: A Review of the Latest Advances in Materials, Fabrication Techniques, and Stability Enhancement Strategies. *Micromachines* **2024**, *15* (2), 192. https://doi.org/10.3390/mi15020192.

(107) *Saule Technologies Launches The First Production Line*. Saule Technologies. https://sauletech.com/launching-production-line/ (accessed 2025-07-31).

(108) Aljafari, B.; Vijaya, S.; Takshi, A.; Anandan, S. Copper Doped Manganese Dioxide as Counter Electrode for Dye-Sensitized Solar Cells. *Arab. J. Chem.* **2022**, *15* (9), 104068. https://doi.org/10.1016/j.arabjc.2022.104068.

(109) Mir, N.; Salavati-Niasari, M. Photovoltaic Properties of Corresponding Dye Sensitized Solar Cells: Effect of Active Sites of Growth Controller on TiO2 Nanostructures. *Sol. Energy* **2012**, *86* (11), 3397–3404. https://doi.org/10.1016/j.solener.2012.08.016.

(110) Dwivedi, G.; Munjal, G.; Bhaskarwar, A. N.; Chaudhary, A. Dye-Sensitized Solar Cells with Polyaniline: A Review. *Inorg. Chem. Commun.* **2022**, *135*, 109087. https://doi.org/10.1016/j.inoche.2021.109087.

(111) Li, H.; Zhang, Y.; Wang, J. ZnO Nanosheets Derived from Surfactant-Directed Process: Growth Mechanism, and Application in Dye-Sensitized Solar Cells. *J. Am. Ceram. Soc.* **2012**, *95* (4), 1241–1246. https://doi.org/10.1111/j.1551-2916.2011.05030.x.

(112) Yadav, S. K.; Kumari, R.; Gunsaria, R. K. ROLE OF DYE PHOTOSENSITIZER AND SURFACTANT IN SOLAR ENERGY: A REVIEW. *J. Adv. Sci. Res.* **2022**, *13* (04), 12–18. https://doi.org/10.55218/JASR.202213402.

(113) Katoh, R. Quantitative Evaluation of Electron Injection Efficiency in Dye-Sensitized TiO2 Films. *Ambio* **2012**, *41* (Suppl 2), 143–148. https://doi.org/10.1007/s13280-012-0277-2.

(114) Mozaffari, S.; Nateghi, M. R.; Zarandi, M. B. An Overview of the Challenges in the Commercialization of Dye Sensitized Solar Cells. *Renew. Sustain. Energy Rev.* **2017**, *71*, 675–686. https://doi.org/10.1016/j.rser.2016.12.096.

(115) Dokoohaki, M. H.; Zolghadr, A. R.; Klein, A. Highly Efficient Dye-Sensitized Solar Cells Based on Electrolyte Solutions Containing Choline Chloride/Ethylene Glycol Deep Eutectic Solvent: Electrolyte Optimization. *Ind. Eng. Chem. Res.* **2022**, *61* (31), 11464–11473. https://doi.org/10.1021/acs.iecr.2c01324.

(116) Kusama, H.; Arakawa, H. Influence of Alkylaminopyridine Additives in Electrolytes on Dye-Sensitized Solar Cell Performance. *Sol. Energy Mater. Sol. Cells* **2004**, *81* (1), 87–99. https://doi.org/10.1016/j.solmat.2003.09.001.

(117) Ren, Y.; Zhang, D.; Suo, J.; Cao, Y.; Eickemeyer, F. T.; Vlachopoulos, N.; Zakeeruddin, S. M.; Hagfeldt, A.; Grätzel, M. Hydroxamic Acid Pre-Adsorption Raises the Efficiency of Cosensitized Solar Cells. *Nature* **2023**, *613* (7942), 60–65. https://doi.org/10.1038/s41586-022-05460-z.

(118) Nozik, A. J. Quantum Dot Solar Cells. *Phys. E Low-Dimens. Syst. Nanostructures* **2002**, *14* (1), 115–120. https://doi.org/10.1016/S1386-9477(02)00374-0.

(119) Chern, M.; Kays, J. C.; Bhuckory, S.; Dennis, A. M. Sensing with Photoluminescent Semiconductor Quantum Dots. *Methods Appl. Fluoresc.* **2019**, *7* (1), 012005. https://doi.org/10.1088/2050-6120/aaf6f8.

(120) Bera, D.; Qian, L.; Tseng, T.-K.; Holloway, P. H. Quantum Dots and Their Multimodal Applications: A Review. *Materials* **2010**, *3* (4), 2260–2345. https://doi.org/10.3390/ma3042260.

(121) Rasal, A. S.; Yadav, S.; Kashale, A. A.; Altaee, A.; Chang, J.-Y. Stability of Quantum Dot-Sensitized Solar Cells: A Review and Prospects. *Nano Energy* **2022**, *94*, 106854. https://doi.org/10.1016/j.nanoen.2021.106854.

(122) Chung, N. T. K.; Nguyen, P. T.; Tung, H. T.; Phuc, D. H. Quantum Dot Sensitized Solar Cell: Photoanodes, Counter Electrodes, and Electrolytes. *Molecules* **2021**, *26* (9), 2638. https://doi.org/10.3390/molecules26092638.

(123) Yang, Y.; Wang, W. A New Polymer Electrolyte for Solid-State Quantum Dot Sensitized Solar Cells. *J. Power Sources* **2015**, *285*, 70–75. https://doi.org/10.1016/j.jpowsour.2015.03.061.

(124) Aqoma, H.; Lee, S.-H.; Imran, I. F.; Hwang, J.-H.; Lee, S.-H.; Jang, S.-Y. Alkyl Ammonium Iodide-Based Ligand Exchange Strategy for High-Efficiency Organic-Cation Perovskite Quantum Dot Solar Cells. *Nat. Energy* **2024**, *9* (3), 324–332. https://doi.org/10.1038/s41560-024-01450-9.

(125) Cotter, J. E.; Guo, J. H.; Cousins, P. J.; Abbott, M. D.; Chen, F. W.; Fisher, K. C. P-Type Versus n-Type Silicon Wafers: Prospects for High-Efficiency Commercial Silicon Solar Cells. *IEEE Trans. Electron Devices* **2006**, *53* (8), 1893–1901. https://doi.org/10.1109/TED.2006.878026.

(126) ur Rehman, A.; Lee, S. H. Advancements in N-Type Base Crystalline Silicon Solar Cells and Their Emergence in the Photovoltaic Industry. *Sci. World J.* **2013**, *2013* (1), 470347. https://doi.org/10.1155/2013/470347.

(127) Zhang, C.; Zhang, Y.; Guo, H.; Jiang, Q.; Dong, P.; Zhang, C. Efficient Planar Hybrid N-Si/PEDOT:PSS Solar Cells with Power Conversion Efficiency up to 13.31% Achieved by Controlling the SiOx Interlayer. *Energies* **2018**, *11* (6), 1397. https://doi.org/10.3390/en11061397.

(128) Moritz, D. C.; Calvet, W.; Zare Pour, M. A.; Paszuk, A.; Mayer, T.; Hannappel, T.; Hofmann, J. P.; Jaegermann, W. Dangling Bond Defects on Si Surfaces and Their Consequences on Energy Band Diagrams: From a Photoelectrochemical Perspective. *Sol. RRL* **2023**, *7* (9), 2201063. https://doi.org/10.1002/solr.202201063.

(129) Gogolin, R.; Harder, N. P. Trapping Behavior of Shockley-Read-Hall Recombination Centers in Silicon Solar Cells. *J. Appl. Phys.* **2013**, *114* (6), 064504. https://doi.org/10.1063/1.4817910.

(130) Sheng, J.; Fan, K.; Wang, D.; Han, C.; Fang, J.; Gao, P.; Ye, J. Improvement of the SiOx Passivation Layer for High-Efficiency Si/PEDOT:PSS Heterojunction Solar Cells. *ACS Appl. Mater. Interfaces* **2014**, *6* (18), 16027–16034. https://doi.org/10.1021/am503949g.

(131) Zhang, H.; Xu, J.; Wen, Y.; Wang, Z.; Zhang, J.; Ding, W. Conducting Poly(3,4-Ethylenedioxythiophene):Poly(Styrene- Sulfonate) Film Electrode with Superior Long-Term Electrode Stability in Water and Synergistically Enhanced Electrocatalytic Ability for Application in Electrochemical Sensors. *Synth. Met.* **2015**, *204*, 39–47. https://doi.org/10.1016/j.synthmet.2015.03.010.

(132) Seiti, M.; Giuri, A.; Corcione, C. E.; Ferraris, E. Advancements in Tailoring PEDOT: PSS Properties for Bioelectronic Applications: A Comprehensive Review. *Biomater. Adv.* **2023**, *154*, 213655. https://doi.org/10.1016/j.bioadv.2023.213655.

(133) Jonas, F.; Schrader, L. Conductive Modifications of Polymers with Polypyrroles and Polythiophenes. *Synth. Met.* **1991**, *41* (3), 831–836. https://doi.org/10.1016/0379-6779(91)91506-6.

(134) Kirchmeyer, S.; Reuter, K. Scientific Importance, Properties and Growing Applications of Poly(3,4-Ethylenedioxythiophene). *J. Mater. Chem.* **2005**, *15* (21), 2077–2088. https://doi.org/10.1039/B417803N.

(135) Iyer, A.; Hack, J.; Angel Trujillo, D. A.; Tew, B.; Zide, J.; Opila, R. Effects of Co-Solvents on the Performance of PEDOT:PSS Films and Hybrid Photovoltaic Devices. *Appl. Sci.* **2018**, *8* (11), 2052. https://doi.org/10.3390/app8112052.

(136) Lu, B.; Yuk, H.; Lin, S.; Jian, N.; Qu, K.; Xu, J.; Zhao, X. Pure PEDOT:PSS Hydrogels. *Nat. Commun.* **2019**, *10* (1), 1043. https://doi.org/10.1038/s41467-019-09003-5.

(137) Belaineh, D.; Andreasen, J. W.; Palisaitis, J.; Malti, A.; Håkansson, K.; Wågberg, L.; Crispin, X.; Engquist, I.; Berggren, M. Controlling the Organization of PEDOT:PSS on Cellulose Structures. *ACS Appl. Polym. Mater.* **2019**, *1* (9), 2342–2351. https://doi.org/10.1021/acsapm.9b00444.

(138) Ouyang, J.; Xu, Q.; Chu, C.-W.; Yang, Y.; Li, G.; Shinar, J. On the Mechanism of Conductivity Enhancement in Poly(3,4-Ethylenedioxythiophene):Poly(Styrene Sulfonate) Film through Solvent Treatment. *Polymer* **2004**, *45* (25), 8443–8450. https://doi.org/10.1016/j.polymer.2004.10.001.

(139) Palathinkal Thomas, J.; Zhao, L.; McGillivray, D.; Tong Leung, K. High-Efficiency Hybrid Solar Cells by Nanostructural Modification in PEDOT:PSS with Co-Solvent Addition. *J. Mater. Chem. A* **2014**, *2* (7), 2383–2389. https://doi.org/10.1039/C3TA14590E.

(140) McGillivray, D.; Thomas, J. P.; Abd-Ellah, M.; Heinig, N. F.; Leung, K. T. Performance Enhancement by Secondary Doping in PEDOT:PSS/Planar-Si Hybrid Solar Cells. *ACS Appl. Mater. Interfaces* **2016**, *8* (50), 34303–34308. https://doi.org/10.1021/acsami.6b09704.

(141) Feng-Xing, J.; Jing-Kun, X.; Bao-Yang, L.; Yu, X.; Rong-Jin, H.; Lai-Feng, L. Thermoelectric Performance of Poly(3,4-Ethylenedioxythiophene): Poly(Styrenesulfonate). *Chin. Phys. Lett.* **2008**, *25* (6), 2202. https://doi.org/10.1088/0256-307X/25/6/076.

(142) Sangeeth, C. S. S.; Jaiswal, M.; Menon, R. Correlation of Morphology and Charge Transport in Poly(3,4-Ethylenedioxythiophene)–Polystyrenesulfonic Acid (PEDOT–PSS) Films. *J. Phys. Condens. Matter* **2009**, *21* (7), 072101. https://doi.org/10.1088/0953-8984/21/7/072101.

(143) Ouyang, J. "Secondary Doping" Methods to Significantly Enhance the Conductivity of PEDOT:PSS for Its Application as Transparent Electrode of Optoelectronic Devices. *Displays* **2013**, *34* (5), 423–436. https://doi.org/10.1016/j.displa.2013.08.007.

(144) Qian, X.; Qiu, J.; Hu, B.; Yao, J.; Zuo, M.; Wu, Z.; Shan, G.; Song, Y.; Zheng, Q.; Peng, B.; Li, H.; Du, M. Metal-Like Conductivity in Acid-Treated PEDOT:PSS Films: Surpassing 15,000 S/Cm. *ACS Appl. Mater. Interfaces* **2025**, *17* (11), 17164–17178. https://doi.org/10.1021/acsami.4c19958.

(145) Park, C. S.; Lee, C.; Kwon, O. S. Conducting Polymer Based Nanobiosensors. *Polymers* **2016**, *8* (7), 249. https://doi.org/10.3390/polym8070249.

(146) Wang, Z.; Wang, Z.; Zhang, H.; Duan, X.; Xu, J.; Wen, Y. Electrochemical Sensing Application of Poly(Acrylic Acid Modified EDOT- Co -EDOT):PSS and Its Inorganic Nanocomposite with High Soaking Stability, Adhesion Ability and Flexibility. *RSC Adv.* **2015**, *5* (16), 12237–12247. https://doi.org/10.1039/C4RA10970H.

(147) Xia, Y.; Yan, G.; Lin, J. Review on Tailoring PEDOT:PSS Layer for Improved Device Stability of Perovskite Solar Cells. *Nanomaterials* **2021**, *11* (11), 3119. https://doi.org/10.3390/nano11113119.

(148) Butt, M. A. Thin-Film Coating Methods: A Successful Marriage of High-Quality and Cost-Effectiveness—A Brief Exploration. *Coatings* **2022**, *12* (8), 1115. https://doi.org/10.3390/coatings12081115.

(149) Wen, Y.; Xu, J. Scientific Importance of Water-Processable PEDOT–PSS and Preparation, Challenge and New Application in Sensors of Its Film Electrode: A Review. *J. Polym. Sci. Part Polym. Chem.* **2017**, *55* (7), 1121–1150. https://doi.org/10.1002/pola.28482.

(150) Schultheiss, A.; Gueye, M.; Carella, A.; Benayad, A.; Pouget, S.; Faure-Vincent, J.; Demadrille, R.; Revaux, A.; Simonato, J.-P. Insight into the Degradation Mechanisms of Highly Conductive Poly(3,4-Ethylenedioxythiophene) Thin Films. *ACS Appl. Polym. Mater.* **2020**, *2* (7), 2686–2695. https://doi.org/10.1021/acsapm.0c00301.

(151) Jørgensen, M.; Norrman, K.; Krebs, F. C. Stability/Degradation of Polymer Solar Cells. *Sol. Energy Mater. Sol. Cells* **2008**, *92* (7), 686–714. https://doi.org/10.1016/j.solmat.2008.01.005.

(152) Fan, X.; E. Stott, N.; Zeng, J.; Li, Y.; Ouyang, J.; Chu, L.; Song, W. PEDOT:PSS Materials for Optoelectronics, Thermoelectrics, and Flexible and Stretchable Electronics. *J. Mater. Chem. A* **2023**, *11* (35), 18561–18591. https://doi.org/10.1039/D3TA03213B.

(153) Shan, X.; Fang, M.; Wu, L.; Rong, H.; Liao, Q.; Qian, D.; Lin, M. Enhanced Water Resistance of PEDOT:PSS through Crosslinking Agent Incorporation for Efficient and Stable Organic

Solar Cells. *Sci. China Mater.* **2025**, *68* (5), 1452–1461. https://doi.org/10.1007/s40843-024-3273-2.

(154) Yeom, H. R.; Heo, J.; Kim, G.-H.; Ko, S.-J.; Song, S.; Jo, Y.; Kim, D. S.; Walker, B.; Kim, J. Y. Optimal Top Electrodes for Inverted Polymer Solar Cells. *Phys. Chem. Chem. Phys.* **2014**, *17* (3), 2152–2159. https://doi.org/10.1039/C4CP04788E.

(155) Kim, J. B.; Kim, C. S.; Kim, Y. S.; Loo, Y.-L. Oxidation of Silver Electrodes Induces Transition from Conventional to Inverted Photovoltaic Characteristics in Polymer Solar Cells. *Appl. Phys. Lett.* **2009**, *95* (18), 183301. https://doi.org/10.1063/1.3257361.

(156) Nardes, A. M.; Kemerink, M.; de Kok, M. M.; Vinken, E.; Maturova, K.; Janssen, R. A. J. Conductivity, Work Function, and Environmental Stability of PEDOT:PSS Thin Films Treated with Sorbitol. *Org. Electron.* **2008**, *9* (5), 727–734. https://doi.org/10.1016/j.orgel.2008.05.006.

(157) Sun, X.; Lin, T.; Ding, C.; Guo, S.; Ismail, I.; Wang, Z.; Wei, J.; Luo, Q.; Lin, J.; Zhang, D.; Ma, C.-Q. Fabrication of Opaque Aluminum Electrode-Based Perovskite Solar Cells Enabled by the Interface Optimization. *Org. Electron.* **2022**, *104*, 106475. https://doi.org/10.1016/j.orgel.2022.106475.

(158) Semaltianos, N. G. Thermally Evaporated Aluminium Thin Films. *Appl. Surf. Sci.* **2001**, *183* (3), 223–229. https://doi.org/10.1016/S0169-4332(01)00565-7.

(159) Trowell, K. A.; Goroshin, S.; Frost, D. L.; Bergthorson, J. M. Aluminum and Its Role as a Recyclable, Sustainable Carrier of Renewable Energy. *Appl. Energy* **2020**, *275*, 115112. https://doi.org/10.1016/j.apenergy.2020.115112.

(160) Budida, J.; Srinivasan, K. Review of Thin Film Deposition and Techniques. *Mater. Today Proc.* **2023**, *92*, 1030–1033. https://doi.org/10.1016/j.matpr.2023.05.004.

(161) Westwood, W. D. Physical Vapor Deposition. In *Microelectronic Materials and Processes*; Levy, R. A., Ed.; Springer Netherlands: Dordrecht, 1989; pp 133–201. https://doi.org/10.1007/978-94-009-0917-5_4.

(162) Bashir, A.; Awan, T. I.; Tehseen, A.; Tahir, M. B.; Ijaz, M. Chapter 3 - Interfaces and Surfaces. In *Chemistry of Nanomaterials*; Awan, T. I., Bashir, A., Tehseen, A., Eds.; Elsevier, 2020; pp 51–87. https://doi.org/10.1016/B978-0-12-818908-5.00003-2.

(163) Chung, T.-Y.; Cha, H.-C.; Chuang, C.-M.; Tsao, C.-S.; Glowienka, D.; Wang, Y.-H.; Wu, H.-C.; Huang, Y.-C. Developing Screen-Printing Processes for Silver Electrodes Towards All-Solution Coating Processes for Solar Cells. *Polymers* **2024**, *16* (21), 3012. https://doi.org/10.3390/polym16213012.

(164) Aydin, E.; Altinkaya, C.; Smirnov, Y.; Yaqin, M. A.; Zanoni, K. P. S.; Paliwal, A.; Firdaus, Y.; Allen, T. G.; Anthopoulos, T. D.; Bolink, H. J.; Morales-Masis, M.; De Wolf, S. Sputtered Transparent Electrodes for Optoelectronic Devices: Induced Damage and Mitigation Strategies. *Matter* **2021**, *4* (11), 3549–3584. https://doi.org/10.1016/j.matt.2021.09.021.

(165) Song, N.; Deng, S.; Song, N.; Deng, S. Thin Film Deposition Technologies and Application in Photovoltaics. In *Thin Films - Deposition Methods and Applications*; IntechOpen, 2022. https://doi.org/10.5772/intechopen.108026.

(166) Sensors, Data Storage and Communication Technologies. In *Cyber-Physical and Gentelligent Systems in Manufacturing and Life Cycle*; Elsevier, 2017; pp 7–278. https://doi.org/10.1016/B978-0-12-811939-6.00002-9.

(167) Qin, D.; Xia, Y.; Whitesides, G. M. Soft Lithography for Micro- and Nanoscale Patterning. *Nat. Protoc.* **2010**, *5* (3), 491–502. https://doi.org/10.1038/nprot.2009.234.

(168) Knowles, M. R. H.; Rutterford, G.; Karnakis, D.; Ferguson, A. Micro-Machining of Metals, Ceramics and Polymers Using Nanosecond Lasers. *Int. J. Adv. Manuf. Technol.* **2007**, *33* (1), 95–102. https://doi.org/10.1007/s00170-007-0967-2.

(169) Dong, Y.; Chen, L.; Mao, H.; Yang, H. High-Performance Low-Temperature Silver Paste Used for Silicon Heterojunction Solar Cells Through Material Selection and Formulation Optimization. *J. Electron. Mater.* **2025**, *54* (6), 4606–4617. https://doi.org/10.1007/s11664-025-11922-7.

(170) Amin, N.; Santhiran, S.; Kassim, N. M.; Alkahtani, A. A.; Islam, M. A.; Mohd Yusof, M. Y. Impact Analysis of Metallization Design and Recombination Losses on Performance of Crystalline Silicon Solar Cells. *Energies* **2023**, *16* (18), 6505. https://doi.org/10.3390/en16186505.

(171) Mehta, V. R.; Ravindra, N. M. Screen Printing to 3D Printing of Solar Cells—An Overview. In *TMS 2020 149th Annual Meeting & Exhibition Supplemental Proceedings*; Springer International Publishing: Cham, 2020; pp 1935–1944. https://doi.org/10.1007/978-3-030-36296-6_178.

(172) *Handbook of Photovoltaic Science and Engineering*, Repr.; Luque López, A., Hegedus, S., Eds.; Wiley: Chichester, 2009.

(173) *X-Ray Photoelectron Spectroscopy*, 1st ed.; John Wiley & Sons, Ltd, 2011. https://doi.org/10.1002/9781118162897.

(174) Electron Spectroscopy for Surface Analysis. In *Materials Characterization*; John Wiley & Sons, Ltd, 2013; pp 221–251. https://doi.org/10.1002/9783527670772.ch7.

(175) Greczynski, G.; Kugler, T.; Keil, M.; Osikowicz, W.; Fahlman, M.; Salaneck, W. R. Photoelectron Spectroscopy of Thin Films of PEDOT–PSS Conjugated Polymer Blend: A Mini-Review and Some New Results. *J. Electron Spectrosc. Relat. Phenom.* **2001**, *121* (1), 1–17. https://doi.org/10.1016/S0368-2048(01)00323-1.

(176) Jönsson, S. K. M.; Birgerson, J.; Crispin, X.; Greczynski, G.; Osikowicz, W.; Denier Van Der Gon, A. W.; Salaneck, W. R.; Fahlman, M. The Effects of Solvents on the Morphology and Sheet Resistance in Poly(3,4-Ethylenedioxythiophene)–Polystyrenesulfonic Acid (PEDOT–PSS) Films. *Synth. Met.* **2003**, *139* (1), 1–10. https://doi.org/10.1016/S0379-6779(02)01259-6.

(177) Graham, D. J.; Gamble, L. J. Back to the Basics of Time-of-Flight Secondary Ion Mass Spectrometry of Bio-Related Samples. I. Instrumentation and Data Collection. *Biointerphases* **2023**, *18* (2), 021201. https://doi.org/10.1116/6.0002477.

(178) Binnig, G.; Quate, C. F.; Gerber, Ch. Atomic Force Microscope. *Phys. Rev. Lett.* **1986**, *56* (9), 930–933. https://doi.org/10.1103/PhysRevLett.56.930.

(179) García, R. Dynamic Atomic Force Microscopy Methods. *Surf. Sci. Rep.* **2002**, *47* (6–8), 197–301. https://doi.org/10.1016/S0167-5729(02)00077-8.

(180) Tamayo, J.; García, R. Deformation, Contact Time, and Phase Contrast in Tapping Mode Scanning Force Microscopy. *Langmuir* **1996**, *12* (18), 4430–4435. https://doi.org/10.1021/la9601891.

(181) Sanviti, M.; Mester, L.; Hillenbrand, R.; Alegría, A.; Martínez-Tong, D. E. Solvent-Structured PEDOT:PSS Surfaces: Fabrication Strategies and Nanoscale Properties. *Polymer* **2022**, *246*, 124723. https://doi.org/10.1016/j.polymer.2022.124723.

(182) Ouyang, L.; Musumeci, C.; Jafari, M. J.; Ederth, T.; Inganäs, O. Imaging the Phase Separation Between PEDOT and Polyelectrolytes During Processing of Highly Conductive PEDOT:PSS Films. *ACS Appl. Mater. Interfaces* **2015**, *7* (35), 19764–19773. https://doi.org/10.1021/acsami.5b05439.

(183) Pathak, C. S.; Kumar, S. *Recent Developments in Atomic Force Microscopy and Raman Spectroscopy for Materials Characterization*; BoD – Books on Demand, 2022.

(184) Ramadan, A. A.; Gould, R. D.; Ashour, A. On the Van Der Pauw Method of Resistivity Measurements. *Thin Solid Films* **1994**, *239* (2), 272–275. https://doi.org/10.1016/0040-6090(94)90863-X.

(185) *Semiconductor Material and Device Characterization*, 1st ed.; John Wiley & Sons, Ltd, 2005. https://doi.org/10.1002/0471749095.

(186) Kim, Y. H.; Sachse, C.; Machala, M. L.; May, C.; Müller-Meskamp, L.; Leo, K. Highly Conductive PEDOT:PSS Electrode with Optimized Solvent and Thermal Post-Treatment for ITO-Free Organic Solar Cells. *Adv. Funct. Mater.* **2011**, *21* (6), 1076–1081. https://doi.org/10.1002/adfm.201002290.

(187) Emery, K.; Osterwald, C. Measurement of Photovoltaic Device Current as a Function of Voltage, Temperature, Intensity and Spectrum. *Sol. Cells* **1987**, *21* (1–4), 313–327. https://doi.org/10.1016/0379-6787(87)90130-X.

(188) *ASTM E927-19, Standard Specification for Solar Simulation for Photovoltaic Testing. ASTM International, West Conshohocken, PA, 2019 - Google Search*. https://standards.iteh.ai/catalog/standards/astm/a1ce4c3d-c50d-4455-bc3b-3cb535ab657a/astm-e927-19 (accessed 2025-08-06).

(189) Nelson, J. A. *The Physics Of Solar Cells*; World Scientific Publishing Company, 2003.

(190) QEX10 Solar Cell Quantum Efficiency Measurement System. https://pvmeasurements.com/wp-content/uploads/2021/08/PVM_QEX10.pdf (accessed 2025-11-03).

(191) Würfel, P.; Würfel, U. *Physics of Solar Cells: From Basic Principles to Advanced Concepts*; John Wiley & Sons, 2016.

(192) Kolb, F.; El Gemayel, M.; Khan, I.; Dostalek, J.; Trattnig, R.; Sommer, C.; List-Kratochvil, E. J. W. The Impact of Plasmonic Electrodes on the Photocarrier Extraction of Inverted Organic Bulk Heterojunction Solar Cells. *Appl. Phys. Mater. Sci. Process.* **2023**, *129* (3), 230. https://doi.org/10.1007/s00339-023-06492-6.

(193) Li, M.; Ma, H.; Liu, H.; Wu, D.; Niu, H.; Cai, W. Effect of Electrode Geometry on Photovoltaic Performance of Polymer Solar Cells. *J. Phys. Appl. Phys.* **2014**, *47* (43), 435104. https://doi.org/10.1088/0022-3727/47/43/435104.

(194) Zhang, M.; Wilkinson, B.; Liao, Y.; Zheng, J.; Lau, C. F. J.; Kim, J.; Bing, J.; Green, M. A.; Huang, S.; Ho-Baillie, A. W.-Y. Electrode Design to Overcome Substrate Transparency Limitations for Highly Efficient 1 Cm2 Mesoscopic Perovskite Solar Cells. *Joule* **2018**, *2* (12), 2694–2705. https://doi.org/10.1016/j.joule.2018.08.012.

(195) Zhang, T.; Iqbal, S.; Zhang, X.-Y.; Wu, W.; Su, D.; Zhou, H.-L. Recent Advances in Highly Efficient Organic-Silicon Hybrid Solar Cells. *Sol. Energy Mater. Sol. Cells* **2020**, *204*, 110245. https://doi.org/10.1016/j.solmat.2019.110245.

(196) Thomas, J. P.; Rahman, M. A.; Srivastava, S.; Kang, J.-S.; McGillivray, D.; Abd-Ellah, M.; Heinig, N. F.; Leung, K. T. Highly Conducting Hybrid Silver-Nanowire-Embedded Poly(3,4-Ethylenedioxythiophene):Poly(Styrenesulfonate) for High-Efficiency Planar Silicon/Organic Heterojunction Solar Cells. *ACS Nano* **2018**, *12* (9), 9495–9503. https://doi.org/10.1021/acsnano.8b04848.

(197) Khasim, S.; Pasha, A.; Lakshmi, M.; Chellasamy, P.; Kadarkarai, M.; Darwish, A. A. A.; Hamdalla, T. A.; Al-Ghamdi, S. A.; Alfadhli, S. Post Treated PEDOT-PSS Films with Excellent Conductivity and Optical Properties as Multifunctional Flexible Electrodes for Possible Optoelectronic and Energy Storage Applications. *Opt. Mater.* **2022**, *125*, 112109. https://doi.org/10.1016/j.optmat.2022.112109.

(198) Shahrim, N. A.; Ahmad, Z.; Wong Azman, A.; Fachmi Buys, Y.; Sarifuddin, N. Mechanisms for Doped PEDOT:PSS Electrical Conductivity Improvement. *Mater. Adv.* **2021**, *2* (22), 7118–7138. https://doi.org/10.1039/D1MA00290B.

(199) Huang, Y.; Tang, L.; Jiang, Y. Chemical Strategies of Tailoring PEDOT:PSS for Bioelectronic Applications: Synthesis, Processing and Device Fabrication. *CCS Chem.* **2024**, *6* (8), 1844–1867. https://doi.org/10.31635/ccschem.024.202403858.

(200) Khademi, S.; Pourabbas, B.; Foroutani, K. Synthesis and Characterization of Poly(Thiophene-Co-Pyrrole) Conducting Copolymer Nanoparticles via Chemical Oxidative Polymerization. *Polym. Bull.* **2018**, *75* (9), 4291–4309. https://doi.org/10.1007/s00289-017-2264-z.

(201) Kim, J.-R.; Jung, J. H.; Shin, W. S.; So, W.-W.; Moon, S.-J. Efficient TCO-Free Organic Solar Cells with Modified Poly(3,4-Ethylenedioxythiophene): Poly(Styrenesulfonate) Anodes. *J. Nanosci. Nanotechnol.* **2011**, *11* (1), 326–330. https://doi.org/10.1166/jnn.2011.3173.

(202) Greco, C.; Melnyk, A.; Kremer, K.; Andrienko, D.; Daoulas, K. Ch. Generic Model for Lamellar Self-Assembly in Conjugated Polymers: Linking Mesoscopic Morphology and Charge Transport in P3HT. *Macromolecules* **2019**, *52* (3), 968–981. https://doi.org/10.1021/acs.macromol.8b01863.

(203) Łapkowski, M.; Pron, A. Electrochemical oxidation of poly(3,4-ethylenedioxythiophene) — "in situ" conductivity and spectroscopic investigations. *Synthetic Metals* **2000**, https://doi.org/10.1016/S0379-6779(99)00271-4

(204) Mahato, S.; Puigdollers, J.; Voz, C.; Mukhopadhyay, M.; Mukherjee, M.; Hazra, S. Near 5% DMSO Is the Best: A Structural Investigation of PEDOT: PSS Thin Films with Strong Emphasis on Surface and Interface for Hybrid Solar Cell. *Appl. Surf. Sci.* **2020**, *499*, 143967. https://doi.org/10.1016/j.apsusc.2019.143967.

(205) Srivastava, A.; Sharma, R. K.; Sharma, D.; Tawale, J. S.; Agrawal, V. V.; Srivastava, S. K. Unveiling the Role of Ethylene Glycol for Enhanced Performance of PEDOT:PSS/Silicon Hybrid Solar Cells. *Opt. Mater.* **2022**, *134*, 112922. https://doi.org/10.1016/j.optmat.2022.112922.

(206) Srivastava, A.; Sharma, R. K.; Sharma, D.; Kumari, P.; Agrawal, V. V.; Srivastava, S. K. Influence of Alcoholic Polar Surfactants on PEDOT:PSS for Enhanced Performance of Organic/Si Hybrid Solar Cell. *Surf. Interfaces* **2023**, *38*, 102822. https://doi.org/10.1016/j.surfin.2023.102822.

(207) Cruz-Cruz, I.; Reyes-Reyes, M.; Aguilar-Frutis, M. A.; Rodriguez, A. G.; López-Sandoval, R. Study of the Effect of DMSO Concentration on the Thickness of the PSS Insulating Barrier in PEDOT:PSS Thin Films. *Synth. Met.* **2010**, *160* (13), 1501–1506. https://doi.org/10.1016/j.synthmet.2010.05.010.

(208) Howells, C. T.; Saylan, S.; Kim, H.; Marbou, K.; Aoyama, T.; Nakao, A.; Uchiyama, M.; Samuel, I. D. W.; Kim, D.-W.; Dahlem, M. S.; André, P. Influence of Perfluorinated Ionomer in PEDOT:PSS on the Rectification and Degradation of Organic Photovoltaic Cells. *J. Mater. Chem. A* **2018**, *6* (33), 16012–16028. https://doi.org/10.1039/C8TA04098B.

(209) Jørgensen, M.; Norrman, K.; Gevorgyan, S. A.; Tromholt, T.; Andreasen, B.; Krebs, F. C. Stability of Polymer Solar Cells. *Adv. Mater.* **2012**, *24* (5), 580–612. https://doi.org/10.1002/adma.201104187.

(210) Vedovatte, R. M.; Saccardo, M. C.; Costa, E. L.; Cava, C. E. PEDOT:PSS Post-Treated by DMSO Using Spin Coating, Roll-to-Roll and Immersion: A Comparative Study. *J. Mater. Sci. Mater. Electron.* **2020**, *31* (1), 317–323. https://doi.org/10.1007/s10854-019-02524-1.

(211) Lin, Y.-J.; Lee, J.-Y.; Chen, S.-M. Changing Electrical Properties of PEDOT:PSS by Incorporating with Dimethyl Sulfoxide. *Chem. Phys. Lett.* **2016**, *664*, 213–218. https://doi.org/10.1016/j.cplett.2016.10.038.

(212) Lee, I.; Kim, G. W.; Yang, M.; Kim, T.-S. Simultaneously Enhancing the Cohesion and Electrical Conductivity of PEDOT:PSS Conductive Polymer Films Using DMSO Additives. *ACS Appl. Mater. Interfaces* **2016**, *8* (1), 302–310. https://doi.org/10.1021/acsami.5b08753.

(213) Zhang, S.; Kumar, P.; Nouas, A. S.; Fontaine, L.; Tang, H.; Cicoira, F. Solvent-Induced Changes in PEDOT:PSS Films for Organic Electrochemical Transistors. *APL Mater.* **2014**, *3* (1), 014911. https://doi.org/10.1063/1.4905154.

(214) Js, Yeo; Jm, Yun; Dy, Kim; S, Park; Ss, Kim; Mh, Yoon; Tw, Kim; Si, Na Significant Vertical Phase Separation in Solvent-Vapor-Annealed Poly(3,4-Ethylenedioxythiophene):Poly(Styrene Sulfonate) Composite Films Leading to Better Conductivity and Work Function for High-Performance Indium Tin Oxide-Free Optoelectronics. *ACS Appl. Mater. Interfaces* **2012**, *4* (5). https://doi.org/10.1021/am300231v.

(215) Crispin, X.; Jakobsson, F. L. E.; Crispin, A.; Grim, P. C. M.; Andersson, P.; Volodin, A.; van Haesendonck, C.; Van der Auweraer, M.; Salaneck, W. R.; Berggren, M. The Origin of the High Conductivity of Poly(3,4-Ethylenedioxythiophene)−Poly(Styrenesulfonate) (PEDOT−PSS) Plastic Electrodes. *Chem. Mater.* **2006**, *18* (18), 4354–4360. https://pubs.acs.org/doi/10.1021/cm061032%2B.

(216) Zhang, Y.; Wang, Q.; Hu, F.; Wang, Y.; Wu, D.; Wang, R.; Duhm, S. Photoelectron Spectroscopy Reveals the Impact of Solvent Additives on Poly(3,4-Ethylenedioxythiophene):Poly(Styrenesulfonate) Thin Film Formation. *ACS Phys. Chem. Au* **2023**, *3* (3), 311–319. https://doi.org/10.1021/acsphyschemau.2c00073.

(217) Peng, B.; Guo, X.; Cui, C.; Zou, Y.; Pan, C.; Li, Y. Performance Improvement of Polymer Solar Cells by Using a Solvent-Treated Poly(3,4-Ethylenedioxythiophene):Poly(Styrenesulfonate) Buffer Layer. *Appl. Phys. Lett.* **2011**, *98* (24), 243308. https://doi.org/10.1063/1.3600665.

(218) Zhu, Q.; Yildirim, E.; Wang, X.; Soo, X. Y. D.; Zheng, Y.; Tan, T. L.; Wu, G.; Yang, S.-W.; Xu, J. Improved Alignment of PEDOT:PSS Induced by in-Situ Crystallization of "Green" Dimethylsulfone Molecules to Enhance the Polymer Thermoelectric Performance. *Front. Chem.* **2019**, *7*, 783. https://doi.org/10.3389/fchem.2019.00783.

(219) Yildirim, E.; Wu, G.; Yong, X.; Tan, T. L.; Zhu, Q.; Xu, J.; Ouyang, J.; Wang, J.-S.; Yang, S.-W. A Theoretical Mechanistic Study on Electrical Conductivity Enhancement of DMSO Treated PEDOT:PSS. *J. Mater. Chem. C* **2018**, *6* (19), 5122–5131. https://doi.org/10.1039/C8TC00917A.

(220) Yu, L.-M.; Chen, T.; Feng, N.; Wang, R.; Sun, T.; Zhou, Y.; Wang, H.; Yang, Y.; Lu, Z.-H. Highly Conductive and Wettable PEDOT:PSS for Simple and Efficient Organic/c-Si Planar Heterojunction Solar Cells. *Sol. RRL* **2020**, *4* (4), 1900513. https://doi.org/10.1002/solr.201900513.

(221) Pietsch, M.; Bashouti, M. Y.; Christiansen, S. The Role of Hole Transport in Hybrid Inorganic/Organic Silicon/Poly(3,4-Ethylenedioxy-Thiophene):Poly(Styrenesulfonate) Heterojunction Solar Cells. *J. Phys. Chem. C* **2013**, *117* (18), 9049–9055. https://doi.org/10.1021/jp308349f.

(222) Kumar, S. R. S.; Kurra, N.; Alshareef, H. N. Enhanced High Temperature Thermoelectric Response of Sulphuric Acid Treated Conducting Polymer Thin Films. *J. Mater. Chem. C* **2016**, *4* (1), 215–221. https://doi.org/10.1039/C5TC03145A.

(223) Fan, X.; Nie, W.; Tsai, H.; Wang, N.; Huang, H.; Cheng, Y.; Wen, R.; Ma, L.; Yan, F.; Xia, Y. PEDOT:PSS for Flexible and Stretchable Electronics: Modifications, Strategies, and Applications. *Adv. Sci.* **2019**, *6* (19), 1900813. https://doi.org/10.1002/advs.201900813.

(224) Mengistie, D. A.; Wang, P.-C.; Chu, C.-W. Effect of Molecular Weight of Additives on the Conductivity of PEDOT:PSS and Efficiency for ITO-Free Organic Solar Cells. *J. Mater. Chem. A* **2013**, *1* (34), 9907–9915. https://doi.org/10.1039/C3TA11726J.

(225) Sharma, R. K.; Srivastava, A.; Punia, U.; Bansal, R.; Prajapat, P.; Gupta, G.; Srivastava, S. K. Multifunctioning Graphene Oxide Capping Layer for Highly Efficient and Stable PEDOT:PSS–Silicon Hybrid Solar Cells. *Sustain. Energy Fuels* **2024**. https://doi.org/10.1039/D4SE00889H.

(226) Cameron, J.; Skabara, P. J. The Damaging Effects of the Acidity in PEDOT:PSS on Semiconductor Device Performance and Solutions Based on Non-Acidic Alternatives. *Mater. Horiz.* **2020**, *7* (7), 1759–1772. https://doi.org/10.1039/C9MH01978B.

(227) Wang, X.; Ge, M.; Feng, G. The Effects of DMSO on Structure and Properties of PVA/PEDOT:PSS Blended Fiber. *Fibers Polym.* **2015**, *16* (12), 2578–2585. https://doi.org/10.1007/s12221-015-5616-z.

(228) Yousefian, H.; Babaei-Ghazvini, A.; Isari, A. A.; Hashemi, S. A.; Acharya, B.; Ghaffarkhah, A.; Arjmand, M. Solvent-Doped PEDOT:PSS: Structural Transformations towards Enhanced Electrical Conductivity and Transferable Electromagnetic Shields. *Surf. Interfaces* **2024**, *51*, 104481. https://doi.org/10.1016/j.surfin.2024.104481.

(229) Ren, Q.; Qiu, J.; Lv, X.; Li, H.; Yan, L.; Meng, C.; Yang, Y.; Mai, Y. Tailoring the Vertical Morphology of Organic Films for Efficient Planar-Si/Organic Hybrid Solar Cells by Facile Nonpolar Solvent Treatment. *ACS Appl. Mater. Interfaces* **2020**, *12* (22), 25075–25080. https://doi.org/10.1021/acsami.0c02063.

(230) Luo, Z.; Yang, C.; Chen, X.; Ma, W.; Li, S.; Fu, K. Improving Open-Circuit Voltage and Short-Circuit Current of High-Efficiency Silicon-Based Planar Heterojunction Solar Cells by

Combining V2O5 with PEDOT:PSS. *J. Materiomics* **2023**, *9* (3), 438–446. https://doi.org/10.1016/j.jmat.2022.12.008.

(231) Zhang, G.; Peng, H.; Wei, Q.; Zhou, Z.; Wu, H.; Luo, J.; Wang, J.; Wen, X.; Yang, Y. Improving the Performance of Si/PEDOT:PSS Hybrid Solar Cells with More Economical and Environmentally Friendly Alcohol Ether Solvents. *ACS Omega* **2024**, *9* (13), 15040–15051. https://doi.org/10.1021/acsomega.3c09187.

(232) Jiang, L.; Zhou, Z.; Zhang, G.; Li, C.; Feng, Q.; Wei, Q.; Li, J.; Wu, H.; Shi, Y.; Wang, J.; Yang, Y. Waterborne Acrylic Resin-Modified PEDOT:PSS as a Hole-Transporting Layer for Silicon/Organic Solar Cells with Improved Efficiency and Stability. *ACS Appl. Energy Mater.* **2024**, *7* (9), 3927–3936. https://doi.org/10.1021/acsaem.4c00277.

(233) Um, H.-D.; Choi, D.; Choi, A.; Seo, J. H.; Seo, K. Embedded Metal Electrode for Organic–Inorganic Hybrid Nanowire Solar Cells. *ACS Nano* **2017**, *11* (6), 6218–6224. https://doi.org/10.1021/acsnano.7b02322.

(234) Yang, Z.; Gao, P.; He, J.; Chen, W.; Yin, W.-Y.; Zeng, Y.; Guo, W.; Ye, J.; Cui, Y. Tuning of the Contact Properties for High-Efficiency Si/PEDOT:PSS Heterojunction Solar Cells. *ACS Energy Lett.* **2017**, *2* (3), 556–562. https://doi.org/10.1021/acsenergylett.7b00015.

(235) Han, Y.; Liu, Y.; Yuan, J.; Dong, H.; Li, Y.; Ma, W.; Lee, S.-T.; Sun, B. Naphthalene Diimide-Based n-Type Polymers: Efficient Rear Interlayers for High-Performance Silicon-Organic Heterojunction Solar Cells. *ACS Nano* **2017**, *11* (7), 7215–7222. https://doi.org/10.1021/acsnano.7b03090.

(236) Jeong, H.; Song, H.; Pak, Y.; Kwon, I. K.; Jo, K.; Lee, H.; Jung, G. Y. Enhanced Light Absorption of Silicon Nanotube Arrays for Organic/Inorganic Hybrid Solar Cells. *Adv. Mater.* **2014**, *26* (21), 3445–3450. https://doi.org/10.1002/adma.201305394.

(237) Sharma, M.; Pudasaini, P. R.; Ruiz-Zepeda, F.; Elam, D.; Ayon, A. A. Ultrathin, Flexible Organic–Inorganic Hybrid Solar Cells Based on Silicon Nanowires and PEDOT:PSS. *ACS Appl. Mater. Interfaces* **2014**, *6* (6), 4356–4363. https://doi.org/10.1021/am500063w.

(238) Wang, H.-P.; Lin, T.-Y.; Tsai, M.-L.; Tu, W.-C.; Huang, M.-Y.; Liu, C.-W.; Chueh, Y.-L.; He, J.-H. Toward Efficient and Omnidirectional N-Type Si Solar Cells: Concurrent Improvement in Optical and Electrical Characteristics by Employing Microscale Hierarchical Structures. *ACS Nano* **2014**, *8* (3), 2959–2969. https://doi.org/10.1021/nn500257g.

(239) Machín, A.; Márquez, F. Advancements in Photovoltaic Cell Materials: Silicon, Organic, and Perovskite Solar Cells. *Materials* **2024**, *17* (5), 1165. https://doi.org/10.3390/ma17051165.

(240) Schmidt, J.; Titova, V.; Zielke, D. Organic-Silicon Heterojunction Solar Cells: Open-Circuit Voltage Potential and Stability. *Appl. Phys. Lett.* **2013**, *103* (18), 183901. https://doi.org/10.1063/1.4827303.

(241) Schmidt, J.; Peibst, R.; Brendel, R. Surface Passivation of Crystalline Silicon Solar Cells: Present and Future. *Sol. Energy Mater. Sol. Cells* **2018**, *187*, 39–54. https://doi.org/10.1016/j.solmat.2018.06.047.

(242) He, J.; Gao, P.; Yang, Z.; Yu, J.; Yu, W.; Zhang, Y.; Sheng, J.; Ye, J.; Amine, J. C.; Cui, Y. Silicon/Organic Hybrid Solar Cells with 16.2% Efficiency and Improved Stability by Formation of Conformal Heterojunction Coating and Moisture-Resistant Capping Layer. *Adv. Mater.* **2017**, *29* (15), 1606321. https://doi.org/10.1002/adma.201606321.

(243) Ma, S.; Yuan, G.; Zhang, Y.; Yang, N.; Li, Y.; Chen, Q. Development of Encapsulation Strategies towards the Commercialization of Perovskite Solar Cells. *Energy Environ. Sci.* **2022**, *15* (1), 13–55. https://doi.org/10.1039/D1EE02882K.

(244) Groenendaal, L.; Jonas, F.; Freitag, D.; Pielartzik, H.; Reynolds, J. R. Poly(3,4-Ethylenedioxythiophene) and Its Derivatives: Past, Present, and Future. *Adv. Mater.* **2000**, *12* (7), 481–494. https://advanced.onlinelibrary.wiley.com/doi/epdf/10.1002/%28SICI%291521-4095%28200004%2912%3A7%3C481%3A%3AAID-ADMA481%3E3.0.CO%3B2-C.

(245) Xu, B.; Gopalan, S.-A.; Gopalan, A.-I.; Muthuchamy, N.; Lee, K.-P.; Lee, J.-S.; Jiang, Y.; Lee, S.-W.; Kim, S.-W.; Kim, J.-S.; Jeong, H.-M.; Kwon, J.-B.; Bae, J.-H.; Kang, S.-W. Functional Solid Additive Modified PEDOT:PSS as an Anode Buffer Layer for Enhanced Photovoltaic Performance and Stability in Polymer Solar Cells. *Sci. Rep.* **2017**, *7* (1), 45079. https://doi.org/10.1038/srep45079.

(246) Kim, J. Y.; Jung, J. H.; Lee, D. E.; Joo, J. Enhancement of Electrical Conductivity of Poly(3, 4-Ethylenedioxythiophene)/Poly(4-Styrenesulfonate) by a Change of Solvents. *Synth. Met.* **2002**, *126* (2–3), 311–316. https://doi.org/10.1016/S0379-6779(01)00576-8.

(247) Crispin, X.; Marciniak, S.; Osikowicz, W.; Zotti, G.; van der Gon, A. W. D.; Louwet, F.; Fahlman, M.; Groenendaal, L.; De Schryver, F.; Salaneck, W. R. Conductivity, Morphology, Interfacial Chemistry, and Stability of Poly(3,4-Ethylene Dioxythiophene)–Poly(Styrene Sulfonate): A Photoelectron Spectroscopy Study. *J. Polym. Sci. Part B Polym. Phys.* **2003**, *41* (21), 2561–2583. https://doi.org/10.1002/polb.10659.

(248) Lin, Y.-J.; Ni, W.-S.; Lee, J.-Y. Effect of Incorporation of Ethylene Glycol into PEDOT:PSS on Electron Phonon Coupling and Conductivity. *J. Appl. Phys.* **2015**, *117*, 215501. https://doi.org/10.1063/1.4921930.

(249) Alemu, D.; Wei, H.-Y.; Ho, K.-C.; Chu, C.-W. Highly Conductive PEDOT:PSS Electrode by Simple Film Treatment with Methanol for ITO-Free Polymer Solar Cells. *Energy Environ. Sci.* **2012**, *5* (11), 9662–9671. https://doi.org/10.1039/C2EE22595F.

(250) Dimitriev, O. P.; Grinko, D. A.; Noskov, Yu. V.; Ogurtsov, N. A.; Pud, A. A. PEDOT:PSS Films—Effect of Organic Solvent Additives and Annealing on the Film Conductivity. *Synth. Met.* **2009**, *159* (21–22), 2237–2239. https://doi.org/10.1016/j.synthmet.2009.08.022.

(251) Lee, S. H.; Sohn, J. S.; Kulkarni, S. B.; Patil, U. M.; Jun, S. C.; Kim, J. H. Modified Physico–Chemical Properties and Supercapacitive Performance via DMSO Inducement to PEDOT:PSS

Active Layer. *Org. Electron.* **2014**, *15* (12), 3423–3430. https://doi.org/10.1016/j.orgel.2014.09.020.

(252) Chou, T.-R.; Chen, S.-H.; Chiang, Y.-T.; Lin, Y.-T.; Chao, C.-Y. Highly Conductive PEDOT:PSS Films by Post-Treatment with Dimethyl Sulfoxide for ITO-Free Liquid Crystal Display. *J. Mater. Chem. C* **2015**, *3* (15), 3760–3766. https://doi.org/10.1039/C5TC00276A.

(253) Lingstedt, L. V.; Ghittorelli, M.; Lu, H.; Koutsouras, D. A.; Marszalek, T.; Torricelli, F.; Crăciun, N. I.; Gkoupidenis, P.; Blom, P. W. M. Effect of DMSO Solvent Treatments on the Performance of PEDOT:PSS Based Organic Electrochemical Transistors. *Adv. Electron. Mater.* **2019**, *5* (3), 1800804. https://doi.org/10.1002/aelm.201800804.

(254) Dong, J.; Portale, G. Role of the Processing Solvent on the Electrical Conductivity of PEDOT:PSS. *Adv. Mater. Interfaces* **2020**, *7* (18), 2000641. https://doi.org/10.1002/admi.202000641.

(255) Choi, Y. K.; Kim, T. H.; Song, J. H.; Jung, B. K.; Kim, W.; Bae, J. H.; Choi, H. J.; Kwak, J.; Shim, J. W.; Oh, S. J. Charge Transport Transition of PEDOT:PSS Thin Films for Temperature-Insensitive Wearable Strain Sensors. *Nanoscale* **2023**, *15* (17), 7980–7990. https://doi.org/10.1039/D2NR05688G.

(256) Yildirim, E.; Zhu, Q.; Wu, G.; Tan, T. L.; Xu, J.; Yang, S.-W. Self-Organization of PEDOT:PSS Induced by Green and Water-Soluble Organic Molecules. *J. Phys. Chem. C* **2019**, *123* (15), 9745–9755. https://doi.org/10.1021/acs.jpcc.9b01716.

(257) Mahajan, M. S.; Marathe, D. M.; Ghosh, S. S.; Ganesan, V.; Sali, J. V. Changes in In-Plane Electrical Conductivity of PEDOT:PSS Thin Films Due to Electric Field Induced Dipolar Reorientation. *RSC Adv.* **2015**, *5* (105), 86393–86401. https://doi.org/10.1039/C5RA13610E.

(258) Cruz-Cruz, I.; Servín-Quintero, R. I.; Lozano, L. M.; Sustaita, A. O. In-Plane Electrical Conductivity of PEDOT:PSS/Halloysite Composite Thin Films. *Heliyon* **2024**, *10* (20), e39114. https://doi.org/10.1016/j.heliyon.2024.e39114.

(259) van de Ruit, K.; Katsouras, I.; Bollen, D.; van Mol, T.; Janssen, R. A. J.; de Leeuw, D. M.; Kemerink, M. The Curious Out-of-Plane Conductivity of PEDOT:PSS. *Adv. Funct. Mater.* **2013**, *23* (46), 5787–5793. https://doi.org/10.1002/adfm.201301175.

(260) He, W. W.; Wu, K. J.; Wang, K.; Shi, T. F.; Wu, L.; Li, S. X.; Teng, D. Y.; Ye, C. H. Towards Stable Silicon Nanoarray Hybrid Solar Cells. *Sci. Rep.* **2014**, *4* (1), 3715. https://doi.org/10.1038/srep03715.

(261) Wilderspin, T. J.; De Rossi, F.; Watson, T. M. A Simple Method to Evaluate the Effectiveness of Encapsulation Materials for Perovskite Solar Cells. *Sol. Energy* **2016**, *139*, 426–432. https://doi.org/10.1016/j.solener.2016.09.038.

(262) Choi, E. Y.; Kim, J.; Lim, S.; Han, E.; Ho-Baillie, A. W. Y.; Park, N. Enhancing Stability for Organic-Inorganic Perovskite Solar Cells by Atomic Layer Deposited $Al_2O_3$ Encapsulation. *Sol. Energy Mater. Sol. Cells* **2018**, *188*, 37–45. https://doi.org/10.1016/j.solmat.2018.08.016.

(263) Lee, C.-Y.; Tsao, C.-S.; Lin, H.-K.; Cha, H.-C.; Chung, T.-Y.; Sung, Y.-M.; Huang, Y.-C. Encapsulation Improvement and Stability of Ambient Roll-to-Roll Slot-Die-Coated Organic Photovoltaic Modules. *Sol. Energy* **2021**, *213*, 136–144. https://doi.org/10.1016/j.solener.2020.11.021.

(264) Ramasamy, E.; Karthikeyan, V.; Rameshkumar, K.; Veerappan, G. Glass-to-Glass Encapsulation with Ultraviolet Light Curable Epoxy Edge Sealing for Stable Perovskite Solar Cells. *Mater. Lett.* **2019**, *250*, 51–54. https://doi.org/10.1016/j.matlet.2019.04.082.

(265) Mariani, P.; Molina-García, M. Á.; Barichello, J.; Zappia, M. I.; Magliano, E.; Castriotta, L. A.; Gabatel, L.; Thorat, S. B.; Del Rio Castillo, A. E.; Drago, F.; Leonardi, E.; Pescetelli, S.; Vesce, L.; Di Giacomo, F.; Matteocci, F.; Agresti, A.; De Giorgi, N.; Bellani, S.; Di Carlo, A.; Bonaccorso, F. Low-Temperature Strain-Free Encapsulation for Perovskite Solar Cells and Modules Passing Multifaceted Accelerated Ageing Tests. *Nat. Commun.* **2024**, *15* (1), 4552. https://doi.org/10.1038/s41467-024-48877-y.

(266) Dong, X.; Hu, H.; Lin, B.; Ding, J.; Yuan, N. The Effect of ALD-Zno Layers on the Formation of $CH_3NH_3PbI_3$ with Different Perovskite Precursors and Sintering Temperatures. *Chem. Commun.* **2014**, *50* (92), 14405–14408. https://doi.org/10.1039/C4CC04685D.

(267) Sarkar, S.; Culp, J. H.; Whyland, J. T.; Garvan, M.; Misra, V. Encapsulation of Organic Solar Cells with Ultrathin Barrier Layers Deposited by Ozone-Based Atomic Layer Deposition. *Org. Electron.* **2010**, *11* (12), 1896–1900. https://doi.org/10.1016/j.orgel.2010.08.020.

(268) Uddin, A.; Upama, M. B.; Yi, H.; Duan, L. Encapsulation of Organic and Perovskite Solar Cells: A Review. *Coatings* **2019**, *9* (2), 65. https://doi.org/10.3390/coatings9020065.

(269) Yang, W.; Zhang, Y.; Xiao, C.; Yang, J.; Shi, T. A Review of Encapsulation Methods and Geometric Improvements of Perovskite Solar Cells and Modules for Mass Production and Commercialization. *Nano Mater. Sci.* **2025**. https://doi.org/10.1016/j.nanoms.2025.02.005.

(270) Madogni, V. I.; Agbomahéna, M.; Kounouhéwa, B. B.; Douhéret, O.; Lazzaroni, R. Effects of Residual Oxygen in the Degradation of the Performance of Organic Bulk Heterojunction Solar Cells: Stability, Role of the Encapsulation. *Adv. Mater. Phys. Chem.* **2018**, *8* (9), 321–339. https://doi.org/10.4236/ampc.2018.89022.

(271) Ritruksa, M.; Wongrerkdee, S.; Lohawet, K.; Kaewprajak, A.; Kumnorkaew, P.; Wongrerkdee, S. Surface Modification of PEDOT: PSS Film by Chemical Vapor Texturing Process for Enhanced Organic Photovoltaics. *Surf. Interfaces* **2020**, *21*, 100716. https://doi.org/10.1016/j.surfin.2020.100716.

(272) Pathak, C. S.; Singh, J. P.; Singh, R. Effect of Dimethyl Sulfoxide on the Electrical Properties of PEDOT:PSS/*n*-Si Heterojunction Diodes. *Curr. Appl. Phys.* **2015**, *15* (4), 528–534. https://doi.org/10.1016/j.cap.2015.01.020.

(273) Fang, W.; Wang, P.; Ni, Z.; Sun, T.; Xiang, C.; Yue, K.; Wang, R.; Yang, J.; Zhou, Y.; Wang, C.; Yang, Y. Planar Organic-Si Hybrid Solar Cell with MoOx Mixed PEDOT:PSS as Hole

Injection Layer Profits from Mo5+ and Mo6+ Synergistic Effects. *Adv. Mater. Interfaces* **2020**, *7* (19), 2000754. https://doi.org/10.1002/admi.202000754.

(274) Sprachman, M. M.; Wipf, P. A Bifunctional Dimethylsulfoxide Substitute Enhances the Aqueous Solubility of Small Organic Molecules. *Assay Drug Dev. Technol.* **2012**, *10* (3), 269–277. https://doi.org/10.1089/adt.2011.0421.

(275) Sun, Z.; He, Y.; Xiong, B.; Chen, S.; Li, M.; Zhou, Y.; Zheng, Y.; Sun, K.; Yang, C. Performance-Enhancing Approaches for PEDOT:PSS-Si Hybrid Solar Cells. *Angew. Chem. Int. Ed.* **2021**, *60* (10), 5036–5055. https://doi.org/10.1002/anie.201910629.

(276) Niederhausen, J.; Mazzio, K. A.; MacQueen, R. W. Inorganic–Organic Interfaces in Hybrid Solar Cells. *Electron. Struct.* **2021**, *3* (3), 033002. https://doi.org/10.1088/2516-1075/ac23a3.

(277) Koch, N.; Vollmer, A.; Elschner, A. Influence of Water on the Work Function of Conducting Poly(3,4-Ethylenedioxythiophene)/Poly(Styrenesulfonate). *Appl. Phys. Lett.* **2007**, *90* (4), 043512. https://doi.org/10.1063/1.2435350.

(278) Khenkin, M. V.; Katz, E. A.; Abate, A.; Bardizza, G.; Berry, J. J.; Brabec, C.; Brunetti, F.; Bulović, V.; Burlingame, Q.; Di Carlo, A.; Cheacharoen, R.; Cheng, Y.-B.; Colsmann, A.; Cros, S.; Domanski, K.; Dusza, M.; Fell, C. J.; Forrest, S. R.; Galagan, Y.; Di Girolamo, D.; Grätzel, M.; Hagfeldt, A.; von Hauff, E.; Hoppe, H.; Kettle, J.; Köbler, H.; Leite, M. S.; Liu, S. (Frank); Loo, Y.-L.; Luther, J. M.; Ma, C.-Q.; Madsen, M.; Manceau, M.; Matheron, M.; McGehee, M.; Meitzner, R.; Nazeeruddin, M. K.; Nogueira, A. F.; Odabaşı, Ç.; Osherov, A.; Park, N.-G.; Reese, M. O.; De Rossi, F.; Saliba, M.; Schubert, U. S.; Snaith, H. J.; Stranks, S. D.; Tress, W.; Troshin, P. A.; Turkovic, V.; Veenstra, S.; Visoly-Fisher, I.; Walsh, A.; Watson, T.; Xie, H.; Yıldırım, R.; Zakeeruddin, S. M.; Zhu, K.; Lira-Cantu, M. Consensus Statement for Stability Assessment and Reporting for Perovskite Photovoltaics Based on ISOS Procedures. *Nat. Energy* **2020**, *5* (1), 35–49. https://doi.org/10.1038/s41560-019-0529-5.

(279) Ramos-Hernández, R.; Pérez-Gutiérrez, E.; Calvo, F. D.; Beristain, M. F.; Cerón, M.; Percino, M. J. Solvent Effect on Small-Molecule Thin Film Formation Deposited Using the Doctor Blade Technique. *Coatings* **2023**, *13* (2), 425. https://doi.org/10.3390/coatings13020425.

(280) Birnie, D. P. Rational Solvent Selection Strategies to Combat Striation Formation during Spin Coating of Thin Films. *J. Mater. Res.* **2001**, *16* (4), 1145–1154. https://doi.org/10.1557/JMR.2001.0158.

(281) Strawhecker, K. E.; Kumar, S. K.; Douglas, J. F.; Karim, A. The Critical Role of Solvent Evaporation on the Roughness of Spin-Cast Polymer Films. *Macromolecules* **2001**, *34* (14), 4669–4672. https://doi.org/10.1021/ma001440d.

(282) Fowler, P. D.; Ruscher, C.; McGraw, J. D.; Forrest, J. A.; Dalnoki-Veress, K. Controlling Marangoni-Induced Instabilities in Spin-Cast Polymer Films: How to Prepare Uniform Films. *Eur. Phys. J. E* **2016**, *39* (9), 90. https://doi.org/10.1140/epje/i2016-16090-9.

(283) Palumbiny, C. M.; Liu, F.; Russell, T. P.; Hexemer, A.; Wang, C.; Müller-Buschbaum, P. The Crystallization of PEDOT:PSS Polymeric Electrodes Probed In Situ during Printing. *Adv. Mater.* **2015**, *27* (22), 3391–3397. https://doi.org/10.1002/adma.201500315.

(284) Zhanshayeva, L.; Favaron, V.; Lubineau, G. Macroscopic Modeling of Water Uptake Behavior of PEDOT:PSS Films. *ACS Omega* **2019**, *4* (26), 21883–21890. https://doi.org/10.1021/acsomega.9b02866.

(285) Wang, L.; Cao, S.; Sun, K.; Tan, Z.; Li, J.; Liu, H.; Liu, Q.; He, D. Photovoltaic Performance Improvement of PEDOT:PSS/n-Si Hybrid Solar Cells via Device Structural Optimization. *J. Alloys Compd.* **2025**, *1036*, 182054. https://doi.org/10.1016/j.jallcom.2025.182054.

(286) Xiao, P.; Zhang, M.; Wu, X.; Ding, K.; Pan, J.; Jie, J. Enhancing the Efficiency and Stability of Organic/Silicon Solar Cells Using Graphene Electrode and Double-Layer Anti-Reflection Coating. *Sol. Energy* **2022**, *234*, 111–118. https://doi.org/10.1016/j.solener.2022.01.063.

(287) Torres, J. F.; Petrakopoulou, F. A Closer Look at the Environmental Impact of Solar and Wind Energy. *Glob. Chall.* **2022**, *6* (8), 2200016. https://doi.org/10.1002/gch2.202200016.

(288) *Electricity Data Explorer*. Ember. https://ember-energy.org/data/electricity-data-explorer (accessed 2025-06-25).

(289) Chavan, G. T.; Kim, Y.; Khokhar, M. Q.; Hussain, S. Q.; Cho, E.-C.; Yi, J.; Ahmad, Z.; Rosaiah, P.; Jeon, C.-W. A Brief Review of Transparent Conducting Oxides (TCO): The Influence of Different Deposition Techniques on the Efficiency of Solar Cells. *Nanomaterials* **2023**, *13* (7), 1226. https://doi.org/10.3390/nano13071226.

(290) Tepner, S.; Lorenz, A. Printing Technologies for Silicon Solar Cell Metallization: A Comprehensive Review. *Prog. Photovolt. Res. Appl.* **2023**, *31* (6), 557–590. https://doi.org/10.1002/pip.3674.

(291) Burwell, G.; Burridge, N.; Sandberg, O. J.; Bond, E.; Li, W.; Meredith, P.; Armin, A. Metal Grid Structures for Enhancing the Stability and Performance of Solution-Processed Organic Light-Emitting Diodes. *Adv. Electron. Mater.* **2020**, *6* (12), 2000732. https://doi.org/10.1002/aelm.202000732.

(292) Burwell, G.; Burridge, N.; Bond, E.; Li, W.; Meredith, P.; Armin, A. Parameterization of Metallic Grids on Transparent Conductive Electrodes for the Scaling of Organic Solar Cells. *Adv. Electron. Mater.* **2021**, *7* (6), 2100192. https://doi.org/10.1002/aelm.202100192.

(293) Zeng, Y.; Peng, C.-W.; Hong, W.; Wang, S.; Yu, C.; Zou, S.; Su, X. Review on Metallization Approaches for High-Efficiency Silicon Heterojunction Solar Cells. *Trans. Tianjin Univ.* **2022**, *28* (5), 358–373. https://doi.org/10.1007/s12209-022-00336-9.

(294) Khorasani, A.; Mohamadkhani, F.; Marandi, M.; Luo, H.; Abdi-Jalebi, M. Opportunities, Challenges, and Strategies for Scalable Deposition of Metal Halide Perovskite Solar Cells and Modules. *Adv. Energy Sustain. Res.* **2024**, *5* (7), 2300275. https://doi.org/10.1002/aesr.202300275.

(295) Kamel, M. S. A.; Oelgemöller, M.; Jacob, M. V. Chemical Vapor Deposition-Grown Graphene Transparent Conducting Electrode for Organic Photovoltaics: Advances towards Scalable Transfer-Free Synthesis. *Renew. Sustain. Energy Rev.* **2024**, *203*, 114740. https://doi.org/10.1016/j.rser.2024.114740.

(296) Saha, S.; Johnson, M.; Altayaran, F.; Wang, Y.; Wang, D.; Zhang, Q. Electrodeposition Fabrication of Chalcogenide Thin Films for Photovoltaic Applications. *Electrochem* **2020**, *1* (3), 286–321. https://doi.org/10.3390/electrochem1030019.

(297) Kelly, P. J.; Arnell, R. D. Magnetron Sputtering: A Review of Recent Developments and Applications. *Vacuum* **2000**, *56* (3), 159–172. https://doi.org/10.1016/S0042-207X(99)00189-X.

(298) Londhe, P. U.; Desarada, S.; Rane, S.; Chaure, N.; Kale, B. A Novel Combined Thermal Evaporation and Solvothermal Approach to Produce Highly Crystalline and Compact CIG(S1-xSex)2 Thin Films. *Appl. Mater. Today* **2023**, *35*, 101932. https://doi.org/10.1016/j.apmt.2023.101932.

(299) Mecomber, J. S.; Hurd, D.; Limbach, P. A. Enhanced Machining of Micron-Scale Features in Microchip Molding Masters by CNC Milling. *Int. J. Mach. Tools Manuf.* **2005**, *45* (12–13), 1542–1550. https://doi.org/10.1016/j.ijmachtools.2005.01.016.

(300) Lee, J. H.; Yoon, J. W.; Kim, I. G.; Oh, J. S.; Nam, H. J.; Jung, D. Y. Fabrication of Polydimethylsiloxane Shadow Masks for Chemical Solution Deposition of CdS Thin-Film Transistors. *Thin Solid Films* **2008**, *516* (18), 6492–6498. https://doi.org/10.1016/j.tsf.2008.02.041.

(301) Allen, D. M. Photochemical Machining: From 'Manufacturing's Best Kept Secret' to a $6 Billion per Annum, Rapid Manufacturing Process. *CIRP Ann.* **2004**, *53* (2), 559–572. https://doi.org/10.1016/S0007-8506(07)60029-8.

(302) Kay, R.; Desmulliez, M. A Review of Stencil Printing for Microelectronic Packaging. *Solder. Surf. Mt. Technol.* **2012**, *24* (1), 38–50. https://doi.org/10.1108/09540911211198540.

(303) Du, K.; Ding, J.; Liu, Y.; Wathuthanthri, I.; Choi, C.-H. Stencil Lithography for Scalable Micro- and Nanomanufacturing. *Micromachines* **2017**, *8* (4), 131. https://doi.org/10.3390/mi8040131.

(304) Ding, J.; Zhai, Z.; He, J.; Li, J.; Wang, X.; Huang, W. Micro Device Mould Fabrication Based on Two-Photon Polymerization and Electroforming. In *2010 IEEE 5th International Conference on Nano/Micro Engineered and Molecular Systems*; 2010; pp 1074–1078. https://doi.org/10.1109/NEMS.2010.5592564.

(305) Elhami Nik, F.; Matthiesen, I.; Herland, A.; Winkler, T. E. Low-Cost PVD Shadow Masks with Submillimeter Resolution from Laser-Cut Paper. *Micromachines* **2020**, *11* (7), 676. https://doi.org/10.3390/mi11070676.

(306) Cha, C.; Jo, E.; Kim, Y.; Choi, A. J.; Han, K. 3D-Printed Shadow Masks for Micro-Patterned Electrodes. *RSC Adv.* **2024**, *14* (47), 34586–34593. https://doi.org/10.1039/D4RA06298A.

(307) Wojnowski, W.; Marć, M.; Kalinowska, K.; Kosmela, P.; Zabiegała, B. Emission Profiles of Volatiles during 3D Printing with ABS, ASA, Nylon, and PETG Polymer Filaments. *Molecules* **2022**, *27* (12), 3814. https://doi.org/10.3390/molecules27123814.

(308) Romanowski, H.; Bierkandt, F. S.; Luch, A.; Laux, P. Summary and Derived Risk Assessment of 3D Printing Emission Studies. *Atmos. Environ.* **2023**, *294*, 119501. https://doi.org/10.1016/j.atmosenv.2022.119501.

(309) Azimi, P.; Zhao, D.; Pouzet, C.; Crain, N. E.; Stephens, B. Emissions of Ultrafine Particles and Volatile Organic Compounds from Commercially Available Desktop Three-Dimensional Printers with Multiple Filaments. *Environ. Sci. Technol.* **2016**, *50* (3), 1260–1268. https://doi.org/10.1021/acs.est.5b04983.

(310) Chuang, Y.-S.; Berekute, A. K.; Hsu, H.-Y.; Wei, H.-S.; Gong, W.-C.; Hsu, Y.-Y.; Tsai, C.-J.; Yu, K.-P. Assessment of Emissions and Exposure in 3D Printing Workplaces in Taiwan. *J. Occup. Environ. Hyg.* **2024**, *21* (4), 270–286. https://doi.org/10.1080/15459624.2024.2313655.

(311) *A1*. Bambu Lab Wiki. https://wiki.bambulab.com/en/a1 (accessed 2025-06-24).

(312) N. Turner, B.; Strong, R.; A. Gold, S. A Review of Melt Extrusion Additive Manufacturing Processes: I. Process Design and Modeling. *Rapid Prototyp. J.* **2014**, *20* (3), 192–204. https://doi.org/10.1108/RPJ-01-2013-0012.

(313) Fallah, A.; Saleem, Q.; Koc, B. Assessment of Mechanical Properties and Shape Memory Behavior of 4D Printed Continuous Fiber-Reinforced PETG Composites. *Compos. Part Appl. Sci. Manuf.* **2024**, *181*, 108165. https://doi.org/10.1016/j.compositesa.2024.108165.

(314) Pašák, M.; Cuninková, E.; Pekarčíková, M.; Drienovský, M.; Krajčovič, J.; Šimon, Š.; Hulačová, S.; Skarba, M. Thermo-physical and Mechanical Properties of the 3D-printing Materials Applicable for Formers of Superconducting Cables. *Polym. Compos.* **2025**, *46* (8), 7734–7753. https://doi.org/10.1002/pc.29462.

(315) Wang, X.; Liu, W.; Zhou, H.; Liu, B.; Li, H.; Du, Z.; Zhang, C. Study on the Effect of Dispersion Phase Morphology on Porous Structure of Poly (Lactic Acid)/Poly (Ethylene Terephthalate Glycol-Modified) Blending Foams. *Polymer* **2013**, *54* (21), 5839–5851. https://doi.org/10.1016/j.polymer.2013.08.050.

(316) Kahya, Ç.; Tunçel, O.; Çavuşoğlu, O.; Tüfekci, K. Thermal Annealing Optimization for Improved Mechanical Performance of PLA Parts Produced via 3D Printing. *Polym. Test.* **2025**, *144*, 108735. https://doi.org/10.1016/j.polymertesting.2025.108735.

(317) Petousis, M.; Mountakis, N.; Spyridaki, M.; Gkagkanatsiou, K.; Valsamos, I.; Moutsopoulou, A.; Stratakis, E.; Vidakis, N. Process Optimization of Material Extrusion Additive Manufacturing with ASA: Robust Design and Predictive Models for Engineering Response

Metrics. *Int. J. Adv. Manuf. Technol.* **2025**, *138* (9), 4431–4453. https://doi.org/10.1007/s00170-025-15779-2.

(318) Gong, H.; Runzi, M.; Wang, Z.; Wu, L.; Zhang, Y. Influence of Filament Moisture on 3D Printing Nylon. *Technologies* **2025**, *13* (8), 376. https://doi.org/10.3390/technologies13080376.

(319) Novotny, J.; Svobodova, Z.; Ilicova, M.; Hruskova, D.; Kostalova, J.; Bilkova, Z.; Foret, F. Advantages of Stereolithographic 3D Printing in the Fabrication of the Affiblot Device for Dot-Blot Assays. *Mikrochim. Acta* **2024**, *191* (8), 442. https://doi.org/10.1007/s00604-024-06512-z.

(320) Kim, D.; Shim, J.-S.; Lee, D.; Shin, S.-H.; Nam, N.-E.; Park, K.-H.; Shim, J.-S.; Kim, J.-E. Effects of Post-Curing Time on the Mechanical and Color Properties of Three-Dimensional Printed Crown and Bridge Materials. *Polymers* **2020**, *12* (11), 2762. https://doi.org/10.3390/polym12112762.

(321) Zhang, Q.; Davis, A. Y.; Black, M. S. Emissions and Chemical Exposure Potentials from Stereolithography Vat Polymerization 3D Printing and Post-Processing Units. *ACS Chem. Health Saf.* **2022**, *29* (2), 184–191. https://doi.org/10.1021/acs.chas.2c00002.

(322) Keough, M.; McLeod, J. F.; Salomons, T.; Hillen, P.; Pei, Y.; Gibson, G.; McEleney, K.; Oleschuk, R.; She, Z. Realizing New Designs of Multiplexed Electrode Chips by 3-D Printed Masks. *RSC Adv.* **2021**, *11* (35), 21600–21606. https://doi.org/10.1039/D1RA03482K.

(323) Rahiminejad, S.; Köhler, E.; Enoksson, P. Direct 3D Printed Shadow Mask on Silicon. *J. Phys. Conf. Ser.* **2016**, *757*, 012021. https://doi.org/10.1088/1742-6596/757/1/012021.

(324) Rahman, M.; Schott, N. R.; Sadhu, L. K. Glass Transition of ABS in 3D Printing. **2016**.

(325) *Bambu Lab A1 Mini series - FDM 3D printer*. Filament2Print. https://filament2print.com/en/filament-fdm/2327-bambu-lab-a1-mini-series-fdm-3d-printers.html?utm_source=chatgpt.com (accessed 2025-09-23).

(326) Panda, T.; Sadhukhan, S.; Acharyya, S.; Banerjee, P.; Nandi, A.; Bose, S.; Mondal, N.; Das, G.; Maity, S.; Chaudhuri, P.; Saha, H. Impact of Multi-Busbar Front Grid Patterns on the Performance of Industrial Type c-Si Solar Cell. *Sol. Energy* **2022**, *236*, 790–801. https://doi.org/10.1016/j.solener.2022.03.051.

(327) Hannebauer, H.; Dullweber, T.; Baumann, U.; Falcon, T.; Brendel, R. 21.2%-Efficient Fineline-Printed PERC Solar Cell with 5 Busbar Front Grid. *Phys. Status Solidi RRL – Rapid Res. Lett.* **2014**, *8* (8), 675–679. https://doi.org/10.1002/pssr.201409190.

(328) Metz, A.; Adler, D.; Bagus, S.; Blanke, H.; Bothar, M.; Brouwer, E.; Dauwe, S.; Dressler, K.; Droessler, R.; Droste, T.; Fiedler, M.; Gassenbauer, Y.; Grahl, T.; Hermert, N.; Kuzminski, W.; Lachowicz, A.; Lauinger, T.; Lenck, N.; Manole, M.; Martini, M.; Messmer, R.; Meyer, C.; Moschner, J.; Ramspeck, K.; Roth, P.; Schönfelder, R.; Schum, B.; Sticksel, J.; Vaas, K.; Volk, M.; Wangemann, K. Industrial High Performance Crystalline Silicon Solar Cells and

Modules Based on Rear Surface Passivation Technology. *Sol. Energy Mater. Sol. Cells* **2014**, *120*, 417–425. https://doi.org/10.1016/j.solmat.2013.06.025.

(329) Yarbrough, K. A.; Behera, M. K.; Pradhan, S. K.; Bahoura, M. A Novel, Single-Step 3D-Printed Shadow Mask Fabrication Method for TFTs. *Processes* **2025**, *13* (9), 2976. https://doi.org/10.3390/pr13092976.

(330) Wang, X.; Yuan, J.; Wu, X.; Nie, J.; Zhang, Y.; Zhang, X.; Yang, W.; Li, F.; Hoex, B. Higher-Efficiency TOPCon Solar Cells in Mass Production Enabled by Laser-Assisted Firing: Advanced Loss Analysis and Near-Term Efficiency Potential. *Prog. Photovolt. Res. Appl.* **2025**, *33* (7), 771–781. https://doi.org/10.1002/pip.3921.

(331) Flat, A.; Milnes, A. G. Optimization of Multi-Layer Front-Contact Grid Patterns for Solar Cells. *Sol. Energy* **1979**, *23* (4), 289–299. https://doi.org/10.1016/0038-092X(79)90122-1.

(332) Blachowicz, T.; Ehrmann, A. 3D Printed MEMS Technology—Recent Developments and Applications. *Micromachines* **2020**, *11* (4), 434. https://doi.org/10.3390/mi11040434.

(333) Kalkal, A.; Kumar, S.; Kumar, P.; Pradhan, R.; Willander, M.; Packirisamy, G.; Kumar, S.; Malhotra, B. D. Recent Advances in 3D Printing Technologies for Wearable (Bio)Sensors. *Addit. Manuf.* **2021**, *46*, 102088. https://doi.org/10.1016/j.addma.2021.102088.

(334) Lee, Y.-C.; Chen, Y.-C.; Lin, H.-T.; Xu, L.; Lee, M.-T.; Juang, J.-Y. Maskless Deposition of Patterned Transparent Conductive Oxides via Laser-Assisted Atmospheric Pressure Plasma Jet. *J. Alloys Compd.* **2023**, *931*, 167607. https://doi.org/10.1016/j.jallcom.2022.167607.

(335) Selemani, M. A.; Cenhrang, K.; Azibere, S.; Singhateh, M.; Martin, R. S. 3D Printed Microfluidic Devices with Electrodes for Electrochemical Analysis. *Anal. Methods Adv. Methods Appl.* **2024**, *16* (41), 6941–6953. https://doi.org/10.1039/d4ay01701c.

(336) Sebechlebská, T.; Vaněčková, E.; Choińska-Młynarczyk, M. K.; Navrátil, T.; Poltorak, L.; Bonini, A.; Vivaldi, F.; Kolivoška, V. 3D Printed Platform for Impedimetric Sensing of Liquids and Microfluidic Channels. *Anal. Chem.* **2022**, *94* (41), 14426–14433. https://doi.org/10.1021/acs.analchem.2c03191.

(337) Shen, Y.; Li, H.; Li, Y.; Wang, Y.; Chen, K.; Li, J.; Ma, J.; Chen, S.; Hu, Y.; Wen, J.; Hou, X.; Li, J. Designing and Integrating Microfluidic Electrodes for Biosensing and Micromanipulation. *Device* **2025**, 100964. https://doi.org/10.1016/j.device.2025.100964.

(338) Wang, L.; Zhu, W.; Zhang, J.; Zhu, J.-J. Miniaturized Microfluidic Electrochemical Biosensors Powered by Enzymatic Biofuel Cell. *Biosensors* **2023**, *13* (2), 175. https://doi.org/10.3390/bios13020175.

(339) Hornik, T.; Terry, M.; Krause, M.; Catterlin, J. K.; Joiner, K. L.; Aragon, S.; Sarmiento, A.; Arias-Thode, Y. M.; Kartalov, E. P. Experimental Proof of Principle of 3D-Printed Microfluidic Benthic Microbial Fuel Cells (MBMFCs) with Inbuilt Biocompatible Carbon-Fiber Electrodes. *Micromachines* **2024**, *15* (7), 870. https://doi.org/10.3390/mi15070870.

(340) Hu, T.; Zhou, Y.; Lu, T.; Sun, M.; Tu, W.; Zhang, C.; Li, X.; Ni, Z. A 3D-Printed Microfluidic Fuel Cell with Innovative Multichannel Structure for Enhanced Energy Harvesting. *Electrochem. Commun.* **2025**, *177*, 107947. https://doi.org/10.1016/j.elecom.2025.107947.

(341) Janmohammadi, M.; Shi, B.; Adyel, T. M.; McCarthy, D. 3D-Printed Single-Chamber Microbial Fuel Cell Biosensor Reliably Measures Nitrates in Environmental Waters. *J. Environ. Chem. Eng.* **2025**, *13* (3), 116277. https://doi.org/10.1016/j.jece.2025.116277.

(342) Pitaro, M.; Alonso, J. S.; Mario, L. D.; Romero, D. G.; Tran, K.; Zaharia, T.; Johansson, M. B.; Johansson, E. M. J.; Loi, M. A. A Carbazole-Based Self-Assembled Monolayer as the Hole Transport Layer for Efficient and Stable Cs0.25FA0.75Sn0.5Pb0.5I3 Solar Cells. *J. Mater. Chem. A* **2023**, *11* (22), 11755–11766. https://doi.org/10.1039/D3TA01276J.

(343) Li, Z.; Guo, J.; Li, Z.; Han, W.; Ren, G.; Liu, C.; Shen, L.; Guo, W. Incorporating Self-Assembled Silane-Crosslinked Carbon Dots into Perovskite Solar Cells to Improve Efficiency and Stability. *J. Mater. Chem. A* **2020**, *8* (11), 5629–5637. https://doi.org/10.1039/D0TA00123F.

(344) Phung, N.; Verheijen, M.; Todinova, A.; Datta, K.; Verhage, M.; Al-Ashouri, A.; Köbler, H.; Li, X.; Abate, A.; Albrecht, S.; Creatore, M. Enhanced Self-Assembled Monolayer Surface Coverage by ALD NiO in p-i-n Perovskite Solar Cells. *ACS Appl. Mater. Interfaces* **2022**, *14* (1), 2166–2176. https://doi.org/10.1021/acsami.1c15860.

(345) Xia, Y.; Sun, K.; Ouyang, J. Solution-Processed Metallic Conducting Polymer Films as Transparent Electrode of Optoelectronic Devices. *Adv. Mater.* **2012**, *24* (18), 2436–2440. https://doi.org/10.1002/adma.201104795.

(346) Liu, L.; Dong, R.; Ge, H.; Piao, J.; Wang, Y.; Li, S.; Shen, W.; Cao, K.; Chen, S. Basic Amino Acids Modulated Neutral-pH PEDOT:PSS for Stable Blue Perovskite Light-Emitting Diodes. *ACS Appl. Mater. Interfaces* **2022**, *14* (24), 28133–28144. https://doi.org/10.1021/acsami.2c06727.

(347) Liu, D.; Li, Y.; Yuan, J.; Hong, Q.; Shi, G.; Yuan, D.; Wei, J.; Huang, C.; Tang, J.; Fung, M.-K. Improved Performance of Inverted Planar Perovskite Solar Cells with F4-TCNQ Doped PEDOT:PSS Hole Transport Layers. *J. Mater. Chem. A* **2017**, *5* (12), 5701–5708. https://doi.org/10.1039/C6TA10212C.

(348) Srivastava, A.; Sharma, D.; Kumari, P.; Dutta, M.; Srivastava, S. K. Highly Efficient PEDOT:PSS/Silicon Hybrid Solar Cells via Effective Surface Microengineering of Low-Cost Solar-Grade Silicon Wafers. *ACS Appl. Energy Mater.* **2021**, *4* (4), 4181–4198. https://doi.org/10.1021/acsaem.1c00511.

(349) Liu, X.; Coxon, P. R.; Peters, M.; Hoex, B.; Cole, J. M.; Fray, D. J. Black Silicon: Fabrication Methods, Properties and Solar Energy Applications. *Energy Environ. Sci.* **2014**, *7* (10), 3223–3263. https://doi.org/10.1039/C4EE01152J.

(350) Li, K.; Haque, S.; Martins, A.; Fortunato, E.; Martins, R.; Mendes, M. J.; Schuster, C. S. Light Trapping in Solar Cells: Simple Design Rules to Maximize Absorption. *Optica* **2020**, *7* (10), 1377–1384. https://doi.org/10.1364/OPTICA.394885.

(351) Halbwax, M.; Sarnet, T.; Delaporte, Ph.; Sentis, M.; Etienne, H.; Torregrosa, F.; Vervisch, V.; Perichaud, I.; Martinuzzi, S. Micro and Nano-Structuration of Silicon by Femtosecond Laser: Application to Silicon Photovoltaic Cells Fabrication. *Thin Solid Films* **2008**, *516* (20), 6791–6795. https://doi.org/10.1016/j.tsf.2007.12.117.

(352) Asadollahbaik, A.; Boden, S. A.; Charlton, M. D. B.; Payne, D. N. R.; Cox, S.; Bagnall, D. M. Reflectance Properties of Silicon Moth-Eyes in Response to Variations in Angle of Incidence, Polarisation and Azimuth Orientation. *Opt. Express* **2014**, *22* (S2), A402. https://doi.org/10.1364/OE.22.00A402.

(353) Lin, G.; Gao, Z.; Gao, T.; Chen, Y.; Geng, Q.; Li, Y.; Chen, L.; Li, M. Research Progress in Improving the Performance of PEDOT:PSS/Micro- and Nano-Textured Si Heterojunction for Hybrid Solar Cells. *J. Materiomics* **2021**, *7* (5), 1161–1179. https://doi.org/10.1016/j.jmat.2020.12.013.

(354) Jiang, X.; Zhang, P.; Zhang, J.; Wang, J.; Li, G.; Fang, X.; Yang, L.; Chen, X. High Performance of PEDOT:PSS/n-Si Solar Cells Based on Textured Surface with AgNWs Electrodes. *Nanoscale Res. Lett.* **2018**, *13* (1), 53. https://doi.org/10.1186/s11671-018-2462-0.

(355) Savin, H.; Repo, P.; von Gastrow, G.; Ortega, P.; Calle, E.; Garín, M.; Alcubilla, R. Black Silicon Solar Cells with Interdigitated Back-Contacts Achieve 22.1% Efficiency. *Nat. Nanotechnol.* **2015**, *10* (7), 624–628. https://doi.org/10.1038/nnano.2015.89.

(356) Pudasaini, P. R.; Ruiz-Zepeda, F.; Sharma, M.; Elam, D.; Ponce, A.; Ayon, A. A. High Efficiency Hybrid Silicon Nanopillar-Polymer Solar Cells. *ACS Appl. Mater. Interfaces* **2013**, *5* (19), 9620–9627. https://doi.org/10.1021/am402598j.

(357) Parashar, P. K. Effective Suppression of Nano-Textured Black Silicon Surface Recombination Channels through Sputtered Aluminum Oxide: A Comparison Study with ALD Grown Films. *Nanotechnology* **2020**. https://doi.org/10.1088/1361-6528/aba141.

(358) Ju, S.; Byun, M.; Kim, M.; Jun, J.; Huh, D.; Kim, D. S.; Jo, Y.; Lee, H. Fabrication of Perovskite Solar Cell with High Short-Circuit Current Density ($J_{SC)}$ Using Moth-Eye Structure of SiOX. *Nano Res.* **2020**, *13* (4), 1156–1161. https://doi.org/10.1007/s12274-020-2763-3.

(359) Reese, M. O.; Gevorgyan, S. A.; Jørgensen, M.; Bundgaard, E.; Kurtz, S. R.; Ginley, D. S.; Olson, D. C.; Lloyd, M. T.; Morvillo, P.; Katz, E. A.; Elschner, A.; Haillant, O.; Currier, T. R.; Shrotriya, V.; Hermenau, M.; Riede, M.; R. Kirov, K.; Trimmel, G.; Rath, T.; Inganäs, O.; Zhang, F.; Andersson, M.; Tvingstedt, K.; Lira-Cantu, M.; Laird, D.; McGuiness, C.; Gowrisanker, S. (Jimmy); Pannone, M.; Xiao, M.; Hauch, J.; Steim, R.; DeLongchamp, D. M.; Rösch, R.; Hoppe, H.; Espinosa, N.; Urbina, A.; Yaman-Uzunoglu, G.; Bonekamp, J.-B.; van Breemen, A. J. J. M.; Girotto, C.; Voroshazi, E.; Krebs, F. C. Consensus Stability Testing Protocols for Organic Photovoltaic Materials and Devices. *Sol. Energy Mater. Sol. Cells* **2011**, *95* (5), 1253–1267. https://doi.org/10.1016/j.solmat.2011.01.036.

# Appendix

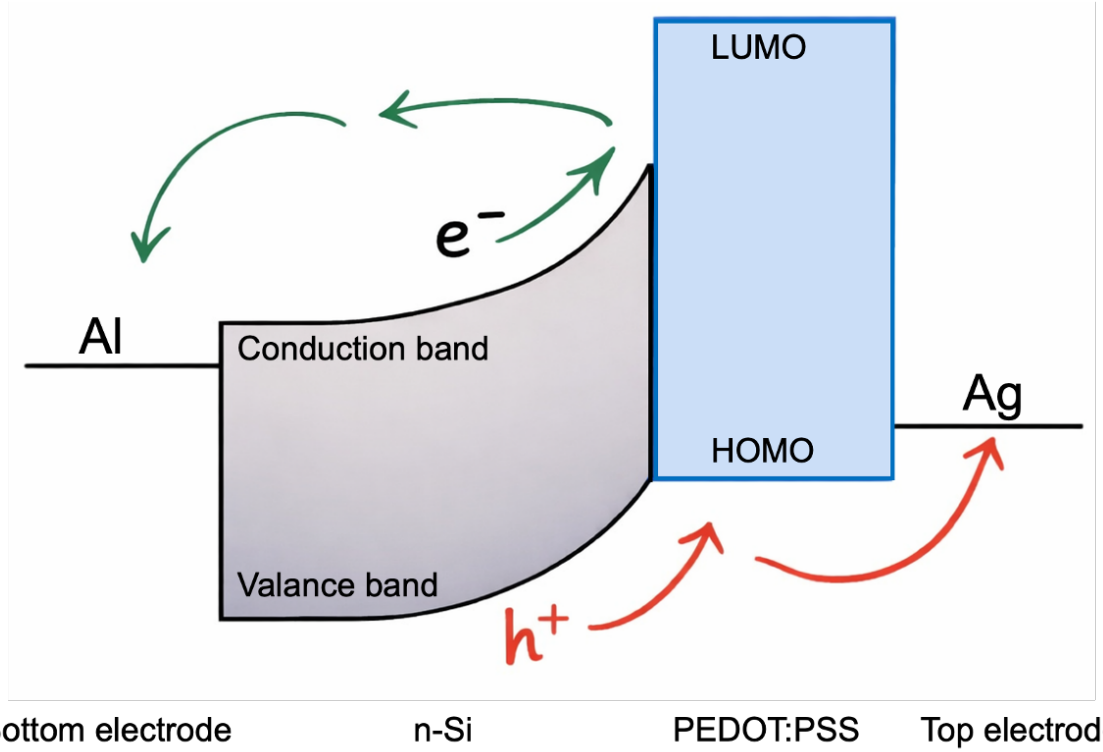



**Figure S1-1:** Energy band diagram of the Al/n-Si/PEDOT:PSS/Ag junction illustrating selective charge transport: electrons are extracted through n-Si to the Al electrode, while holes are transported through PEDOT:PSS to the Ag electrode.

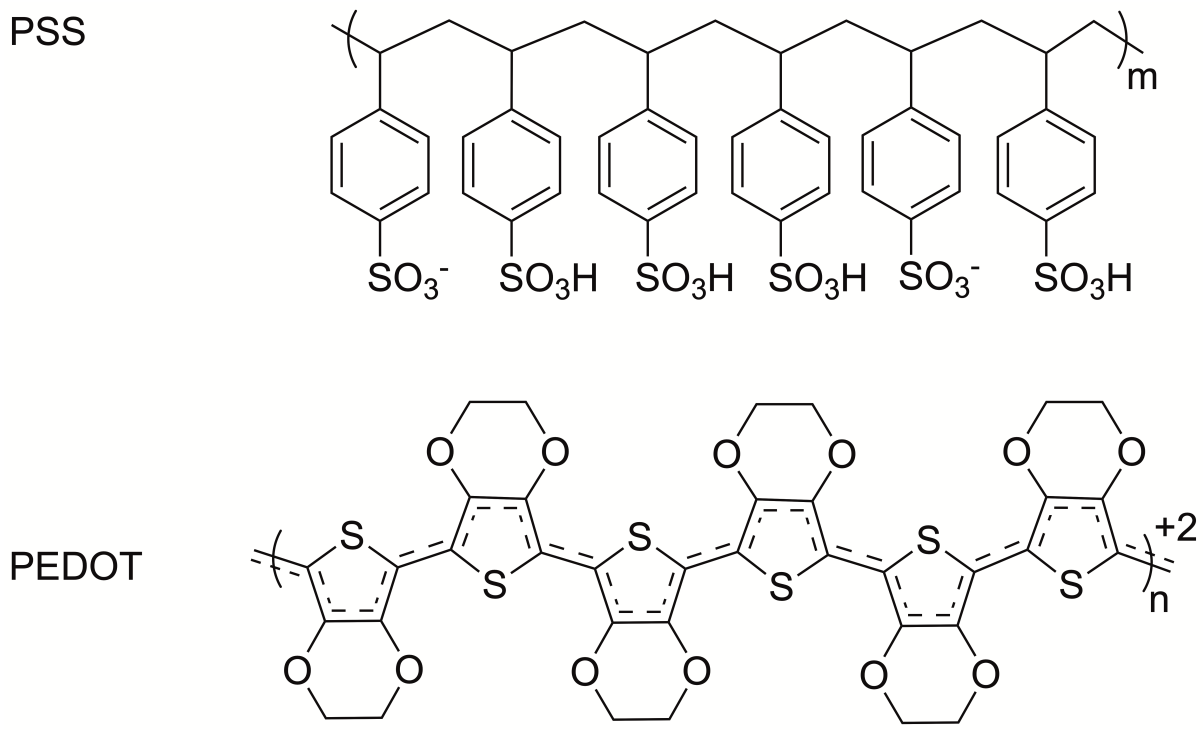



**Figure S1-2:** Chemical structure of the conducting polymer PEDOT:PSS, showing positively charged PEDOT chains electrostatically associated with the sulfonate groups of PSS polyanion.

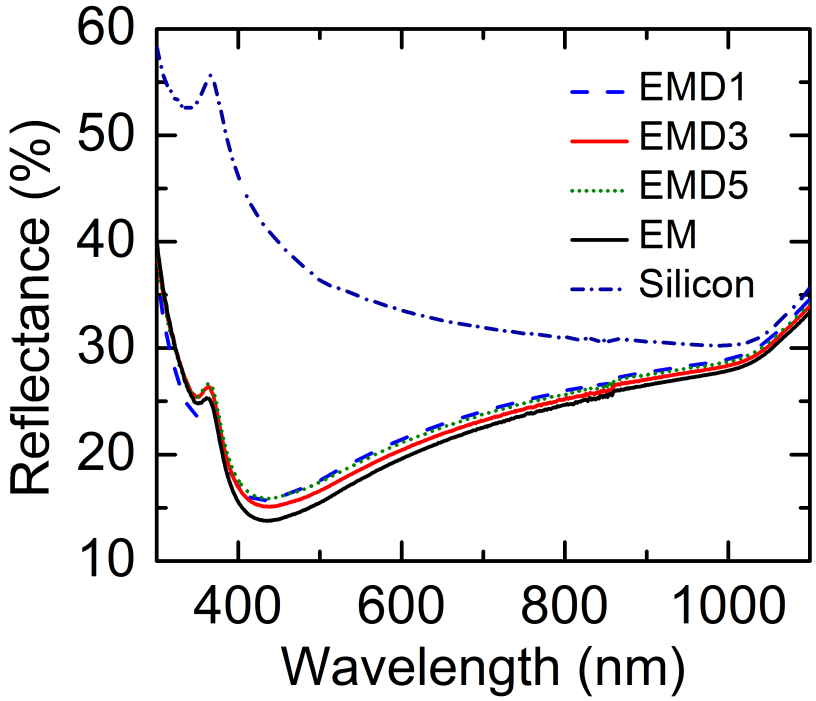



**Figure S2-1:** Reflectance spectra of silicon, and EM, EMD1, EMD3 and EMD5 films deposited on silicon.

**Table S2-1:** Performance data of solar cells fabricated with cosolvent-added PEDOT:PSS EM (used as the control solution), and EM with added DMSO of selected concentrations: 1 wt% (EMD1), 3 wt% (EMD3), and 5 wt% (EMD5).

| Solar cell based on as-deposited PEDOT:PSS film | $J_{SC}$ ($mA/cm^2$) | $V_{OC}$ (mV) | FF (%) | PCE (%) |
|---|---|---|---|---|
| EMD1 | 28.9 | 632.9 | 61.6 | 11.3 |
| EMD3 | 30.1 | 642.4 | 69.4 | 13.4 |
| EMD5 | 27.8 | 571.7 | 60.7 | 9.6 |
| EM | 28.1 | 645.1 | 62.6 | 11.4 |

**Table S2-2:** Performance data of as-fabricated solar cells with cosolvent-added PEDOT:PSS EMD3 and EM films and after ambient storage of selected hours.

| Solar cell sample | $J_{SC}$ ($mA/cm^2$) | $V_{OC}$ (mV) | FF (%) | PCE (%) |
|---|---|---|---|---|
| EMD3 – 0 h | 30.1 | 642.4 | 69.4 | 13.4 |
| EMD3 – 48 h | 29.9 | 631.3 | 66.4 | 12.5 |
| EMD3 – 72 h | 29.6 | 630.6 | 64.1 | 12.0 |
| EMD3 – 144 h | 29.6 | 624.4 | 61.0 | 11.3 |
| EMD3 – 168 h | 29.4 | 617.9 | 58.7 | 10.7 |
| EMD3 – 216 h | 29.2 | 613.0 | 53.9 | 9.7 |
| EM – 0 h | 28.1 | 645.1 | 62.6 | 11.4 |
| EM – 24 h | 28.0 | 579.7 | 45.8 | 7.4 |
| EM – 72 h | 27.7 | 526.8 | 38.9 | 5.7 |

**Table S2-3:** Performance data of solar cells fabricated with cosolvent-added PEDOT:PSS EMD3 and EM films after 72 h of ambient storage. Data for as-fabricated solar cells (without any ambient storage) are given in parentheses. The corresponding reductions (Red.) for the data after 72 h of ambient storage are also given in percentage of the respective as-fabricated values. Percentage changes were computed using unrounded data. The three EMD3 cells separately prepared are labelled as #1, #2, and #3.

| Solar cell sample after 72 h ambient storage | $J_{SC}$ ($mA/cm^2$) | Red. (%) | $V_{OC}$ (mV) | Red. (%) | FF (%) | Red. (%) | PCE (%) | Red. (%) |
|---|---|---|---|---|---|---|---|---|
| EMD3 #1 | 29.6 (30.1) | 1.5 | 630.6 (642.4) | 1.8 | 64.1 (69.4) | 7.5 | 12.0 (13.4) | 10.6 |
| EMD3 #2 | 30.1 (30.3) | 0.5 | 639.5 (648.6) | 1.4 | 53.2 (63.1) | 15.7 | 10.3 (12.4) | 17.3 |
| EMD3 #3 | 30.0 (30.0) | 0.3 | 639.2 (646.1) | 1.1 | 56.6 (64.8) | 12.7 | 10.8 (12.6) | 13.9 |
| Average | 29.9 ± 0.3 (30.1 ± 0.2) | 0.8 | 636.4 ± 5.1 (645.7 ± 3.1) | 1.4 | 58.0 ± 5.6 (65.8 ± 3.3) | 12.0 | 11.0 ± 0.9 (12.8 ± 0.5) | 13.9 |
| EM | 27.7 (28.1) | 1.4 | 526.8 (645.1) | 18.3 | 38.9 (62.6) | 37.9 | 5.7 (11.4) | 50.1 |

**Table S2-4:** Performance data of six solar cells fabricated with cosolvent-added PEDOT:PSS EMD3 films.

| Solar cell as-fabricated with EMD3 | $J_{SC}$ ($mA/cm^2$) | $V_{OC}$ (mV) | FF (%) | PCE (%) |
|---|---|---|---|---|
| #1 | 30.1 | 642.4 | 69.4 | 13.4 |
| #2 | 30.3 | 648.6 | 63.1 | 12.4 |
| #3 | 30.0 | 646.1 | 64.8 | 12.6 |
| #4 | 29.9 | 619.9 | 64.7 | 12.0 |
| #5 | 28.6 | 644.9 | 65.0 | 12.0 |
| #6 | 28.8 | 645.1 | 63.7 | 11.8 |
| Average | 29.6 ± 0.7 | 641.2 ± 10.6 | 65.1 ± 2.2 | 12.4 ± 0.6 |

**Table S2-5:** Repeated measurement test of performance data for solar cells fabricated with cosolvent-added PEDOT:PSS EMD3 and EM films

| Solar cell as-fabricated with cosolvent-added PEDOT:PSS | $J_{SC}$ ($mA/cm^2$) | $V_{OC}$ (mV) | FF (%) | PCE (%) |
|---|---|---|---|---|
| EMD3 – first measurement | 29.9 | 642.2 | 69.3 | 13.3 |
| EMD3 – second measurement | 30.1 | 642.4 | 69.4 | 13.4 |
| Average | 30.0 ± 0.1 | 642.3 ± 0.1 | 69.4 ± 0.1 | 13.4± 0.1 |
| | | | | |
| EM – first measurement | 28.03 | 643.8 | 62.6 | 11.3 |
| EM – second measurement | 28.1 | 645.1 | 62.6 | 11.4 |
| Average | 28.1 ± 0.1 | 644.5 ± 0.9 | 62.6 ± 0.0 | 11.4 ± 0.1 |

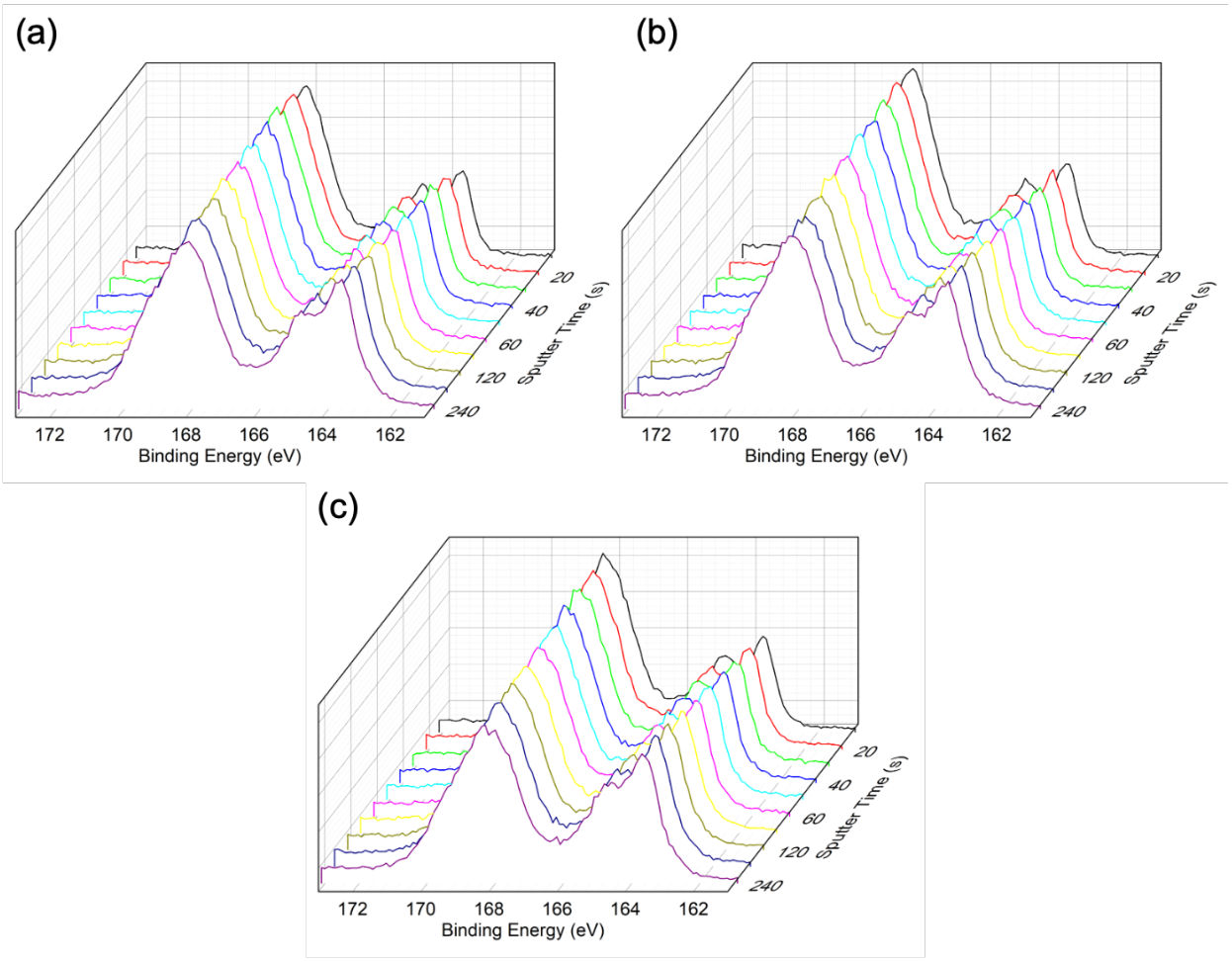



**Figure S3-1:** Depth-profiling XPS spectra of the S 2p region for (a) EM, (b) ED2 and (c) EMD2 films deposited on silicon as functions of sputtering time.

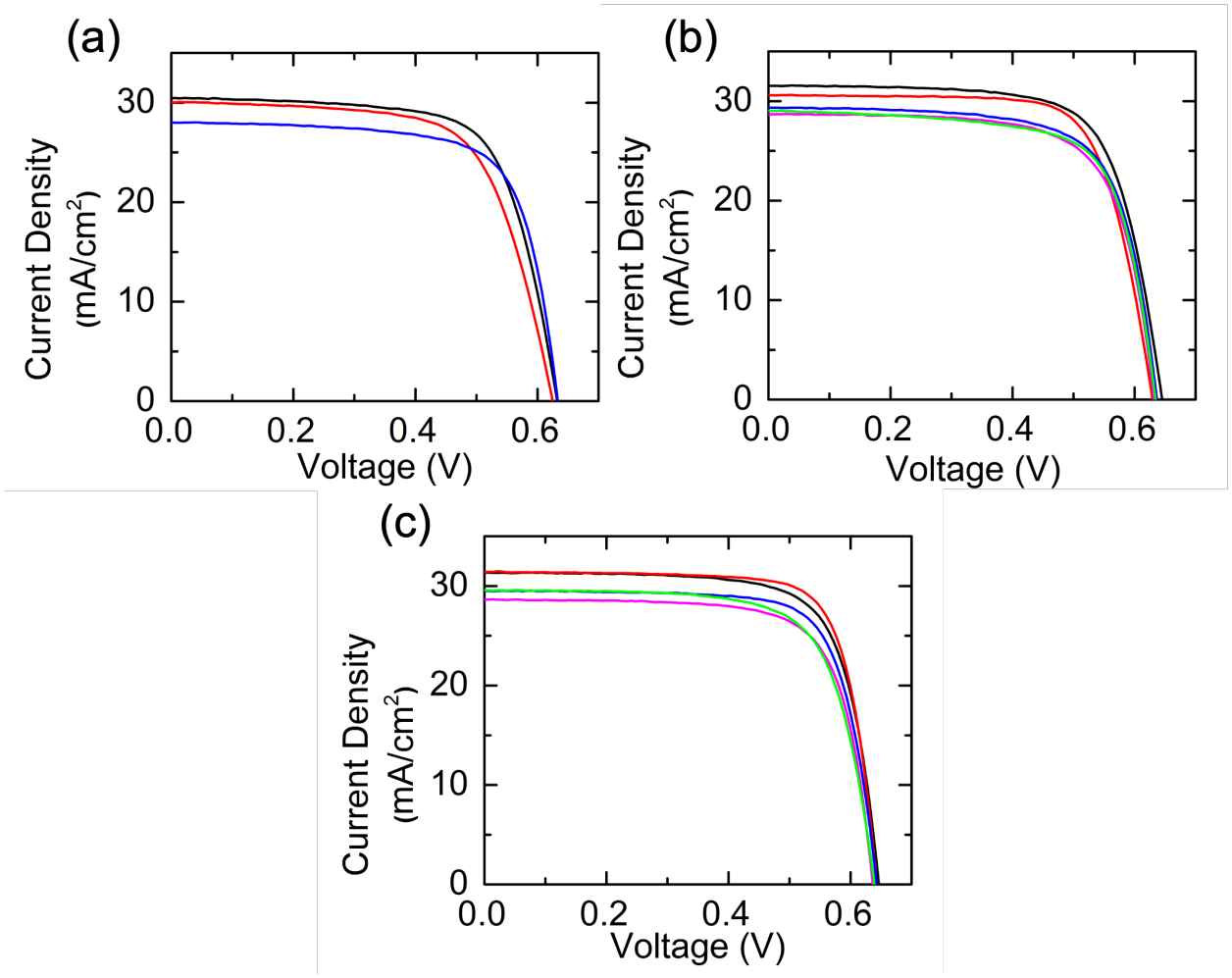



**Figure S3-2:** Current density-voltage (J-V) curves for as-fabricated (a) EM, (b) ED2 and (c) EMD2 solar cell samples.

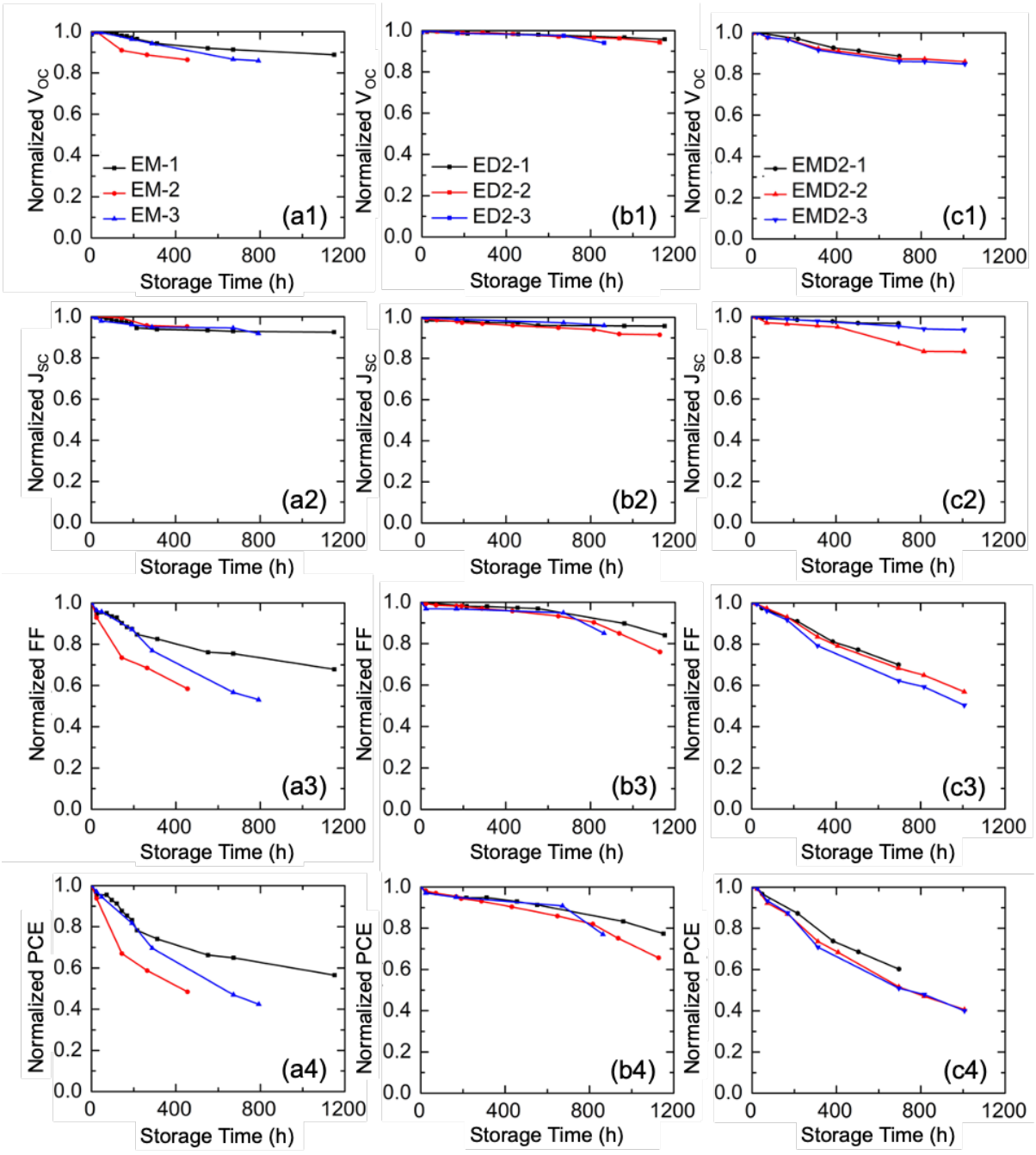



**Figure S3-3:** Degradation trends of solar cell performance metrics normalized to their respective as-fabricated value: $V_{OC}$, $J_{SC}$, FF and PCE as functions of ambient storage time for (a) EM (b) ED2 and (c) EMD2 solar cells.

**Table S3-1:** Initial PCE, PCE at $T_{80}$ (80% of the initial PCE), and corresponding $T_{80}$ duration for EM, ED2, and EMD2 solar cells. When the 80%-point falls between two measurement points, $T_{80}$ is obtained by linear interpolation. Average values are reported as mean ± standard deviation.

| Samples | Initial PCE (%) | PCE at $T_{80}$ (%) | $T_{80}$ (h) |
|---|---|---|---|
| EM-1 | 13.41 | 10.73 | 208.46 |
| EM-2 | 12.67 | 10.14 | 85.78 |
| EM-3 | 12.52 | 10.02 | 205.78 |
| Average | 12.87 ± 0.48 | 10.30 ± 0.38 | 166.44 ± 69.86 |
| ED2-1 | 14.48 | 11.58 | 1065.76 |
| ED2-2 | 13.21 | 10.57 | 850.81 |
| ED2-3 | 12.80 | 10.24 | 822.85 |
| Average | 13.50 ± 0.88 | 10.80 ± 0.70 | 913.14 ± 132.91 |
| EMD2-1 | 14.19 | 13.35 | 306.61 |
| EMD2-2 | 15.50 | 12.40 | 243.44 |
| EMD2-3 | 13.36 | 10.69 | 232.91 |
| Average | 14.35 ± 1.08 | 12.15 ± 1.35 | 260.99 ± 39.86 |

For silicon/PEDOT:PSS solar cells (and not perovskites solar cells), linear interpolation is acceptable and used in IEC 61215, ISOS-D-1 protocols.[359] The following linear interpolation formula is used:

$$T_{80} = t_1 + (t_2 - t_1) \times \frac{PCE_{t1} - PCE_{target}}{PCE_{t1} - PCE_{t2}} \qquad \text{(Equation S3-1)}$$

where $PCE_{t1}$ and $PCE_{t2}$ are two PCE measurement points at $t_1$ and $t_2$, respectively, that are adjacent to the $PCE_{target}$ (i.e. 80% of the PCE value for the as-fabricated cell)

**Table S4-1:** Solar cell performance data of EMD2 solar cells fabricated with selected 3D-printed top electrode designs (comb-like busbar, crossed busbar, and central busbar). The last digit in the cell label identifies the cell number. For example, there are three separate cells made with comb-like busbar top electrodes, and they are numbered by 1 to 3 for the last digit.

| **Comb-like busbar** | **$V_{OC}$ (mV)** | **$J_{SC}$ (mA/cm$^2$)** | **FF (%)** | **PCE (%)** |
|---|---|---|---|---|
| EMD2-1 | 634.4 | 29.1 | 63.6 | 11.9 |
| EMD2-2* | 646.1 | 29.8 | 63.2 | 12.2 |
| EMD2-3 | 633.7 | 29.1 | 63.4 | 11.7 |
| Average | 641.1 ± 6.5 | 29.3 ± 0.4 | 63.4 ± 0.2 | 11.9 ± 0.3 |
| **Crossed busbar** | **$V_{OC}$ (mV)** | **$J_{SC}$ (mA/cm$^2$)** | **FF (%)** | **PCE (%)** |
| EMD2-1 | 625 | 26.6 | 70.4 | 11.7 |
| EMD2-2 | 633.1 | 27.4 | 70.7 | 12.3 |
| EMD2-3* | 641.9 | 27.7 | 73.1 | 13.0 |
| EMD2-4 | 618.2 | 27.9 | 67.5 | 11.6 |
| Average | 629.6 ± 10.2 | 27.4 ± 0.6 | 70.4 ± 2.3 | 12.2 ± 0.6 |
| **Central busbar** | **$V_{OC}$ (mV)** | **$J_{SC}$ (mA/cm$^2$)** | **FF (%)** | **PCE (%)** |
| EMD2-1 | 643.2 | 29.5 | 74.7 | 14.2 |
| EMD2-2* | 642.8 | 31.6 | 76.5 | 15.5 |
| EMD2-3 | 636.4 | 28.6 | 73.4 | 13.4 |
| EMD2-4 | 646.3 | 31.3 | 73.5 | 14.9 |
| EMD2-5 | 639.0 | 29.6 | 71.2 | 13.4 |
| Average | 641.5 ± 3.9 | 30.1 ± 1.3 | 73.8 ± 2 | 14.3 ± 0.9 |

*The most efficient (i.e. best performing) cell in each group is the sample used for Figure 4.7.

**Table S4-2:** Solar cell performance data of ED2 solar cells fabricated with selected 3D-printed top electrode designs (comb-like busbar, crossed busbar, and central busbar). The last digit in the cell label identifies the cell number. For example, there are four separate cells made with comb-like busbar top electrodes, and they are numbered by 1 to 4 by the last digit.

| **Comb-like busbar** | **$V_{OC}$ (mV)** | **$J_{SC}$ (mA/cm$^2$)** | **FF (%)** | **PCE (%)** |
|---|---|---|---|---|
| ED2-1* | 620.9 | 29.2 | 66.0 | 12.0 |
| ED2-2 | 635.6 | 27.7 | 60.7 | 10.7 |
| ED2-3 | 613.9 | 29.4 | 60.4 | 10.9 |
| ED2-4 | 641.8 | 28.9 | 59.2 | 11.0 |
| Average | 628.1 ± 12.9 | 28.8 ± 0.8 | 61.6 ± 3.0 | 11.1 ± 0.6 |
| **Crossed busbar** | **$V_{OC}$ (mV)** | **$J_{SC}$ (mA/cm$^2$)** | **FF (%)** | **PCE (%)** |
| ED2-1 | 619.4 | 25.9 | 67.7 | 10.9 |
| ED2-2* | 631.1 | 26.7 | 73.0 | 12.3 |
| ED2-3 | 624.5 | 26.6 | 68.8 | 11.4 |
| ED2-4 | 629.2 | 24.4 | 69.1 | 10.6 |
| Average | 626.1 ± 5.2 | 25.9 ± 1.0 | 69.6 ± 2.3 | 11.3 ± 0.7 |
| **Central busbar** | **$V_{OC}$ (mV)** | **$J_{SC}$ (mA/cm$^2$)** | **FF (%)** | **PCE (%)** |
| ED2-1* | 645.1 | 31.6 | 71.1 | 14.5 |
| ED2-2 | 636.6 | 29.4 | 70.7 | 13.2 |
| ED2-3 | 632.3 | 28.7 | 70.6 | 12.8 |
| ED2-4 | 629.4 | 30.6 | 73 | 14.1 |
| ED2-5 | 634.5 | 29.0 | 70.7 | 13.0 |
| Average | 635.6 ± 6 | 29.8 ± 1.2 | 71.2 ± 1 | 13.5 ± 0.7 |

*The most efficient (i.e. best performing) cell in each group is the sample used for Figure 4.7.